

STUDIES ON PLASMA ANODIZATION IN A DC GLOW DISCHARGE

by

Graham Olive

B.Sc., Brunel University 1965

M.A.Sc., University of British Columbia 1970

A THESIS SUBMITTED IN PARTIAL FULFILMENT OF
THE REQUIREMENTS FOR THE DEGREE OF
DOCTOR OF PHILOSOPHY

in the Department
of
Electrical Engineering

We accept this thesis as conforming to the
required standard

THE UNIVERSITY OF BRITISH COLUMBIA

August 1973

In presenting this thesis in partial fulfilment of the requirements for an advanced degree at the University of British Columbia, I agree that the Library shall make it freely available for reference and study. I further agree that permission for extensive copying of this thesis for scholarly purposes may be granted by the Head of my Department or by his representatives. It is understood that copying or publication of this thesis for financial gain shall not be allowed without my written permission.

Department of

Electrical Engineering

The University of British Columbia
Vancouver 8, Canada

Date

Oct 9th '73

ABSTRACT

The phenomenon of anodization in the plasma of a dc low pressure oxygen glow discharge is investigated, both from the viewpoint of the mechanisms involved and for potential applications. Aspects studied include the effect of discharge conditions on anodization rate, the significance of negative oxygen ions in the plasma, the ionic current-field strength relation in the oxide, and the anodization of metal films on silicon for MIS devices.

It was found that the process does not utilize gaseous negative ions from the neutral plasma, and that species transport through the oxide is by high field ionic conduction. The variation of anodization rate with discharge conditions was attributed principally to a dependence of the oxide field strength on the electron energy distribution and density in the plasma. Double oxide layer MIS structures were fabricated, and charge storage effects were investigated.

TABLE OF CONTENTS

| | <u>Page</u> |
|---|-------------|
| ABSTRACT | i |
| TABLE OF CONTENTS | ii |
| LIST OF ILLUSTRATIONS | v |
| LIST OF TABLES | x |
| ACKNOWLEDGEMENT | xi |
| 1. INTRODUCTION | 1 |
| 2. REVIEW OF PREVIOUS WORK ON PLASMA ANODIZATION | 4 |
| 3. COMPARISON OF PLASMA- AND SOLUTION-ANODIZATION | 7 |
| 3.1 General Features of Solution Anodization | 7 |
| 3.2 The High Field Ionic Conduction Process - Classical Theory | 9 |
| 3.3 General Features of Plasma Anodization | 12 |
| 4. THEORETICAL ASPECTS OF PLASMA ANODIZATION | 17 |
| 4.1 Introduction | 17 |
| 4.2 Plasma Sheath Theory | 17 |
| 4.2.1 General | 17 |
| 4.2.2 The Plasma Anodization Case | 20 |
| 4.3 The Metal/Oxide/Space Charge Sheath/Plasma System | 20 |
| 4.4 The Formation of Gaseous Negative Ions | 26 |
| 4.5 The Low Pressure Cold Cathode Glow Discharge in Oxygen | 29 |
| 5. PROBE TECHNIQUES IN PLASMA DIAGNOSTICS | 35 |
| 5.1 Introduction | 35 |
| 5.2 Simplified Treatment of the Langmuir Probe Method | 35 |
| 5.3 The Effect of Negative Ions on Langmuir Probe Measurements | 40 |
| 6. THE APPLICATION OF ELLIPSONOMETRY TO ANODIZATION STUDIES | 42 |
| 6.1 Introduction | 42 |
| 6.2 Principles of Ellipsometry | 43 |
| 6.2.1 Reflection of a Plane Wave at an Interface Between Two Isotropic Media and at a Film- Covered Surface | 43 |
| 6.2.2 The Poincaré Sphere Representation of Ellip- cally Polarized Light | 45 |

| | <u>Page</u> |
|--|-------------|
| 6.2.3 Theory and Operation of the Ellipsometer | 49 |
| 6.2.4 The Analysis of Ellipsometry Data | 54 |
| 7. EXPERIMENTAL CONSIDERATIONS | 58 |
| 7.1 The Discharge Tube and Vacuum System - Design and Fabrication | 58 |
| 7.2 The Optical System | 65 |
| 7.2.1 The Automated Ellipsometer | 65 |
| 7.2.2 Ellipsometer Alignment | 69 |
| 7.2.3 Treatment of Errors in <u>in situ</u> Ellipsometry | 76 |
| 8. INVESTIGATION OF DISCHARGE PARAMETERS AFFECTING RATES OF ANODIZATION | 82 |
| 8.1 Introduction | 82 |
| 8.2 Sample Preparation | 82 |
| 8.3 Measurements and Results | 84 |
| 8.3.1 Optical Constants of the Substrates | 84 |
| 8.3.2 Oxygen Flow Through the Cell | 90 |
| 8.3.3 Plasma Density | 91 |
| 8.3.4 Gas Pressure | 98 |
| 8.3.5 Discharge Current | 105 |
| 8.3.6 Sample Current Density | 106 |
| 8.4 Discussion | 112 |
| 9. THE ROLE OF PLASMA NEGATIVE IONS | 121 |
| 9.1 Introduction | 121 |
| 9.2 Electron Filter Experiments | 122 |
| 9.3 Modulation of the Negative Ion Flux to a Sample by the Simultaneous Application of rf and dc Biases | 128 |
| 9.3.1 Constant dc Voltage Approach | 128 |
| 9.3.2 Constant dc Current Approach | 132 |
| 9.3.3 Experiment and Results | 135 |
| 9.3.4 Discussion | 138 |
| 10. THE RELATION BETWEEN OXIDE GROWTH RATE, ELECTRIC FIELD STRENGTH IN THE OXIDE AND OXIDE TEMPERATURE DURING PLASMA ANODIZATION | 140 |
| 10.1 Introduction | 140 |
| 10.2 The Estimation of Field Strengths in the Oxide | 141 |
| 10.3 Variation of Voltage with Time at Constant Total Current | 145 |
| 10.4 Voltage vs. Thickness for Steady-state Conditions | 147 |
| 10.5 Thickness and Oxide Potential Difference vs. Time During a Formation | 147 |

| | <u>Page</u> |
|---|-------------|
| 10.6 Variation of Ionic Current with Estimated Oxide Field | 147 |
| 10.7 Dependence of Ionic Current on Temperature | 155 |
| 10.8 Discussion | 162 |
| 11. THE PRODUCTION OF DIELECTRIC FILMS FOR METAL-INSULATOR- SEMICONDUCTOR DEVICES | 165 |
| 11.1 Introduction | 165 |
| 11.2 Dielectric Materials for Gate Insulation | 166 |
| 11.3 Brief Review of Recent Work on Metal Oxide Thin Films Useful for Gate Insulation | 168 |
| 11.4 Plasma Anodization of Metal Films on Silicon | 169 |
| 11.4.1 Introduction | 169 |
| 11.4.2 Ellipsometric Considerations | 170 |
| 11.4.3 C(V) Measurements | 173 |
| 11.4.4 Experimental | 177 |
| 11.4.5 Results | 179 |
| 11.5 Discussion | 188 |
| 12. CONCLUSIONS | 192 |
| REFERENCES | 195 |
| APPENDICES | 201 |
| Appendix A: Velocity and Energy Distributions | 201 |
| Appendix B: Mean Free Path Lengths and Sheath Thickness | 202 |
| Appendix C: The 'Sounding Probe' Method of Determining Plasma Potential | 205 |
| Appendix D: Summary of in situ Ellipsometry Results for the Plasma Anodization of Niobium and Tantalum | 207 |

LIST OF ILLUSTRATIONS

| | | <u>Page</u> |
|----------|--|-------------|
| Fig. 3.1 | Supposed potential energy of ion versus distance with and without an applied field | 11 |
| Fig. 3.2 | Biasing arrangements for plasma anodization | 14 |
| Fig. 4.1 | One-dimensional electron energy band diagram for an oxide-covered metal sample drawing a current density less than $(j_{es} + j_{+s})$, and nearby floating probe | 21 |
| Fig. 4.2 | Electrostatic field and potential distributions in the metal/oxide/space charge sheath/plasma system, neglecting potential gradients in plasma | 23 |
| Fig. 4.3 | The space charge, electric field and potential distributions in the dc cold cathode glow discharge | 30 |
| Fig. 5.1 | Ideal current-voltage characteristics of a Langmuir probe | 37 |
| Fig. 6.1 | Reflection and refraction at an interface | 44 |
| Fig. 6.2 | The locus of the electric vector for elliptically polarized light in a plane normal to the direction of propagation | 46 |
| Fig. 6.3 | Representation of polarized light on the Poincaré sphere | 48 |
| Fig. 6.4 | Arrangement of the ellipsometer | 50 |
| Fig. 6.5 | Poincaré sphere representation of an ellipsometer null | 52 |
| Fig. 6.6 | Computed ellipsometry curves for single film ($N_1 = 2.25$) on niobium ($N_2 = 3.6 - j3.6$) at $\theta_0 = 65^\circ$ and $\lambda = 5461\text{\AA}$ in air and water | 55 |
| Fig. 6.7 | Two layer model | 56 |
| Fig. 7.1 | Schematic of anodization cell and pumping station (system B) | 59 |
| Fig. 7.2 | The water-cooled adjustable sample holder | 61 |
| Fig. 7.3 | Discharge and sample biasing circuits | 64 |

| | <u>Page</u> |
|--|-------------|
| Fig. 7.4 Schematic of computer-controlled ellipsometer system | 66 |
| Fig. 7.5 Angle of incidence (A.I.) zero error determination | 71 |
| Fig. 7.6 Calibration of the polarizer and analyzer scales (shaft encoder outputs) | 73 |
| Fig. 8.1 Schematic of discharge system used by Lee et al. 1970 (system A) | 83 |
| Fig. 8.2 Ellipsometry data for Ta ₂ O ₅ on Ta in air used to obtain the optical constants of Ta at $\lambda = 6328\text{\AA}$ | 86 |
| Fig. 8.3 Circuit used to monitor sample and probe potentials | 89 |
| Fig. 8.4 Sample current-voltage characteristics: x gold-plated sample in negative glow of system A, $I_d = 10\text{mA}$, $p = 55$ mtorr; o suspended niobium sample in positive column of system B, $I_d = 40$ mA, $p = 60$ mtorr; • as o except mounted on sample holder | 94 |
| Fig. 8.5 Location of constrictors: (a) stainless steel 'top hat', (b) borosilicate funnel | 95 |
| Fig. 8.6 Effect of constrictor on probe characteristics | 97 |
| Fig. 8.7 Ring cathode-base plate anode plasma anodization system | 100 |
| Fig. 8.8 (a) Current efficiencies versus pressure for anodization of sample Ta2 at $I_s = 0.1$ mA, 0.2 mA and 0.3 mA in the positive column (b) Electron density and mean electron energy versus pressure | 102 |
| Fig. 8.9 Current-voltage characteristics for gold-plated sample in the positive column at various pressures | 103 |
| Fig. 8.10 Electron current-voltage characteristic obtained from 60 mtorr curve of Fig. 8.9, and electron and positive ion currents to gold ball probe used as a 'sounding probe' | 104 |
| Fig. 8.11 Oxide thickness and growth rate during constant current anodization of niobium sample Nb5 at $1\text{mA}/\text{cm}^2$, $I_d = 5\text{mA}$, $p = 60$ mtorr (system A negative glow) | 107 |

| | <u>Page</u> |
|---|-------------|
| Fig. 8.12 Ellipsometer readings obtained during anodization of sample Ta2 in positive column of system B . . . | 108 |
| Fig. 8.13 Oxide growth during anodization of Ta2 at 0.1 mA and 0.3 mA in positive column | 111 |
| Fig. 8.14 Variation of oxide growth rate (expressed as ionic current density) with total current to sample Ta2 in positive column of system B at pressures of 60, 100 and 150 mtorr | 113 |
| Fig. 8.15 Electron energy diagram for anodizing sample drawing current density less than ($j_{es} + j_{+s}$), showing effect of plasma electron energy distribution | 117 |
| Fig. 9.1 Electron filter | 123 |
| Fig. 9.2 Circuit used for electron filter experiments . . . | 124 |
| Fig. 9.3 Dependence of the current-voltage characteristics of a gold-plated sample on the dc and rf voltages V_{gdc} and V_{grf} applied to the grid | 126 |
| Fig. 9.4 Variation of sample current at fixed sample voltage with grid rf voltage, for different grid dc voltages | 127 |
| Fig. 9.5 (a) Circuit for simultaneous application of dc and rf biases to a sample (b) I-V relations for sample subject to dc and dc+rf bias conditions at a pressure of 60 mtorr . . . | 129 |
| Fig. 9.6 Current decay through aluminum sample (from O'Hanlon and Pennebaker 1971) | 131 |
| Fig. 10.1 Estimation of oxide field from sample-probe potential and oxide thickness data | 143 |
| Fig. 10.2 Typical variation of sample potential with respect to a floating probe during a constant current formation | 146 |
| Fig. 10.3 Variation of sample-probe voltage with thickness for a niobium sample (Nb1) as recorded at the end of four formations at the same constant total current of 0.5 mA | 148 |
| Fig. 10.4 Variation of oxide thickness and estimated voltage across oxide during anodization of a | |

| | <u>Page</u> |
|--|-------------|
| niobium sample (Nb5) at 1 mA/cm^2 in the negative glow of system A | 149 |
| Fig. 10.5 Ionic current versus estimated oxide field (Tafel plot) for anodization of sample Nb2 at 30°C in the negative glow of system A, showing data uncorrected, and corrected for V_{OI} factors | 150 |
| Fig. 10.6 Ionic current (from incremental growth rates) versus estimated oxide field during a particular constant current formation on sample Nb5 | 152 |
| Fig. 10.7 Ionic current density versus oxide field for the anodization of sample Ta2 at 30°C in the positive column of system B at different pressures | 153 |
| Fig. 10.8 Ellipsometry data for the anodization of evaporated aluminum (sample Al1) in the negative glow of system B | 157 |
| Fig. 10.9 Ionic current densities and estimated oxide fields for the anodization of sample Al1 (negative glow, system B) at 40°C and 70°C | 159 |
| Fig. 10.10 Rates of anodization of silicon at various temperatures in the dc and rf discharges | 161 |
| Fig. 11.1 Computed ellipsometry curve for the anodization of an 800Å evaporated aluminum film on silicon to 1280Å of Al_2O_3 and the subsequent growth of an intermediate film of SiO_2 | 172 |
| Fig. 11.2 Computed ellipsometry curve for the anodization of a 450Å sputtered tantalum film on silicon to 1071Å of Ta_2O_5 and the subsequent growth of an intermediate film of SiO_2 | 174 |
| Fig. 11.3 Form of high frequency capacitance-voltage curve for an ideal MIS capacitor (n-type semiconductor) | 176 |
| Fig. 11.4 Probe for <u>in situ</u> capacitance measurements | 178 |
| Fig. 11.5 Ellipsometry data for the anodization of an evaporated aluminum film on a silicon substrate (sample Al-Sil) in the negative glow of system B | 180 |
| Fig. 11.6 High frequency capacitance-voltage curves obtained <u>in situ</u> at point Y in Fig. 11.5 | 182 |

| | | |
|------------|--|-----|
| Fig. 11.7 | Ellipsometry data for the anodization of a 200Å ^o evaporated aluminum film on silicon (sample Al-Si2), system B, negative glow) | 184 |
| Fig. 11.8 | High frequency capacitance-voltage curves for Al ₂ O ₃ -SiO ₂ -Si sample (Al-Si2) anodized to point Y in Fig. 11.7 obtained with evaporated gold counterelectrode | 186 |
| Fig. 11.9 | High frequency capacitance-voltage curve for gold electrode on sample Al-Si2 adjacent to MIS diode of Fig. 11.8, showing larger hysteresis | 187 |
| Fig. 11.10 | High frequency capacitance voltage curves for sample Al-Si2 after annealing for 30 minutes at 300°C in nitrogen and then for one hour at 350°C in hydrogen | 189 |
| Fig. 11.11 | High frequency capacitance-voltage curve for sample Si1 anodized in the positive column of system B | 190 |
| Fig. C.1 | Sounding probe current versus reference probe voltage for various values of sounding probe bias . . | 206 |

LIST OF TABLES

| | | <u>Page</u> |
|-----------|--|-------------|
| Table 8.1 | Rates of anodization for various experimental configurations | 92 |
| Table 8.2 | Variation of growth rate with position in the negative glow | 98 |
| Table 8.3 | Oxide growth rates obtained on a tantalum sample at different pressures and current densities | 101 |
| Table 9.1 | The effect of the rf bias on the oxide growth rate and field strength | 137 |
| Table 9.2 | Comparison of expected change in j_i on application of rf bias, with that measured by ellipsometry . . . | 139 |

ACKNOWLEDGEMENT

The author wishes to express his gratitude for the encouragement and guidance received from his research supervisor Dr. L. Young and also from Dr. D.L. Pulfrey during the course of this work.

The author also thanks Messrs. J. Stuber, C. Chubb, A. MacKenzie and H. Black for their valuable technical assistance, and Miss N. Duggan for her patience in typing the manuscript.

Finally the financial support of the United States Air Force under contract no. F33615-71-C-1886, and later the National Research Council of Canada under operating grant no. NRC A-3392 is gratefully acknowledged.

1. INTRODUCTION

The production of thin insulating films by the anodic oxidation of certain metals and semiconductors in various liquid electrolytes has been studied for many years. The dielectric properties of these films are well documented, and indeed such films on tantalum and aluminum are extensively utilized in the fabrication of capacitors. More recently, developments in solid state electronic devices have produced special requirements for thin dielectric films and the methods by which they are fabricated which leave much room for improvement over present realities. For instance, whereas anodization in aqueous electrolytes is still used in the fabrication of tantalum thin film RC micro-circuits, this process is a source of ionic contamination and it would be advantageous if the dielectric film were produced by a vacuum technique, in common with other process stages. The most widely used dielectric in the active device field is silicon dioxide produced by thermal oxidation, but the high oxidation temperatures required create several problems, and the resulting films are relatively poor barriers to ionic contaminants. This latter property reduces the effectiveness of SiO_2 for surface passivation, and together with a low permittivity and poor radiation resistance renders it far from ideal in the important application of the gate dielectric in insulated gate field effect devices.

The process of plasma anodization studied here is an alternative method of fabricating thin insulating films that is potentially applicable to the above-mentioned areas. It is similar to anodization in ionic liquid solutions except that the liquid electrolyte is replaced by a gaseous oxygen plasma, which may be produced by any of several types

of electrical discharge, e.g., dc low pressure glow, dc arc, rf or microwave. Attributes common to both processes are that oxidation can be carried out without high temperatures, and that oxidation rates and oxide thicknesses are electrically controlled. Being a vacuum technique, the plasma method has the important advantage of freedom from electrolyte ionic contamination, and it can be used to produce films of materials which are soluble in liquid electrolytes. There has been considerable interest in the technique, and it has been utilized in the experimental fabrication of thin film capacitors, metal-oxide-semiconductor transistors (MOST's) and Josephson junctions. The use of alumina produced by plasma anodization as gate insulator in silicon MOST's has resulted in improved performance over thermal SiO_2 insulated devices in the areas of radiation resistance and long term stability (Micheletti et al. 1970). However, application of the process has as yet been restricted to these experimental investigations, in which control was achieved in a largely empirical manner. This can be attributed in part to a limited understanding of the nature of the phenomenon, and a portion of the present work is aimed at improving this situation by studying the kinetics of the process, that is the dependence of the oxide growth rate on measurable parameters. Related to this aspect of the work is the question of whether the oxygen atoms incorporated in the oxide originated as negative ions in the plasma as has been assumed by many investigators, and specific experiments were devised to resolve this point. The production of thin insulating films of metal oxides on silicon is also investigated for MOS device applications. To facilitate the task of relating anodization rates to conditions in the plasma, the relatively well documented dc cold cathode glow discharge was selected for the plasma source, and an automated

ellipsometer was used for continuous in situ monitoring of the thickness of the growing oxide. The transition metals tantalum and niobium were used predominantly as sample materials since they exhibit consistent anodization behaviour in aqueous electrolyte systems.

The remainder of the thesis is divided up as follows. The next chapter is a review of previous work on plasma anodization, chapter 3 compares the overall features of the process with those of solution anodization, and chapter 4 examines some theoretical aspects of plasma-solid interfaces and gas discharge phenomena. Chapters 5 and 6 deal respectively with the techniques of Langmuir probe diagnostics and ellipsometry as applied to anodization studies, and experimental considerations are given in chapter 7. Chapters 8 to 10 describe experimental investigations into three aspects of plasma anodization: the effect of discharge conditions; the role of plasma negative ions; and the ionic current-oxide field relation. The application of the process in the fabrication of insulated gate devices is considered in chapter 11, and conclusions are presented in chapter 12.

2. REVIEW OF PREVIOUS WORK ON PLASMA ANODIZATION

Observations on the oxidation of the surface of a metal sample in electrical contact with the anode of an electrical discharge in oxygen have been made for many years (Ignatov 1946, 1957), and the phenomenon was also observed with silicon and germanium (Nazarova 1962). However, Miles and Smith 1963 appear to have been the first to utilize the process for the controlled production of oxide films by locating and biasing the sample separately from the discharge anode. These workers were able to anodize a wide variety of metals and semiconductors (Al, Ta, Mg, Cr, Sb, Bi, Be, Ge, Si) and the method has since been applied to other materials by Tibol 1965 (Ti), Whitmore and Vossen 1965 (La-Ti), Weinrich 1966 (GaAs) Ramasubramanian 1970 (Zr, zircalloy), Lee et al. 1970 (Nb), Norris and Zaininger 1970 (Hf), O'Hanlon 1970 (La, Mo, W), Simpson and Lucas 1970 (Y, Gd, Y-Fe, Gd-Fe) and Husted et al. 1971 (V). The literature on plasma anodization up to 1970 has been reviewed recently by Dell'Oca et al. 1971 and will be dealt with only briefly here. Much of the early work was concerned with the application of anodization in the negative glow region of the dc discharge to the production of thin film capacitors (Miles et al. 1963; Tibol and Hull 1964; Tibol and Kaufmann 1964; Johnson 1964) and later to MOS transistor fabrication (Waxman and Mark 1969; Micheletti et al. 1970). Other methods of producing the plasma have been investigated, including rf induced (Woorledge and White 1967; Mikhailkin and Odynets 1970; Scholtz 1971) and microwave excited (Ligenza 1965; Kraitchman 1967; Skelt and Howells 1967) discharges, and more recently a hot cathode dc arc discharge (Ligenza and Kuhn 1970). All of these methods of plasma anodization yielded very low values of current

efficiency, i.e., the fraction of the sample current which is ionic (oxide producing), these values usually being less than 5% in contrast to up to 99% attainable in solution anodization. However, the actual growth rates varied considerably, from a few Å/min in dc cold cathode discharges (Lee et al. 1970) to up to 400 Å/min in dense microwave plasmas (Kraitchman 1967), although the relative influence of plasma parameters and sample temperature on these rates was not clarified. In this respect, it should be pointed out that most workers have not attempted to control substrate temperature, and very few have used in situ methods of oxide thickness determination (Locker and Skolnick 1968, Lee et al. 1970) and even these were not continuous monitoring systems.

Thus while many experiments on plasma anodization have been described, the data sheds little light on the mechanisms involved, a better understanding of which is important for improved control and optimum application of the process. For instance, it has been largely assumed that the oxide growth process was analogous to that occurring in solution anodization, with the forming voltage across the oxide simply given by the bias voltage applied to the sample. In more recent studies, Olive et al. 1970, Ramasubramanian 1970, Lee et al. 1970 and O'Hanlon 1970 have attempted to clarify this situation. Some of this work is reviewed in more detail in sections 4.2 and 10.2. Also Miles and Smith's original postulate (1963) that the negative ions in the plasma were the source of the oxygen incorporated in the oxide appears to have been generally accepted. This point was investigated recently by O'Hanlon and Pennebaker 1971, but their conclusions (which supported Miles and Smith's postulate) are shown in section 9.3 to be unjustified, and in fact incorrect.

Dielectric films produced by plasma anodization have been found to have similar properties to films of the respective materials produced by solution anodization, for instance Waxman and Zaininger 1968 obtained Al_2O_3 films having a relative permittivity of 7.6 and loss factor of 2% @ 1 kHz, which are comparable with wet-anodic Al_2O_3 , and Lee et al. 1970 found plasma-grown Ta_2O_5 and Nb_2O_5 films to have permittivities of 17 and 34 respectively, and loss factors around 1% @ 1 kHz. The latter permittivity values are somewhat lower than the respective values of 27 and 42 for solution-grown oxides of Ta and Nb, and this was supported by lower values of refractive index as determined by ellipsometry. Plasma anodization of silicon in a dc arc discharge (Ligenza and Kuhn 1970) has provided oxides with high dielectric strengths and very stable interface properties equal to the very best reported for thermal oxides.

3. COMPARISON OF PLASMA- AND SOLUTION-ANODIZATION

3.1 General Features of Solution Anodization

Oxide films may be grown on many metals and some group IV and III-V semiconductors by immersing the material and a cathode in a suitable electrolyte solution and biasing the material anodically (Young 1961). The transport of metal and/or oxygen ions in the film, which must occur for the film to grow, is aided by the electric field established in the film by the applied voltage, the electrolyte serving as a conducting medium and source of oxygen. The total current through the oxide, as registered in the biasing circuit, is found to be almost entirely ionic for many materials, e.g., Ta, Nb and Al, the electronic component being very small. If the current density through the oxide is maintained constant by the biasing circuitry, then the film will grow at a constant rate, and any desired thickness D can be obtained simply by terminating the current after a certain time when the appropriate charge Q has been passed. For an oxide of formula M_xO_y whose density is ρ , Q is given by Faraday's law of electrolysis as

$$Q = 2y\rho FDA/m\eta \quad (3.1)$$

where A is the sample area, F is the Faraday, m is the molecular weight of the oxide and η the current efficiency, i.e., the proportion of charge used on oxide growth. During formation at constant current density, the voltage increases linearly with thickness to maintain the oxide field constant.

In making films for applications, it is usual to form at constant current until a certain voltage is reached, and then hold the anodization cell at this constant voltage for a fixed time of some hours. During

this period the film continues to grow, but at a continuously decreasing rate due to the decreasing oxide field, and the current decays with time towards leakage (non film-forming) levels. It is believed that weak spots in the film may be 'patched' during this final constant voltage period, producing films with lower leakage currents. The anodization constant or film thickness-voltage ratio obtained for the above method is often referred to, and is sometimes interpreted as the reciprocal of the oxide field strength at the end of the formation process, but strictly this implies formation at constant voltage to a fixed current level (independent of voltage) rather than for a fixed time.

During both constant current and constant voltage formation the relation between ionic current density J_i , mean oxide field intensity E and temperature T is found to be approximated by the empirical equation

$$J_i = A \exp(BE) \quad (3.2)$$

where

$$A = J_o \exp(-W/kT)$$

$$B = C/T,$$

k is Boltzmann's constant and J_o , W and C are independent of T and E .

In arriving at such a dependence, the field E is generally obtained from the overpotential, defined as the excess of the cell voltage over the theoretical reversible value, corrected for any ohmic potential differences in the solution.

The field strengths required to produce ionic current densities in the range of 10^{-8} to 10^{-1} A/cm² are usually in the range 10^6 to 10^7 V/cm, and the maximum film thicknesses attainable by solution anodization are generally limited by the voltage across the film exceeding some breakdown threshold, either at flaws in the film or at the film/masking material

interface.

Considerable quantities of electrolyte species may be incorporated into solution grown films, particularly with more concentrated solutions (e.g., of H_2SO_4 or H_3PO_4), as has been shown by tracer (Randall et al. 1965) and activation studies (Amsel et al. 1969). These impurities, and perhaps also those from the metal substrate if the latter is a sputtered film, appreciably affect properties of the oxide such as refractive index, permittivity and ionic conductivity, as was shown in a recent study utilizing ellipsometry (Dell'Oca 1969). The presence of such ionic and potentially mobile impurities is strongly at variance with the requirements of insulating films for active solid state devices. Another phenomenon which causes changes in the oxide properties is that of photostimulated growth under ultra-violet irradiation (Dell'Oca 1969). During this process, in addition to the presence of a photoelectronic current, the ionic current at a given field strength is enhanced, and the resulting photogrown material has optical properties very different from those of the normal oxide.

3.2 The High Field Ionic Conduction Process - Classical Theory

With some notable exceptions, the kinetics of solution anodization as expressed by Eqn. 3.2 are well accounted for by theories of high field ionic conduction (Dell'Oca et al. 1971). In the classical picture of ionic conduction, which was originally applied to the motion of defects (i.e. interstitial ions or vacant lattice sites) in a crystalline solid, the potential energy of an ion is taken to be a time-independent periodic function of the co-ordinates of the ion. The application of a field E (the macroscopic field in the dielectric) is supposed to

add a term $(-qxE)$, where x is the coordinate of the ion resolved in the direction of E and q is the charge on the ion (Fig. 3.1). Thus to a first approximation, if a is the distance between the positions of minima and maxima of the potential energy, the energy barrier opposing a jump from one site to the next is reduced from W to $W-qaE$. The ion is treated as a nearly independent harmonic oscillator whose loose coupling to the lattice at temperature T causes it to have a chance of having the activation energy $W-qaE$ equal to $\exp[-(W-qaE)/kT]$. If the frequency of vibration of the ion about its mean position is ν , and the concentration of defects is n , then at fields high enough to make jumps against the field unlikely the ionic current density is

$$J_i = 2qan\nu \exp[-(W-qaE)/kT] \quad (3.3)$$

While this equation is clearly of the experimentally observed form 3.2, the application of this theory to anodic oxides is complicated by the fact that a range of activation energies and distances would be expected in such amorphous films. Another problem is that the classical theory suggests that one type of ion, either metal or oxygen, should dominate in the conduction process through a lower activation energy, whereas with tantalum, niobium, tungsten and aluminum both metal and oxygen ions are mobile (Davies et al. 1965), and to about equal extents for aluminum and tantalum (Randall et al. 1965).

Precise work over a wide range of currents using optical methods of thickness measurement on tantalum (Young 1960a) and niobium (Young and Zobel 1966) has shown that the results are more exactly described by a quadratic dependence of $\log J_i$ on field E :

$$J_i = J_o \exp -[(W-\alpha E + \beta E^2)/kT]$$

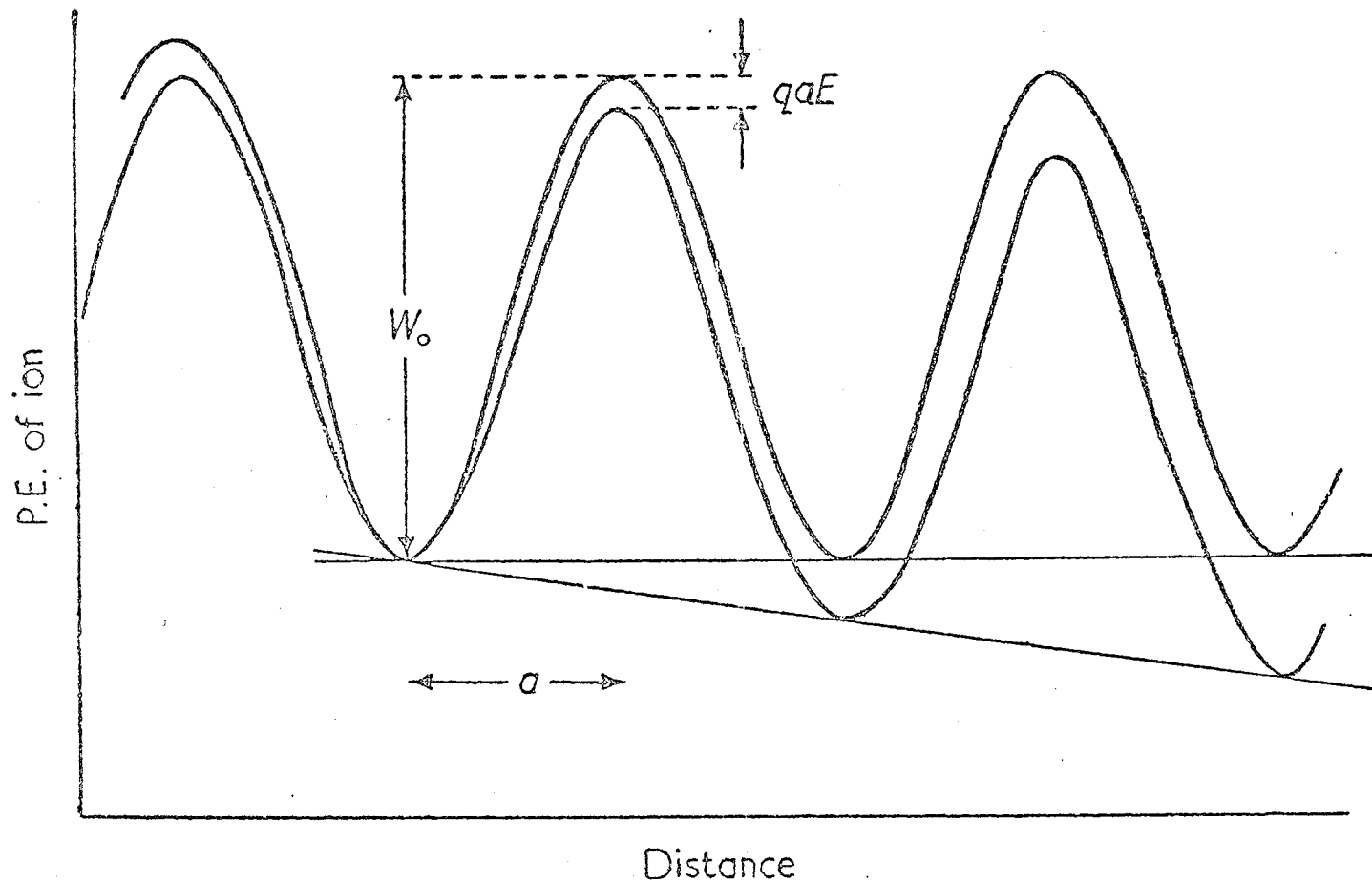


Fig. 3.1 Supposed potential energy of ion versus distance with and without an applied field.

Explanations of this nonlinear dependence have been proposed, e.g. by Young and Zobel 1966 in terms of a channelling model of ionic conduction, and by Ord et al. 1972 in terms of variations in the local effective field/applied field ratio due to a field dependence of the relative permittivity which has been observed experimentally.

Finally, the classical approach can be extended to account for some (but not all) types of transient behaviour by introducing the idea of field-assisted thermal activation of ions from lattice sites into interstitial sites to create Frenkel defects (Bean et al. 1956). This gives a mechanism which causes a delayed change in the concentration of mobile species on changing the field, and qualitatively explains such effects as the field going through a maximum when the current is increased from one constant value to another.

3.3 General Features of Plasma Anodization

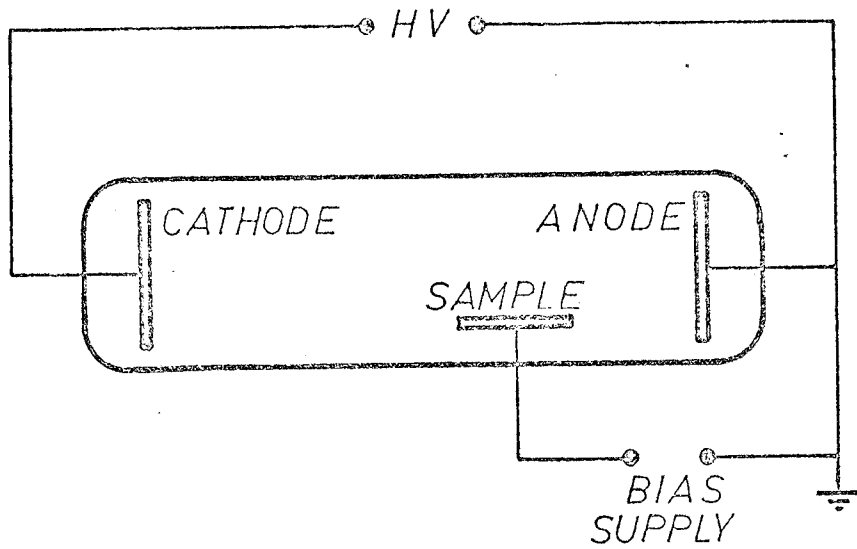
The term plasma anodization is here restricted to the process in which an oxide film is made to grow on the surface of a material exposed to an electrical discharge in oxygen by externally biasing the sample so that it draws a positive current from the discharge*. As a consequence of the properties of gaseous plasmas (Engel 1965, Cobine 1958) the substitution of an oxygen plasma for the solution electrolyte gives rise to various departures from solution anodization conditions:

* Oxides can be formed by exposure of a material to a plasma without drawing a net current from the latter via an external biasing source, and the growth is reported to follow either a logarithmic law in dc discharges (Miles and Smith 1963), or a parabolic law in microwave discharges (Kraitchman 1967).

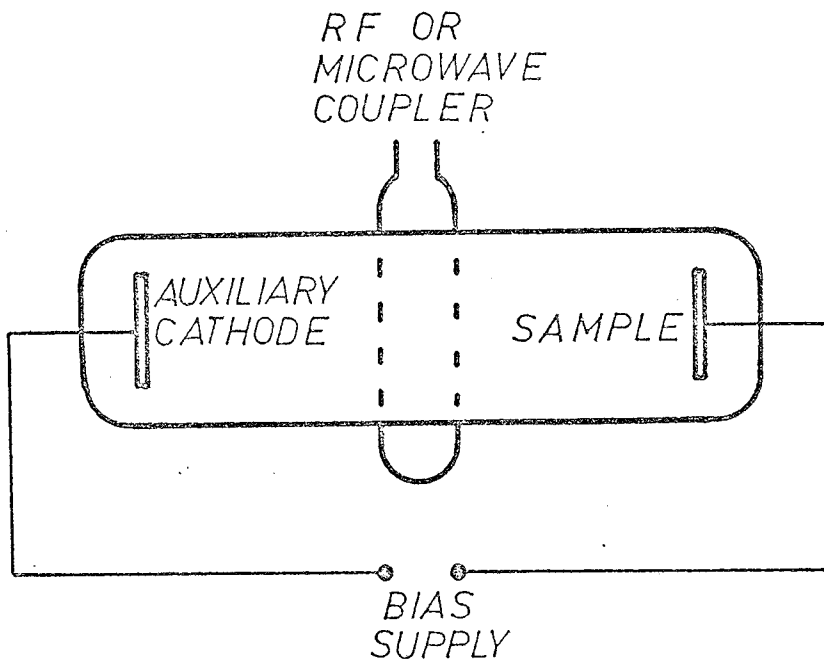
(1) The method of biasing the sample will depend on whether or not the discharge is excited via internal electrodes, as shown in Fig. 3.2. For instance in the dc discharges (hot or cold cathode, glow or arc) the anode provides a convenient potential reference, usually grounded, and the sample may be biased with respect to this reference. In discharges excited by an externally induced rf or microwave field, an additional electrode must be introduced to complete the dc circuit, and this arrangement is perhaps more analogous to solution anodization.

(2) In solution anodization cells, the potential drop through the electrolyte is typically of the order of a volt and is stable, but in the plasma systems the potential drop through the discharge from the reference electrode to the vicinity of the sample may be much larger, and variable with time. In the dc discharge this potential difference can be as large as 100 V, depending on the pressure, discharge current, configuration and condition of the electrodes and the sample location. This, together with space charge sheath regions usually present at plasma/solid interfaces, can lead to large errors in estimating the potential difference across the oxide film, as will be pointed out in section 4.1.

(3) An important difference from solution anodization conditions is that liquid electrolytes contain few, if any, free electrons, whereas the plasmas involved here have large concentrations of electrons ($10^7 - 10^{13} \text{ cm}^{-3}$) with mean energies of a few electron-volts. Many of these electrons are able to enter the oxide, and this coupled with the much lower energies of the various ionic species may be the major cause of the large electronic fraction of the total current



(a) *dc DISCHARGE*



(b) *hf - EXCITED DISCHARGE*

Fig. 3.2 Biasing arrangements for plasma anodization.

density in plasma anodization.

(4) As mentioned in section 3.1, liquid electrolytes act as a source of contaminant species for the oxide film, whereas the electrolyte in the gaseous system contains only oxygen. Thus the plasma-anodized oxides can be expected to be purer than those formed by wet anodization (in practice there may be contamination from the discharge chamber walls or electrodes).

(5) Liquid electrolytes generally have some degree of solvent action, which may hinder the formation of oxides on certain materials such as Ge, GaAs and V. The plasma electrolyte enables oxide films to be grown on these materials, as reported in chapter 2. However, during plasma anodization the oxide surface is continually bombarded by various charged and uncharged particles, and under certain conditions sputtering of the oxide film by energetic species can occur (Locker and Skolnick 1968), and compete with the anodization process in a manner somewhat similar to oxide dissolution.

(6) Whereas sample temperatures in solution anodization do not normally exceed the 0 - 100°C range, a much wider range is possible in plasma anodization, but temperature control and measurement is generally more difficult.

(7) The plasma is a continuous source of uv radiation, absorption of which during oxide growth may lead to structural differences from ordinary anodic oxides (see section 3.1).

In spite of the major complications represented by (2) and (3) above, the gross behaviour of anodic oxide growth in low pressure dc discharges is similar to solution anodization. Thus, when the current drawn by the sample is maintained constant, the oxide grows at a constant

rate and the sample potential rises approximately linearly with time, whereas with a constant voltage applied to the sample the growth rate and current both decrease with time. In view of the extremely low current efficiencies, however, these observations alone are not sufficient evidence for identical mechanisms in the two processes.

The anodization of silicon in a highly ionized microwave discharge has been found to follow a parabolic growth law indicative of diffusion control (Ligenza 1965; Kraitchman 1967), but in this case both the sample temperature and discharge pressure were relatively high, about 400°C and 500 mtorr respectively.

4. THEORETICAL ASPECTS OF PLASMA ANODIZATION

4.1 Introduction

In attempting to formulate an understanding of the plasma anodization process, various questions of a fundamental nature need to be dealt with. For instance, what is the principal mechanism by which the oxide-forming species are transported through the oxide film, and what are the roles of the plasma and its various constituent species? To investigate whether a high field ionic conduction mechanism is operative in the plasma oxide as in solution anodization, some estimate of the electrostatic field in the oxide must be made from measurements of the potential of the sample being anodized. This requires cognizance of certain plasma properties, in particular the behaviour of sheath regions, as outlined in the following section. In the subsequent section it is shown that across-the-sheath transport of plasma negative ions could account for the observed dependence of anodization rate on estimated oxide field, and in the final two sections the production of gaseous negative ions and the plasma properties of the low pressure cold cathode dc glow discharge in oxygen are examined.

4.2 Plasma Sheath Theory

4.2.1 General

A gaseous plasma is a collection of positive, negative and neutral particles having only a small or zero net charge density. In discharges in electropositive gases the charged particles consist of electrons and positive ions, whereas oxygen plasmas also contain the singly charged negative ions O^- and O_2^- . Since the plasma electrons diffuse much more rapidly than the heavier ions, any surface exposed to

the plasma but drawing no net current from the latter acquires a negative charge and a balancing sheath of positive space charge develops over the surface, such that the potential difference V_{sh} across this sheath repels all electrons except a flux which will recombine exactly with the flux of positive ions reaching the surface. To a first approximation the electric field in the sheath decreases to zero at its outer boundary with the electrically neutral plasma, so that the particles cross this boundary by virtue of their random thermal velocities. The resulting flux of positive ions is therefore independent of V_{sh} , and constitutes the random positive ion current density to the surface given by (see Appendix A)

$$j_{+s} = n_+ e v_+ / 4 \quad (4.1)$$

where e is the magnitude of the electron charge (ions assumed singly charged), v_+ is the mean random velocity of the ions and n_+ their number density.

The electron current to the surface is given by those electrons crossing the outer sheath boundary from the plasma which overcome the retarding potential V_{sh} . If it is assumed that due to randomising collisions the plasma electrons are in thermal equilibrium and have a Maxwell distribution of velocities with temperature T_e (see Appendix A), then the fraction having an energy greater than eV_{sh} is given by the Boltzmann factor, $\exp[-eV_{sh}/kT_e]$, and so in the absence of collisions in the sheath region the electron current density reaching the surface is

$$j_e = (-n_e e v_e / 4) \exp[-eV_{sh}/kT_e]$$

$$\doteq j_{es} \exp[-eV_{sh}/kT_e] \quad (4.2)$$

where n_e and v_e are the number density and mean random velocity of the electrons respectively. For the electrically isolated surface, the sheath space charge is such that V_{sh} gives $j_e = -j_{+s}$. In this situation V_{sh} is typically a few volts, being a measure of the higher electron energies in the plasma, and the surface is said to be at 'floating' or 'wall' potential V_f .

In the case of the surface of a metal electrode, V_{sh} can be increased or decreased by external biasing so that j_e as given by Eqn. 4.2 no longer balances j_{+s} , and a net current is drawn from the plasma. If the electrode is biased positively with respect to V_f (as in plasma anodization), more electrons are able to overcome the reduced retarding potential V_{sh} and a net electron current is drawn from the plasma. This electron current increases with increasing positive bias until $V_{sh} = 0$, at which point the positive sheath disappears and the surface draws the saturation value of electron current j_{es} defined in Eqn. 4.2 in addition to j_{+s} . The metal surface is now removing the same number of each species as would cross from one side of an imaginary plane replacing the surface, and the electrode is considered to register plasma potential V_p , in that the rest energy of an electron is constant at its bulk plasma level up to the surface. Further positive biasing produces a negative space charge sheath and a potential barrier which repels positive ions, so that Eqns. 4.1 and 4.2 no longer apply and the net current to the electrode increases by decreasing the positive ion current j_+ . As j_+ is reduced to zero the net current should saturate at j_{es} but in practice it continues to increase by the attraction of electrons from further regions of the plasma and by impact ionization in the sheath field.

4.2.2 The plasma anodization case

The plasma anodization case of an oxide-covered metal sample electrode drawing a current density less than $(j_{es} + j_{+s})$ from the plasma is represented by the electron energy diagram of Fig. 4.1, which also shows an auxiliary floating electrode located nearby. For a known oxide thickness, estimation of the mean electrostatic field in the oxide requires the determination of V_{ox} , the difference in potential between two points just inside the inner and outer oxide surfaces. It is evident that the measurable potential difference, i.e., the difference in the metal Fermi levels, includes potential drops across sheath regions in addition to gradients in the bulk plasma and work function differences, and the sample sheath pd is a function of sample current.

4.3 The Metal/Oxide/Space Charge Sheath/Plasma System

In previous work involving ellipsometry and plasma probe measurements which recognized the complications mentioned in the preceding section, evidence of an exponential dependence of ionic current on estimated oxide field strength was obtained for the anodization of tantalum and niobium in the negative glow of a dc cold cathode discharge (Olive 1969; Lee et al. 1970). On the other hand, Thompson 1961a (see section 4.5) had estimated a random current density of $1.8 \mu\text{A}/\text{cm}^2$ due to negative ions from the plasma of a cold cathode oxygen glow discharge, which is similar to the oxide ionic currents obtained in the above anodization studies. It is possible then, that the oxygen ions incorporated in the oxide originated as negative ions in the plasma, and for this reason the transport of negative ions and electrons across the sheath and the potential distribution in the metal/oxide/space charge sheath/plasma

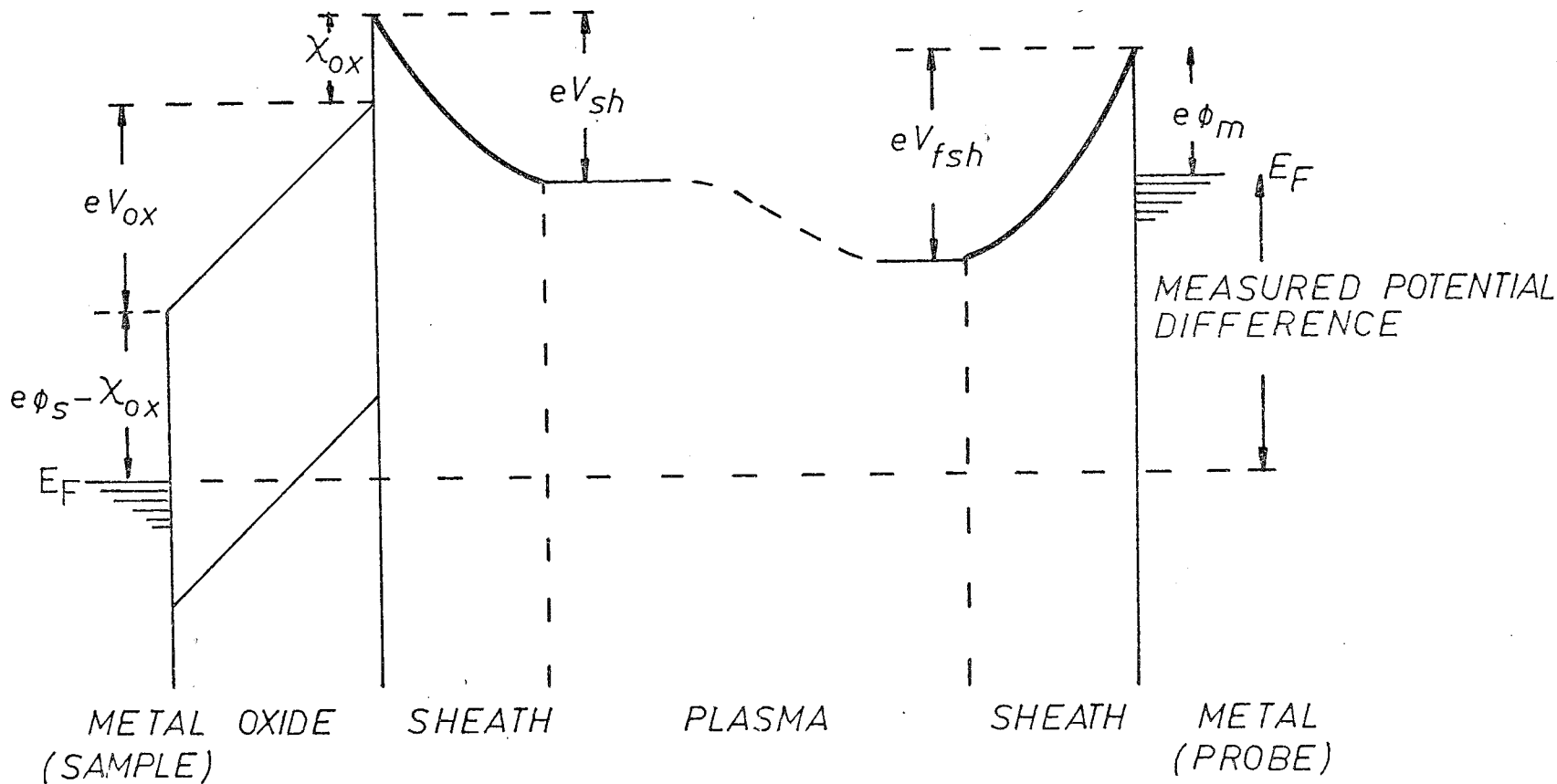


Fig. 4.1 One-dimensional electron energy band diagram for an oxide-covered metal sample drawing a current density less than $(j_{es} + j_{+s})$, and nearby floating probe. E_F = Fermi energy level; ϕ_s = sample metal work function; χ_{ox} = electron affinity of the oxide; V_{ox} = potential difference across the oxide; V_{sh} = potential difference across sample sheath; V_{fsh} = potential difference across floating probe sheath; ϕ_m = probe metal work function.

system should be examined.

The expected electrostatic field and potential distributions in this system during plasma anodization, in the absence of oxide space charge, are shown in Fig. 4.2. A finite electric field exists in the oxide, and the electron current density across the sheath j_e exceeds the saturated positive ion current j_{+s} , so that in the absence of any secondary emission or reflection of electrons, a net electron current density of

$$J = j_e + j_{+s} < j_{es} + j_{+s} \quad (4.3)$$

enters the oxide, where j_e and j_{+s} are given by equations 4.2 and 4.1 respectively.

It would seem that once electrons from the plasma have overcome the retarding potential V_{sh} and reached the oxide surface, there is no energy barrier against entry into the oxide. Electron transport through the oxide is thus likely to be determined by a bulk mechanism such as the field-assisted thermal excitation of trapped electrons into the conduction band (Poole-Frenkel emission). If the Poole-Frenkel effect is operative, the dependence of electron current on oxide field E_{ox} is given (Goruk et al. 1966) by

$$J = G_o E_{ox} \exp\left[\frac{-e}{kT}(\phi_B - \sqrt{eE_{ox}/\pi\epsilon_{ox}})\right] \quad (4.4)$$

where ϕ_B is the depth of the trap potential well, ϵ_{ox} is the (high frequency) permittivity of the oxide, and G_o is a constant*. This expression

* A similar dependence has been observed in wet anodic Ta_2O_5 , Nb_2O_5 and Al_2O_3 by Jaeger et al. 1972 for electronic current densities up to $10\text{mA}/\text{cm}^2$ injected with the aid of a semiconducting oxide layer over the valve metal oxide.

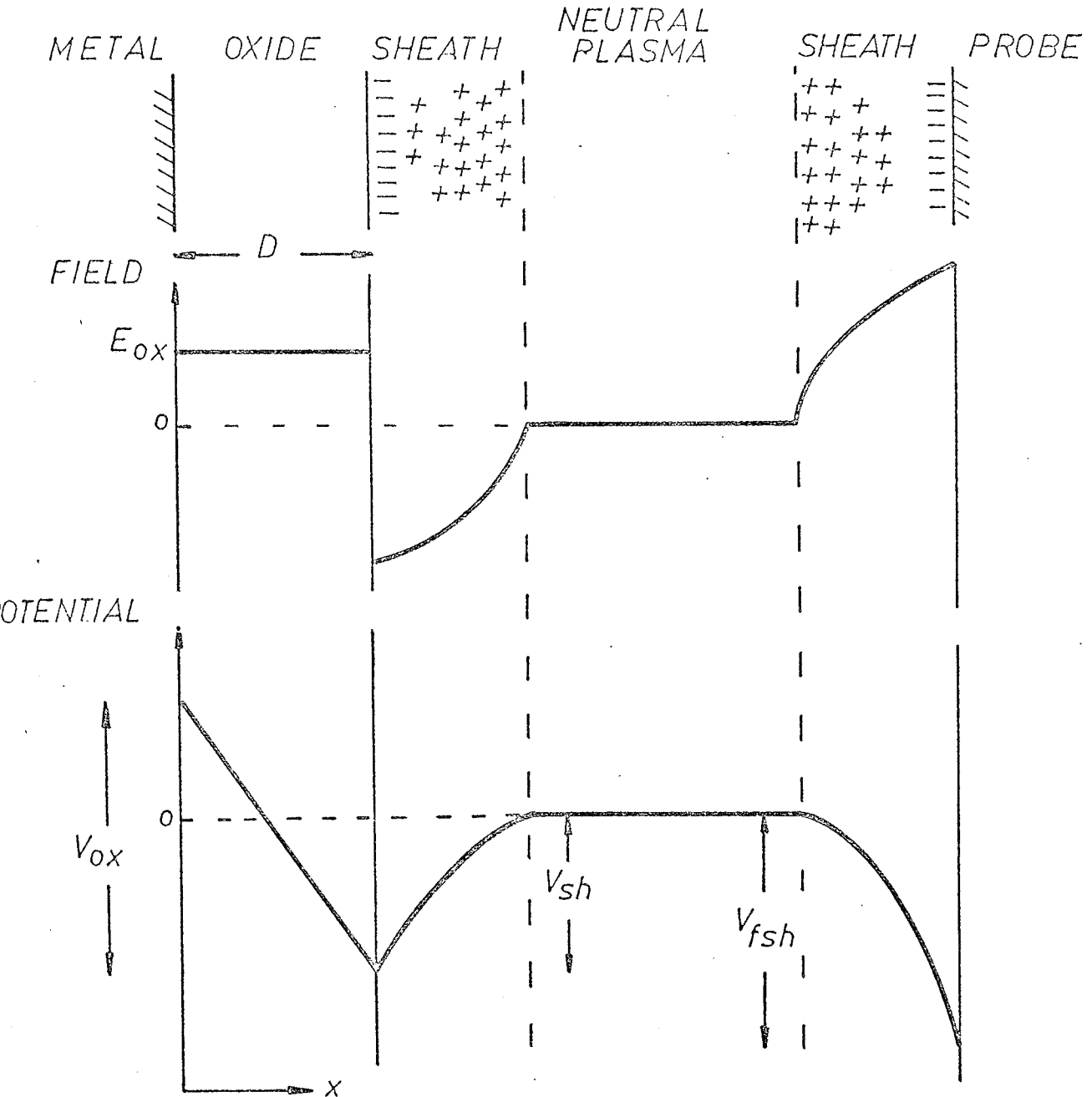


Fig. 4.2 Electrostatic field and potential distributions in the metal/oxide/space charge sheath/plasma system, neglecting potential gradients in plasma.

will be dominated by the exponential dependence on $(E_{ox})^{1/2}$. It may be argued that in the steady state the surface charge density located at the outer oxide surface has a value such that V_{sh} and E_{ox} yield electron currents given by Eqns. 4.3 and 4.4 which are equal. This is equivalent to assuming that the field in the oxide is determined solely by the electronic conduction mechanism in the bulk of the oxide and the electronic current continuity requirement.

Now if the negative ions in the plasma have a Maxwellian velocity distribution with an equivalent temperature T_- , then the negative ion flux across the sheath to the oxide surface will be given by a relation similar to Eqn. 4.2:

$$j_- = j_{-s} \exp [-eV_{sh}/kT_-] \quad (4.5)$$

where j_{-s} is the random negative ion current density incident on the outer sheath boundary. Equations 4.2 and 4.5 give

$$\ln j_- = (T_e/T_-) [\ln j_e - \ln j_{es}] + \ln j_{-s} \quad (4.6)$$

Furthermore, for practical levels of anodizing current, j_{+s} can be neglected in 4.3, so that using 4.4, equation 4.6 becomes

$$\ln j_- = (T_e/T_-) [\ln E_{ox} + (e/kT)(eE_{ox}/\pi\epsilon_{ox})^{1/2} + A] + \ln j_{-s} \quad (4.7)$$

where A is independent of j_- . This can be rewritten as

$$j_- = B(E_{ox})^{T_e/T_-} \exp[(T_e/T_-)(e/kT)(eE_{ox}/\pi\epsilon_{ox})^{1/2}]$$

where B is independent of E_{ox} . That is, for large oxide fields the current of negative ions reaching the oxide from the plasma is exponentially dependent on the square root of the oxide field. Thus, if the supply of negative oxygen ions from the plasma was the rate determining step in plasma anodization, an exponential dependence of oxide growth rate on

$(E_{ox})^{1/2}$ might be expected*. In examining experimental growth rate-oxide field data for a square law or linear dependence of $\ln j_i$ on E_{ox} , the range of the data should be considered. Furthermore, the measured values for E_{ox} are only estimations, given by for example V_{sp}/D where D is the oxide thickness (determined by ellipsometry) and V_{sp} is the metal sample potential measured with respect to a floating reference electrode (probe) located just outside the space charge sheath of the sample. Referring to Fig. 4.2 and neglecting work function differences,

$$V_{sp} = V_{ox} - V_{sh} + V_{fsh} \quad (4.8)$$

where V_{fsh} is the potential drop across the sheath of the floating probe, and from equation 4.7,

$$V_{ox} = \alpha [\ln(j_-/C)]^2 \quad (4.9)$$

where

$$\alpha = (kT/e)^2 (\pi\epsilon_{ox} D/e)$$

and

$$\ln C = (T_e/T_-) [\ln G_o E_{ox} - \ln j_{es} - (e\phi_B/kT)] - \ln j_{-s}$$

Also if the sheath pd of the sample when the latter is electrically isolated, i.e. when $j_e = j_{+s}$, is equal to the floating probe sheath pd V_{fsh} , then equation 4.2 becomes

$$j_{+s} = j_{es} \exp[-eV_{fsh}/kT_e] \quad (4.10)$$

and equations 4.2 and 4.10 yield

$$V_{fsh} - V_{sh} = (kT_e/e) \ln (j_e/j_{+s}) \quad (4.11)$$

* It is interesting to note that a similar dependence, deduced from a channeling model of ionic conduction analogous to the Poole-Frenkel effect, accounted reasonably well for the curvature in $\log J_i$ - E data obtained from solution anodization of tantalum and niobium. (Young and Zobel 1966).

Finally using 4.6, 4.9 and 4.11 in 4.8,

$$\begin{aligned} V_{sp} &= \alpha [\ln(j_-/C)]^2 + (kT_-/e) \ln(j_-/j_{-s}) + (kT_e/e) \ln(j_{es}/j_{+s}) \\ &= \alpha (\ln j_-)^2 + \beta \ln j_- + \gamma \end{aligned} \quad (4.12)$$

where

$$\beta = kT_-/e - 2\alpha \ln C.$$

Thus depending on the magnitude* of the coefficients α and β , the current of negative ions across the sheath may vary approximately exponentially with either $(V_{sp})^{1/2}$ or V_{sp} , and it is possible that negative ion transport across the sheath could give rise to a rate of anodization exponentially dependent on estimated oxide field strength as observed by Lee et al. 1970 if the oxygen incorporated in the oxide originated as negative ions in the plasma. If the latter were the case, then an additional ionization stage would have to be involved, since the process of metal oxide construction utilizes doubly charged oxygen, O^{--} , whereas only singly charged negative ions (O^- , O_2^-) are considered to exist in gaseous plasmas (McDaniel 1964). This further ionization might occur at the oxide surface or at the final location in the oxide, and it would not preclude the possibility of sheath transport being the rate-determining step in the growth process.

4.4 The Formation of Gaseous Negative Ions

A negative ion is an atom or molecule with a net negative charge, which in the gaseous state is always a single charge. The for-

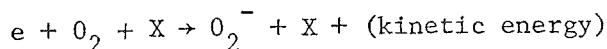
* The coefficient α can be evaluated by assuming a typical high frequency dielectric constant for the oxide, but the evaluation of β is frustrated by the Poole-Frenkel factor G_0 in $\ln C$ which is not usually known explicitly.

mation of negative ions in the inert gases is very improbable, since the outer electron shells are completely full and the binding energy of higher quantum number states is small. However, in the electronegative gases such as the halogens and oxygen with one or two vacancies in the outer shell, the outer electrons have very little effect in shielding an approaching electron from the attractive field of the nucleus, and a negative ion is likely. For stability, the binding energy of the negative ion must be greater than that of the original neutral atom, the energy difference being termed the electron affinity.

Negative ions can be formed by a number of mechanisms in the gaseous state. MacDaniel 1964 lists the following:

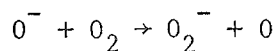
- (a) radiative capture by a neutral atom or molecule
- (b) capture by an atom or molecule with a third body taking up the energy
- (c) capture by a molecule to give an excited ion, de-excitation by a third body collision
- (d) dissociative attachment by a molecule
- (e) ion-pair production, or non-capture dissociation of a molecule
- (f) charge transfer collisions
- (g) surface reactions e.g. sputtering by positive ions, thermionic emission or surface ionization

According to McDaniel processes (b) and (d) are important to negative ion formation in oxygen. The three-body process (b) of capture by an oxygen molecule

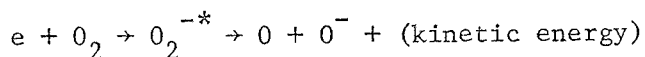


depends on the availability (and suitability) of third bodies X, and so dominates at higher pressures p, or more precisely, at values of

reduced field $E/p < 3V/cm\text{-torr}$, where E is the electric field strength in the gas. This is equivalent to average electron energies less than $1eV$, and this process has a peak attachment coefficient at $0.1eV$. The electron affinity of the O_2 molecule is approximately $0.46eV$, being a measure of the stability of the O_2^- ion, and the attachment coefficient is proportional to p^2 . Although process (b) is insignificant at low pressures, O_2^- ions can still be produced from O^- ions by a charge exchange process (Thompson 1961b):



The two-body process (d) of dissociative attachment,



where O_2^{-*} is an excited vibrational state, dominates for $E/p > 3V/cm/torr$. The attachment coefficient is proportional to p , and the process has a peak cross-section at $6.7eV$.

The electron affinity of the oxygen atom is approximately $1.5eV$, so that the atomic ion is less susceptible than the molecular ion to destruction mechanisms. The latter possibilities include the thermodynamically reverse equivalents of (a) to (f), and in the presence of positive ions,

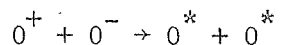
(g) three-body recombination

(h) radiative recombination

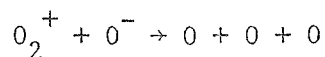
(i) mutual neutralization through charge exchange and excitation

(j) detachment by collisions with surfaces.

At pressures less than a few torr process (g) can be neglected compared with the two-body processes (h) and (i), of which (h) may be neglected (except at extremely low pressures) compared with (i):



or



Although collisions of negative ions with surfaces (j) provide the most effective means of all of electron detachment if the work function of the surface exceeds the electron affinity, the plasma sheath potential barrier will normally prevent negative ions from reaching such surfaces in significant quantity.

4.5 The Low Pressure Cold Cathode Glow Discharge in Oxygen

As mentioned before, both high frequency and dc gas discharges have been utilized in plasma anodization studies. According to Francis 1960, discharges sustained by high frequency excitation can contain higher electron densities ($\sim 10^{13} \text{ cm}^{-3}$) and higher gas temperatures than dc discharges. However, the latter are also of interest in that they possess spatially separated regions of widely different species content, and can generate large volume plasmas. The main regions of the dc cold cathode discharge between plane, parallel electrodes at pressures of the order of 1 torr are shown in Fig. 4.3, together with the space charge, electric field and potential distributions. Electrons are emitted from the cathode mainly by positive ion bombardment (Cobine 1958) and form a negative space charge close to its surface, but they are then accelerated by the electric field, some of them causing excitation of gas molecules which results in the cathode glow. The high density of positive ions attracted to the cathode results in a large net positive space charge in the Crookes dark space, and electrons accelerated by the associated potential gradient produce intense ionization and multiplication. Towards the end of the Crookes dark space the electron density increases

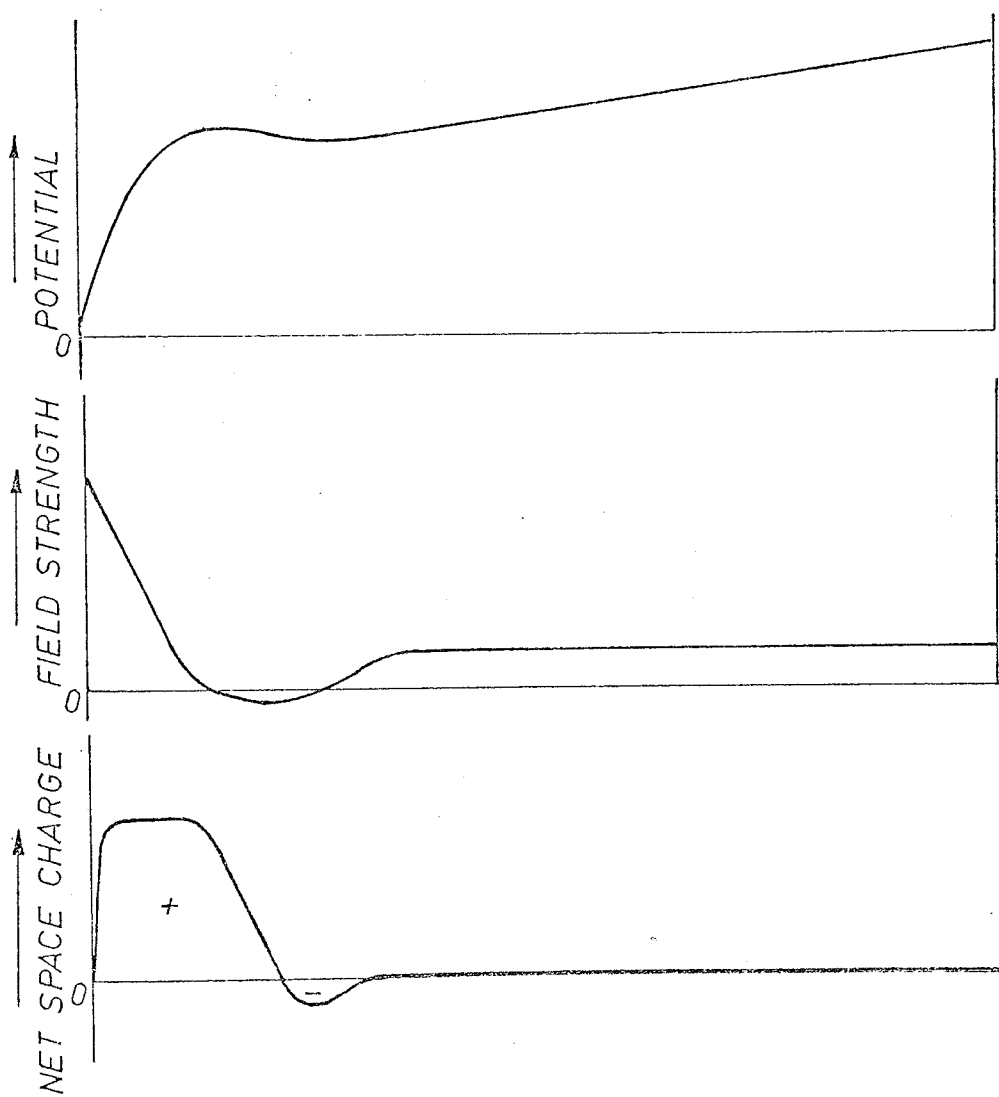
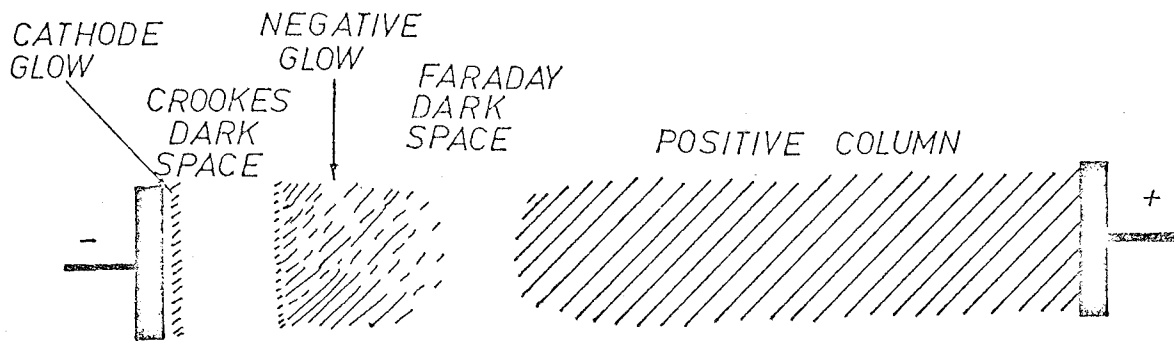


Fig. 4.3 The space charge, electric field and potential distributions in the dc cold cathode glow discharge.

so much that the net positive space charge decreases sharply and the field becomes very small or even reverses. The electrons now consist of two groups: a fast group which originated at or near the cathode and have not suffered many collisions in the dark space, and a larger group which were created in the dark space and are relatively slow, having energies below the ionization level. Thus in this next region most of the electrons lose energy by excitation collisions, giving the negative glow. As the electrons are slowed down further the space charge reaches a negative maximum, the excitation decreases and the Faraday dark space begins. The electron density decreases by recombination and diffusion in the dark space until the space charge is reduced to zero and the field rises to a constant small value, accelerating the electrons once more to excitation and ionization energies, and producing the positive column. The field in the latter assumes a value just sufficient to maintain along the length of the column the degree of ionization required to carry the discharge current. The phenomena occurring at or near the cathode, including the Faraday dark space, are essential to the discharge, whereas the positive column merely serves to maintain a conducting path for the current. Thus on reducing the pressure, the negative glow and Faraday dark space expand at the expense of the positive column, which eventually disappears completely. Similarly, if the distance between the electrodes is varied at constant gas pressure and current, the region from the cathode to and including the Faraday dark space moves as a body and is unaltered in length while the length of the positive column varies. Furthermore, the negative zones will move with a rotating cathode as if they were fixed to the latter. These observations indicate that the motion of the charged particles in the negative zones is of a beam-like nature,

whereas in the positive column the motion must be essentially random. Consequently, there should be little influence from the walls of the discharge tube in the cathode region, while in the positive column the light emitted and the potential distribution depend on the tube diameter: decreasing the latter increases the potential gradient.

The positive column is often divided up into distinct alternating bright and dark striations, which are associated with variations in electric field strength and species concentrations. The phenomenon appears to occur when the energy distribution of the electrons leaving the Faraday dark space consists of two distinctly separate groups of electrons (Twiddy 1961).

If a cylindrical hollow cathode (Engel 1965) is used instead of a plane electrode, the cathode fall region follows the internal geometry of the cathode and the negative glow is also partly compressed inside the cylinder. The radial electric field in the Crookes dark space contributes to increased ionization, and the ultra-violet radiation of the negative glow is more efficiently utilized for photo-emission from the cathode, so that for a given cathode fall voltage the discharge current density is increased. Also a discharge with a positive column can be obtained within a shorter discharge tube.

Both the negative glow and positive column can be said to constitute plasmas, although the space charge neutrality condition is not as well satisfied in the negative glow region. The electron and ion concentrations in the negative glow may be as high as 10^{11} cm^{-3} , compared with around 10^8 to 10^{10} cm^{-3} in the positive column. At levels of discharge current I_d in the abnormal glow region, when the cathode is completely covered with the cathode glow, then these carrier densities

increase with I_d and pressure.

The electrons have considerably higher energies than the charged or neutral particles, and numerous elastic collisions have a randomising effect giving the electrons an equilibrium energy distribution which can approach Maxwellian form with an associated temperature T_e that may be around $50,000^\circ\text{K}$. The ion temperature is close to that of the gas, which is seldom over 100°C in the positive column. In the latter region, T_e decreases with increasing R_p , the product of discharge tube radius and pressure, but in molecular gases it is relatively independent of I_d .

The cold cathode dc glow discharge in oxygen has been investigated in detail by Thompson 1961a using sophisticated current probe techniques and an rf mass spectrometer probe. Thompson reported that in his discharge between cylindrical hollow swedish iron electrodes the negative glow was green and the positive column consisted of blue grey striations. At a pressure of 40 mtorr he found the negative glow and Faraday dark space to be virtually field free, but that in the positive column steps of potential of about 11V occurred at each striation head (cathode end). By measuring the second derivative of probe current-voltage characteristics, Thompson determined the energy distributions and concentrations of the charged particles for a discharge current of 4 mA, and the mass spectrometer probe provided some information on the relative abundance of various ions. The negative glow and Faraday dark space were found to be characteristic of an electropositive plasma of positive ions and electrons, with very few negative ions present. In the positive column, however, positive and negative ions were present in almost equal concentrations of about $4 \times 10^8 \text{ cm}^{-3}$, with mean energies of 0.15eV, compared

with an electron density of $2 \times 10^7 \text{ cm}^{-3}$ and mean energy around 4eV. The ions of greatest abundance were O_2^+ and O^- . The latter were assumed to be produced by dissociative attachment (process (d), section 4.4) and their density was highest at the head of a striation on the discharge tube axis. The negative ion random current density j_{-s} near a striation tail was $1.8 \text{ } \mu\text{A/cm}^2$. Thompson 1961b also deduced that the negative ion density is proportional to the $2/3$ power of the discharge current I_d between 0 and 10 mA, and that the negative ion to electron ratio of 20 at $I_d = 4 \text{ mA}$ would decrease with increasing I_d according to

$$n_-/n_e \propto I_d^{-1/3}$$

reaching a value of 2 at $I_d \sim 9 \text{ mA}$, at which point the plasma ceases to be electronegative in character. Above 10 mA the positive column behaved as a weakly ionized electropositive plasma with n_+ proportional to I_d but the negative ion density was not determined.

5. PROBE TECHNIQUES IN PLASMA DIAGNOSTICS

5.1 Introduction

This chapter deals with the application of electrical probes to the measurement of various plasma parameters, such as electrostatic field strength, floating potential, plasma potential, and charge carrier concentrations and temperatures. A number of other diagnostic techniques are available, for instance microwave transmission, reflection or cavity resonance measurements, optical interferometry, optical spectroscopy, and mass spectrometer analysis, but the Langmuir probe technique is particularly appropriate since the anodization sample itself can be considered as a large plane probe. Much of the theory applicable to probes has already been introduced in section 4.2.1.

The use of the Loeb electron filter and the simultaneous application of rf and dc bias to a probe are dealt with separately in chapter 9.

5.2 Simplified Treatment of the Langmuir Probe Method

The theory of the flow of charge carriers to an electrical probe can be extremely complex, and has been treated in some detail by Swift and Schwarz 1970. An elementary theory applicable to low pressure plasmas found in a glow discharge at pressures below 100 mtorr is presented here, with the following assumptions:

1. Negative ions are absent, and electron and positive ion concentrations are equal (see section 5.3 for the effect of negative ions).
2. Electron and ion mean free paths are much larger than the probe dimensions (see Appendix B).
3. The probe dimensions are much larger than the Debye length (see

Appendix B).

4. There is a Maxwellian distribution of electron and positive ion velocities (see Appendix A).
5. The electron temperature T_e is much greater than the positive ion temperature T_+ .

The circuit shown in Fig. 3.2(a) represents a Langmuir probe circuit if the electrode marked 'sample' is a sphere, cylindrical wire or plane disc of unreactive metal. If this probe is biased so as to draw zero net current from the discharge, then the probe registers the floating potential for that plasma location. A series of such floating probes can yield an estimate of the electrostatic field strength in the plasma. By varying the potential of the single probe with respect to the anode, an I-V characteristic of the general form shown in Fig. 5.1 will be obtained.

(a) Strongly negative probe

As the probe is biased negatively from its floating potential V_f , progressively more electrons will be repelled by the increasing electric field in the space surrounding the probe until eventually the current drawn i_{+s} is entirely due to positive ions.

In section 4.2(a) it was assumed that the whole of the potential variation in the region surrounding a negative surface was confined to the positive ion space charge sheath. However, between the space charge sheath and the undisturbed plasma there is a quasi-neutral transition region in which ions and electrons are present in almost equal quantities but across which a small potential drop occurs due to the withdrawal of positive ions to the probe. The sheath begins when the electron concentration starts to decrease appreciably, so that V_t , the pd across the

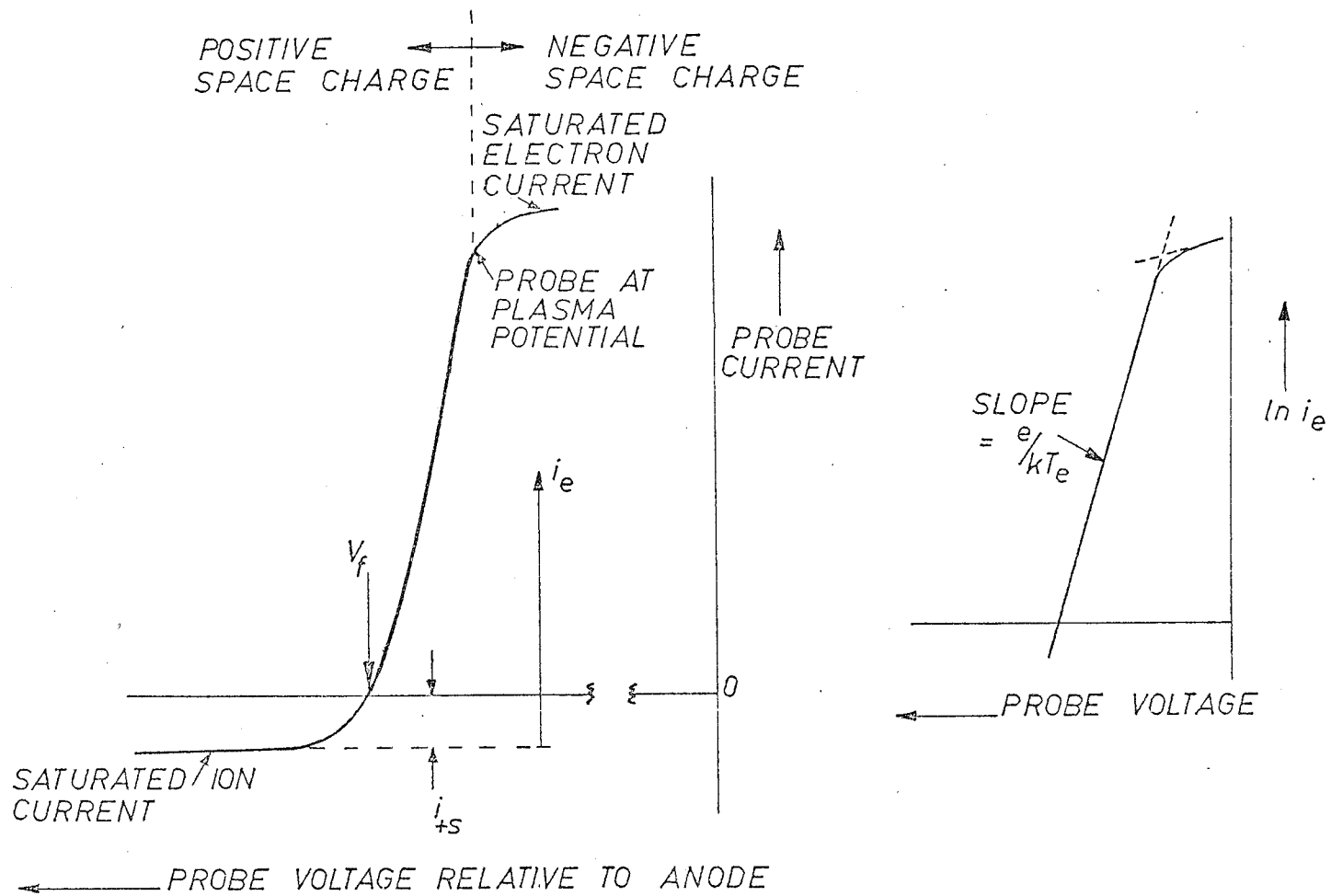


Fig. 5.1 Ideal current-voltage characteristics of a Langmuir probe.

transition region, must be just large enough to prevent a significant fraction of the electrons in the discharge from entering the sheath, i.e. $eV_t \approx kT_e/2$. However, since the mean ion energy is much smaller than the mean electron energy, even this weak field penetrating the transition region greatly distorts the random ion motion, and in effect gives the ions at the sheath edge a directed velocity v_t towards the probe:

$$v_t = (2eV_t/m_+)^{1/2}$$

where m_+ is the ionic mass.

Now the electron concentration n_t at the sheath boundary is given by Boltzmann's law:

$$n_t = n_e \exp[-eV_t/kT_e]$$

where n_e is the concentration in the undisturbed plasma. Since the ion and electron concentrations at the sheath edge are still approximately equal we have for the ion current i_{+s} to the probe

$$i_{+s} = A_p e (2eV_t/m_+)^{1/2} n_e \exp[-eV_t/kT_e]$$

where A_p is the area of the probe. Replacing eV_t by $kT_e/2$ we obtain, instead of Eqn. 4.1,

$$i_{+s} = 0.607 A_p e n_e (kT_e/m_+)^{1/2} = 0.607 A_p e n_+ (kT_e/m_+)^{1/2}$$

Thus the ion current to the probe is a function of the mean electron energy rather than the mean ion energy, so that the latter cannot be obtained from this ion collection region of the characteristic.

(b) Probe biased positively from floating potential

When the potential difference across the space between the probe and plasma is decreased, as explained in section 4.2.1 electrons begin

to reach the probe in increasing numbers until the retarding field disappears and the probe is at plasma potential V_p . Throughout this region the probe draws a constant positive ion current (i_{+s}) and the velocity distribution of the electrons will determine the variation of total probe current with potential.

Assuming a Maxwellian distribution and a pressure low enough for collisions in the sheath to be unimportant (according to assumptions (2) and (3)), the electron current to the probe is given by Eqn. 4.2 as

$$i_e = i_{es} \exp[-eV_{sh}/kT_e] \quad (5.1)$$

where V_{sh} is the retarding potential between the probe and the plasma, and i_{es} is the electron current to the probe when the latter is at plasma potential ($V_{sh} = 0$). This random electron current is given by

$$i_{es} = -(1/4)n_e \bar{v}_e e A_p = -n_e e A_p (kT_e/2\pi m_e)^{1/2} \quad (5.2)$$

where \bar{v}_e is the mean thermal speed of an electron (see Appendix A).

The measured potential V_s of the probe with respect to the anode is given by

$$V_s = -V_{as} - V_{sh}$$

where V_{as} includes the potential drop through the discharge from the anode to the probe, and the work functions of the probe and anode metals. Thus under constant discharge conditions, Eqn. 5.1 gives

$$\ln(-i_e) = \ln(-i_{es}) + eV_s/kT_e + \text{const.}$$

and a graph of $\ln(-i_e)$ versus probe voltage in this region is linear, having a slope (e/kT_e) from which the electron temperature T_e can be obtained. The value of i_e is obtained from the total probe current by correcting for the positive ion contribution as indicated in Fig. 5.1.

Further positive biasing of the probe causes ions to be repelled and produces an accelerating field for the electrons so that the law governing the increase of electron current changes. This is manifested by a break at V_p in the I-V characteristic, which should then reach a saturation current due only to electrons. However, impact ionization commences in the sheath field, increasing the current to the probe, and the latter may become a subsidiary anode.

Knowledge of the electron current i_{es} reaching the probe at plasma potential V_p enables n_e to be found from Eqn. 5.2 since T_e is now known. However, the sharpness of the break in the characteristic at V_p depends markedly on discharge conditions. It is often located by extrapolating the linear part of the $\ln i_e$ versus V_s characteristic to meet the best straight line obtained from the electron accelerating region as shown in Fig. 5.1. Another method for determining V_p , proposed by Dote et al. 1966, depends on the charged particle density in the sheath region becoming a maximum when plasma potential is reached, and involves the use of a very small sounding probe located close to a larger reference probe (see Appendix C). This electrode arrangement corresponded to the sample and probe combination utilized in the present work, and the method was investigated as reported in section 8.3.4.

5.3 The Effect of Negative Ions on Langmuir Probe Measurements

If, as can occur in the positive column of the oxygen glow discharge, negative and positive ions are present in much larger numbers than electrons (n_-/n_e can be as large as 20 in oxygen - see section 4.5), then clearly the ratio of the electron and positive ion saturation currents will greatly decrease, and more care is required in eliminating the positive

ion contribution to the probe current as mentioned above. However, since the ratio of the negative ion and electron saturation currents is given (see Eqn. 5.2) by

$$i_{-s}/i_{es} = (n_-/n_e)(m_e T_-/m_- T_e)^{1/2}$$

then provided $n_-/n_e \ll (m_- T_e/m_e T_-)^{1/2}$ the negative ion current will always be small compared with the electron current. For an 'active' discharge (i.e. $T_e \gg T_+ \approx T_-$) in oxygen this condition approximates $n_-/n_e \ll 10^3$, and so electron concentration and temperature can still be obtained from the electron collection part of the probe characteristic by the methods of section 5.2 as if negative ions were absent. Furthermore, Boyd and Thompson 1959 have shown that for an electronegative plasma with $n_-/n_e \gg 2$, the positive ion current collected is the random current across the sheath edge, i.e. $(1/4) n_+ e (8kT_+/\pi m_+)^{1/2}$ as in Eqn. 4.1. Thus in both electropositive and electronegative plasmas the ion current is a function of ion density, i.e. the plasma density.

6. THE APPLICATION OF ELLIPSOMETRY TO ANODIZATION STUDIES

6.1 Introduction

A method of determining the thickness of the anodic oxide film as a function of time is clearly essential to the study of the kinetics of the plasma anodization process. The method should preferably be rapid and non-destructive and should ideally be an in situ measurement, that is, it should be possible to determine the film thickness from readings taken while the sample is being anodized. Methods which might be considered include (a) intensity reflectivity of linearly polarized light (Masing et al. 1961); (b) minimum reflectivity spectrophotometry (Dignam et al. 1965) and (c) ellipsometry (Winterbottom 1955; Archer 1962; McCrackin et al. 1963; Passaglia et al. 1963).

The spectrophotometric and ellipsometric methods of examination are generally the most accurate, provided that accurate information is available for the optical constants of the substrate, and recent developments (Ord 1969) have considerably improved the speed of ellipsometer measurements. Other advantages of ellipsometry are that it is a null detection method, and a single null measurement yields two parameters of the optical system if all others are known.

As will become evident later in this chapter, studies of the growth and optical properties of anodic oxide films are a near ideal application for ellipsometry, and the technique has been used extensively in this area (Barrett 1963; Kumagai and Young 1964; Young and Zobel 1966; Dell'Oca and Young 1969; Ord et al. 1972).

Method (a) has been utilized recently in a study of the plasma anodization of silicon in an rf induced discharge (Hathorn, Pulfrey and Young, unpublished; Pulfrey and Reche 1973).

6.2 Principles of Ellipsometry

6.2.1 Reflection of a plane wave at an interface between two isotropic media and at a film-covered surface

The study of the optical properties of surfaces and surface films by ellipsometry involves measuring the changes in the state of polarization of a beam of elliptically polarized monochromatic light which occur when the beam is reflected by the surface. By elliptically polarized light is meant light whose electric (or magnetic) disturbance can be resolved into two linearly polarized vibrations differing in orientation and phase - the locus of the end of the electric vector in a plane perpendicular to the direction of propagation is then an ellipse.

The case of elliptically polarized light incident on the boundary separating two isotropic media, each characterized by a complex refractive index of the form $N = n - jk$, is considered first (Fig. 6.1).

The problem is most conveniently dealt with by examining the effect on the components E_p and E_s of the electric vector of the incident plane wave in and normal to the plane of incidence respectively:

$$E_p = a_p \cos(\omega t - \vec{k} \cdot \vec{r} + \delta_p), \quad E_s = a_s \cos(\omega t - \vec{k} \cdot \vec{r} + \delta_s)$$

where $|\vec{k}| = 2\pi N_0 / \lambda$, N_0 being the complex refractive index of the first medium. The state of polarization of the wave can be specified by the amplitudes a_p and a_s and the phase difference $\delta_p - \delta_s$ of these components*. In general, the process of reflection has different effects on the ampli-

* For instance, if $\delta_p - \delta_s = m\pi$ where $m = 0, 1, 2, \dots$, the wave is linearly polarized, whereas if $\delta_p - \delta_s = m\pi/2$ where $m = 1, 3, 5, \dots$, and $a_p = a_s$, the wave is circularly polarized.

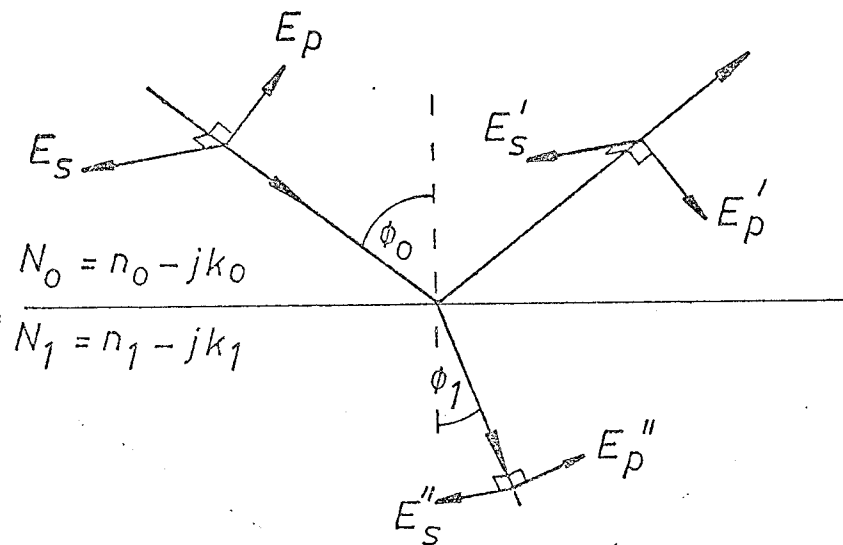


Fig. 6.1 Reflection and refraction at an interface between two isotropic media. The diagram shows the incident ray in the upper medium (refractive index $N_0 = n_0 - jk_0$) and the reflected and refracted rays. The incident ray is decomposed into s-polarized (E_s) and p-polarized (E_p) components. The reflected ray is decomposed into s-polarized (E'_s) and p-polarized (E'_p) components. The refracted ray is decomposed into s-polarized (E''_s) and p-polarized (E''_p) components. The angles of incidence and refraction are ϕ_0 and ϕ_1 respectively. The refractive indices of the media are $N_0 = n_0 - jk_0$ and $N_1 = n_1 - jk_1$.

$$E'_p = r_p E_p = a'_p \cos(\omega t - \bar{k} \cdot \bar{r} + \delta'_p), \quad E'_s = r_s E_s = a'_s \cos(\omega t - \bar{k} \cdot \bar{r} + \delta'_s)$$

where r_p and r_s are the Fresnel reflection coefficients for p and s light respectively.

The relative amplitude reduction, $\tan \psi$, and relative phase change Δ which characterize the changes in the state of polarization on reflection are found as the modulus and argument of the complex reflectance ratio, ρ :

$$\rho = \frac{r_p}{r_s} = \frac{E'_p/E_p}{E'_s/E_s} = \frac{a'_p/a'_s}{a_p/a_s} \exp j[(\delta'_p - \delta_p) - (\delta'_s - \delta_s)]$$

$$\approx \tan \psi \exp j\Delta$$

Using the boundary conditions on phase and amplitude of the electric field components gives r_p and r_s as

$$r_p = \frac{N_1 \cos \phi_o - N_o \cos \phi_1}{N_1 \cos \phi_o + N_o \cos \phi_1}; \quad r_s = \frac{N_1 \cos \phi_1 - N_o \cos \phi_o}{N_1 \cos \phi_1 + N_o \cos \phi_o}$$

where the subscripts refer to the media and ϕ_o and ϕ_1 are the angles of incidence and refraction respectively. Thus the quantities Δ and ψ which are measured by ellipsometry are functions of the refractive indices and angle of incidence.

For reflection from a film-covered surface, Δ and ψ also become functions of the refractive index of the film, its thickness d_1 , and the wavelength λ , through the total reflection coefficients R_p and R_s which include the contributions of reflections from both interfaces:

$$\rho = \tan \psi \exp j\Delta = \frac{R_p}{R_s} \quad (6.1)$$

and each R is of the form

$$R = \frac{r_{o1} + r_{12} \exp -2j\delta_1}{1 + r_{o1} r_{12} \exp -2j\delta_1}$$

where $\delta_1 = (2\pi N_1 d_1 \cos \phi_1)/\lambda$ and N_1 is now the refractive index of the film, the Fresnel reflection coefficient subscripts referring to the sequence in which the wave encounters the media.

6.2.2 The Poincaré sphere representation of elliptically polarized light

To understand how the quantities ψ and Δ are measured by ellipsometry, a representation for elliptically polarized light is required.

As already mentioned, the polarization can be specified by the amplitudes a_p and a_s and the phase difference $\delta = \delta_p - \delta_s$ of linearly polarized component vibrations in and perpendicular to a reference plane.

Alternatively, the representation may be made in terms of the ellipse traced out by the electric vector (Fig. 6.2), using the ratio of the semi-axes $\frac{b}{a}$ and the azimuth ϕ , i.e. the inclination of the major axis with the reference plane.

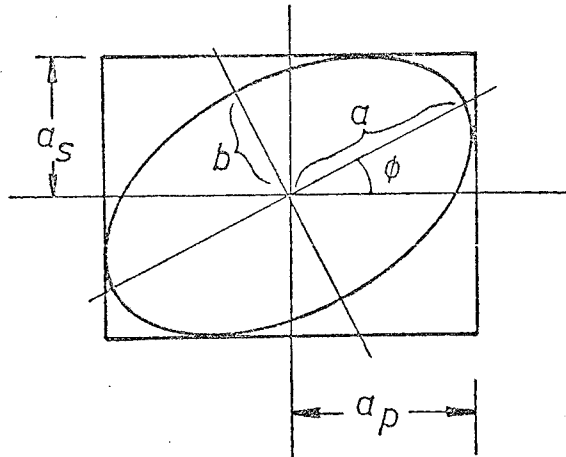


Fig. 6.2 The locus of the electric vector for elliptically polarized light in a plane normal to the direction of propagation

A comprehensive notation for the representation is the Stokes vector $\{s_0, s_1, s_2, s_3\}$. Using the auxiliary angles α and χ defined by

$$\tan \alpha = \frac{a_s}{a_p}, \quad \tan \chi = \pm \frac{b}{a},$$

it can be shown (Born and Wolf 1959) that the two forms for the vector relating to the two sets of quantities above are

$$\begin{aligned}
1 &= s_0 = 1 \\
\cos 2\alpha &= s_1 = \cos 2\chi \cos 2\phi \\
\sin 2\alpha \cos \delta &= s_2 = \cos 2\chi \sin 2\phi \\
\sin 2\alpha \sin \delta &= s_3 = \sin 2\chi
\end{aligned} \tag{6.2}$$

normalized so that the intensity parameter $s_0 = 1$. It can be seen that $s_0 = 1$, 2ϕ , 2χ are the spherical co-ordinates equivalent to cartesian co-ordinates s_1 , s_2 , s_3 , that is, the state of polarization can be represented by a point C on a sphere of unit radius. This sphere, called the Poincaré sphere, is shown in Fig. 6.3.

The intersection I of the positive s_1 axis with the equator represents the linearly polarized component in the reference plane. The longitude of the point measured clockwise from I represents twice the azimuth ϕ , and the latitude of the point twice the ellipticity, χ . Thus points on the equator, $\chi = 0$, represent linear polarizations of various azimuths from 0 to π , and the poles, $\chi = \pm 45^\circ$, represent circularly polarized light. By convention, the northern hemisphere is associated with left-handed ellipses, the southern with right-handedness. The opposite end S of the diameter through I represents a linear polarization of azimuth given by $2\phi = \pi$, i.e. the other component vibration in the plane perpendicular to the reference plane.

Returning to the expressions for s_1 , s_2 and s_3 , equations 6.2, we have

$$\frac{s_3}{s_2} = \tan \delta = \frac{\tan 2\chi}{\sin 2\phi} \tag{6.3}$$

and it can be seen that the angle between the perpendicular from C to the diameter IS and the equatorial plane is the phase angle between the linearly polarized components of C represented by I and S. Thus rotation

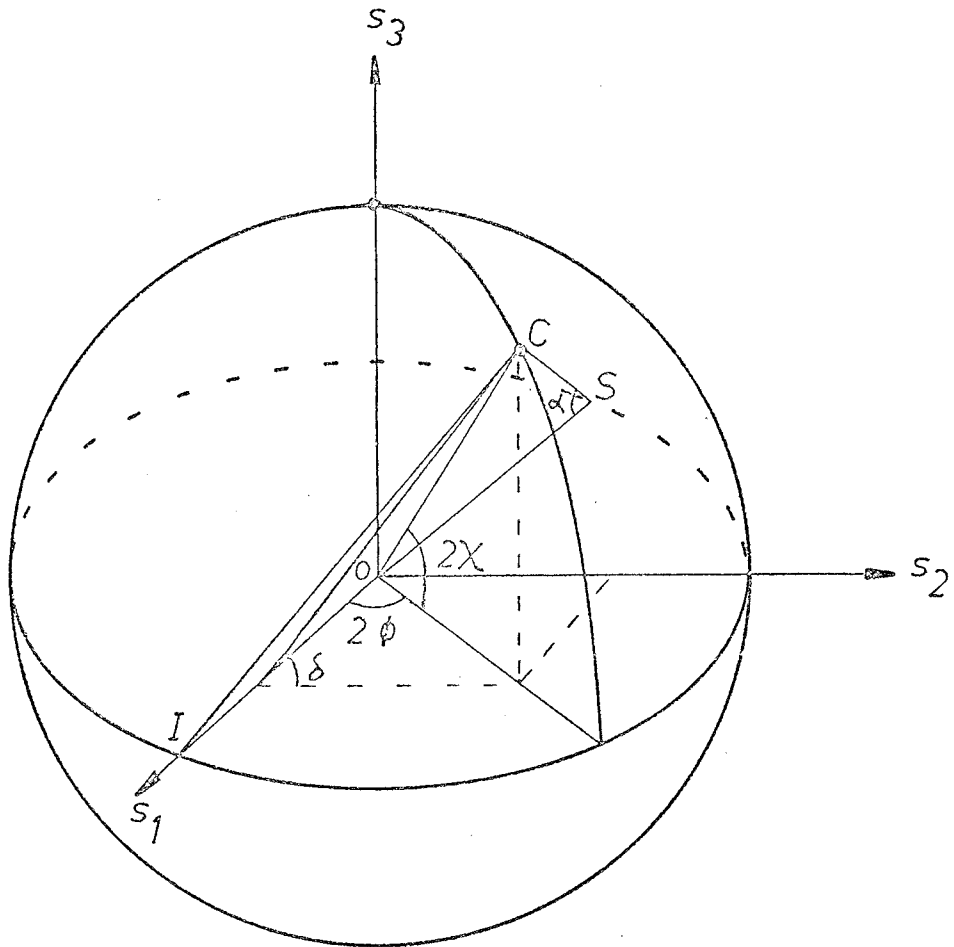


Fig. 6.3 Representation of polarized light on the Poincaré sphere.

of C about the diameter IS is equivalent to changing the phase difference δ between the components I and S.

Also

$$\frac{s_2}{s_1} = \tan 2\alpha \cos \delta = \tan 2\phi$$

so that $\hat{I}\hat{O}C = 2\alpha$, using the above result for δ .

$$\therefore \hat{C}\hat{S}I = \alpha \quad (\text{isosceles } \Delta \text{ CSO})$$

$$\text{and} \quad \frac{CI}{CS} = \tan \alpha = \frac{a_s}{a_p} \quad (6.4)$$

Thus in the triangle formed by C and the component diameter the amplitude ratio of the components is given by the length ratio of the triangle sides opposite the respective component points. Movement of C along a great circle containing I, C and S is therefore, equivalent to changing the ratio a_p/a_s of the components I and S.

The operation of the ellipsometer can now be considered, in particular the effects of a birefringent plate and reflection on the state of polarization of the light beam.

6.2.3 Theory and operation of the ellipsometer

The usual ellipsometer arrangement (Fig. 6.4) consists of a monochromatic light source(S), collimator(C), linear polarizer(P), quarter wave plate(Q), test surface(T), analyzer(A) (another linear polarizer) and detector(D).

Elliptic polarization is produced by passing a linearly polarized beam through the quarter wave plate, which is a birefringent plate of thickness such that the phase difference introduced between the components of the beam parallel to the fast and slow axes of the plate is $\pi/2$. On the Poincaré sphere this operation is represented by rotation

through an angle of $\pi/2$ about an equatorial diameter passing through the doubled azimuths of the fast and slow axes. It can be seen that this combination of a polarizer and a quarter wave plate can produce light of any ellipticity and azimuth.

The reflection of the elliptically polarized light at the test surface introduces an additional phase difference Δ between the p and s

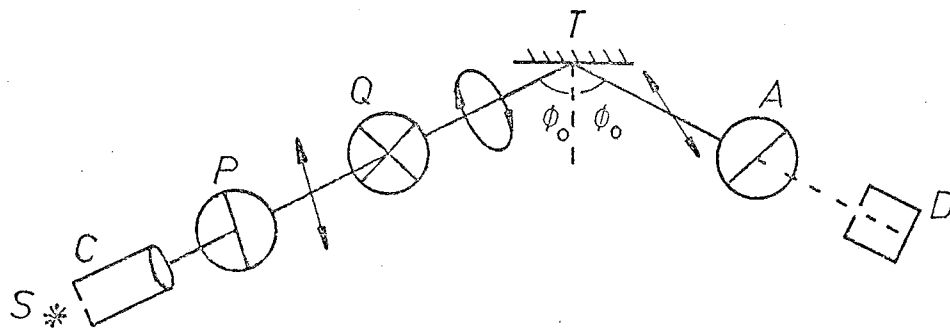


Fig. 6.4 Arrangement of the ellipsometer

components, and changes the ratio of their amplitudes by a factor $\tan\psi$. This is represented by rotation about an equatorial diameter passing through the doubled azimuths I and S of the planes of incidence and of the surface through an angle Δ , and movement of the resultant point C along a great circle through I and S until the ratio of the chords CI/CS has changed by the factor $\tan\psi$.

For a measurement, the ellipsometer is nulled by varying the parameters of the incident elliptic polarization until the reflected

polarization is linear and can therefore be extinguished by the (crossed) analyzer A. If this parameter variation is accomplished by rotating the polarizer P with the quarter wave plate fast axis at exactly $\pm \pi/4$ azimuth, the calculation of Δ and $\tan\psi$ from the extinction azimuths of P and A is greatly simplified, as can be seen on the Poincaré sphere shown in Fig. 6.5.

All azimuths are measured from the plane of incidence I, and we consider the quarter wave plate fast axis azimuth set at $-\pi/4$, as represented by the point Q_f . At null, a point on the equator representing the light emerging from the polarizer must be translated by the combined effect of the wave plate and surface reflection to another point on the equator (i.e. linear polarization) for complete extinction by the analyzer.

Assume that the polarizer has an azimuth between zero (point I) and $+\pi/4$ (point Q_s) so that the light emerging from it is represented by P in Fig. 6.5. The introduction of a $\pi/2$ phase difference by the quarter wave plate rotates P over the sphere about the diameter $Q_f Q_s$ through an angle $\pi/2$ to R on the great circle through Q_f and Q_s . Now since the phase difference Δ introduced by reflection causes a rotation about the diameter IS which is perpendicular to $Q_f Q_s$, and since the final point must be on the equator irrespective of the magnitude of $\tan\psi$, this rotation must move the point from R around the great circle to Q_f , so that angle $\widehat{RQ_f} = \Delta$. The relative amplitude reduction on reflection causes a movement around the equator from Q_f until the ratio of the chords subtended at I and S has changed by the factor $\tan\psi$. However, since at Q_f the chords $Q_f I$ and $Q_f S$ are equal, the chord ratio at the final point T, TS/TI , is simply equal to $\tan\psi$, and angle $\widehat{SIT} = \psi$.

The reflected light represented by T is extinguished by the analyzer in an orientation denoted by A, and it can be seen that angle $\widehat{AOI} = 2\psi$. Thus the angle ψ is given by the azimuth A of the analyzer at null. Also angle $\widehat{POQ}_f = \text{angle } \widehat{ROQ}_f = \Delta$, so that the phase change Δ is given by

$$\Delta = \text{angle } Q_f \widehat{OI} + \text{angle } I \widehat{OP} = \pi/2 + 2P \quad (6.5)$$

where P is the polarizer azimuth at null.

In the above example depicted in Fig. 6.5, the analyzer azimuth A is less than $\pi/2$. For the quarter wave plate fast axis at $-\pi/4$ azimuth, there is a second combination of polarizer and analyzer azimuths (apart from those differing by π), in which $A > \pi/2$, that also results in a null, but which has different $\psi - A$ and $\Delta - P$ relationships. These two sets of P and A values are termed zones, and are numbered 1 and 3 respectively. Similarly a quarter wave plate set at $+\pi/4$ gives two more zones, numbered 2 and 4, making four independent sets of P and A readings in all. Ideally, the Δ , ψ values obtained from measurements in all four zones should be identical; but due to various imperfections in the optical components and the alignment of the ellipsometer, the different zones yield slightly different values for the angles Δ and ψ . The subject of instrumental errors and ellipsometer alignment is treated in chapter 7.

Returning to section 6.2.1, Eqn. 6.1, it is seen that values of Δ and ψ obtained from one ellipsometer measurement enable the real and imaginary parts of Eqn. 6.1 to be solved for two unknown quantities of the film-substrate system, such as the thickness and refractive index of the film, if the latter is homogeneous and non-absorbing. If there are more than two unknowns, for instance if the film is absorbing and/or optically non-uniform (e.g. layered), or if the substrate optical

constants are not known, then a number of ellipsometry measurements must be used in a curve fitting procedure. These measurements may be obtained as a function of angle of incidence or of the immersion medium, but in anodization studies they are most easily obtained as a function of changing film thickness from in situ measurements during the oxide growth process.

6.2.4 The analysis of ellipsometry data

As a homogeneous non-absorbing film ($N_1 = n_1$) on a thick substrate ($N_2 = n_2 - jk_2$) increases in thickness, a curve is traced out in the Δ - ψ plane which recycles continuously. The curve may be an open or a closed loop, depending on the relative magnitudes of the optical constants of the substrate, film and ambient medium, and typical examples are shown in Fig. 6.6. The recycling can be understood from the expression for the reflection coefficients R_p and R_s in Eqn. 6.1, which are of the form $R(x)$, where $x = \delta_1 \bmod \pi$, δ_1 being the phase retardation for a single passage through the film.

If the film is absorbing ($k_1 \neq 0$) then the curve does not retrace itself on successive cycles but instead tends to lower values of ψ with increasing thickness. Alternatively, if the film consists of two uniform layers of oxide as shown in Fig. 6.7, growing at constant rates, then in general the ellipsometry curve does not retrace itself after one cycle, although if both layers are non-absorbing approximate retracing does occur after two cycles. In the latter case, depending on whether n_1 is less than or greater than n_2 , the second cycle moves to higher or lower ψ values than the first cycle respectively.

Thus by curve fitting computed Δ , ψ values for an assumed theoretical model to experimental Δ , ψ values obtained at various stages

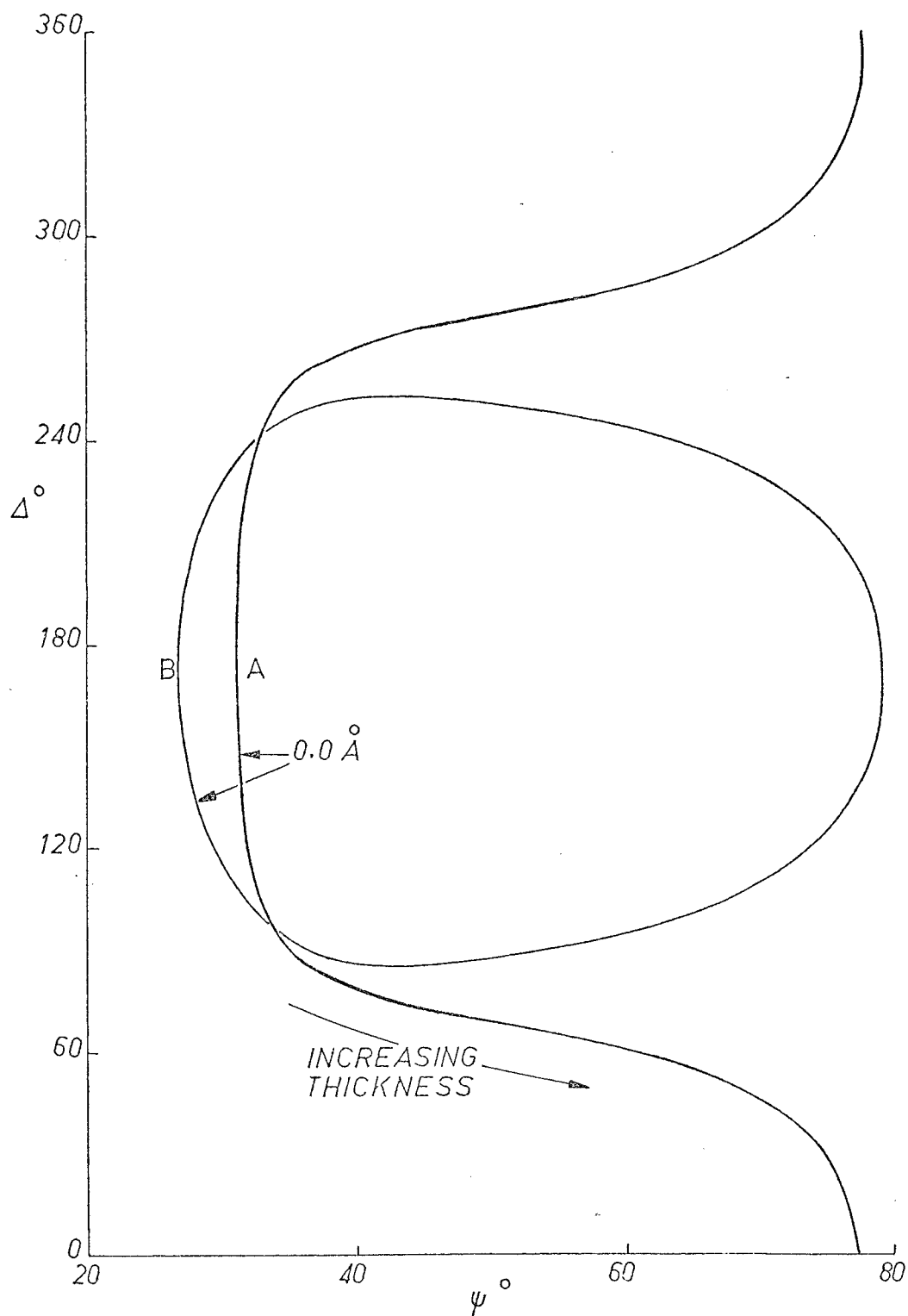
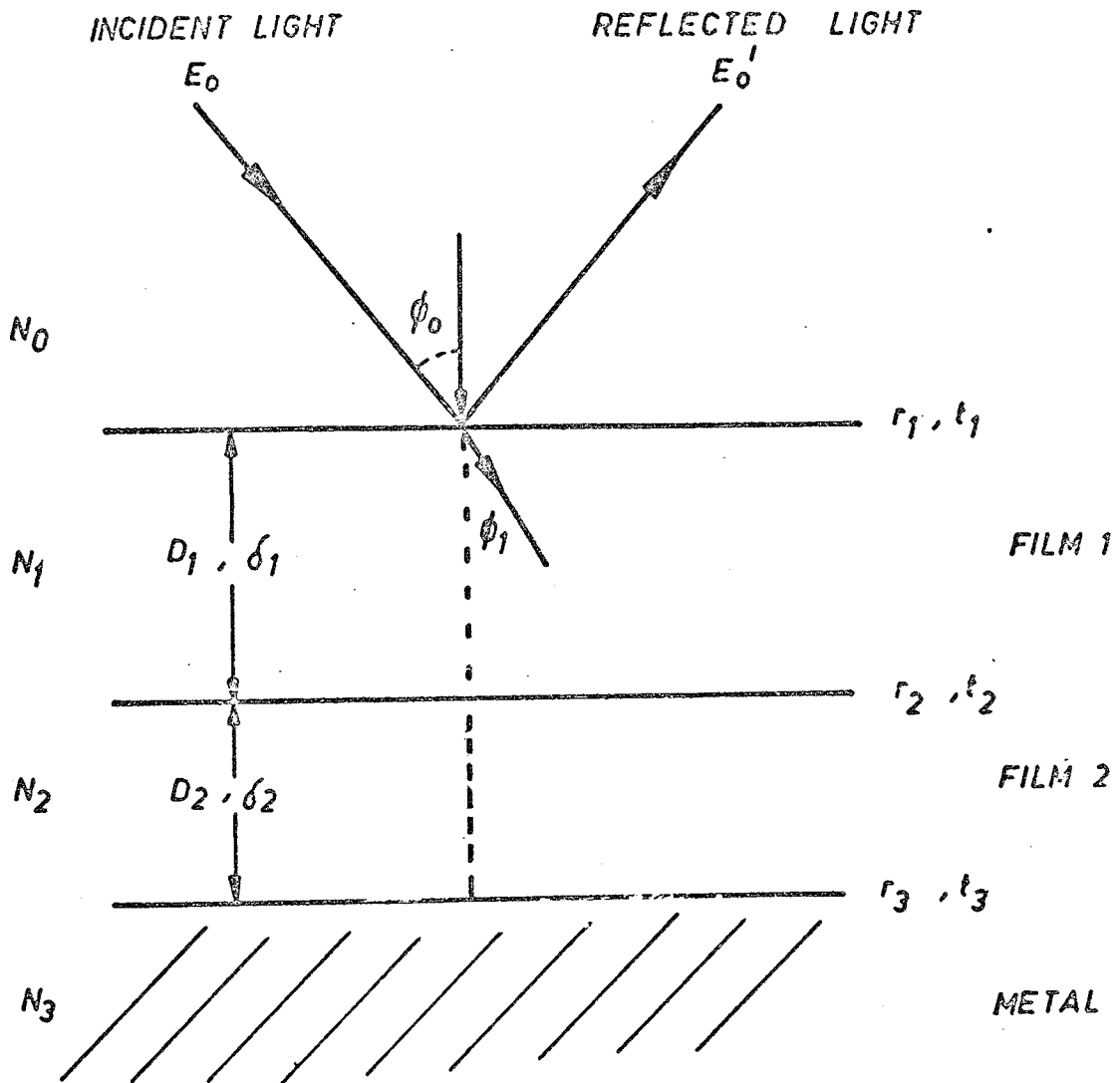


Fig. 6.6 Computed ellipsometry curves for single film ($N_1 = 2.25$) on niobium ($N_2 = 3.6 - j3.6$) at $\phi_0 = 65^\circ$ and $\lambda = 5461\text{\AA}$ in air (curve A) and water (curve B).



$N_i = n_i - jk_i$ INDEX OF REFRACTION OF i^{th} MEDIUM

$\delta_i = (2\pi N_i D_i \cos \phi_i) / \lambda$ PHASE RETARDATION OF i^{th} FILM

Fig. 6.7 Two layer model.

during the growth of an anodic oxide film, the optical structure of the film can be determined.

A computer program for analysis of ellipsometer measurements is available from the U.S. National Bureau of Standards (McCrackin 1969) which among other things will compute Δ , ψ values for single or multi-layer films, but which can analyze only single Δ , ψ experimental pairs. This program was obtained and modified for use on the U.B.C. IBM 360/67 computer. A program to fit to multiple experimental Δ , ψ values has been written by Dell'Oca 1969. It was originally designed for the analysis of ellipsometry data on the anodization of tantalum in aqueous electrolytes, and could employ a multi-layer film model with each layer growing so as to be a constant proportion of the total film thickness. In the present work the fitting strategy of this program was modified to accommodate closed Δ , ψ curves with sharp turning points such as are obtained for films of Al_2O_3 growing on aluminum, and the program was used on the U.B.C. computer to calculate values of oxide film thickness and refractive index, and in some cases to determine the substrate refractive index where this was not known at the laser wavelength used.

7. EXPERIMENTAL CONSIDERATIONS

7.1 The Discharge Tube and Vacuum System - Design and Fabrication

The purpose of selecting the dc cold cathode glow discharge as a plasma source was to permit an investigation of the anodization process as a function of plasma conditions. To facilitate this investigation, it was decided to base the principal dimensions of the anodization cell on the discharge tube used by Thompson 1961a, so that his detailed studies on particle concentrations and energy distributions in oxygen reported in section 4.5 could be applied as a guide to the plasma conditions used here. Furthermore, the process of high field ionic conduction in anodic oxides has a strong temperature dependence (see Eqn. 3.3) so that in any attempt to determine the importance of this process relative to other mechanisms associated with plasma conditions, the sample temperature must be closely controlled.

The equipment was therefore designed according to the following criteria:

- (a) To reproduce the experimental configuration used by Thompson 1961a where practical, and to permit anodization in different regions of the discharge.
- (b) To provide ease of optical alignment of the system for ellipsometry.
- (c) To enable control of sample temperature.
- (d) To minimize contamination by impurities, especially those detrimental to MOS applications, such as sodium ions.
- (e) To provide ease of sample replacement.

The anodization cell, shown in Fig. 7.1, consisted of a quartz tube 10 cm in diameter and 60 cm long, fitted with stainless steel end

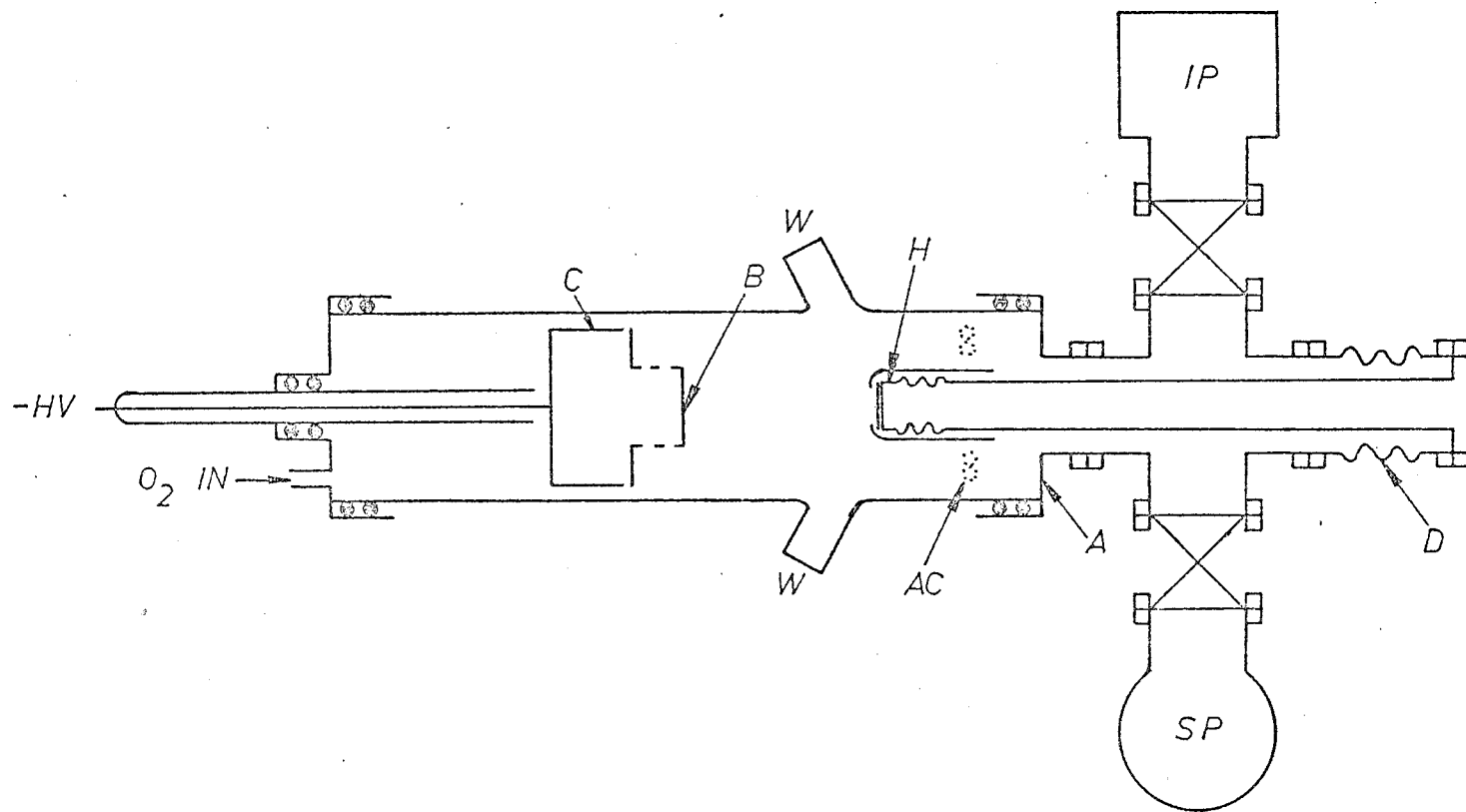


Fig. 7.1 Schematic of anodization cell and pumping station (system B).

caps each sealed by three neoprene 'O' rings. Teflon rings of flat rectangular cross-section were provided to cushion the end faces of the quartz tube. A hollow cathode (C) made of aluminum (for its low sputtering rate) was mounted on the end of an insulated linear motion feedthrough in one of the end caps, and the other end cap (A) served as grounded anode and connected the cell to a pumping system assembled from standard stainless steel components. The anode surface was gold plated by vacuum evaporation to reduce oxide formation and associated plasma potential variations.

An adjustable sample holder (H) electrically isolated from ground entered the discharge tube co-axially through the pumping port in the anode. The holder, shown in Fig. 7.2, consisted of a hollow 2.6 cm diameter stainless steel block joined via stainless steel bellows to a pyrex tube (T) which was mounted on a standard vacuum flange. Water could be circulated via teflon tubes through the block, which had a chromel-alumel thermocouple (TC) embedded in the back of the sample mounting face. The block, bellows and pyrex tube were covered by a two-part tubular quartz shield (Q) held by springs, for isolation from the discharge, and together with a mica mask (M) this shield served to hold the sample (S) in contact with the temperature-controlled block. The entire sample holder assembly could be extracted through the pumping port for sample replacement. Except in early experiments, a line of sight baffle (B) also made of quartz was attached to the front of the cathode to reduce the possibility of sputtered aluminum depositing on the sample*.

* An investigation of the anodized surface of a tantalum sample with an electron probe microanalyzer did not detect any aluminum impurity, but minor particulate contamination present on the oxide surface was found to be rich in silicon, and was attributed to the mica mask.

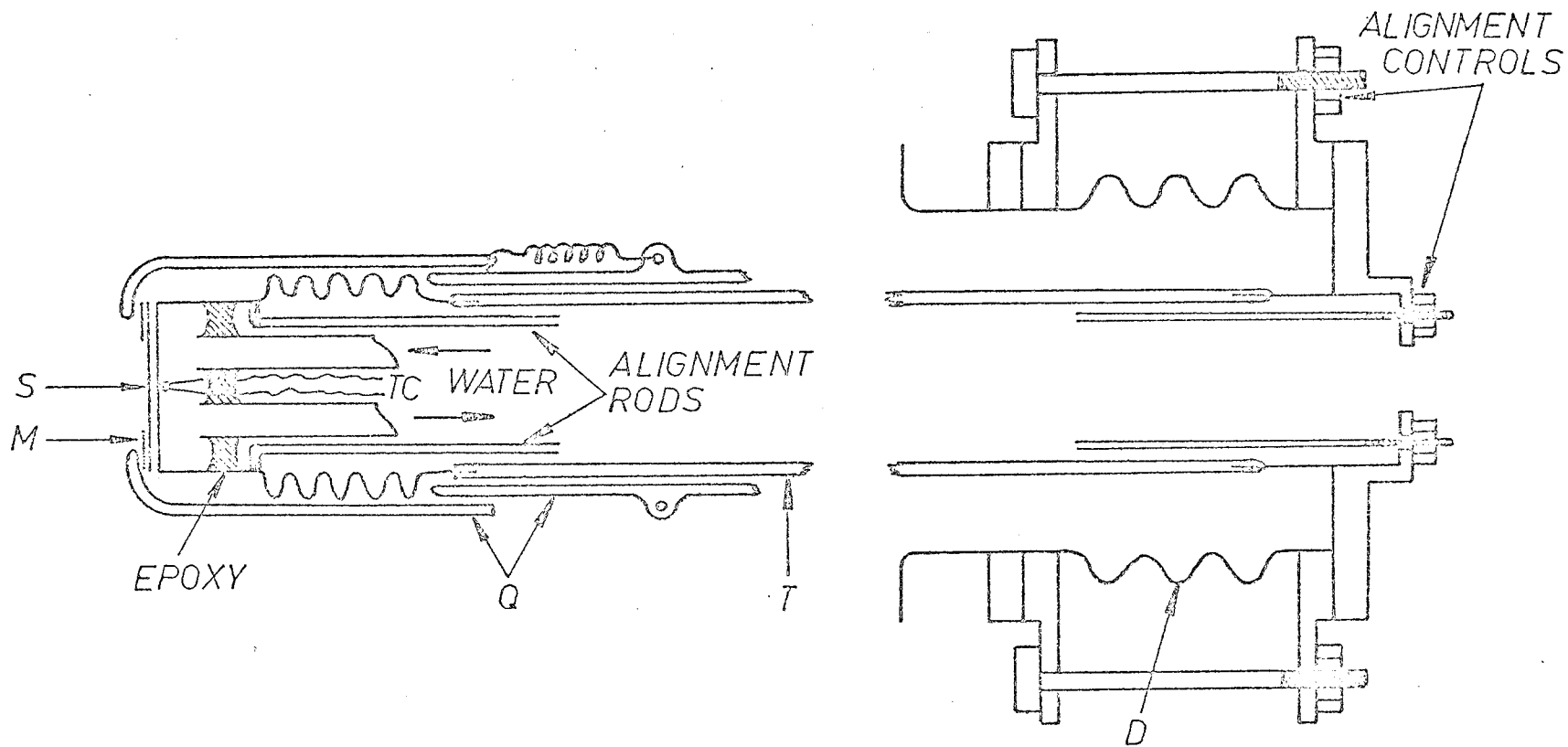


Fig. 7.2 The water-cooled adjustable sample holder.

In order to avoid hydrocarbon contamination from diffusion pumps, a sorption pump (SP) - ion pump (IP) combination was used in the pumping station. The sorption pump (Varian 941-6002) was controlled by a variable leak valve (Granville Phillips model 203) and the 20ℓ/sec differential ion pump (Ultek) was provided with an isolation valve (Granville Phillips type C model 202). A stainless steel gas feed line connected a cylinder of 99.999% oxygen (Matheson research grade) via another leak valve to the cathode end cap. Overnight pumping with the ion pump enabled a base pressure of 2×10^{-7} torr to be reached. The pressure range around 100 mtorr used for operation of the discharge was obtained by continuous sorption pumping of oxygen from the cylinder, to minimize impurity build-up. The pressure could be maintained within ~3% of a desired value (as indicated by the amplified signal from a thermocouple gauge* displayed on a chart recorder) by manual control of the oxygen inlet and pump leak valves. With periodic inspection of the chart trace and appropriate valve adjustment, the pressure could be held constant for the periods of several hours sometimes required to produce the desired oxide thicknesses.

Different regions of the discharge could be located around the sample by moving the cathode via its linear motion feedthrough, and various probes mounted on pyrex tubes could be brought in front of the sample by means of double 'O' ring feedthroughs in the anode end cap. These consisted of a simple 0.5 mm diameter gold ball probe, a triple probe assembly of three platinum wires with 5 mm spacing for field measurements, an electron filter array of 0.08 mm diameter tungsten wires with 1 mm spacing and an indium-coated gold ball probe which was spring-

* This gauge, an Ultek model VT 6, was calibrated against an absolute gauge of the McLeod type.

loaded for MOS capacitance measurements.

The discharge and sample biasing circuits are shown in Fig. 7.3. The high voltage supply (Hewlett Packard model 6525A) was provided with a current limit control and ammeter, which were used to maintain the discharge current constant under varying conditions. The current generator (Northeast Scientific model RI 233) could supply constant currents from 10 μ A up to 225 mA.

The discharge tube was fitted with 2.5 cm diameter plane-parallel quartz windows W (Fig. 7.1) on short side arms to allow entry and exit of the ellipsometer light beam before and after reflection from the sample surface. The arms were mounted for an angle of incidence of 70° at the sample*.

The discharge tube and pumping system were mounted on a carriage fitted with roller bearings and running on a twin rail system. The ellipsometer stood on a rotatable plate also mounted on the heavy steel base of the rail system. The discharge tube could be moved into position between the ellipsometer arms, and aligned by means of various facilities on the carriage until the ellipsometer light beam passed at normal incidence through the tube windows. Alignment of the sample was accomplished by tensioning two sets of threaded rods, one set attached inside the holder at the joint between the hollow block and its bellows, the other attached to the flanges of a larger bellows D which connected the

* This angle was selected on the basis of the sensitivity of the ellipsometer measurement to the thickness of films of Nb_2O_5 on Nb and SiO_2 on Si, obtained from computer calculations using literature values of the refractive indices.

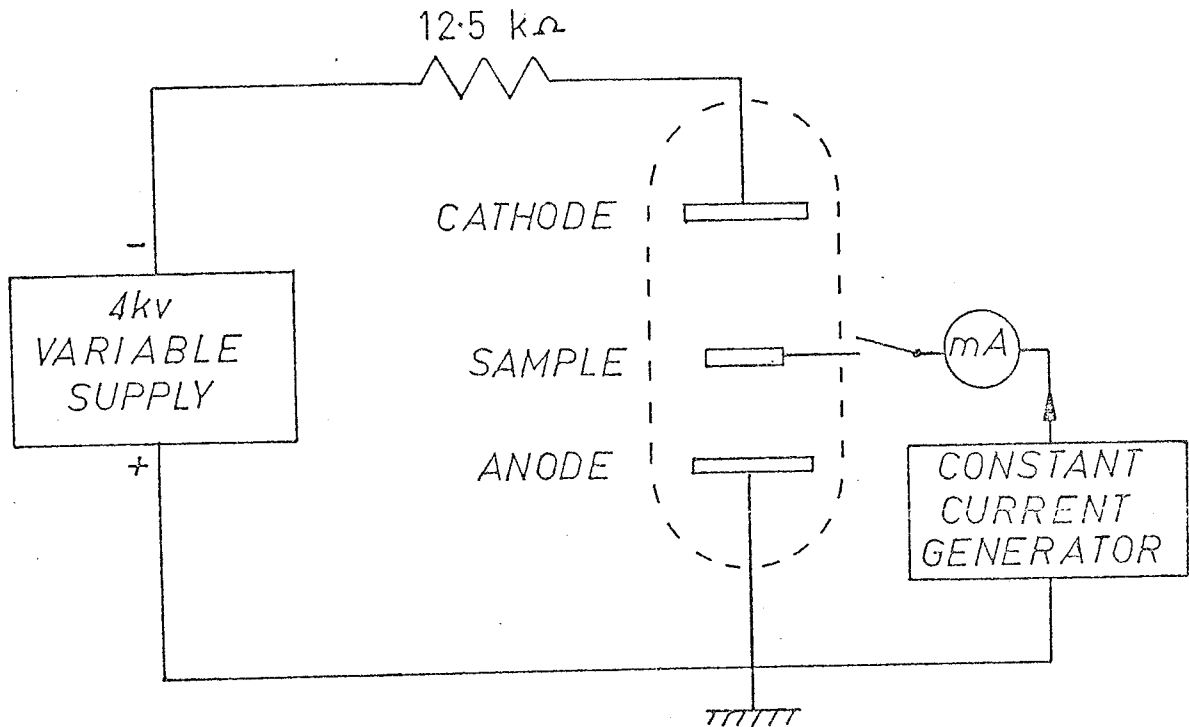


Fig. 7.3 Discharge and sample biasing circuits.

holder to the system (rods not shown in Fig. 7.1).

7.2 The Optical System

7.2.1 The automated ellipsometer

The basic ellipsometer was a Rudolph model 200E. A 1 mW He-Ne laser (Spectra-Physics model 133, not linearly polarized) was used as a light source* and a photomultiplier (RCA 931A tube with Kepco regulated voltage source) as a detector. A protective ground glass diffuser was placed over the photomultiplier window, and a 6328Å filter (100Å bandwidth) was located in front of the diffuser. The laser and filter combination enabled measurements to be made in the presence of normal room lighting, and more importantly, in the presence of the emission from the glow discharge. The Rudolph 5461Å quarter wave plate was replaced initially by a 6328Å mica quarter wave plate, and later by a quartz Soleil-Babinet type compensator (Gaertner model L-135) mounted on the Rudolph wave plate drum and set for quarter wave retardation at 6328Å.

A Digital Equipment Corp. PDP-8/E minicomputer was used to operate the ellipsometer in the following automated system, depicted in Fig. 7.4.

The polarizer and analyzer mounts were each driven via gear trains by separate stepping motors (IMC Magnetics Corporation #PIN 008-008), one step producing .01° rotation, and their azimuthal positions were detected to 0.01° by shaft encoders (Decitrak TR 511-CW/D). The encoder output unit converted the angles to binary-coded decimal form

* all refractive indices determined in this study pertain to the

He-Ne laser wavelength of 6328 Å.

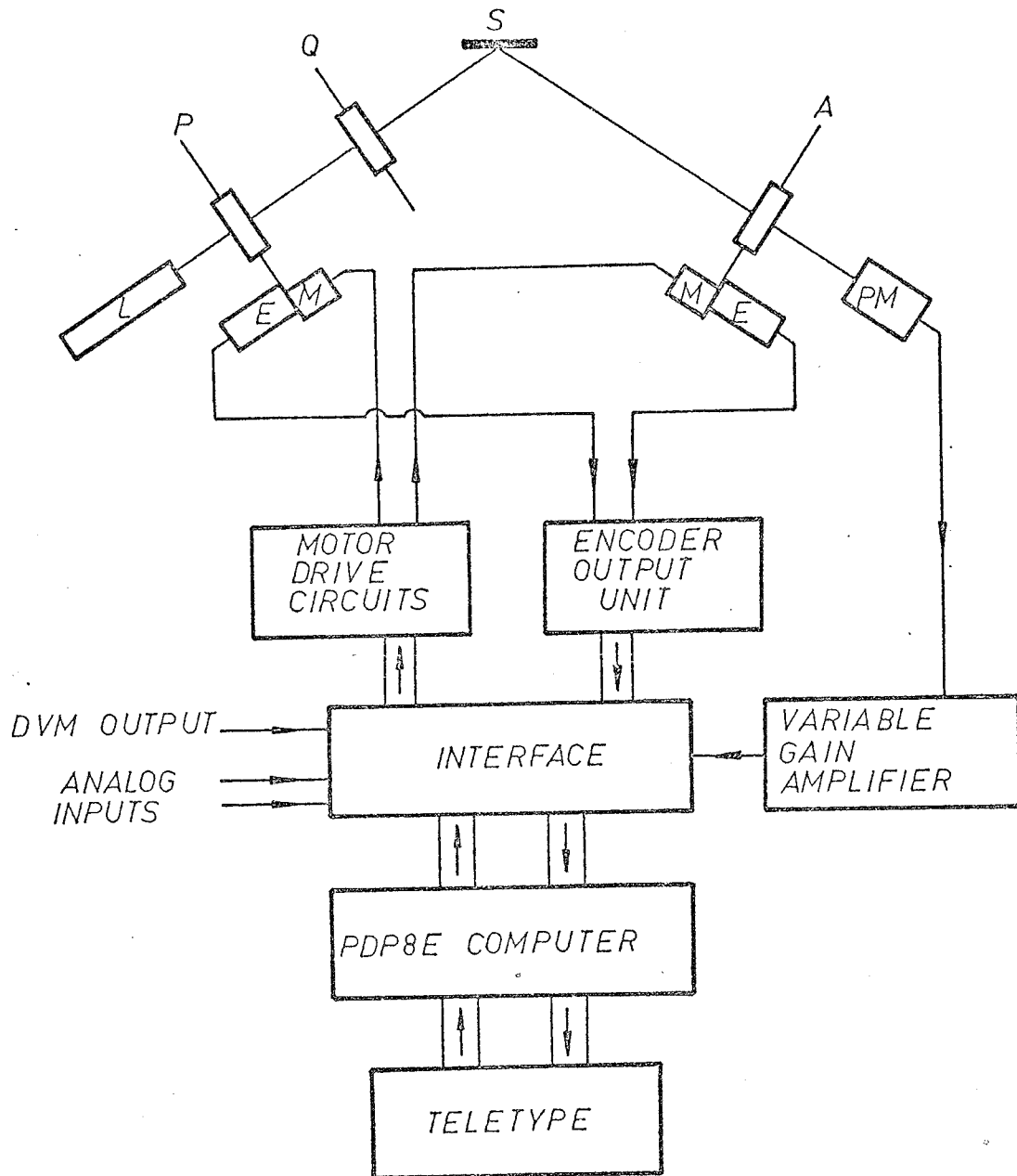


Fig. 7.4 Schematic of computer-controlled ellipsometer system

(BCD) for input to the computer via an interface, which was largely completed independently of this study. The motor drive circuits were also controlled via this interface.

The photomultiplier error signal, after amplification by a variable gain amplifier with an adjustable zero control, was monitored as one of four analog inputs multiplexed in the interface to a single analog-to-digital converter (DEC A811) with an accuracy of 0.1% F.S. The error signal was also displayed on a meter connected to the input of the A/D converter, to permit manual nulling and alignment of the ellipsometer.

The BCD output from a digital voltmeter could be fed to the interface, which also contained a clock consisting of a divide-by-six counter that was triggered by a 60 Hz signal, giving a basic unit of 0.1 seconds, and the 10 Hz pulses were fed to a second counter which was used to obtain specified intervals between successive balances of the ellipsometer.

The strategy employed in automatic balancing of the ellipsometer was based on the principle that the light intensity at the detector (error signal) varies symmetrically with polarizer (or analyzer) rotation about its minimum value for small excursions from the minimum (Archer 1962). Furthermore, the polarizer is adjusted first since its true extinction setting is independent of the exact setting of the analyzer for small deviations of the latter, whereas the converse is not true (Archer 1962). In its balancing routine, the computer program determines which way the polarizer motor must be stepped to reduce the photomultiplier error signal, and then steps the motor in that direction, taking error signal readings after each step. The readings for a certain number of steps (e.g. 64) are summed, and stepping is continued so that the error

signal eventually goes through a minimum and begins to increase again. The program then calculates a second sum of the same number of readings and continuously updates this sum to contain only the 64 most recent readings. When this second sum equals the first sum obtained on the other side of the minimum, the balance point, i.e. the mid-point between the two equal sums, is calculated and the polarizer is stepped to that position. Then the analyzer is adjusted by the same routine. Provision is made for the polarizer or analyzer starting in their (previously) balanced position by driving the motors away from the balance point prior to proceeding as above, and a check for any error due to gear backlash or missed or gratuitous motor steps was made by comparing the change in position of the shaft encoder before and after a balance with the net number of steps taken by the respective motor.

After the analyzer and polarizer have both been balanced, their encoder settings, the minimized error signal, the clock time and the digital voltmeter output are read and stored to await output on a teletype operated on an interrupt basis. The time required to balance the ellipsometer (from a condition close to balance) was about 2 to 3 seconds, and printing the data by the teletype required 5 or 6 seconds. These times presented no problem in the present studies, for which the ellipsometer was balanced at one minute intervals.

To obtain readings in other ellipsometer zones (see section 6.2.3), it was necessary to manually preset the ellipsometer components.

In principle the system could be programmed to alternate readings between two zones not requiring rotation of the quarter wave plate, although the time required to step the polarizer and analyzer from one zone to the other may be excessive for certain applications.

The computer was not used to calculate Δ and ψ from the extinction settings of the polarizer and analyzer due to its limited memory and arithmetic capabilities. The corrections required for quarter wave plate imperfections in these calculations are dealt with in section 7.2.3.

7.2.2 Ellipsometer alignment

Proper alignment of the ellipsometer is critical if meaningful measurements using the full sensitivity of the instrument are to be obtained. This is especially true of automated measurements in one zone only.

Errors which may be present in a misaligned instrument include

- (i) zero error in angle of incidence scale
- (ii) variation of the plane of incidence with angle of incidence
- (iii) zero errors in the polarizer, analyzer and quarter wave plate azimuth scales.

Various methods of alignment have been described. McCrackin et al. 1963 favoured the use of a metal reflecting surface, and presented a method which was independent of any small ellipticity in the polarizer prism. Aspnes and Studna 1971, however, pointed out that the use of a transparent reflecting surface eliminated the effect of first order ellipticities in either prism, and this approach was adopted. The overall alignment procedure was as follows.

(a) Collimator focusing

Although a laser was used as a light source, the collimator was retained since its input pinhole conveniently defined the polarizer arm axis. Focusing was necessary since a condensing lens concentrated the laser beam on this input pinhole. The collimating lens position was adjusted until the exit beam was sharp when viewed through an

auxiliary telescope previously focussed on infinity (the Rudolph analyzer arm eyepiece optics could not be focused on objects more than 2 or 3 feet distant).

(b) Alignment of laser beam with polarizer arm axis

A mounting fabricated for the laser was adjusted until a maximum intensity was transmitted through the stopped down quarter wave plate exit iris diaphragm. This maximum was detected by the photomultiplier with the analyzer arm in the straight through position but with no apertures to restrict the light beam's passage to the ground glass diffuser.

(c) Determination of zero error in angle of incidence scale

With the quarter wave plate iris stopped down as above, and the analyzer arm axis defined by small apertures at the entrance and also immediately in front of the photomultiplier filter, the analyzer arm was rotated in $.01^\circ$ steps through the position of maximum detector signal, noting the error signal meter deflection at each point. The distribution curve thus obtained was reasonably symmetrical, see Fig. 7.5, and the angle of incidence scale error was determined from the peak signal position to be -0.05° .

(d) Determination of the zero error in the polarizer and analyzer azimuth scales*.

The purpose of this procedure is to determine the analyzer and polarizer scale readings P and A when the planes of transmission of their prisms are parallel to the plane of incidence. The latter is defined by the directions of propagation of the incident and reflected beams

*

The theoretical basis for this portion of the alignment procedure is given by Aspnes and Studna 1971.

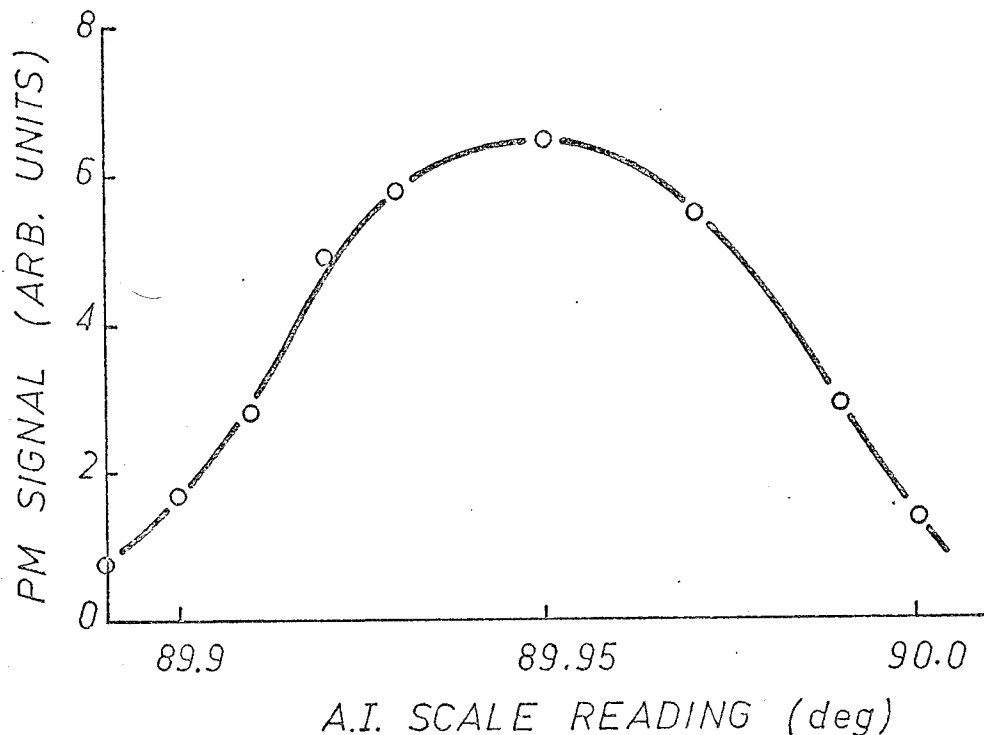


Fig. 7.5 Angle of incidence (A.I.) zero error determination.

and so may move with angle of incidence if either of the polarizer or analyzer arm axes is not perpendicular to the axis about which the analyzer arm pivots. Since the Rudolph ellipsometer is not provided with tilt adjustment on the arms, the procedure should be performed with the analyzer arm at the angle of incidence to be used in subsequent measurements. An extra iris diaphragm aperture was mounted at the exit of the polarizer assembly to permit the establishment of the plane of incidence, with the quarter wave plate assembly removed, as follows.

After setting the desired angle of incidence of 70° (allowing for the zero error determined in (c)), with the compensator removed and with $P \approx A \approx 90^\circ$ a thick optically flat quartz plate was mounted as a

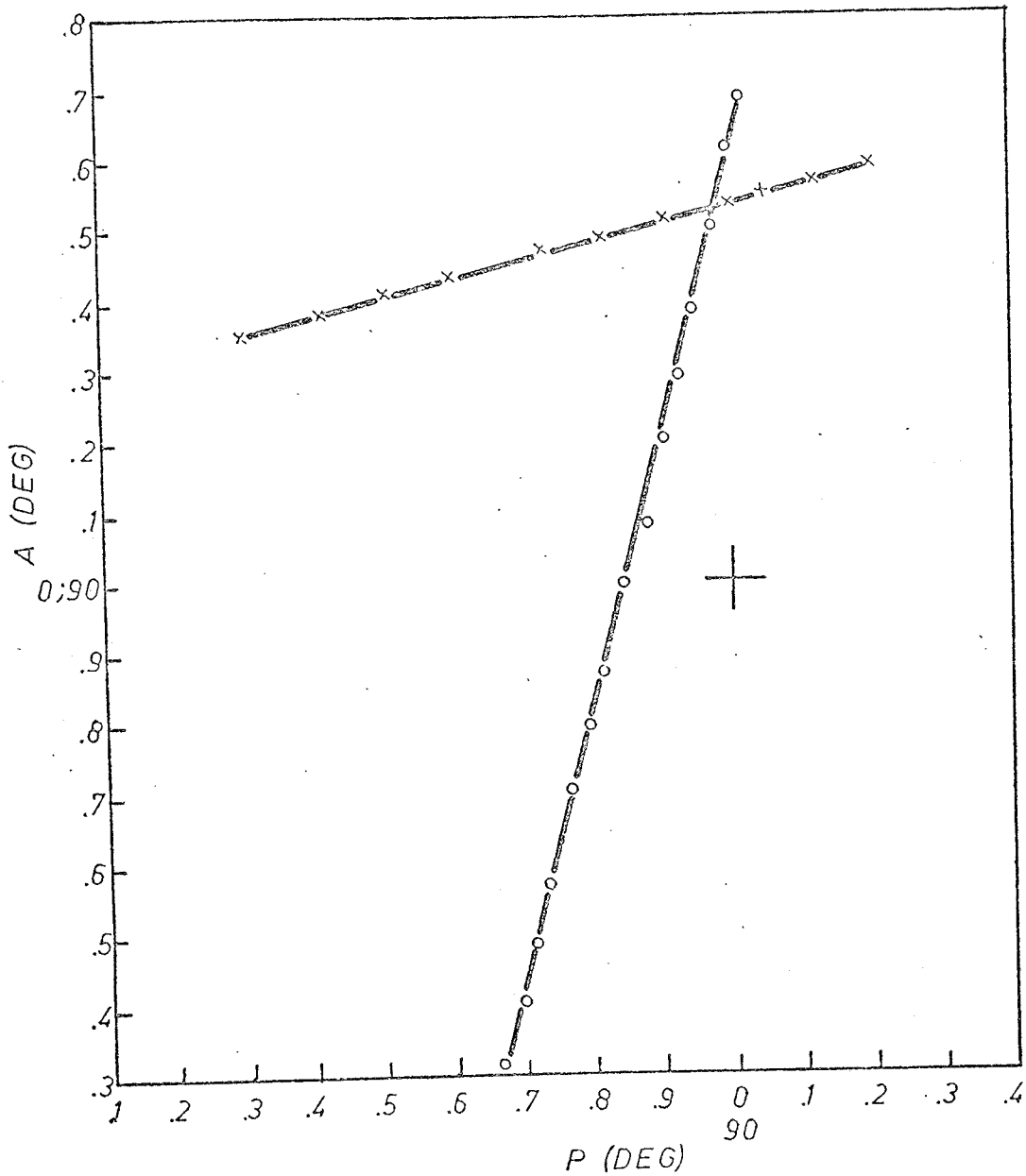
dielectric reflector and its position adjusted until a maximum detector signal was obtained. This adjustment is purely geometric and independent of component imperfections.

With the plane of incidence established in this way, the analyzer was allowed to null near $A = 0^\circ$ for different set values of P about 90° to obtain a straight line plot of A versus P (here the outputs from the shaft encoders). Then the polarizer was allowed to null near $P = 0^\circ$ for different set values of A about 90° to obtain another straight-line plot of P versus A . The results of a typical calibration are shown in Fig. 7.6. At the point of intersection the transmitted field vectors of the polarizer and analyzer prisms are parallel (or perpendicular) to the plane of incidence. The shaft encoder outputs were corrected by first setting the polarizer and analyzer so that the outputs read the intersection values, and then adjusting the shaft encoder positions in their mountings until the encoder outputs read 0.00° (or 90.00°).

It should be noted that the usefulness of this alignment depends on the reproducibility with which any sample reflecting surface can be positioned by maximizing the intensity of light transmitted through the ellipsometer. This point is dealt with further in section 7.2.3.

(e) Determination of the zero error in the quarter wave plate azimuth scale.

With the polarizer and analyzer crossed at 0.00° and 90.00° in the straight through position, the quarter wave plate (QWP) assembly was re-inserted and its azimuth adjusted until minimum transmission was again obtained. In this condition the fast axis of the QWP was parallel to the polarizer transmission axis, i.e. 0.0° azimuth, and the QWP scale



error could be determined.

- (f) Calibration and tuning of a Soleil-Babinet Compensator for use as a near-ideal quarter wave plate.

Ellipsometer measurements made in the fully automated mode were restricted to a single zone. In the calculation of Δ and ψ from such measurements, serious errors can be introduced by quarter wave plate imperfections, i.e. deviations of the relative phase retardation Δ_c and transmittance ratio T_c from the ideal values of 90.0° and 1.0 respectively (see section 7.2.3). It is therefore very desirable to have as perfect a QWP as possible, and in the present study a very carefully adjusted quartz Soleil-Babinet compensator (SBC) was used.

This device consists of two wedges of quartz arranged to slide relative to each other so that they form a parallel plate of variable thickness, mounted on a second parallel plate of fixed thickness. The optic axes of the two plates are in the plane of the plates but mutually perpendicular, so that when light passes through the two plates, a phase difference is introduced between the two components parallel to the axes whose magnitude can be varied by changing the thickness of the sliding wedge plate. The Gaertner model L-135 SBC used here was provided with a micrometer screw for wedge movement.

The parameters Δ_c and T_c are strong functions of angle of incidence, which in turn may be a function of compensator azimuth Q (see section 7.2.3), and so the calibration and tuning were carried out with the SBC fast axis at the azimuth of 315° ($=-45^\circ$) required for subsequent measurements in zone 1 (selected for its simple Δ , P and ψ , A relations). First the approximate micrometer setting for 90° retardation (or $\frac{n\pi}{2}$ where n is an odd integer) for the laser light was determined by mounting

the SBC with its fast axis at approximately 315° between polarizer and analyzer crossed at 0.0° and 90.0° in the straight through position, and noting the micrometer readings which gave extinction at the detector. These are the settings producing $0, 2\pi, 4\pi, \dots$ retardation, i.e. the difference between successive settings represents 2π retardation and should be constant. The $\frac{n\pi}{2}$ retardation condition is obtained by adding one quarter of this difference to any of the above null settings.

With this approximate quarter wave setting, the SBC fast axis azimuth was set to exactly 315.0° by adjusting for a null with $P = 315.0^\circ$, $A = 45.0^\circ$ (equivalent to (e) above).

The final tuning of the SBC micrometer screw was accomplished by minimizing the differences between readings in zones 1 and 3 obtained with a carefully aligned polished metal surface as reflector (the quartz surface could not be used since in the Δ, P and ψ, A relations the compensator imperfection parameters have coefficients of $\sin\Delta$, which equals zero for dielectrics). A glass slide coated with Inconel having a mirror-like finish was used as the reflector, and aligned by maximizing the light reflected at 70° with the SBC assembly removed and $P \approx A \approx 90^\circ$. The alignment was checked and considered good by finding that P balanced at $0.0 \pm 0.01^\circ$ when A was set at 90.0° . The compensator was then replaced and by very careful adjustment of the micrometer, the following minimal spread readings were obtained:

| | P | A |
|--------|--------|--------|
| Zone 1 | 16.82 | 32.75 |
| Zone 3 | 106.75 | 147.22 |

Using these readings in the Δ, P and ψ, A relations, programmed by McCrackin 1969, gave the tuned compensator constants as $\Delta_c = 90.04^\circ$,

$T_c = 0.998$, so that Δ and ψ could be obtained to a good approximation ($\pm 0.1\%$) from either zone 1 or zone 3 measurements using the following simple relations*, providing there were no errors due to cell windows or tilt of the sample surface (see next section):

$$\text{Zone 1 } \left\{ \begin{array}{l} \Delta = 90^\circ + 2P_1, \quad 135^\circ \geq P_1 \geq -45^\circ \\ \psi = A_1, \quad 90^\circ \geq A_1 \geq 0^\circ \end{array} \right\} \quad Q = -45^\circ \quad (7.1a)$$

$$(7.1b)$$

$$\text{Zone 3 } \left\{ \begin{array}{l} \Delta = 2P_3 - 90^\circ, \quad 225^\circ \geq P_3 \geq 45^\circ \\ \psi = 180^\circ - A_3, \quad 180^\circ \geq A_3 \geq 90^\circ \end{array} \right\} \quad Q = -45^\circ \quad (7.1c)$$

$$(7.1d)$$

7.2.3 Treatment of errors in in situ ellipsometry

The analysis and correction of errors in ellipsometry has been the subject of a number of recent papers, for instance McCrackin 1970, Aspnes 1971, Azzam and Bashara 1971. A brief discussion of some of the more important errors will be presented here.

(a) Polarization of the light source

Ideally the light incident on the polarizer should be isotropic, with no linear preferences. This condition was checked for the Spectra-Physics laser used here by inserting a circular polarizer after the laser and noting any change in the null P and A settings for reflection from a surface. The changes observed were negligible for two different angles of incidence and different orientations of the circular polarizer, and the laser was assumed to be sufficiently unpolarized.

* The ideal ellipsometer relations for the other two zones are:

$$\text{Zone 2 } \left\{ \begin{array}{l} \Delta = 270^\circ - 2P_2, \quad 135^\circ \geq P_2 \geq -45^\circ \\ \psi = A_2, \quad 90^\circ \geq A_2 \geq 0^\circ \end{array} \right\} \quad Q = +45^\circ$$

$$\text{Zone 4 } \left\{ \begin{array}{l} \Delta = 90^\circ - 2P_4, \quad 45^\circ \geq P_4 \geq -225^\circ \\ \psi = 180^\circ - A_4, \quad 180^\circ \geq A_4 \geq 90^\circ \end{array} \right\} \quad Q = +45^\circ$$

(b) Polarizer and analyzer prism imperfections

These include leakage, i.e. the transmission of light not polarized parallel to the transmitted field vector of the prism, and depolarization. The degree of polarization of a partially polarized beam of light is the intensity of the polarized part as a fraction of the total intensity. In terms of the Stokes parameters it is given by $(s_1^2 + s_2^2 + s_3^2)^{1/2}/s_0$.

Polarizer prism leakage can be checked by nulling the ellipsometer, in straight through operation with the compensator removed, for various orientations of the polarizer with respect to a partially polarized light source. If the relative azimuth A-P is invariant under this operation, then polarizer leakage is negligible. This was found to be the case for the Rudolph polarizer, and Aspnes 1971 found that leakage was in general undetectable in ellipsometer-quality calcite prisms. He also showed that averaging measurements over four zones would cancel the effect of leakage if the compensator was perfect.

Azzam and Bashara 1971 showed that polarizer depolarization would affect the calculation of ψ and would not be cancelled by four-zone averaging - a 1% depolarization could give an error of 0.15° in a ψ of 22.5° .

All analyzer prism imperfections are cancelled by just two-zone averaging, so that the better prism should be used as polarizer.

(c) Compensator imperfections

The two major imperfections are, as mentioned in section 7.2.2, deviations of the retardation Δ_c and relative transmittance T_c from 90.0° and unity respectively. Holmes 1964 and Oldham 1967 have pointed out that due to multiple internal reflection interference phenomena, Δ_c and

T_c are both oscillating functions of compensator plate thickness, and also strong functions of angle of incidence. The latter means that if the compensator axis of rotation is not well aligned with the direction of propagation of the light, then Δ_c and T_c will be functions of QWP azimuth Q . The mica quarter wave plate used initially in this work showed both of these effects - computer calculations (McCrackin 1969) from four zone measurements on a carefully aligned Inconel surface gave the following values:

| Q | T_c | Δ_c |
|-------------|-------|------------|
| 45° | 1.041 | 91.58 |
| -45° | 1.033 | 92.33 |

On the Poincaré sphere (Fig. 6.5) it may be seen that small deviations in Δ_c mainly affect ψ , and those in T_c affect Δ . McCrackin 1970 has shown that for a quarter wave plate with small imperfections set at $Q = -45^\circ$ the relations between P , A , Δ , ψ and the imperfections $t = T_c - 1$ and $\alpha = \Delta_c - 90^\circ$ are

$$\begin{aligned}
 \text{Zone 1} & \begin{cases} P_1 = (\Delta - 90^\circ - t \sin \Delta) / 2 & 135^\circ \geq P_1 \geq -45^\circ \\ A_1 = \psi - (\alpha \sin \Delta \sin 2\psi) / 2 & 90^\circ \geq A_1 \geq 0^\circ \end{cases} \\
 \text{Zone 3} & \begin{cases} P_3 = (\Delta + 90^\circ + t \sin \Delta) / 2 & 225^\circ \geq P_3 \geq 45^\circ \\ A_3 = 180^\circ - \psi - (\alpha \sin \Delta \sin 2\psi) / 2 & 180^\circ \geq A_3 \geq 90^\circ \end{cases}
 \end{aligned} \tag{7.2}$$

Thus if both these imperfections are small, they may be cancelled by two-zone averaging. The errors are maximum for a surface with $\Delta \approx 90^\circ$ and $\psi \approx 45^\circ$, which implies that a reflecting surface with these values should be chosen for the evaluation of these errors or for their minimization by compensator tuning. This was reasonably satisfied by the Inconel surface ($\Delta \approx 123^\circ$, $\psi \approx 33^\circ$) used in section 7.2.2(f).

Other imperfections which may be present in the compensator are strain birefringence and optical activity. Aspnes 1971 found the former to be absent in quartz components, and the effects of both are expected to be cancelled by averaging over all four zones (Azzam and Bashara 1971).

(d) Cell windows

Strain birefringence in the cell windows may be a major source of error in in situ measurements. The effect can be analyzed by treating each window as a wave plate of fixed azimuth and small relative retardation. If the compensator is near-ideal, the small compensator and window corrections will add algebraically, and McCrackin 1970 has shown that their combined effect on ψ is cancelled by two-zone averaging, but the two-zone-averaged Δ must be corrected by a window correction factor w which is independent of Δ . The equations 7.2 become

$$\text{Zone 1} \quad \left\{ \begin{array}{l} P_1 = [\Delta - 90^\circ - t \sin \Delta - (\alpha_2 / \tan 2\psi) + w] / 2 \\ A_1 = \psi + (\alpha_1 - \alpha) (\sin \Delta \sin 2\psi) / 2 \end{array} \right. \quad \begin{array}{l} (7.3a) \\ (7.3b) \end{array}$$

$$\text{Zone 3} \quad \left\{ \begin{array}{l} P_3 = [\Delta + 90^\circ + t \sin \Delta + (\alpha_2 / \tan 2\psi) + w] / 2 \\ A_3 = 180^\circ - \psi + (\alpha_1 - \alpha) (\sin \Delta \sin 2\psi) / 2 \end{array} \right. \quad \begin{array}{l} (7.3c) \\ (7.3d) \end{array}$$

with the same restrictions on the range of P and A , and where α_1 , α_2 and w are the window correction parameters.

The value of w can be determined from measurement of P_1 and P_3 for a surface with and without the cell windows in position, the change in the sum $(P_1 + P_3)$ being equal to w^* .

* Measurement of w for the windows of the discharge tube described in section 7.1 gave values between 1.5° and 2° , depending on the exact region of the windows utilized. Furthermore, the two-zone-averaged ψ values obtained with and without the windows were always equal within $.05^\circ$, confirming the smallness of the birefringence and the validity of McCrackin's treatment.

If automated single zone in situ measurements are to be corrected, assuming α and t have been determined for this zone setting of the quarter wave plate, α_1 and α_2 can be evaluated from equations 7.3 by using measurements on the surface in air for the values of Δ and ψ . The error terms in 7.3(a) and 7.3(b) could then be estimated for any P_1 , A_1 measured in situ, using the ideal relations (Equations 7.1 a) and 7.1 b) to find $\sin\Delta$, $\sin 2\psi$, and $\tan 2\psi$, with iteration if desired.

The cell windows should be as thin as practical (without producing excessive strain birefringence due to pressure differentials) and should be aligned close to normal to the light beam, to minimize the path length in the windows and hence the birefringence effects and also alignment problems caused by lateral displacement of the light beam (by refraction).

Other window imperfections, such as optical activity, have been shown to be cancelled by two-zone averaging (Azzam and Bashara 1971).

(e) Tilt of the sample surface

Although all samples should be aligned by the method used in section 7.2.2(d), it is possible that the sample surface may be tilted with respect to the surface which was used for establishing the plane of incidence. The main effect of a small rotation of the sample surface by an angle τ about the axis formed by the surface and the original plane of incidence is to change the readings of the polarizer, QWP and analyzer azimuths by the same angle τ , i.e.

$$\begin{aligned} P_1 &= P_1' + \tau, & A_1 &= A_1' + \tau \\ P_3 &= P_3' + \tau, & A_3 &= A_3' + \tau \\ Q &= Q' + \tau \end{aligned}$$

where P_1' , A_1' , P_3' , A_3' and Q' are the actual azimuth readings and P_1 ,

A_1 , P_3 , A_3 and Q are the true azimuths which would be measured if the instrument and surface were properly aligned. It is clear from Eqns.7.1 that whereas averaging measurements over four zones can correct for τ in P and A , the error in the QWP azimuth is not corrected by averaging.

For measurements in air, McCrackin 1969, 1970 has shown that τ can be calculated from P_1' , A_1' , P_3' , A_3' and Q' if T_c and Δ_c are known, and his program will make the necessary corrections to all subsequent readings for the sample and calculate Δ and ψ with the corrected values.

For measurements made on a sample with tilt in a cell, the cell window corrections to P_1' , A_1' , P_3' , A_3' must be made first using previously determined values of w , α_1 and α_2 , then τ computed as above. The readings are then further corrected for τ , and finally averaged to cancel the compensator imperfections t and α and yield Δ and ψ . Thus samples in a cell should be adjusted carefully to eliminate tilt if possible.

8. INVESTIGATION OF DISCHARGE PARAMETERS AFFECTING RATES OF ANODIZATION

8.1 Introduction

The anodization of niobium in a dc cold cathode discharge was studied with in situ ellipsometry in earlier work (Lee et al. 1970). In the system used for that study, denoted system A and shown in Fig. 8.1, the borosilicate glass discharge tube was 5 cm in diameter, and the ellipsometry measurements could only be made between oxide formations with the plasma extinguished. Mean growth rates of from .04 to 3.4 Å/min were obtained for total current densities to the sample of 0.1 to 1.5 mA/cm² respectively. The work was extended by using phase-sensitive detection of ellipsometer nulls, which enabled oxide thickness estimates to be made periodically while anodization was in progress, and some results of these measurements are included here. However, the above studies were restricted to anodization in the negative glow with gas pressures around 60 mtorr and discharge currents not greater than 10 mA.

The main investigations were performed in the 10 cm diameter quartz system B described in section 7.1, and were aimed at complementing the earlier studies with measurements in the positive column while satisfying the requirements detailed in section 7.1. The samples consisted mainly of electropolished polycrystalline tantalum and niobium, and the parameters varied were plasma density, location within the plasma region, gas pressure, and discharge and sample currents.

8.2 Sample Preparation

Samples about 1.5 cm square were cut from 1.6 mm thick Fansteel capacitor grade niobium or 99.99% tantalum and mechanically abraded on

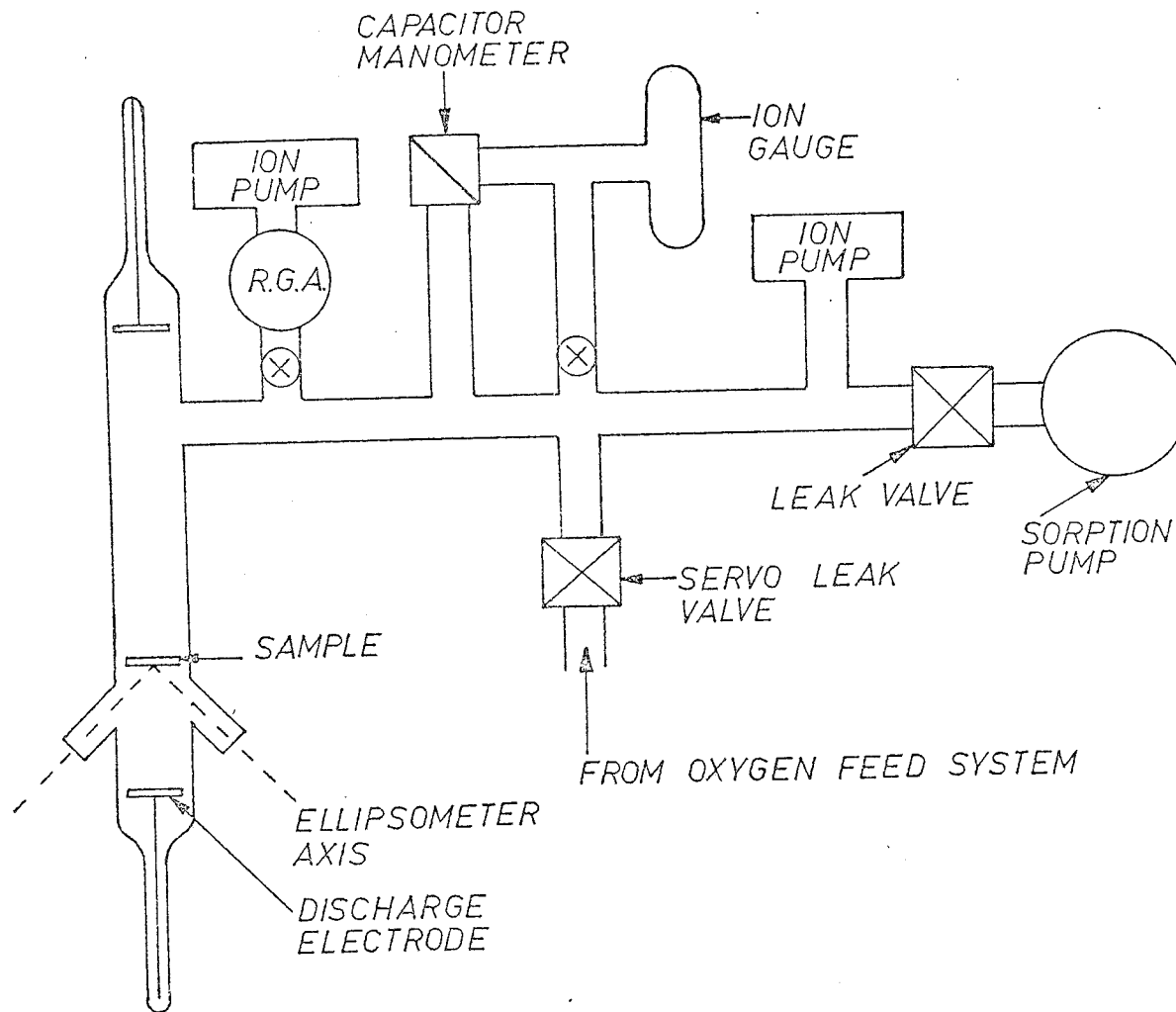


Fig. 8.1 Schematic of discharge system used by Lee et al. 1970 (system A).

emery papers to 4/0 grade. They were then electropolished in a Teflon cell with a platinum electrode to give a good optical reflecting surface. For niobium the electrolyte was 2 parts by volume of 48% HF, 4 parts 98% H_2SO_4 and 5 parts 85% lactic acid (Pelleg 1967) and for tantalum it was one part 48% HF and 9 parts 98% H_2SO_4 . Current densities of between 100 and 150 mA/cm² were used for several minutes with periodic inspection. Both electrolytes were circulated and used warm. After polishing, the samples were rinsed thoroughly in distilled water, dipped in 48% HF for 10 seconds and then rinsed again.

8.3 Measurements and Results

8.3.1 Optical constants of the substrates

Before any in situ ellipsometry data on the plasma anodization of niobium and tantalum could be analyzed, it was necessary to determine the optical constants of these metals at the He-Ne laser wavelength of 6328Å. This was accomplished by solution anodizing a sample of each metal in stages, making ellipsometry measurements at each oxide thickness, until at least one complete cycle of Δ , ψ values had been obtained, and then curve fitting to this data*.

The samples were prepared as in section 8.2, except that a metal stub was provided for electrical contact purposes. Anodization was carried out in dilute (0.2N) H_2SO_4 solution in order to obtain a homogeneous non-absorbing oxide (Young and Zobel 1966) and so simplify

* The optical constants cannot be obtained from a measurement of Δ and ψ for the unanodized substrate because the Δ , ψ values are affected by the few tens of angstroms of oxide present after electro-polishing. In the curve fitting procedure, the unknown refractive index of this pre-existing film is taken to be that of the anodic oxide, but the method is still valid since Δ and ψ are relatively insensitive to refractive index of very thin films (in contrast to film thickness).

the curve-fitting. The constant current density of about 1 mA/cm^2 was interrupted at various predetermined times and the sample removed from the electrolyte, rinsed in distilled water and blown dry with nitrogen gas for the ellipsometry measurements. Alignment was maintained by mounting the sample in a fixture which registered in the aligned mounting jig of the ellipsometer. An angle of incidence of 70° was used, and readings were taken in all four zones using a mica quarter wave plate as compensator.

The Δ , ψ values obtained for the tantalum sample* are shown in Fig. 8.2. The last of the 32 points (oxide thickness = 3307\AA) overlapped into the 3rd cycle, and it can be seen that the initial loop is retraced on subsequent cycles. This establishes that the oxide film is a single homogeneous non-absorbing layer, and the solid curve shown was fitted to the experimental points on this basis using Dell'Oca's program (see section 6.2.4). The refractive indices of the film and tantalum substrate which gave the best fit were $N_1 = n_1 = 2.185$ and $N_2 = 2.46 - j2.56$ respectively. The fitting was accomplished by varying n_1 in steps of .005 and n_2 and k_2 in steps of .01.

The above value of n_1 is in good agreement with the value of 2.19(5) for anodic tantalum pentoxide at 6328\AA predicted by the Hartmann equation reported by Young 1958:

$$n_1(\lambda) = 2.14 + 0.292 [(\lambda/10^3\text{\AA}) - 2.305]^{-1.2}$$

Similar curve-fitting to the data obtained on the niobium

* The work on solution anodization of tantalum was carried out in conjunction with W. Cornish - see Cornish 1972. A similar procedure was also used later to determine the optical constants of a sample of sputtered tantalum supplied by the Northern Electric Co. These were found to be 2.99 - 2.82j at 6328\AA .

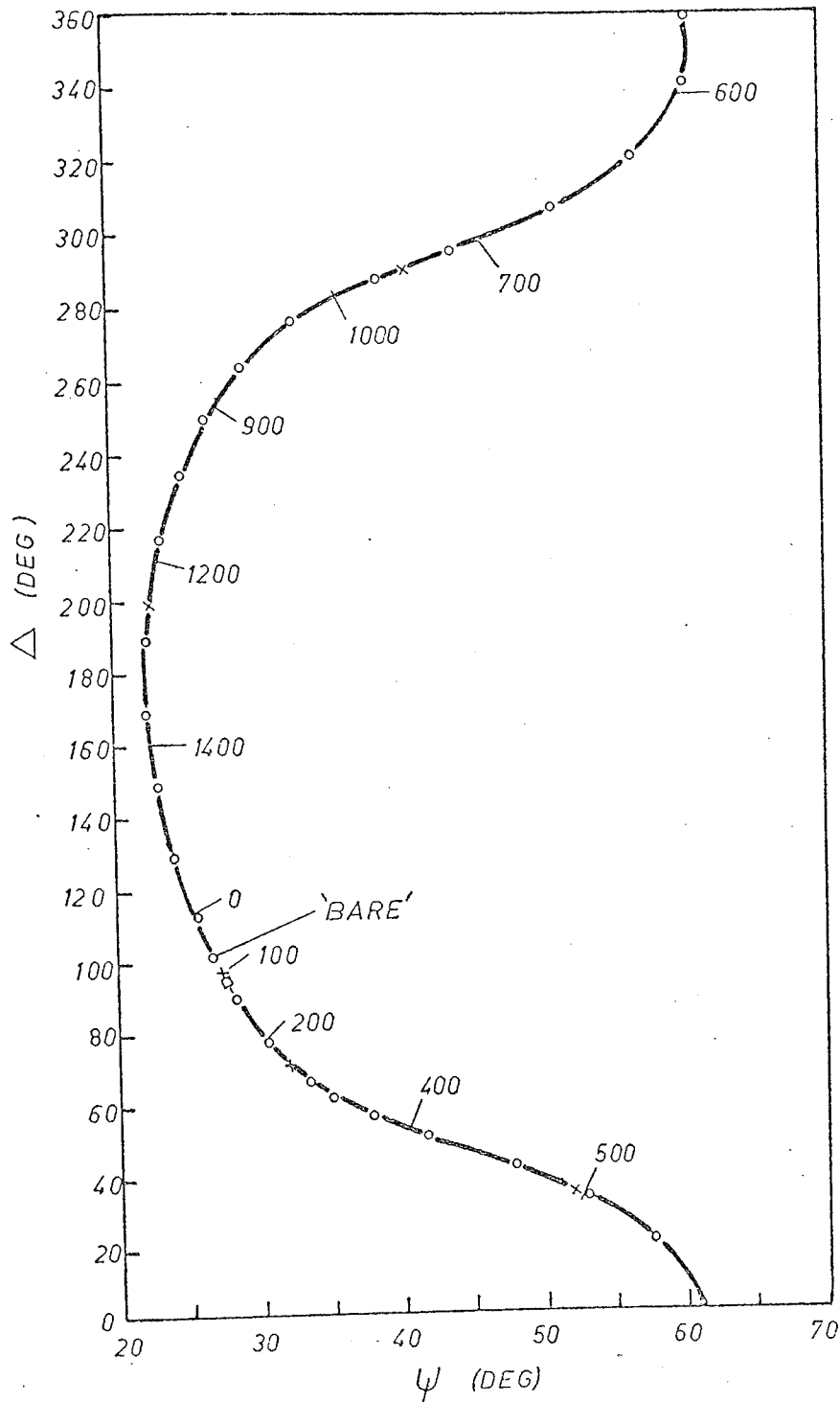


Fig. 8.2 Ellipsometry data for Ta₂O₅ on Ta in air used to obtain the optical constants of Ta at $\lambda = 6328\text{\AA}$. The numbers along the curve are film thicknesses in \AA . The word 'bare' identifies the first measurement on the unanodized sample.

o first cycle
 □ 3rd cycle

x 2nd cycle

sample yielded $N_1 = n_1 = 2.32$ for the oxide and $N_2 = 3.5 - j3.75$ for the niobium substrate. Again the oxide index is in reasonable agreement with the value $n_1 = 2.34(1)$ at $6328\overset{\circ}{\text{Å}}$ calculated from the expression

$$n_1(\lambda) = 2.26 + 0.398 [(\lambda/10^3\overset{\circ}{\text{Å}}) - 2.56]^{-1.2}$$

previously reported by Young 1960b.

Recently, Ord et al. 1972 have published data obtained by in situ ellipsometry on the anodization of tantalum and niobium in dilute sulphuric acid. They found $n_1 = 2.20$ and $N_2 = 3.02 - j2.57$ for tantalum, and $n_1 = 2.30$ and $3.03 - j3.61$ for niobium. The values of the two oxide indices are close to the results presented here, but the substrate indices, particularly the real parts n_2 , are not in agreement. It has been reported by Bellina et al. 1972 that the amount of oxygen absorbed in niobium can change the optical constants of that metal, and both the results found here for niobium and those of Ord et al. are within the range calculated by Bellina et al. This absorbed oxygen effect may apply for tantalum also.

A literature search failed to reveal other determinations of the optical constants of these metals at $6328\overset{\circ}{\text{Å}}$, except for suspect niobium values obtained by neglecting the oxide film present after electropolishing (Golovashkin 1969 - refer also to Burge and Bennett 1964).

For the actual plasma anodization studies, the polished samples were (unless otherwise noted) soldered to the water-coolable sample holder with indium for good thermal contact and covered with a mica mask and the quartz cap so as to expose a $\sim 1\text{cm}$ square of the sample surface. The latter was aligned with respect to the ellipsometer for measurements both before and after discharge cell assembly and evacuation, to obtain the window correction (section 7.2.3(d)).

The general anodizing procedure was as follows:

- (1) The system was evacuated with the sorption pump and then pumped overnight using the ion pump to a base pressure of about 2×10^{-7} torr (as indicated by the pump current).
- (2) The ion pump valve was closed and the pumping function was returned to the sorption pump in order to operate the system in a dynamic flow mode at the desired pressure in the 50-200 mtorr range by allowing oxygen to continually leak into the system and monitoring the thermocouple gauge output.
- (3) With the leak valves adjusted to maintain the required pressure, the substrate holder temperature controlled by water circulated from a thermostatted bath, and the ellipsometer control system programmed to balance at one minute intervals, the discharge was struck and its current I_d adjusted to the required level, usually 40 mA. The discharge was qualitatively similar to that described by Thompson 1961a, operating in the hollow cathode mode (section 4.5) with well-defined striations in the positive column. However, the light emitted from the negative glow was whitish with only a slight green tinge, and the striations were initially pink, only becoming bluish after some time.
- (4) Isolated high input impedance electrometers (Keithley model 602) were used in the circuit shown in Fig. 8.3 to monitor the potential of the sample with respect to a small gold ball probe located nearby, and the potential of this floating probe with respect to the discharge anode. When the discharge had stabilized, as evidenced by the constancy of these potentials and

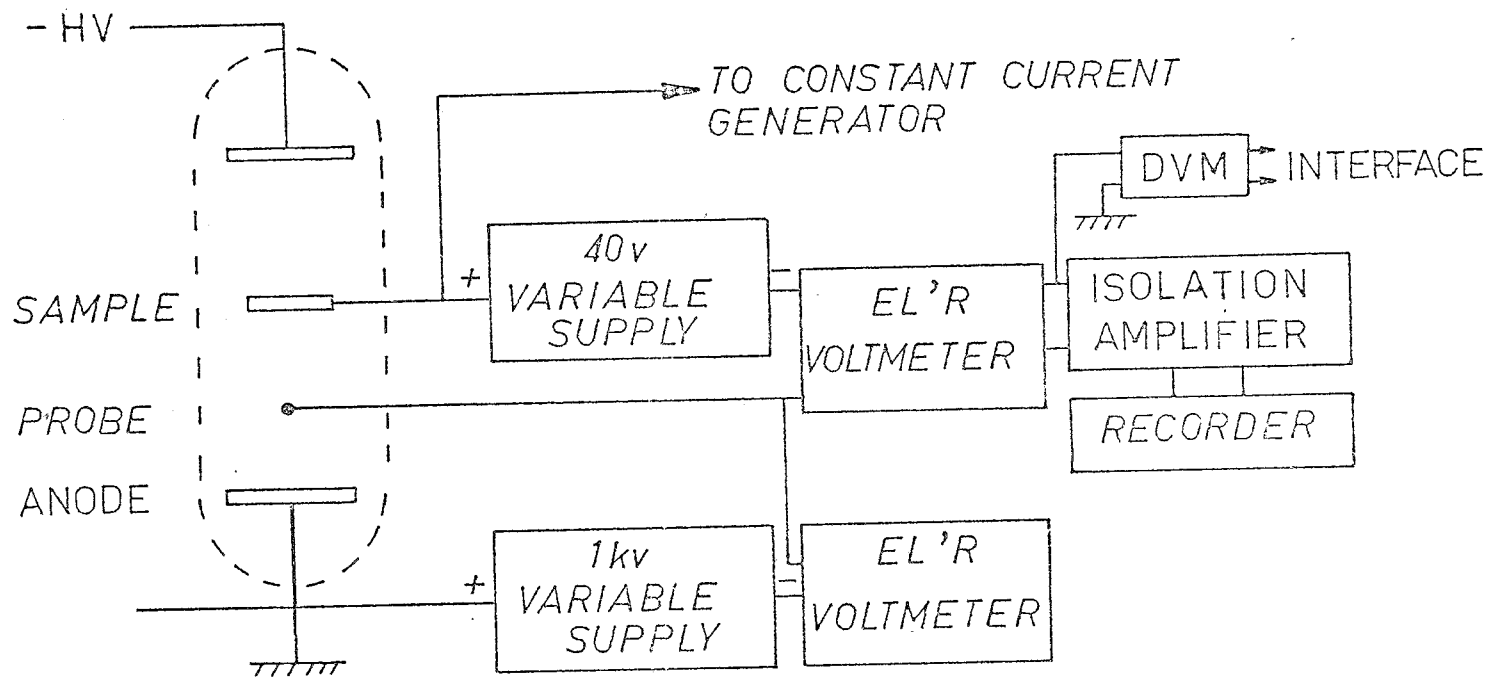


Fig. 8.3 Circuit used to monitor sample and probe potentials.

the relative infrequency of fluctuations in the emitted light, the constant current supply was switched to the sample and anodization commenced*.

Diagnostic measurements were also made by using a dummy sample, coated by vacuum evaporation with a $\sim 5000\text{\AA}$ thick gold film, in place of the anodization sample. Current-voltage characteristics obtained for these gold-plated samples were analyzed as for an ideal plane Langmuir probe.

Four-zone ellipsometer readings were taken at the end of every period of anodization. After several formations on a given sample, oxide thicknesses could be obtained by curve fitting to the Δ, ψ values calculated from these readings. The curve fitting was accomplished by varying the parameters of a simplified model of the oxide film, and usually a model of two non-absorbing layers growing simultaneously was found to be applicable (see also Dell'Oca et al. 1971).

Except as otherwise noted, the sample temperature was maintained at 30°C , and the anodization rates quoted in the following sections are mean oxide growth rates, given by the increase in oxide thickness as determined from ellipsometry readings before and after the formation divided by the time the anodizing current was applied.

8.3.2 Oxygen flow through the cell

In the earlier work (Lee et al. 1970) using system A the pressure in the discharge tube was maintained by admitting oxygen at a point

* An important advantage of anodizing at constant current as opposed to constant voltage is that the conditions in the plasma, specifically the potential difference across the sheath region, should also remain constant (ignoring such effects as work function fluctuations). Maintaining the voltage across the oxide constant during growth is not a straightforward matter, and is certainly not achieved by applying a constant sample bias with respect to the anode (see section 4.2.2).

between the tube and the sorption pump (see Fig. 8.1). This system was subsequently modified so that the oxygen flowed continuously through the active region of the cell, and as can be seen from Table 8.1 this resulted in about a threefold increase in constant current growth rate on a polycrystalline niobium sample. Similar results (not shown in Table 8.1) were obtained with a single crystal niobium sample when the earlier static conditions were approximated by restricting the throughput with the sorption pump and oxygen inlet valves. Since there were no obvious signs of any change in plasma conditions (e.g. as regards light emission or potential difference required for the 5 mA discharge current), the increase was thought to be due to a reduction in the build up of impurities from the discharge tube walls and electrodes. Such an impurity effect may act through changes in the energy distribution and density of the electrons in the plasma (see section 8.4).

8.3.3 Plasma density

Initial attempts to anodize tantalum samples in the 10 cm diameter discharge of system B resulted in very low growth rates in the negative glow, and no detectable growth in the positive column as measured by the rate of change of polariser null setting dP_1/dt , for discharge currents I_d up to 40 mA and anodization currents to the sample I_s of between 0.1 and 2 mA at a pressure of 60 mtorr (see Table 8.1). The growth rates in the negative glow could be increased slightly by positioning a baffle consisting of a 3 cm diameter niobium disc on the tube axis about 2 cm in front of the sample, suggesting a possible influence from high energy electrons emanating from the hollow cathode (Thompson 1961a). However, mounting a quartz baffle on the cathode as described in section 7.1 did not enable anodization to occur in the positive column, and in

Table 8.1 Rates of anodization for various experimental configurations.

| Cell configuration | Sample | Location and orientation | p (mtorr) | I _d (mA) | I _s (mA) | dP ₁ /dt (deg/min) | Mean Growth rate (Å/min) |
|---|------------|--------------------------|-----------|---------------------|---------------------|-------------------------------|--------------------------|
| System A: 5cm dia. pyrex cell, inverse brush cathode, no baffles. | | | | | | | |
| 1. no through flow of oxygen | Nb3,px,ep | ng,fa | 60 | 5 | 1 | | 1.5 |
| 2. oxygen flowed through cell | Nb5,px,ep | ng,fa | 60 | 5 | 1 | | 4 - 6 |
| System B: 10cm dia. quartz cell, hollow cathode. | | | | | | | |
| 1. no baffle on cathode | | | | | | | |
| (a) no baffle near sample | Ta,pxf,cp | pcs,fc | 60 | 20-40 | 0.1-2.0 | <0.005 | -- |
| (b) fixed Nb foil baffle 1.5 cm in front of sample | " | ng,fc | 60 | 20 | 0.4 | ~0.01 | -- |
| (c) movable Ta foil baffle 3cm in front of sample | | | | | | | |
| on axis | " | ng,fc | 60 | 20 | 0.4 | ~0.06 | -- |
| off axis | " | ng,fc | 60 | 20 | 0.4 | <0.005 | -- |
| 2. quartz baffle on cathode | | | | | | | |
| (a) movable Ta baffle 2.8-8 cm in front of sample on axis | " | pcs,fc | 70 | 20-30 | 0.1-3.0 | <0.005 | -- |
| (b) sample on rotatable holder, no baffle | Nb4,sx,ep | pcs,fc | 65 | 30 | 0.2 | ~0.005 | 0.045 |
| (c) rotatable sample holder, constrictor 2 cm in front of sample | | pcs,fa | 65 | 30 | 0.2 | ~0.007 | 0.06 |
| (d) regular sample holder, constrictor 2 cm in front | | pcs,fc | 62 | 40 | 1.0 | 0.11 | ~3 |
| | | pcs,fa | 62 | 40 | 1.0 | 0.10 | ~3 |
| | Nb3*,px,ep | pcs,fc | 60 | 40 | 0.2 | | ~1 |

Key px: polycrystalline, sx: single crystal, ep: electropolished, cp: chemical polish, f: foil, ng: negative glow, pcs: positive column striation, fa: facing anode, fc: facing cathode

* Oxide grown previously in system A removed with ammonium fluoride-buffered HF.

fact moving the niobium disc from an off-axis position in the Faraday dark space onto the tube axis caused the first striation to be shifted forwards to a location immediately behind the disc, which demonstrates that the main ionizing electrons in the Faraday dark space are still on the tube axis, even with the baffled cathode. Nevertheless, these electrons were not the only reason for lack of oxide growth, since a niobium sample oriented with its exposed surface facing the anode by suspending it from a thin quartz tube with the usual sample holder retracted did not anodize either.

A comparison of the current-voltage characteristics obtained for this freely suspended sample (both while facing the cathode and anode) and for a gold-plated sample in the 5 cm dia. system A revealed that the plasma density (as indicated by the positive ion current) was much lower in the 10 cm system, even with equal discharge current densities through the tubes, and was lower in the positive column than in the negative glow. The characteristics for the two extremes, namely the negative glow of system A and the positive column of system B, are shown in Fig. 8.4.

It can be seen that the samples behave as Langmuir probes, the characteristics exhibiting the usual positive ion and electron collection regions. Although the ion current magnitudes are very different, the equal discharge current densities do result in similar electron 'saturation' currents. The lower slope of the curve for the 10 cm system can be partly accounted for by this sample not being gold-plated (the areas of the niobium and gold-plated samples were 1.1 cm^2 and 1.0 cm^2 respectively). Furthermore, the electron current drawn by the niobium sample when mounted on the standard 3 cm diameter holder was especially low, as indicated by the three solid points in Fig. 8.4. This shows that the sample holder

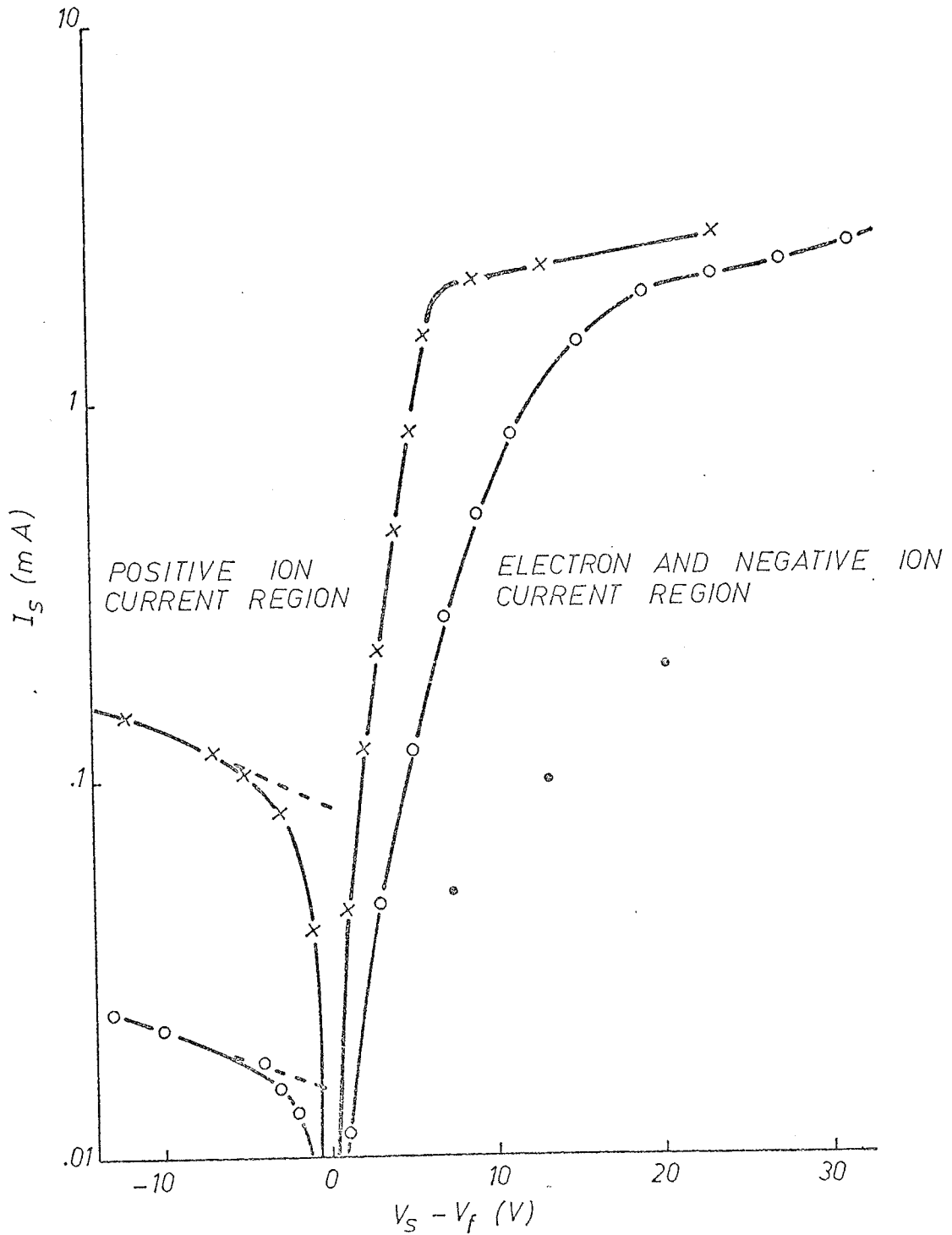


Fig. 8.4 Sample current-voltage characteristics: x gold-plated sample in negative glow of system A, $I_d = 10\text{mA}$, $p = 55$ mtorr; o suspended niobium sample in positive column of system B, $I_d = 40$ mA, $p = 60$ mtorr; e as o except mounted on sample holder.

assembly perturbs the plasma and effectively lowers the plasma density near the sample face by diverting the plasma.

It was found possible to locally increase the plasma density in the positive column of the 10 cm system by the introduction of a plasma constrictor, and in this way anodization rates comparable to those for the 5 cm system could be achieved. Two types of constrictor were tested, with similar results: one was in the form of a 'top hat' made from stainless steel shim; the brim of the hat was 9.5 cm o.d., and the 3.5 cm diameter, 4 cm long central funnel was open ended. The other constrictor consisted of a 10 cm diameter conical borosilicate glass filter funnel with the stem sawn off and legs added for support. The smaller end ('exit') of either constrictor was usually positioned 2 to 3 cm in front of the sample (Fig. 8.5). Both arrangements produced an optically dense plasma ahead of the sample, and increased the ion and electron

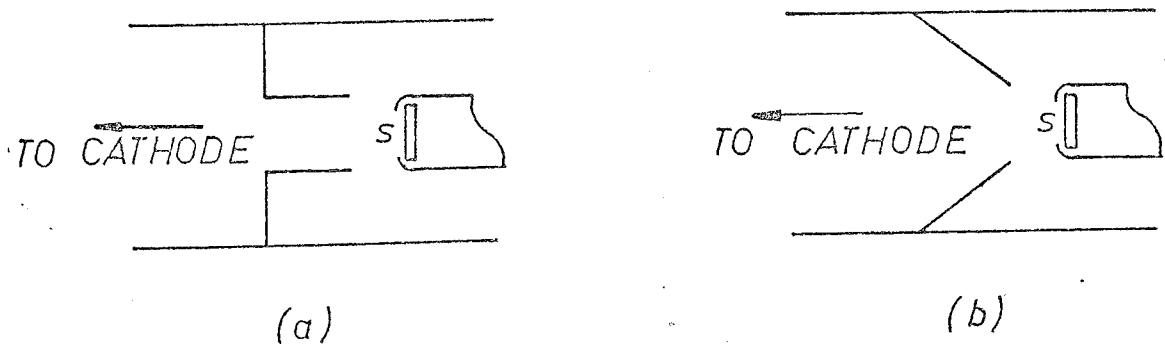


Fig. 8.5 Location of constrictors: (a) stainless steel 'top hat', (b) borosilicate funnel.

currents to the 0.5 mm diameter gold ball probe located in this plasma as shown in Fig. 8.6.

Although the mean electron energy as obtained from the electron retardation region had not changed significantly, being 3.5 eV at this pressure of 60 mtorr, the positive ion current had increased by a factor of two approximately, and in the electron 'saturation' region the increase was a factor of three. This means that with the constrictor present a given current drawn from the plasma requires a smaller potential drop across the sheath region. As an example, it was found that to draw an (anodizing) current of 0.2 mA from the positive column, a 1 cm² gold-plated sample required a bias of less than 1 V above plasma potential with the constrictor compared with ~10 V without it, and for this current density the growth rate on an unplated niobium sample with the constrictor positioned 2 cm in front was approximately 1 Å/min.

The significance of the position of the constrictor relative to the sample holder was not investigated in detail, since movement of the constrictor caused a transition period during which the growth rate always decreased, perhaps while the tapered edge of the oxide film near the mica mask adjusted in thickness to a new potential distribution. However, it was observed that with the constrictor 2 cm from the sample holder, a sample current of 0.4 mA was within the electron saturation region and the sample anodized normally, but when the constrictor was moved 5 cm away the same current caused a visible glow in front of the sample, and the rate of anodization decreased considerably. This glow is analogous to the luminous sheath or anode glow which is present on the main anode of a glow discharge, and its occurrence indicated that the extracting field of the sample was accelerating electrons to excitation

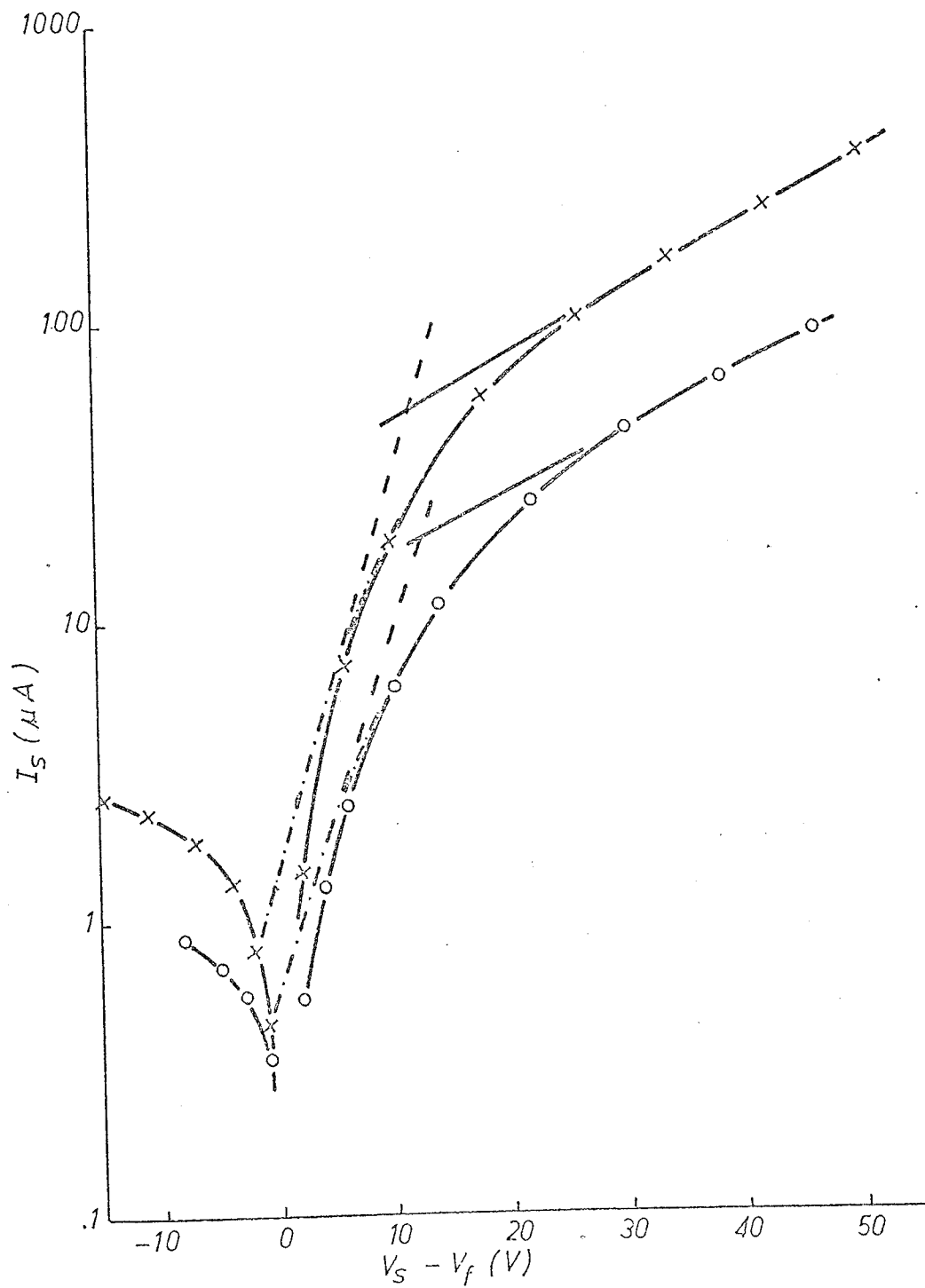


Fig. 8.6. Effect of constrictor on probe characteristics: o without constrictor, x with constrictor. Broken curves are corrected for positive ion current. $I_d = 40\text{mA}$, $p = 60$ mtorr.

and ionizing energies.

A position dependence was also found for the anodization rate of a niobium sample in the negative glow of system A. The sample was shifted from the cathode end to the Faraday dark space end of the glow by moving the inverse brush cathode, and the growth rate increased as shown in Table 8.2. Over this same period, the electric field strength in the oxide was estimated to have increased by 20%. These results may be compared with the fact, mentioned in section 4.5, that electrons are slowed down through the negative glow region, and their density increases towards the Faraday dark space.

Using the constrictor with the suspended niobium sample in the absence of the usual holder, it was found that this sample anodized at the same rate at constant current whether facing the constrictor or the anode.

| Cathode - sample separation (mm) | Growth rate (Å/min) |
|----------------------------------|---------------------|
| 56 | 1.0 |
| 67 | 1.3 |
| 86 | 2.9 |
| 96 | 5.0 |

Table 8.2 Variation of growth rate with position in the negative glow (system A, polycrystalline niobium sample).

8.3.4 Gas pressure

Variation of the gas pressure in a dc glow discharge is accompanied by changes in the dimensions of the different glow and dark space regions, caused by changes in the electron mean free path. This presents a difficulty in attempts to determine the effect of system pressure on rate of anodization. Variations in the anodization rate with pressure

reported (e.g. O'Hanlon 1971) for electrode configurations with a large anode-to-cathode area ratio, such as the ring cathode and base-plate anode system shown in Fig. 8.7, may have been caused in part at least by movement of the discharge regions relative to the sample, particularly since these configurations give discharges which are less well-defined spatially than the cylindrical tube discharge. In this context it was somewhat fortuitous that the constrictor used to increase the plasma density also had the effect of constraining a portion of the discharge, usually a positive column striation, to remain localized at the constrictor irrespective of pressure variations within certain limits, so that the dependence of the anodization rate on pressure could be determined for the positive column.

For this study two polycrystalline tantalum samples were first anodized in dilute sulphuric acid to produce a 3000Å thick oxide mask over their electropolished front surfaces except for a central 8.5 mm diameter circular area on each, and then a gold layer was vapour deposited through a metal mask on the unanodized area of one of the samples. These oxide masks were provided to reduce such undesirable effects as high sheath fields and current leakage at the mica mask edge, which were thought to have caused decreasing growth rates with thickness on previous samples. The masks were fabricated by protecting the central sample area from anodization with a disc of adhesive electrical insulation tape (Scotch brand).

By positioning the constrictor with its exit 2 cm in front of the sample holder, the sample plane was placed in the first striation for the pressure range from 60 to 150 mtorr and a discharge current of 40 mA. Constant currents of 0.1, 0.2 and 0.3 mA were used, and Table 8.3 shows the growth rates obtained in units of Å/min. Current efficiencies

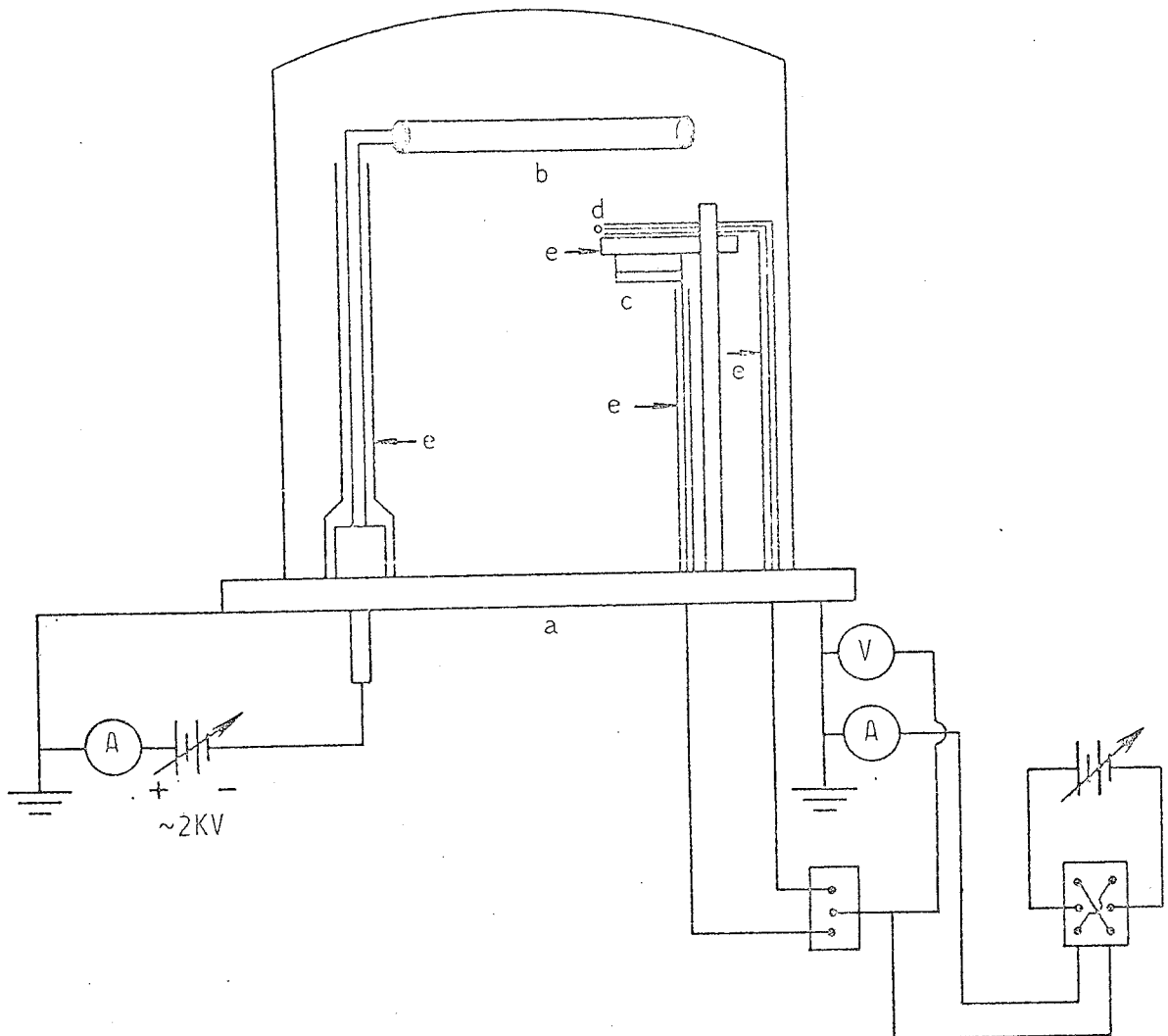


Fig. 8.7 Ring cathode-base plate anode plasma anodization system:

- (a) anode base plate (b) ring cathode (c) sample
 (d) probe and (e) quartz shields for electrical insulation.

| J_s (mA/cm ²) | p(mtorr) | | |
|--------------------------------|----------|------|---------|
| | 60 | 100 | 150 |
| .18 | 0.10 | 0.23 | 0.17 |
| .35 | 0.32 | 0.64 | 0.50 |
| .53 | 0.60 | 1.1 | 0.8-1.3 |

Table 8.3 Oxide growth rates ($\text{\AA}/\text{min}$) obtained on a tantalum sample at different pressures p and sample current densities J_s (system B).

η were calculated from these values by assuming that the oxide produced was stoichiometric with the same density as wet anodic Ta_2O_5 (8.0 gm/cm^3 , Young 1958), giving the results shown in Fig. 8.8(a).

Floating triple probe measurements showed that increasing the pressure p from 60 mtorr to 150 mtorr caused the reduced field E/p , which is proportional to the average energy acquired by an electron along a mean free path in the field direction, to decrease from 60 to $\sim 40 \text{ v/cm-torr}$. The I-V characteristics of the gold-plated sample in the same location as the Ta sample for pressures from 60 to 200 mtorr are shown in Fig. 8.9. These curves were corrected for positive ion components to yield the electron current-voltage characteristics, such as the one for 60 mtorr shown in Fig. 8.10 in semilogarithmic form. The dashed curves in this figure are the electron and positive ion currents I_{pe} and I_{p+} to the small gold ball probe used as a 'sounding probe' (see appendix C), and provide a check on the determination of plasma potential V_p by the extrapolation method. It can be seen that the maxima in the sounding probe currents (corresponding to a maximum carrier density near this probe)

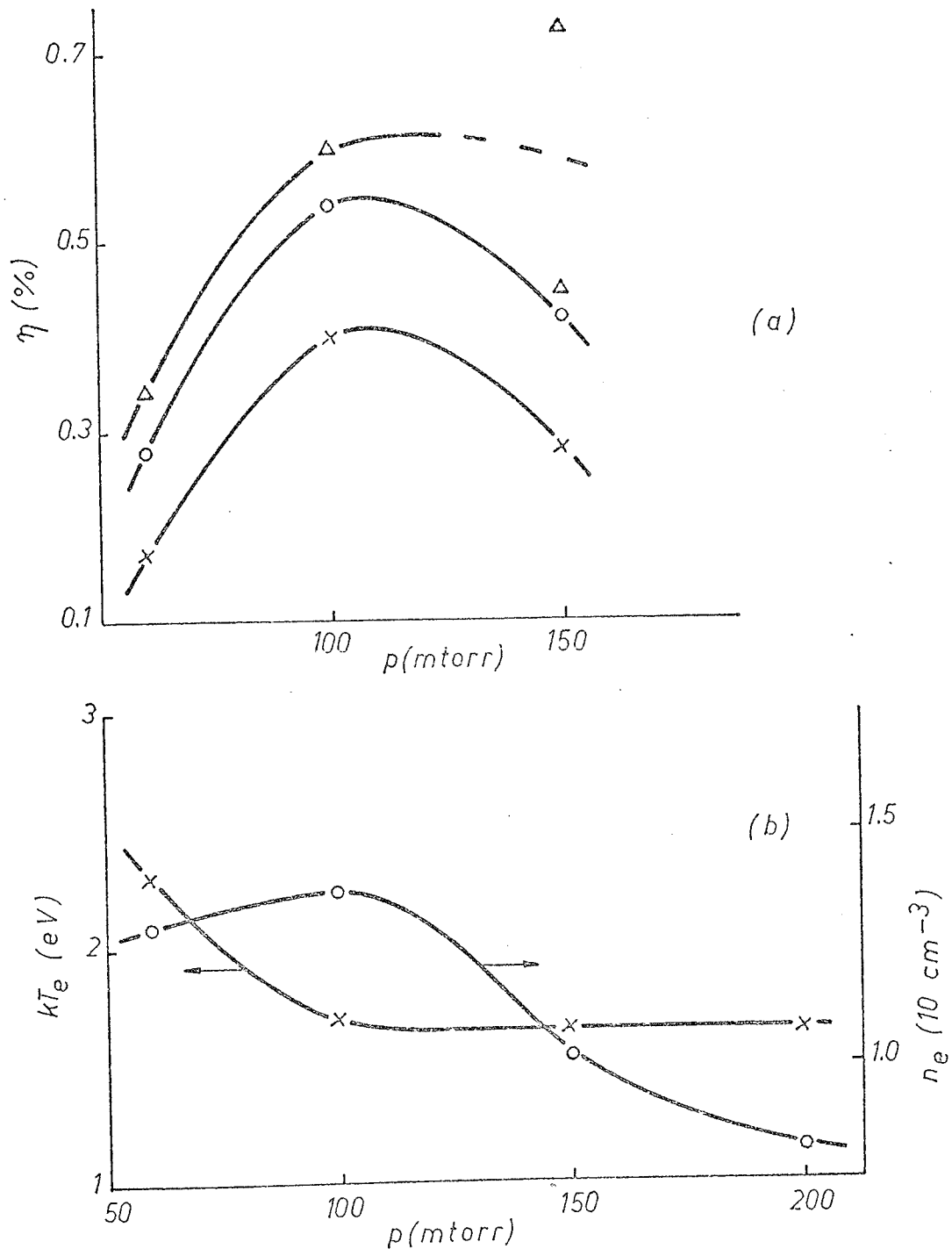


Fig. 8.8 (a) Current efficiencies versus pressure for anodization of sample Ta2 at $I_s = 0.1\text{mA}$ (x), 0.2mA (o) and 0.3mA (Δ) in the positive column. (b) Electron density (o) and mean electron energy (x) versus pressure.

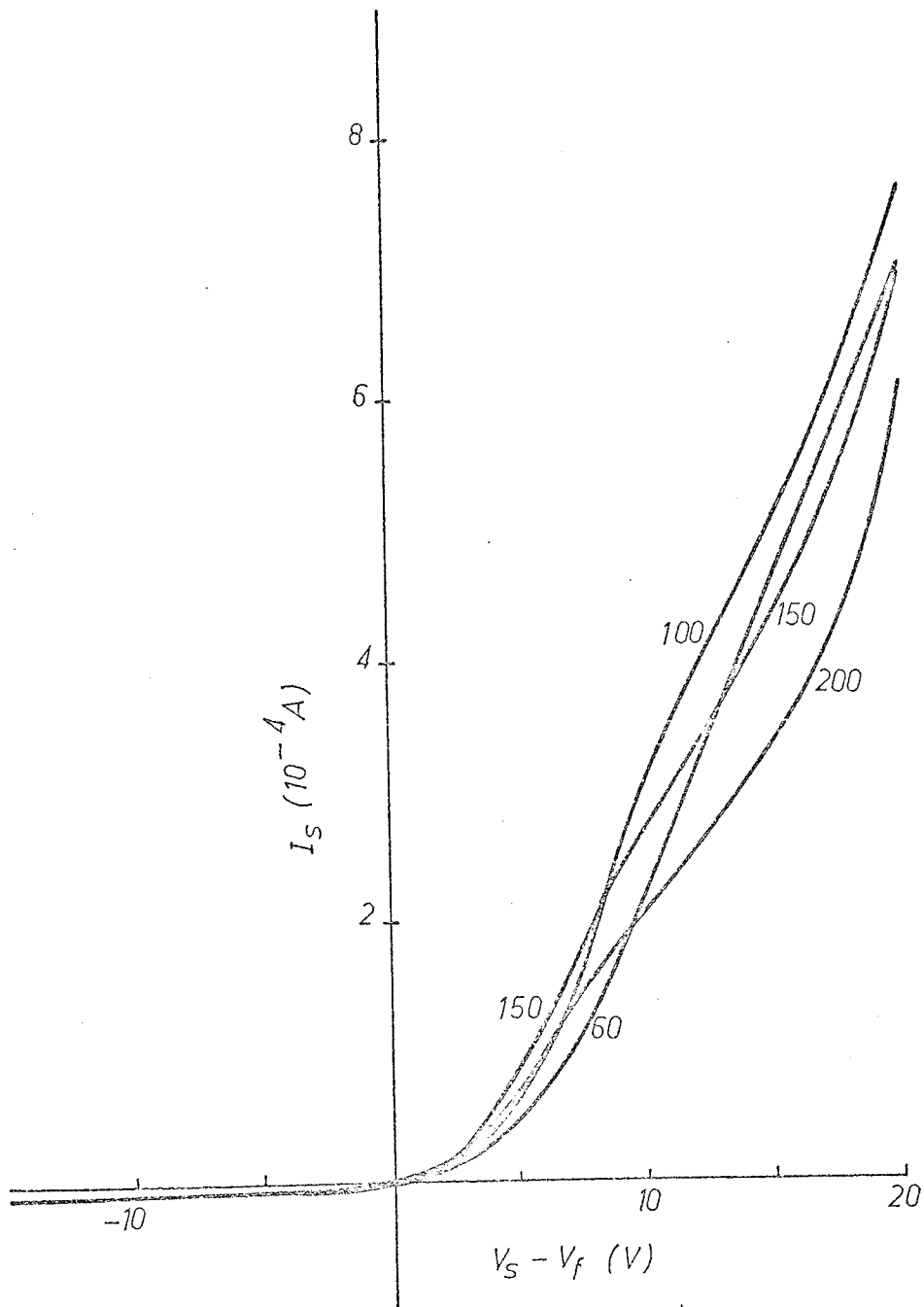


Fig. 8.9 Current-voltage characteristics for gold-plated sample in the positive column at various pressures. Numbers near curves are pressures in mtorr.

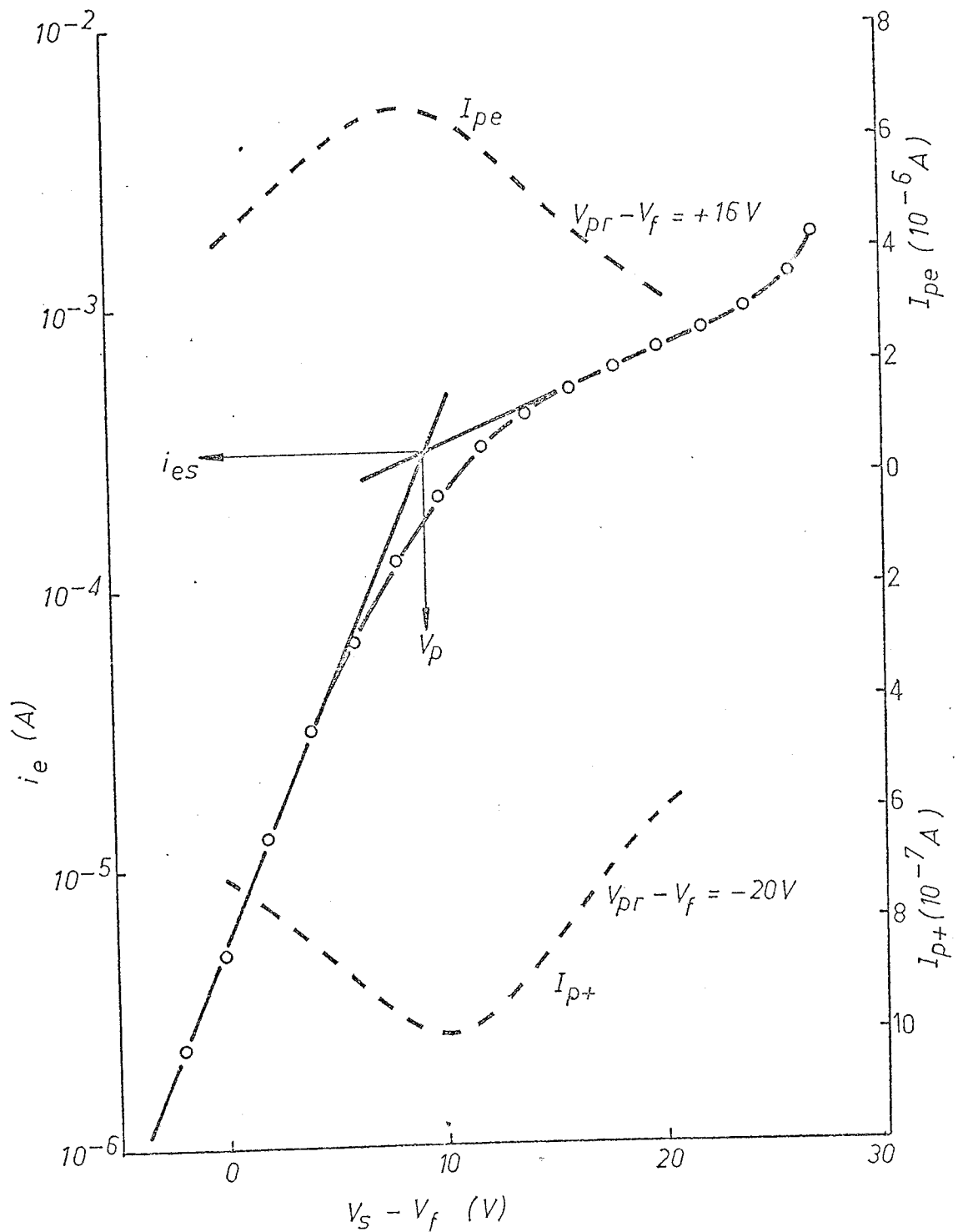


Fig. 8.10 Electron current-voltage characteristic obtained from 60 mtorr curve of Fig. 8.9, and electron and positive ion currents (broken curves) to gold ball probe used as a 'sounding probe'.

coincide on the sample voltage scale with the intersection of the extrapolated lines. This supports the use of the ideal Langmuir probe analysis, even though one extrapolation is based on a rather short portion of the electron accelerating region of the characteristic where the current is not perturbing the plasma too severely.

Values of the mean electron energy kT_e and electron density n_e obtained from the electron current at the intersection points of the electron current-voltage characteristics (according to section 5.2) are shown in Fig. 8.8(b). These characteristics also indicated that as the pressure was increased the larger energies of the electron distribution, as given by the potential difference $V_p - V_f$, decreased from 9eV to ~6eV with the largest change occurring between 60 and 100 mtorr, and the net current flux to the sample at plasma potential also decreased, particularly between 100 and 150 mtorr.

8.3.5 Discharge current

The effect of the current through the discharge on the anodization rate was not as clear as the pressure effect, and was dependent on the anodizing current level and the stage of anodization. For a constant current of 0.2 mA drawn by a tantalum sample at a pressure of 70 mtorr, increasing the discharge current from 10 mA to 40 mA in 10 mA steps during the initial stages of anodization was accompanied by a two-fold growth rate increase, but at a later stage, when the sample had an oxide of ~500Å and was being anodized at 100 mtorr, reducing the discharge current in one step from 40 mA to 10 mA had no apparent effect on the oxide growth rate.

At higher sample currents, however, reducing the discharge current as above could result in the same phenomenon that was produced

by retracting the constrictor away from the sample, namely the appearance of a luminous glow over the sample accompanied by a decrease in the anodization rate.

8.3.6 Sample current density

Preliminary ellipsometry measurements made during anodization in the negative glow of system A by using phase-sensitive detection revealed that the oxide growth rate varied with time even though the current to the sample was maintained constant. Fig. 8.11 shows results for a particular formation on a polycrystalline niobium sample at a current density J_s of 1 mA/cm^2 , in which the growth rate decreased by a factor of four as the formation progressed. The initial rate of growth was especially high for another 1 mA/cm^2 formation which followed an hour-long low current (0.2 mA/cm^2) formation, being 20 \AA/min (see section 10.5).

During this early work it was found that the initial application of the current to the sample caused an almost instantaneous change in the optical behaviour of the sample surface, in a direction which appeared to indicate a decrease in oxide film thickness before net growth occurred. This electro-optic effect was observed much more clearly with the automated ellipsometer used on system B, and while in itself a phenomenon worthy of study (see for example Ord et al. 1972, Cornish 1972), it constituted an additional complication to instrumental imperfections in the analysis of the single zone ellipsometry measurements made during anodization. Zone 1 polarizer and analyzer null readings taken at one minute intervals both during and between anodizations on tantalum sample Ta2 are shown in Fig. 8.12. The initial shifts on applying a bias to the sample actually move the null readings onto a curve of lower oxide refractive index, in agreement with the results of Ord et al. 1972 for solution

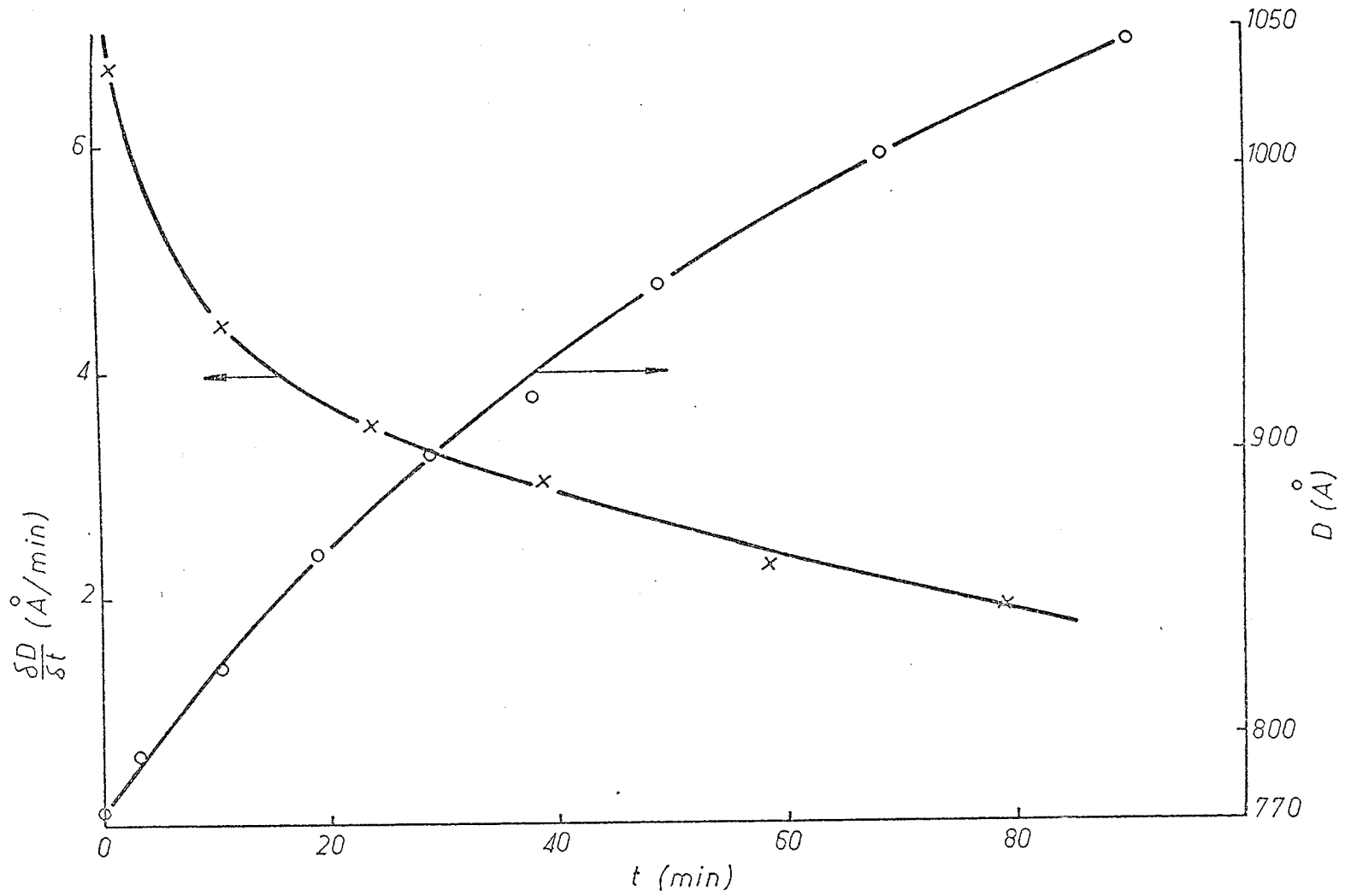


Fig. 8.11 Oxide thickness (o) and growth rate (x) during constant current anodization of niobium sample Nb5 at 1mA/cm^2 , $I_d = 5\text{mA}$, $p = 60$ mtorr (system A negative glow).

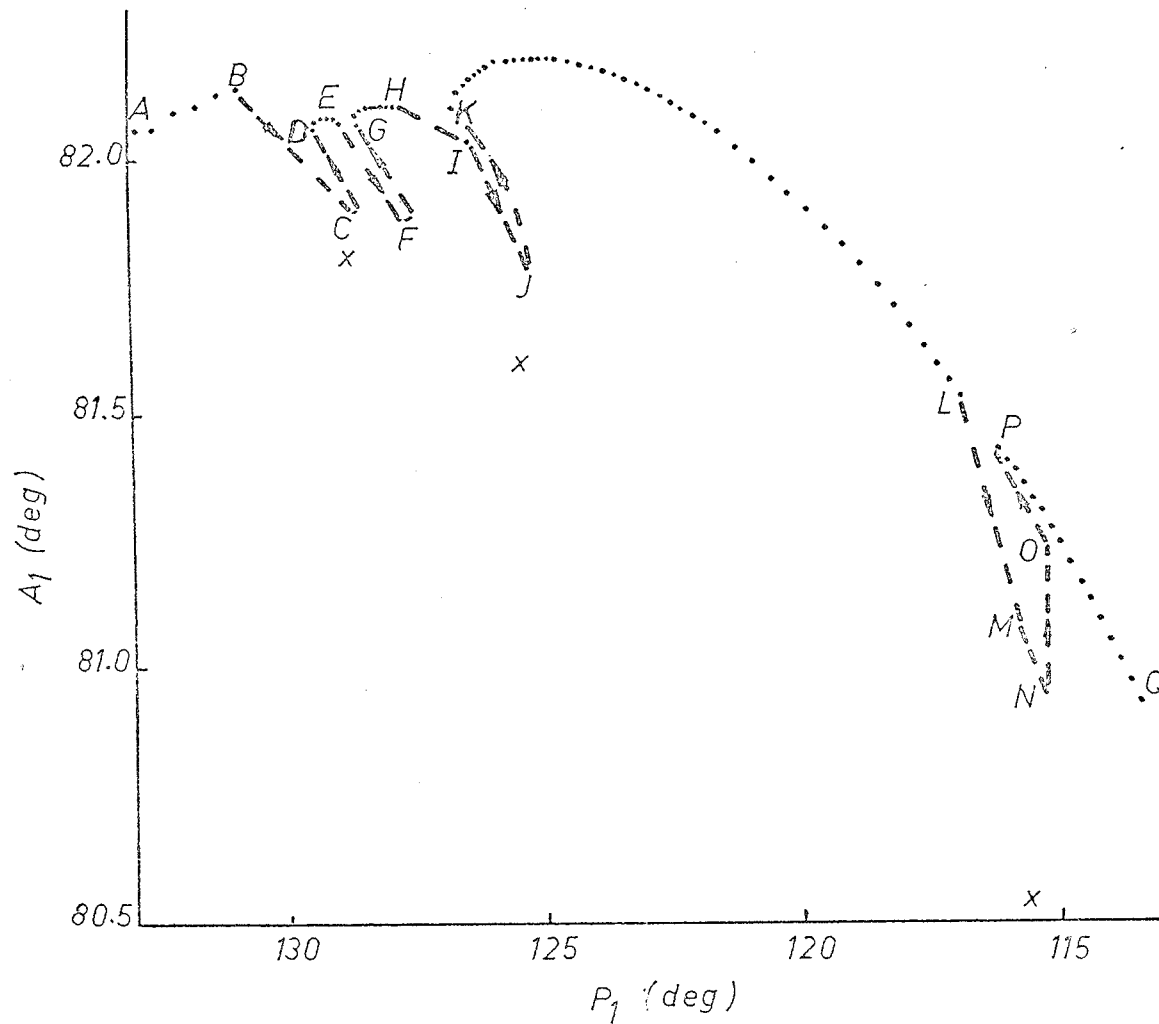


Fig. 8.12 Ellipsometer readings obtained during anodization of sample Ta2 in positive column of system B-see key on next page.

Key for Fig. 8.12

. : zone 1 readings
x : four-zone-averaged values
AB : end portion of a 0.2 mA formation
BC : 0.2 mA switched off
CD : 50 μ A switched on
EF : 50 μ A " off
FG : 50 μ A " on
HIJ : 50 μ A " off
JK : 0.1 mA " on
KL : formation at 0.1 mA
LM : 0.1 mA switched off
MN : exposure to plasma for ~2 hours
NOP : 0.1 mA switched on
PQ : formation at 0.1 mA

anodization. Rather than correct for the deviations of the single zone readings from the four-zone-averaged values (also shown in Fig. 8.12), estimates of oxide thickness (equivalent 'field-free' thickness) were obtained as follows. A quadratic was fitted to the relation between oxide thickness D and single zone polarizer* null setting P_1 (field applied) for two consecutive formations:

$$D = a_0 + a_1 P_1 + a_2 P_1^2 \quad (8.1)$$

The three constants a_0 , a_1 , a_2 were evaluated by associating P_1 values at the beginning and end of the formations with the D values obtained from the fit to the four-zone-averaged ellipsometry readings taken at the end of every formation (field off). This method assumes that the relation 8.1 is not affected by any changes with P in the deviation of single zone readings from the four-zone average, or changes in the oxide field due to current level changes.

Values of D obtained in this way for 0.1 and 0.3 mA formations on sample Ta2 (area = 56.5 mm²) in the positive column are shown as a function of time in Fig. 8.13. For positive column anodization at these current densities (0.18 to 0.53 mA/cm²), the rate of oxide growth was constant with time after an initial transient[†], in contrast to the growth

* Analyzer settings A_1 were used if these were changing faster than P_1 with growth.

† The initial decrease in thickness shown in Fig. 8.13 is a result of the approximate treatment of single zone readings outlined above. The transition NOP in Fig. 8.12, which lasted two minutes, appears to suggest a refractive index decrease followed by a thickness decrease. However, comparison with contours of constant thickness confirms that point P corresponds to a slightly thicker film (of lower index) than that at point N, in agreement with the results of Ord et al. 1972 and Cornish 1972.

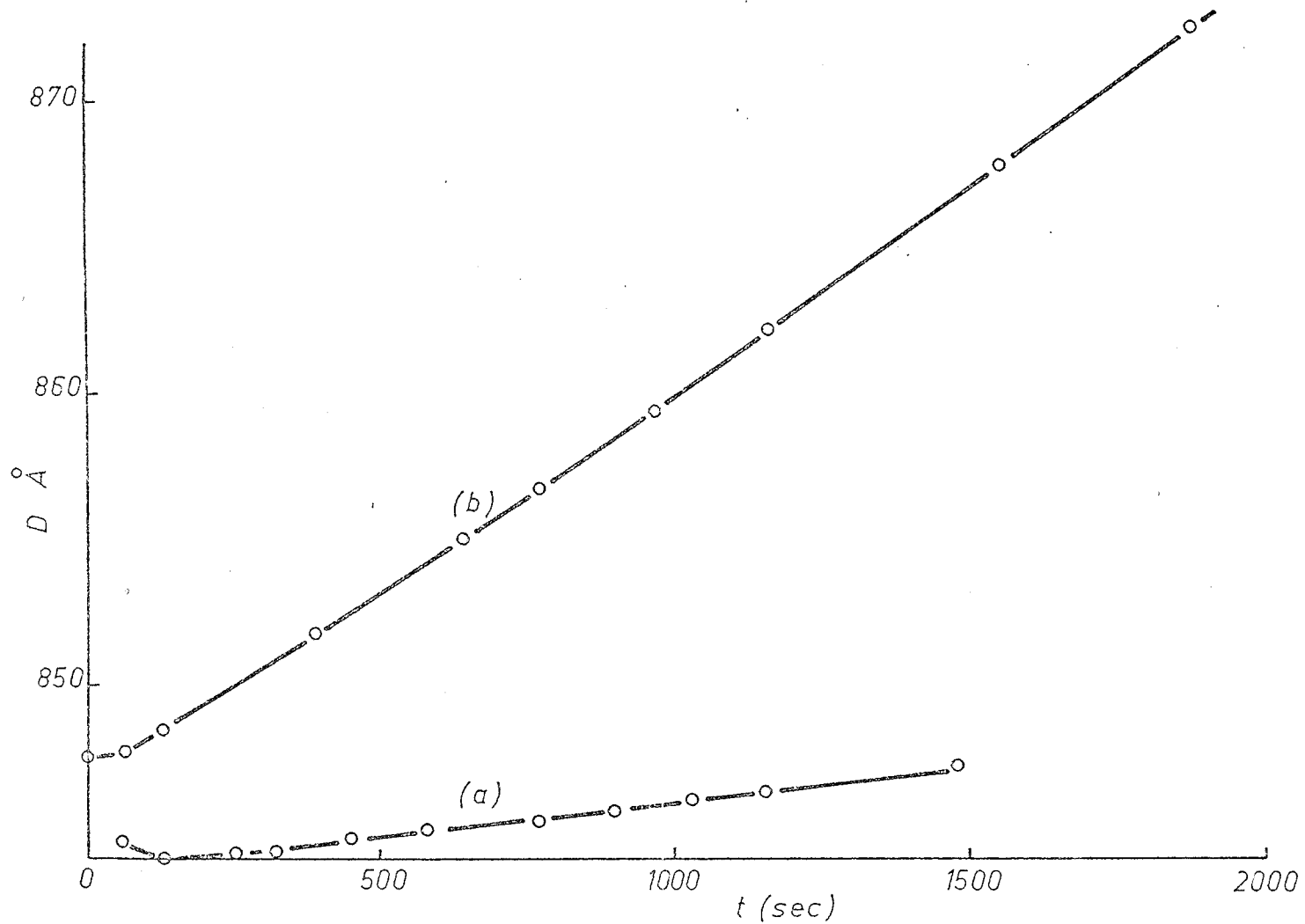


Fig. 8.13 Oxide growth during anodization of Ta₂ at (a) 0.1mA and (b) 0.3mA in positive column ($p = 150$ mtorr).

rate variation associated with formation current history reported above.

The variation of anodization rate with total sample current density J_s at various pressures is given in Fig. 8.14 in the form of $\log j_i$ versus $\log J_s$. The values of ionic current density j_i here are calculated from mean growth rates, i.e. growth rates obtained from the D values at the beginning and end of each formation. It can be seen that $\log j_i$ increases approximately linearly with $\log J_s$ up to $J_s \sim 0.5$ mA, above which j_i peaks and then decreases.

8.4 Discussion

The results of section 8.3.3 concerning anodization rates in the positive column and negative glow and the effect of a constrictor imply that certain plasma conditions have a strong influence on the anodization of metals such as tantalum and niobium. Considering first the suggestion of a number of researchers that the bulk plasma acts as the source of the negative oxygen ions utilized in the oxide growth process, one might expect the positive column to sustain higher oxidation rates than the negative glow, in accordance with the higher negative ion density as determined by Thompson 1961a and Whitlock and Bounden 1961. In fact, as found in this study and also reported by Nilson and McKay 1971, the reverse is true.

Regarding the constrictor, since its introduction caused the positive ion density to increase and since Thompson 1961a found positive and negative ions to be present in approximately equal numbers in the oxygen positive column, it can be assumed that the negative ion density was also increased locally. However, although this would result in an increased flux of negative ions to the sample, it would not necessarily increase the ratio of negative ion flux to electron flux, since the

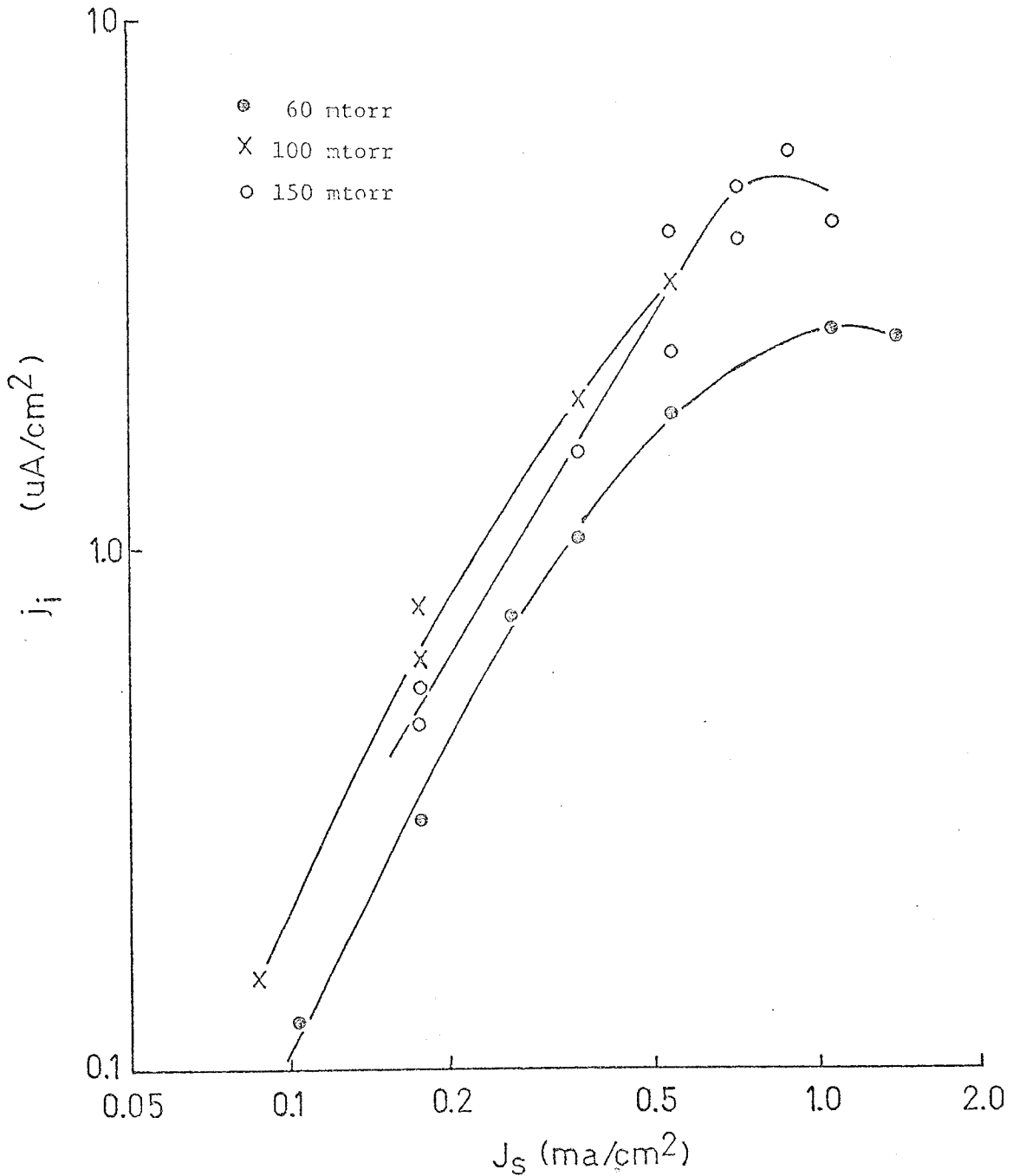


Fig. 8.14 Variation of oxide growth rate (expressed as ionic current density) with total current to sample Ta2 in positive column of system B at pressures of 60 mtorr (⊙), 100 mtorr (x) and 150 mtorr (○).

electron density had also increased. The positive ion and electron density changes are also possible causes of the increased growth rates in the presence of the constrictor. Ligenza and Kuhn 1970 refer to the formation of the naturally occurring oxide ion O^{--} from positive and negative ions implanted in the oxide surface, and in this manner the positive ion and electron densities may both be important. Studies of such a model have been cited (Ligenza 1971), but not published in detail. An additional way in which the plasma electron density could be important, together with the electron energy distribution, will be outlined later in this section.

The E/p values reported in section 8.3.4 indicate that negative ion formation in the positive column is by the two-body process of dissociative attachment (section 4.4 process (d)). The attachment coefficient for this process is proportional to pressure p , so that an increase in negative ion density with p could be expected. On the other hand, Fig. 8.8 shows that as p was increased above 100 mtorr, the anodization rate decreased. O'Hanlon 1971 has inferred a similar peak in the growth rate-pressure dependence from observations of the anodic current decay during anodization of aluminum in the negative glow at constant bias voltage.

Clearly the experimental observations are not consistent with the theory that plasma negative ions are directly involved in the anodization process, and in the next chapter it will be shown that the negative ion flux from the plasma to the sample does not have any major influence on the constant current anodization rate. The pressure variation results displayed in Fig. 8.8(a) and (b) show the growth rates increasing as the mean energy of the electron energy distribution decreased and the electron density increased slightly. When the latter decreased however, the growth rates also fell, suggesting that high electron densities and

low electron energies are conducive to higher anodization rates. The decrease in growth rates which occurs at higher sample current densities (see Fig. 8.14) is thought to be associated with the onset of ionization in the extracting field of the sample. At 150 mtorr the decrease occurs at lower sample currents than at 60 mtorr, which is consistent with the increase in the slope of the log I-V characteristic at around 0.6 mA at the higher pressure compared with 1 mA in Fig. 8.10. This sheath ionization phenomenon, which was also obtained when the constrictor was retracted or the discharge current reduced sufficiently during constant current anodization, is again dependent on the energy distribution and the density of electrons in the plasma. When the externally applied sample current density exceeds the random flux of electrons to the sample, the sheath field may increase to impact ionization values and increase the energy range of electrons reaching the oxide surface. The following is offered as a possible explanation of the influence of electron energy distribution and density on the anodization rate.

The electrons in the plasma have a distribution of energies, which means that those electrons which traverse the sheath region and reach the oxide surface must also have a distribution of energies. Any of these electrons which enter the oxide will initially be hot electrons because of the electron affinity of the oxide^{*}, and will have a finite penetration depth. In experiments with beam-deposited electrons, Pickar 1970 has found that even electrons arriving with zero kinetic energy penetrate to a depth of 50Å in wet-anodic SiO₂ before they lose the electron affinity of 0.9 eV by optical phonon emission and become thermalized.

* Processes competing with this electron 'capture' by the oxide might be capture by adsorbed oxygen atoms to form negative ions, or recombination with adsorbed positive ions.

Some electrons will be incident with a finite velocity component into the oxide, and these will penetrate further before reaching the conduction band edge. Thus the mean oxide field necessary to produce a certain net current density through the oxide to the metal substrate will be a function of the velocity distribution of the incident electrons*. This distribution will in turn depend on the magnitude of the net current density drawn from the plasma relative to the random electron flux. For sample currents less than the random electron flux, the energy distribution at the oxide will be an appropriate portion of the high energy tail of the plasma distribution as shown in Fig. 8.15. Above plasma potential, the plasma electrons will be accelerated across the sheath and the distribution will be shifted to higher energies, with correspondingly deeper penetration depths in the oxide. If the plasma electron density were increased, then the same current across the sheath would require a lower sheath accelerating potential, but the resulting lower incident energies would necessitate a higher potential drop across the oxide to maintain the net current to the substrate, which could mean an increase in the growth rate if the oxide-producing reaction was ionic conduction-limited. If the externally applied current density were to exceed the random electron flux so much that the extracting potential across the sheath reached ionization levels, then the resultant electrons with velocities directed at the oxide and their associated penetration depths could conceivably lead to a decrease in potential difference across the

* This dependence was not taken into account in the analysis of section 4.3.

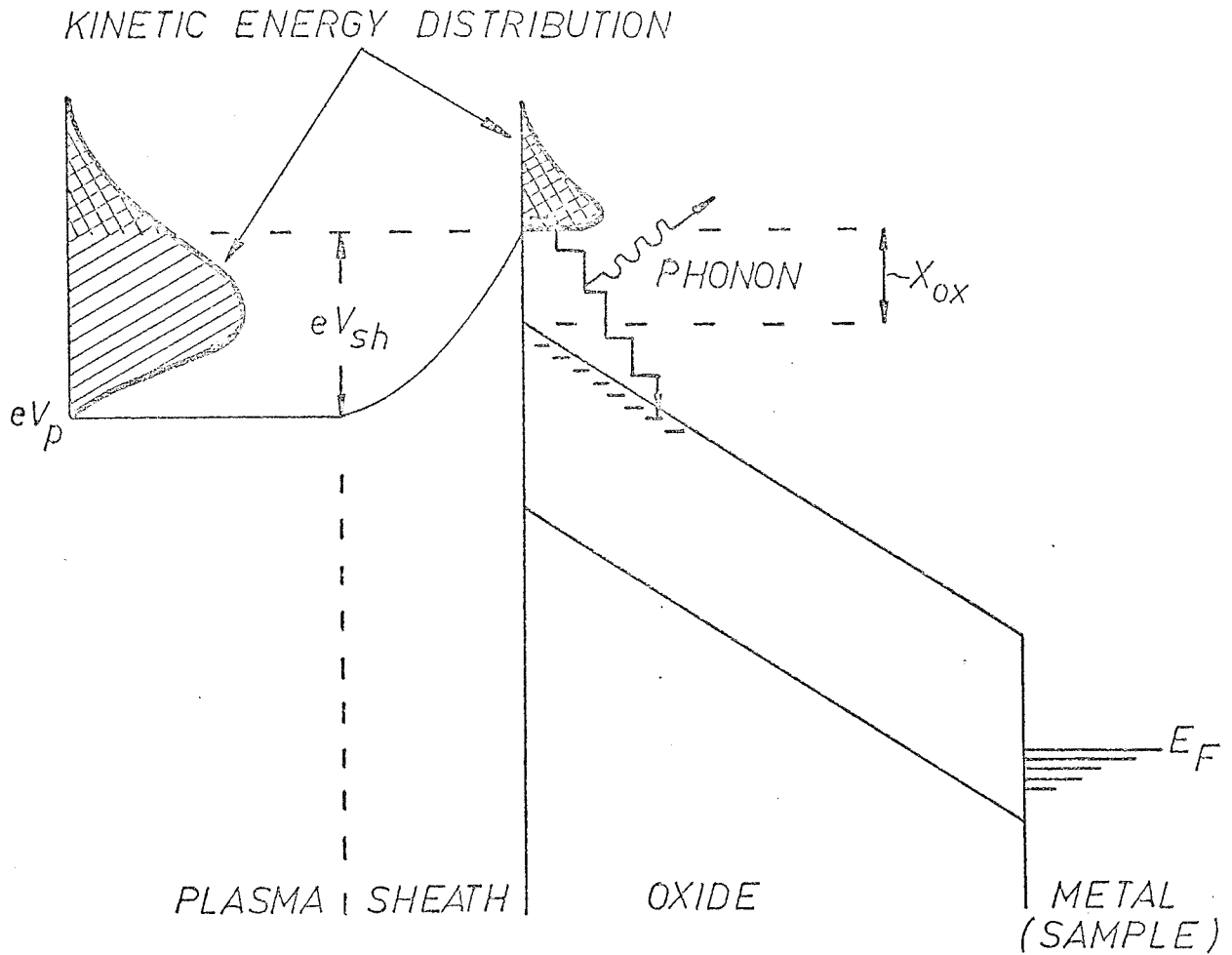


Fig. 8.15 Electron energy diagram for anodizing sample drawing current density less than $(j_{es} + j_{+s})$, showing effect of plasma electron energy distribution.

oxide and a fall in the growth rate^{*}. Another observation made during the course of these studies which may have some bearing on the significance of electron energies is that the application of a magnetic field (from a bar magnet) parallel to the surface of a sample being anodized at constant current caused the growth rate to increase by about a factor of six at the point monitored by the ellipsometer. However, the oxide growth also became very non-uniform over the sample surface, and the effect was not pursued further.

The above explanation of certain experimental observations can be summarized into a number of postulates, which constitute a rudimentary model for plasma anodization in the cold cathode glow discharge in oxygen:

- (a) The oxide-producing process is rate-limited by species transport through the oxide.
- (b) The ion flux in the oxide at a given temperature is determined by the electric field strength in the oxide.
- (c) The mean electric field strength in the oxide is related to the electronic flux through the oxide (\approx total current density) and the electron energy distribution and density in the plasma.

A refinement of the model would include the spatial distribution of negative space charge due to trapped electrons near the outer oxide surface, as determined by the electron energy distribution (through the penetra-

* A different interpretation of anodization rates falling (even to zero) at higher sample currents has been made by Slawewski 1969. Slawewski stated that the rates fall because the destruction of negative oxygen ions by field-stripping of electrons occurs in the high sheath fields, and that the visible glow is due to subsequent electron-positive ion recombination, rather than decay of impact-excited atoms. However, the emission of light due to recombination is in general small (Engel 1965, Llewellyn-Jones 1966), and the unimportance of plasma negative ions is demonstrated in the next chapter.

tion depth).

This approach attributes the low current efficiencies in plasma anodization to the presence of electrons with a wide range of energies in the plasma, which give large electronic currents through the oxide at the field strengths necessary for ionic transport. On this argument, the plasma best suited to anodization would be one in which the electrons all have relatively low energies but are present in sufficient numbers to maintain the conductivity of the plasma. One practical approximation to this case is the plasma of a dc arc discharge with a thermionic cathode. Ligenza and Kuhn 1970 have used such a discharge system, modified to allow prolonged operation in the presence of oxygen, and they reported growth rates for the anodization of silicon of around $50 \text{ \AA}/\text{min}$ at room temperature, i.e. almost two orders of magnitude higher than those obtained in this study. However, analysis of their results suggests that the current efficiencies were still quite low, less than 1%. No estimations of oxide field strengths were given.

Recently, high anodization rates have been obtained in the plasma of an rf excited discharge (on Si by Pulfrey and Reche 1973, on Ta by Mikhalkin and Odyneets 1971 and on Nb by Makara et al. 1971), and in these cases a relation between growth rate and oxide field was found. It appears that with this discharge, as with the hot cathode arc, large current densities* can be drawn to the sample without disturbing the electron

* There is a variety of other evidence showing that large electronic current densities can be passed through normally insulating oxides without damage (see Pickar 1970, Nicollian and Berglund 1970, Jaeger et al. 1972). Destructive breakdown effects (Shousha et al. 1972) occur when the stored energy associated with the charge on a large area conducting electrode is dissipated in a few localized low resistance paths, but if current is uniformly injected in the absence of such an electrode, these flaws will not sustain damage.

energy distribution so much that electrons are incident on the oxide with high kinetic energy.

The contention that the observed variations in anodization rate with conditions in the discharge arise principally through a dependence of electric field strength in the oxide on the energy distribution and density of electrons in the plasma would be strengthened by demonstrating the following:

- (a) That the supply of negative oxygen ions from the plasma is not essential to plasma anodization.
- (b) That the ionic current obtained from anodization rates is a function of oxide field strength.

These points will be dealt with in the next two chapters.

9. THE ROLE OF PLASMA NEGATIVE IONS

9.1 Introduction

It has often been considered that the negative oxygen ions in the plasma are the source of the oxygen in the plasma-anodic film. If this were so then the production of negative ions in the plasma and their transport across the sheath region to the sample might be rate-limiting steps in the anodization process, and it is possible that improvements could be made in the usually inconveniently low oxide growth rates. The measured random positive ion current densities to the sample of about 5 to 10 $\mu\text{A}/\text{cm}^2$ can be used as an indication of the possible magnitude of the negative ion flux, and these current densities are indeed similar to the values of ionic current density in the oxide calculated from measured growth rates (see Fig. 8.14).

To obtain information on the importance of negative ions in the plasma, the following experimental approaches might be considered:

- (a) To measure the actual flux of negative ions reaching a sample being anodized, by removing all electrons from the particle flux from the plasma.
- (b) To change the value of the negative ion flux reaching the sample in a controlled manner while monitoring the oxide growth rate.
- (c) To vary the density of negative ions in the plasma.

Approach (a) calls for a device such as the Loeb electron filter, and (b) should be possible with the simultaneous application of suitable dc and rf signals to the sample. Methods of varying the electron temperature in the plasma (e.g. Alexeff and Jones 1966, MacKenzie et al. 1971) could

make approach (c) possible through the dependence of the cross-section for negative ion production on electron energy. The use of magnetic fields could also be considered for all three methods - for instance a magnetic field applied parallel to the sample surface to deflect electrons could be used in (a) and (b), and a magnetic field applied longitudinally to the cylindrical discharge would reduce the electron temperature for approach (c). However, the necessity to confine these fields makes the magnetic methods more difficult. The methods mentioned initially for approaches (a) and (b) were chosen for investigation since they were the most direct.

9.2 Electron Filter Experiments

The electron filter referred to here is a device developed by Loeb (see Loeb 1955 and McDaniel 1964) for removing electrons from a mixed swarm of electrons and negative ions drifting through a gas in an electric field. It consists of a plane grid of parallel wires mounted perpendicular to the drift direction, alternate wires being connected to opposite sides of a high-frequency oscillator. For an alternating field of appropriate frequency (1 to 10 MHz) and sufficient amplitude established between alternate wires, all electrons attempting to pass through the grid should be captured on it, but the much heavier negative ions are transmitted since they respond only slowly to the rapidly changing field.

The device used in this study was constructed of sixteen .003 inch diameter tungsten wires cemented with 1 mm spacing on a 3 cm square mica frame with a 12 mm square aperture as shown in Fig. 9.1. The two leads from the alternate sets of wires were insulated in quartz tubing and sealed with low outgassing epoxy cement into the end of a borosilicate glass tube. This tube was mounted in a double O-ring feedthrough

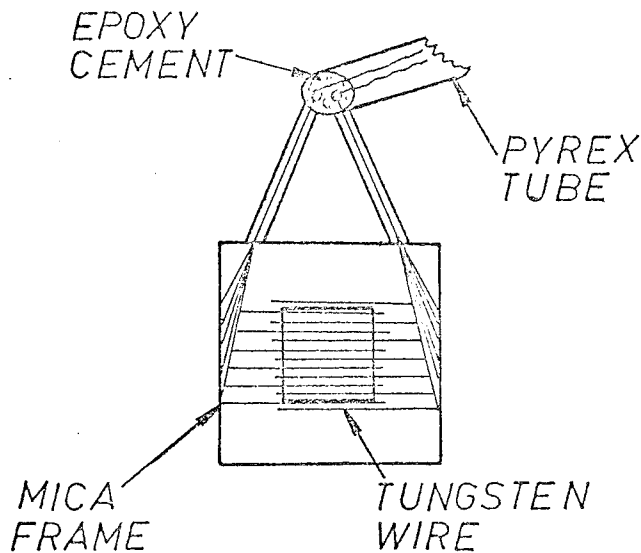


Fig. 9.1 Electron filter.

in the anode end cap of system B, so that the filter could be positioned directly in front of the sample holder.

To obtain suitable voltages across the grid, the latter was connected as the capacitor of a parallel LC circuit, the inductance being a 9 turn 7 cm diameter secondary coil of an air-cored transformer constructed with 1 mm diameter copper wire, and a 5V rf signal generator was connected across the two-turn primary coil as shown in Fig. 9.2. The voltage gain of this tuned amplifier is proportional to $\omega_r QM$ at resonance, where $\omega_r = (LC)^{-1/2}$, Q is the figure of merit for the secondary coil and M is the mutual inductance of the transformer. By tuning the generator with the LC circuit, signals as high as 50 V peak-to-peak at

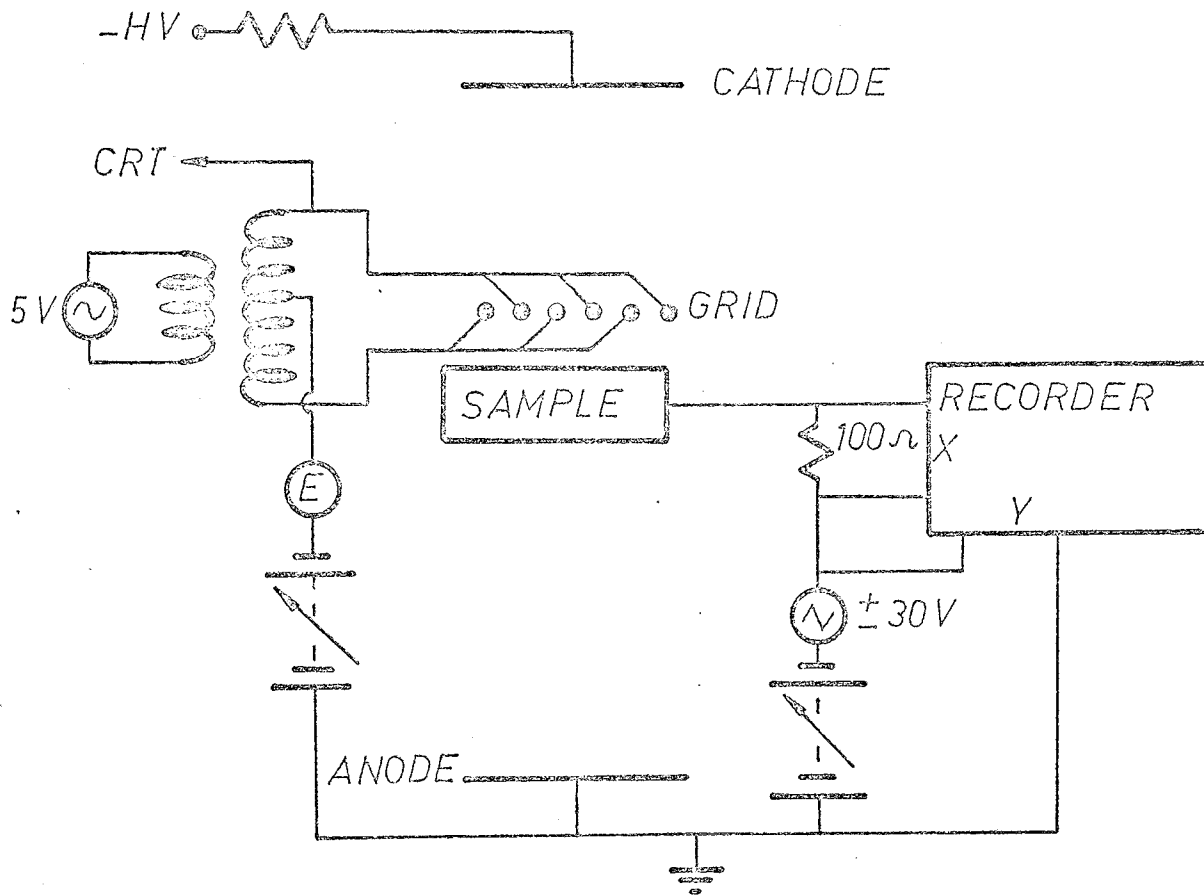


Fig. 9.2 Circuit used for electron filter experiments.

5 MHz could be applied between adjacent grid wires. A dc bias could be applied to the filter via a centre-tap on the transformer secondary coil.

To investigate the performance of the filter, the device was positioned about 3 mm in front of a gold-plated sample in the positive column of system B and the current-voltage (I_s - V_s) characteristic of the sample was measured as a function of the dc and rf voltages V_{gdc} and V_{grf} applied to the grid, all dc voltages measured with respect to ground, for $p = 70$ mtorr and $I_d = 40$ mA.

The following is a summary of the results, some of which are presented in Figures 9.3 and 9.4.

- (a) Introduction of the grid (electrically isolated) in front of the sample reduced the sample current I_s by a factor of ~ 5 in the electron saturation region, and the grid floating potential V_{gf} varied in the same direction as V_s .
- (b) The I_s - V_s curve was a strong and complicated function of the grid dc potential. Raising V_{gdc} above V_{gf} caused $I_s|_{V_s \text{ const.}}$ to increase by up to a factor of 4, decrease through a saddle point and then pass through another maximum.
- (c) Increasing the amplitude V_{grf} of the rf signal superimposed on V_{gdc} caused I_s to decrease, but the expected current minimum plateau was not observed - see Fig. 9.4. The maximum available rf voltage of 50 V produced a maximum decrease of 17% in I_s , irrespective of the value of V_{gdc} .
- (d) As measured by the electrometer E in Fig. 9.2, the maximum current flow from grid to ground caused by the superposition of $V_{grf} = 50$ V on $V_{gdc} = V_{gf}$ was about 2×10^{-5} A, which may

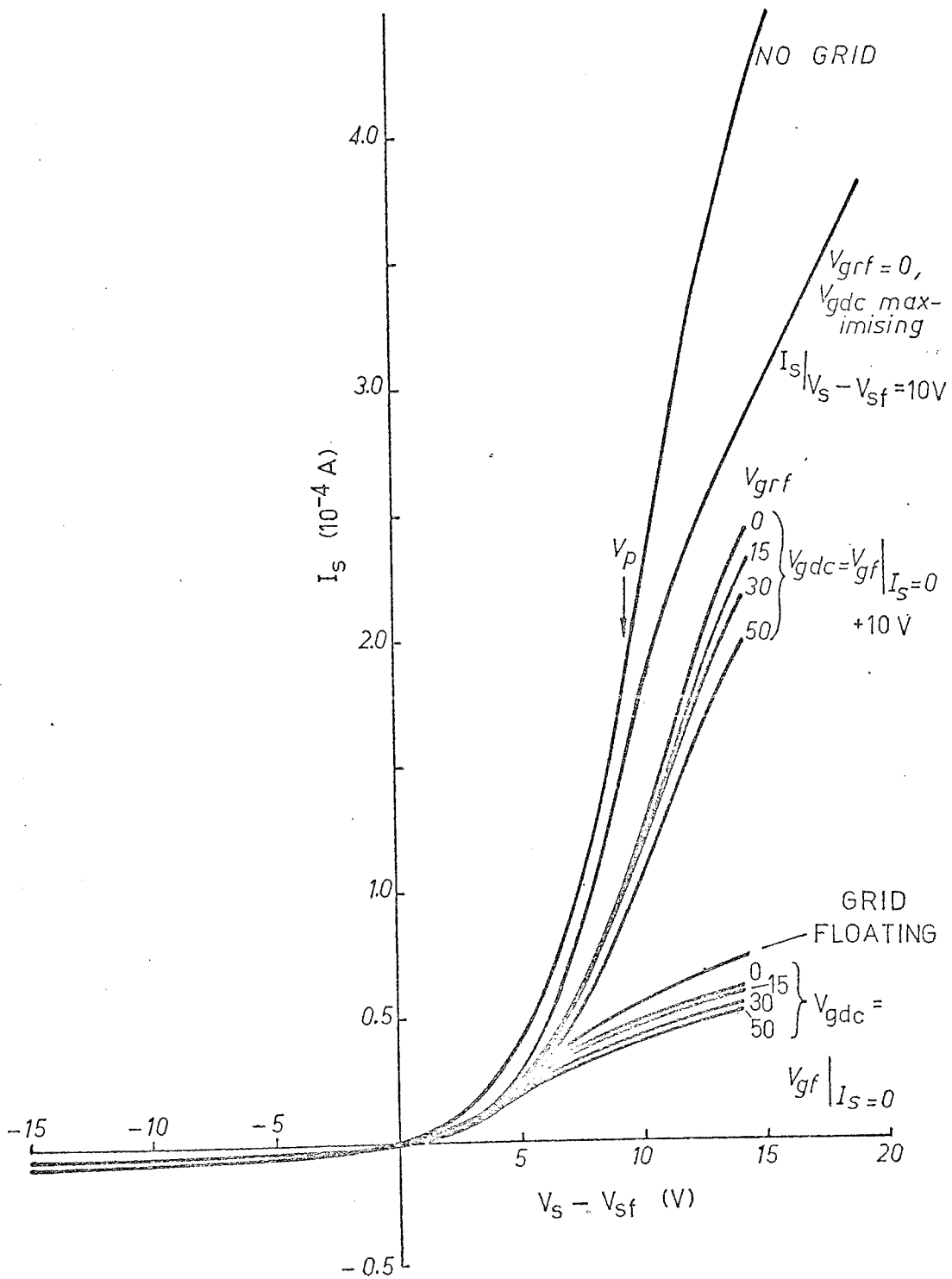


Fig. 9.3 Dependence of the current-voltage characteristics of a gold-plated sample on the dc and rf voltages V_{gdc} and V_{grf} applied to the grid ($p = 70$ mtorr, $I_d = 40$ mA).

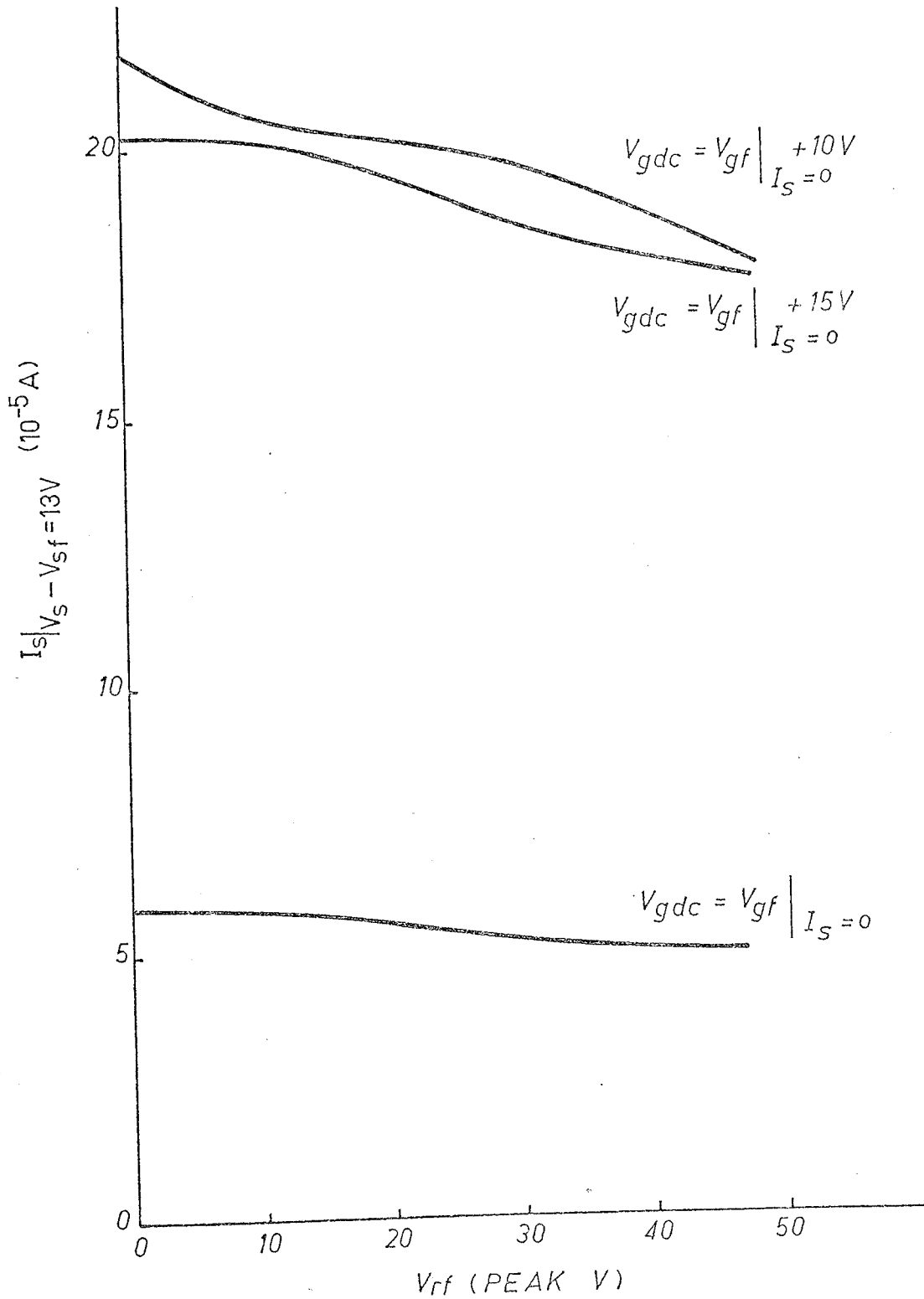


Fig. 9.4 Variation of sample current at fixed sample voltage with grid rf voltage, for different grid dc voltages.

be compared with the decrease of $\sim 1 \times 10^{-5} \text{ A}$ in I_s | $V_s > V_p$ for the same grid conditions.

The geometrical transparency of the grid being about 90%, observations (a) and (b) must be a consequence of the positive ion sheath of each wire extending well into the inter-wire space and partially shielding the sample against slower negative particles from the plasma (the sheath thickness may have been of the same order as the inter-wire space - see Appendix B). This implies that the filter should be operated with V_{gdc} held near to plasma potential so as to reduce the space charge sheath of the grid wires. However, the fractional decrease in I_s due to V_{grf} was quite insensitive to V_{gdc} , and together with the absence of a current plateau this suggests that the device was not functioning well as an electron filter. A closer wire spacing coupled with larger rf amplitudes may have improved the efficiency of electron capture, but the simpler approach of superposition of an rf signal to a sample undergoing constant current anodization was pursued instead, as described in the following section.

9.3 Modulation of the Negative Ion Flux to a Sample by the Simultaneous Application of rf and dc Biases

9.3.1 Constant dc voltage approach

The different responses of electrons and negative ions to a high frequency potential as mentioned in the previous section, together with the non-linearity of the current-voltage characteristic of a Langmuir probe, can be utilized to reduce the negative ion flux component in the anodic current to a sample.

Consider first the circuit of Fig. 9.5(a), which permits the

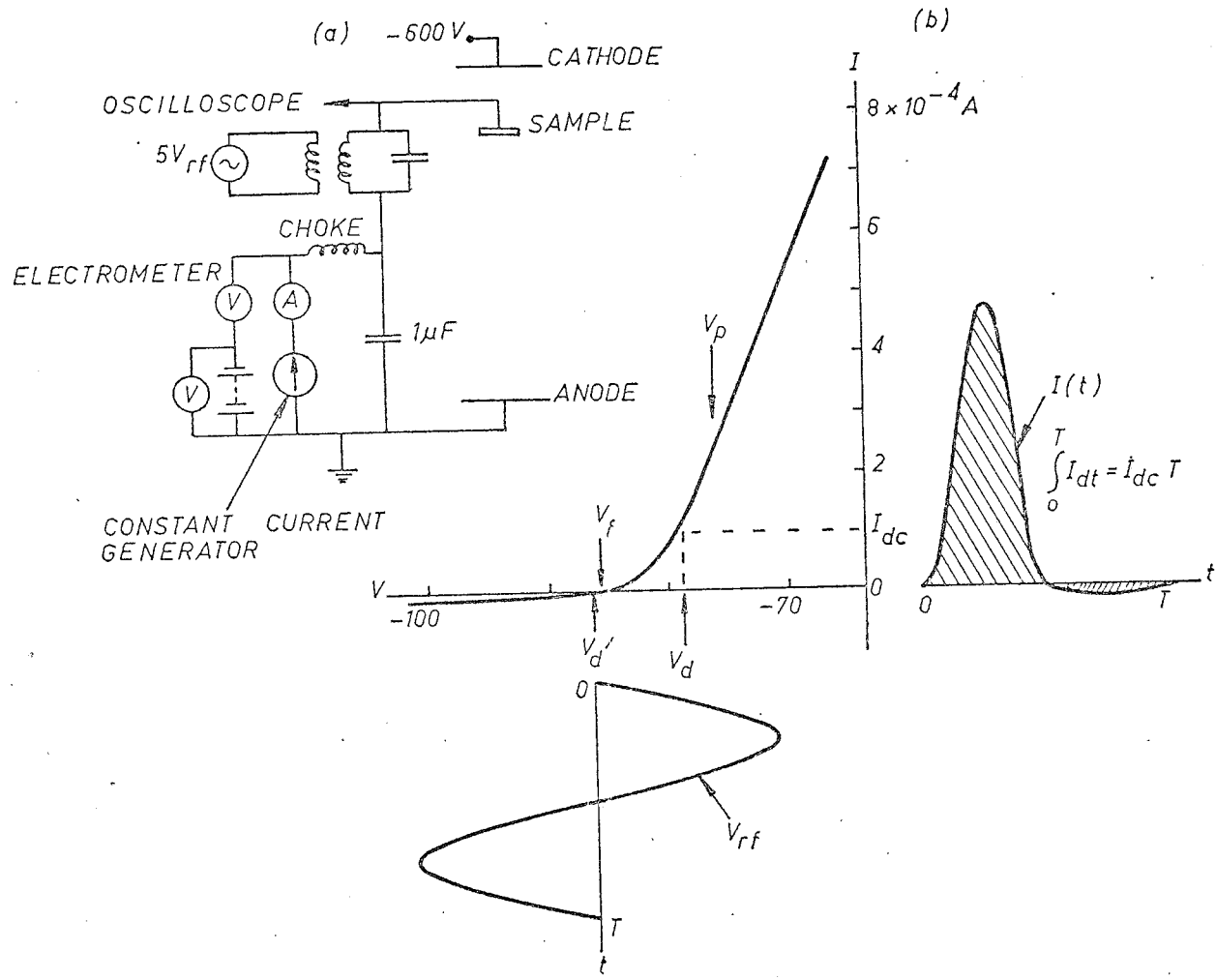


Fig. 9.5 (a) Circuit for simultaneous application of dc and rf biases to a sample.
 (b) I-V relations for sample subject to dc and dc+rf bias conditions at a pressure of 60 mtorr.

application of an rf voltage to a sample that is biased either at constant dc voltage or so as to draw a constant dc current from the plasma. The sample behaves like a large plane probe and in the absence of any rf injection it has the static current-voltage characteristic shown in Fig. 9.5(b). A metal sample isolated from the dc biasing circuit will assume a floating potential V_f which is a few volts negative to the plasma potential V_p . The application of an rf voltage to this dc isolated sample will cause the mean sample potential to assume a new value V_{frf} which is more negative than V_f , since the current to the sample must average to zero over a cycle. If a dc voltage is now applied so as to bias the sample more positively, say to its original potential V_f for instance, then the sample will draw a net anodic current, since the current during the half cycle positive to V_f will greatly exceed the negative half cycle current. However, the plasma negative ions will not be able to reach the sample, since due to their low energy they are unable to surmount the dc potential barrier $V_p - V_f$, and their large mass prevents them from reaching the sample during the portion of the rf cycle when this barrier may be sufficiently reduced - the electrons and negative ions effectively experience different potential barriers.

These conditions of an rf voltage superimposed on a dc voltage bias equal to V_f were applied to an aluminum sample in the negative glow of a dc oxygen discharge by O'Hanlon and Pennebaker 1971. From the behaviour of the sample current with time, curve (a) in Fig. 9.6, they inferred that the sample did not anodize, and concluded that this was due to the elimination of plasma negative ions from the anodic current to the sample. However, an analysis of O'Hanlon and Pennebakers' experiment indicates that oxide growth would not be expected to occur even if negative

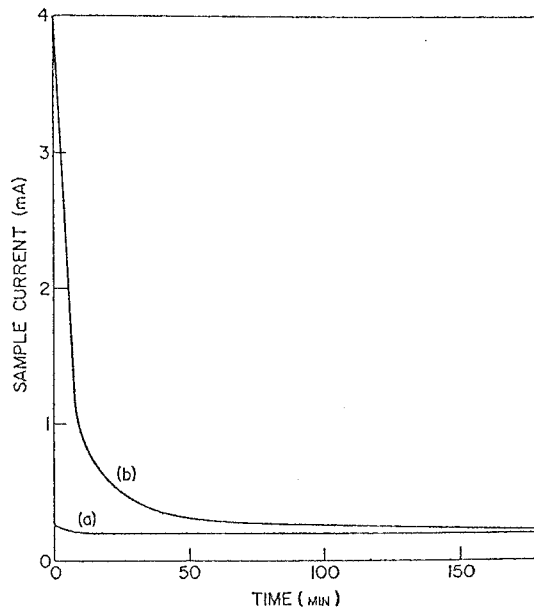


Fig. 9.6 Current decay through aluminum sample: (a) dc bias = V_f , (b) dc bias = $V_f + 5.5V$. In both cases $V_{rf} = 10V$ peak-to-peak (from O'Hanlon and Pennebaker 1971).

ions were available from other processes such as electron attachment at the oxide surface, since their bias conditions rendered the field in the oxide very small. This can be seen as follows. The potential of the unoxidized aluminum sample will vary symmetrically at rf frequency about V_f . This rf potential across the space charge sheath will give rise to a net anodic current to the sample as explained above. If now a thin 'thermal' oxide layer is formed on the sample, as O'Hanlon and Pennebaker suggested, then to a good approximation the rf potential will still appear across the sheath region because the capacitance of the sheath C_{sh} will be much lower than that of the oxide, C_{ox} . The only effect of the oxide will be to present an extra impedance to the dc current, which will decrease slightly, and the new steady state may include a small time

averaged electric field in the oxide film. The time-averaged situation will not be significantly different from that of a sample at floating potential with an equilibrium growth of oxide.

A rough estimate of the field developed in the thermal oxide can be obtained by approximating the sample I-V characteristic to a straight line above V_f , and the rf sine wave to a triangular form. Then the initial 20% decrease in sample current (see Fig. 9.6(a)) would have been caused by a negative shift in the dc potential at the oxide edge of the sheath equal to 10% of the peak rf amplitude of 10 V. This 1 volt potential difference would be developed across the $\sim 20\text{\AA}$ of 'thermal' Al_2O_3 , giving a field strength similar to that in Al_2O_3 at the end of a constant voltage anodization when oxide growth has for practical purposes ceased.

Thus under O'Hanlon and Pennebakers' stated conditions, no high dc field will be developed in the oxide to act as a driving force for ionic motion and further oxidation, and although exclusion of negative ions is accomplished, their experiment does not justify the conclusion that negative ion extraction from the plasma is essential to plasma anodization. However, by using a dc and rf biasing arrangement and also constraining the dc current through the sample to a constant value, information can be obtained as to the importance of plasma negative ions (Olive et al. 1972).

9.3.2 Constant dc current approach

When an rf bias is applied to a sample being anodized at constant dc current (e.g. I_{dc} on Fig. 9.5(b)), the effective dc bias point (V_d on Fig. 9.5(b)) will move to a more negative value, say V'_d , in order that the new current has the same average value as before application

of the rf bias. Because of the relative magnitudes of C_{ox} and C_{sh} the rf voltage will appear across the sheath and since the dc current through the oxide is constant the mean field in the oxide should be unchanged. Thus, for the case of dc and rf bias the potential barrier to oxygen negative ion flow across the sheath to the sample surface will be increased from that for dc bias only. Accordingly, the oxide growth rate should decrease on the application of the rf bias if oxygen negative ions from the plasma are important in plasma anodization.

To obtain a quantitative measure of the expected change in growth rate it is first necessary to obtain an expression for the rate of arrival of plasma negative ions at the oxide surface. If it is assumed that the plasma negative ions have a Maxwellian distribution in velocity then the oxygen negative ion current density across the sheath can be written (c.f. Eqns. 4.2 and 4.5)

$$j_- = j_{-s} \exp(-e\Delta V/kT_-) \quad (9.1)$$

where j_{-s} is the negative ion random current density, T_- the ion temperature, and $-\Delta V$ the sheath potential drop (the minus sign signifies the assumption of a positive space charge in the sheath and thus a retarding potential barrier to negative particle flow from the plasma to the sample). A further assumption implicit in Eqn. 9.1 is that the mean free path of the plasma negative ions is comparable to or greater than the sheath thickness. For the plasma used in this experiment this assumption seemed justified as the Debye shielding length was 0.9 mm and the negative ion mean free path length calculated from Langevin's simple solid elastic sphere expression for mobility was 1 mm (see Appendix B).

Once plasma negative ions reach the oxide surface then, if they are to contribute to oxide growth, presumably one of two mechanisms is

operative, namely (a) the negative ions are embedded in the oxide on first impact or (b) the negative ions are first adsorbed, after which the adion would have to move over the surface to its final location at some low energy site. In case (a) the oxide growth rate and the ionic current density in the oxide j_i , will be linearly dependent on the rate of arrival of negative ions j_- . Thus, assuming that the application of the rf bias to the sample does not affect the bulk plasma negative ion properties, i.e. j_{-s} and kT_-/e , we have from equation 9.1 that the ratio of oxide ionic current without rf bias to that with rf bias is given by

$$\log_{10} \left(\frac{j_i}{j_{irf}} \right) = \frac{e}{kT_-} \frac{(\Delta V_{rf} - \Delta V)}{2.303} \quad (9.2)$$

where ΔV_{rf} is the time-averaged potential drop across the sheath for the condition of dc plus rf bias.

In case (b) it would be expected that adions would compete with each other for the final low energy sites, which will be taken to be near excess metal ions (although another possibility would be near oxygen negative ion vacancies in the oxide). Thus some low power dependence of the concentration $n_{O^{2-}}$ of finally-located oxygen ions on the arrival rate of plasma negative ions, O^- or O_2^- , might be anticipated, e.g.

$$n_{O^{2-}} = \alpha \left[\frac{j_-}{j_0} \right]^x \quad (9.3)$$

where x is less than 1 and α and j_0 are constants. Hence in this case we have

$$j_i = \beta n_M n_{O^{2-}} \quad (9.4)$$

where n_M is the concentration of the metal ions near the surface, and

β is some constant term relating to the field and dielectric properties at the oxide surface. Putting (9.1) and (9.3) into (9.4) and assuming n_M is constant we have that the ratio of ionic current without rf bias to that with rf bias is given by

$$\log_{10}\left(\frac{j_i}{j_{irf}}\right) = x \frac{e}{kT_-} \frac{(\Delta V_{rf} - \Delta V)}{2.303} \quad (9.5)$$

Comparison of the calculated values of ionic current ratio given by equations 9.2 and 9.5 with actual experimental values will thus demonstrate whether bulk plasma negative ions are important to plasma anodization.

9.3.3 Experiment and results

The estimation of the ratio of the oxide ionic currents and the difference in sheath potential drop $\Delta V_{rf} - \Delta V$ for constant current plasma anodization with and without rf bias was carried out in the positive column of system B with a 40 mA discharge current, using the two oxide masked Ta samples described in section 8.3.4.

The ratio of j_i to j_{irf} was calculated from oxide growth rates which were obtained from single zone ellipsometry measurements during anodization by the method outlined in section 8.3.6.

To estimate the sheath potential drop it was assumed that for a given plasma, sample geometry, dc sample current and rf sample bias, ΔV and ΔV_{rf} are independent of the sample surface, whether metallic or oxide coated. With this assumption, $\Delta V_{rf} - \Delta V$ could be estimated from I-V measurements on the sample which was gold-plated, thereby avoiding oxide formation and consequent distortion of the I-V characteristics. For the direct current I_{dc} in Fig. 9.5(b), ΔV is given by $V_p - V_d$ (the voltage reference is the anode). By using the circuit of Fig. 9.5(a)

the time-averaged potential V_d' caused by the application of a 3.5 MHz voltage to the sample, constrained to draw a constant direct current, was determined for various dc currents and rf voltages. This enabled determination of $\Delta V_{rf} - \Delta V$ as given by $V_d - V_d'$ (see Fig. 9.5(b)).

The gold-plated sample I-V data were also used to estimate the field strength E_{ox} in the anodic oxide during growth. Thus, at a given total current I and oxide thickness D, E_{ox} was taken to be given by

$$E_{ox} = \frac{(V_{Ta} - V_{Au})_I - (V_{Ta} - V_{Au})_{I=0}}{D} \quad (9.6)$$

where V_{Ta} (or V_{Au}) was the voltage difference between the tantalum (or gold-plated tantalum) and the anode. Any changes in floating potential during anodization as detected by a small gold probe located 2 mm in front of the oxide were allowed for (the justification for Eqn. 9.6 and other methods of estimating the field in the oxide are given in the next chapter, section 10.2).

The Ta sample was anodized at constant currents of 0.1 and 0.2 mA (i.e. below V_p on the I-V characteristic of Fig. 9.5(b) so that Eqn. 9.1 applies) with a discharge current of 40 mA and pressures of 60 and 100 mtorr, and rf voltages between 10 and 30 volts peak to peak were applied for portions of each formation. The effect of the rf bias voltage on the oxide growth rate and oxide field, while constraining the average dc anodizing current to a constant value, is shown in Table 9.1. Whereas $(V_{Ta})_I$ changed significantly (up to 7 volts), as anticipated in section 9.3.2 the application of the rf bias changed the estimated field in the oxide only marginally. The effect of the rf bias on the oxide growth rate was also small.

| Pressure mtorr | I_s mA | rf bias pk-pk-volts | $\Delta D/\Delta t$ $\text{\AA}/10^2 \text{ sec}$ | $E_{6\text{ox}}$ 10^6 V/cm |
|-------------------|-------------|------------------------|--|---|
| 60 | 0.1 | 0 | 0.14 | 2.82 |
| | | 10 | 0.16 | 2.90 |
| | | 20 | 0.20 | 2.94 |
| | | 0 | 0.18 | 2.86 |
| | | 30 | 0.23 | 3.00 |
| | | 0 | 0.22 | 2.88 |
| 60 | 0.2 | 0 | 0.65 | 3.17 |
| | | 30 | 0.61 | 3.16 |
| | | 0 | 0.65 | 3.17 |
| 100 | 0.1 | 0 | 0.24 | 2.92 |
| | | 20 | 0.43 | 3.04 |
| | | 0 | 0.35 | 2.93 |
| | | 0 | 0.44 | 2.98 |
| | | 30 | 0.58 | 3.10 |
| | | 0 | 0.57 | 2.98 |
| 100 | 0.2 | 0 | 1.45 | 3.19 |
| | | 30 | 0.75 | 3.20 |
| | | 0 | 1.22 | 3.21 |

Table 9.1

The effect of the rf bias on the oxide growth rate and field strength.

9.3.4 Discussion

To compare the data in Table 9.1 with the changes in growth rate expected from the theoretical considerations discussed in section 9.3.2, consider first equation 9.2. It is required to know the negative ion temperature T_- and for this purpose $\frac{kT_-}{e}$ is taken as 0.1 volt as reported by Thompson 1961a. From Table 9.2 it is seen that the large changes in growth rate that would be expected if the plasma negative ions were embedded in the oxide on first impact are not obtained in practice.

The other possible mechanism of plasma negative ion contribution to oxide growth discussed in section 9.3.2 leads to equation 9.5. Inserting the measured changes in ionic current from Table 9.1 into equation 9.5 yields values for the parameter x . It is found that x is always less than 10^{-2} , again showing, through equations 9.3 and 9.4, that the oxide ionic current does not depend upon the rate of supply of negative ions from the plasma.

From these results it must be concluded that if Thompson's mean ion energy and the dependence of rate of supply of negative ions on sheath potential drop given by Eqn. 9.1 are valid, then negative oxygen ions in the plasma are not utilized in plasma anodization. This does not exclude the possibility of negative ions produced by electron attachment at or very close to the oxide surface. However, as was noted in section 4.3 a further ionization process would be required before these ions are incorporated in the oxide film, since gaseous negative ions are invariably singly charged (McDaniel 1964).

| Pressure mtorr | I_s mA | rf bias pk-pk V | $\Delta V_{rf} - \Delta V$ V | j_i/j_{irf} | |
|-------------------|-------------|--------------------|---------------------------------|---------------|----------|
| | | | | from Eqn. 9.2 | measured |
| 60 | 0.1 | 10 | 1.3 | 10^5 | 0.9 |
| | | 20 | 3.9 | 10^{17} | 0.9 |
| | | 30 | 7.25 | 10^{31} | 1.0 |
| | 0.2 | 30 | 5.3 | 10^{23} | 1.1 |
| 100 | 0.1 | 20 | 3.8 | 10^{16} | 0.8 |
| | | 30 | 7.0 | 10^{30} | 1.0 |
| | 0.2 | 30 | 4.5 | 10^{20} | 1.2 |

Table 9.2

Comparison of expected change in j_i on application of rf bias as calculated from equation 9.2, with that measured by ellipsometry.

10. THE RELATION BETWEEN OXIDE GROWTH RATE,
ELECTRIC FIELD STRENGTH IN THE OXIDE AND OXIDE TEMPERATURE
DURING PLASMA ANODIZATION

10.1 Introduction

The formation of an oxide film on a metal or semiconductor, whether by thermal oxidation, anodic oxidation in liquid electrolytes, or plasma anodization, requires the transport of one or more reactant species (metal and/or oxygen) through the oxide. The simplest model of thermal oxidation involves the diffusion of neutral molecules under a concentration gradient. The electrochemical model of thermal film growth assumes the transport of ionic species with counterflow of electrons and holes to maintain electrical neutrality. In solution anodization at room temperature, ionic species are considered to migrate through the oxide by high field transport, and electronic transport usually accounts for less than 1% of the total charge passed. The ionic conduction mechanism involved gives rise to an exponential dependence of oxide growth rate on mean electrostatic field in the oxide, as discussed in section 3.2. The growth mechanism in plasma anodization might also be expected to involve high field ionic conduction. It was reported above that conditions in the dc discharge could affect the growth rate, but that the results were not inconsistent with an ionic conduction-limited growth - see section 8.4. Also discussed in that section were the high growth rates obtainable in high frequency excited discharges. An additional factor which may be contributing in such cases is a higher sample temperature due to a high thermal energy input from the plasma. The aim of the work to be described below was to see whether the ionic current density in the oxide could be identified as a function of the field strength in the oxide and its

temperature T. Data will be presented on niobium, tantalum, aluminum and silicon.

10.2 The Estimation of Field Strengths in the Oxide

In attempting to relate measurable quantities to the field in the oxide during plasma anodization, quite considerable problems arise. These problems have been discussed in the literature (O'Hanlon 1969, Olive et al. 1970, Ramasubramanian 1970), but only partial solutions have been suggested.

The simplest approach, used by most of the early investigators, was to assume that the voltage across the growing oxide was equal to the voltage applied to the sample with respect to the grounded anode. While this approximation may not be too seriously in error in certain bell-jar geometries similar to Fig. 8.7, it becomes meaningless for cylindrical discharges where due to the potential gradient in the plasma, a sample drawing a considerable anodic current may still be tens of volts negative with respect to ground (this situation also necessitated care in the selection of a constant current supply for this study).

The measurement of sample potential with respect to a small electrically isolated metal probe located near to the anodizing sample is a considerable improvement, both in respect of registering the local floating potential and monitoring any variations in the latter with time during anodization. However, even if the probe is sufficiently close to the sample that random variations in time in the potential gradient through the plasma are negligible, this method still neglects (a) work-function differences and (b) changes in the potential drop across the sample sheath when a net current is drawn, as pointed out in section 4.2.2. An attempt was made to overcome these difficulties in the present study by

evaporating a gold electrode onto a patch of thick oxide formed initially on the sample by solution anodization. It was intended to bias such an electrode until it drew the same current density as the main anodizing area, but proneness of the oxide to electrical breakdown on exposure to the plasma prevented their application.

If the phenomena in the plasma sheath adjacent to the oxide may be assumed to be the same for a given current density independent of oxide thickness, it would appear that with constant current anodization an incremental field measurement, as by a determination of oxide thicknesses and sample potentials (with respect to floating probe V_{sp}) at the beginning and end of a formation, would eliminate the problems of sheath potential drops and work function differences. However, such measurements invariably resulted in a large scatter in field values, and this was presumed to be caused by variations in the oxide field during a formation. Relatively small variations (perhaps due to a build-up of space charge in the oxide) can have significant effects on incremental measurements, as may be seen from Fig. 10.1.

If in growing (at constant current) from an oxide thickness D_1 to D_2 the integral oxide field decreases from E_1 to $E_1 - \delta$, then the incremental measurement becomes $E_1 - \frac{\delta D_1}{D_2 - D_1}$, and if the increment $D_2 - D_1$ is small compared to the initial thickness, $\frac{\delta D_1}{D_2 - D_1}$ may be large even for δ small.

A procedure for estimating the potential difference V_0 due to sources (a) and (b) above would be to carry out a series of formations at the same constant current I , plot the p.d. between sample and probe versus oxide thickness D both evaluated at the end of each formation, and extrapolate back to $D = 0$. The intercept on the voltage axis would be the

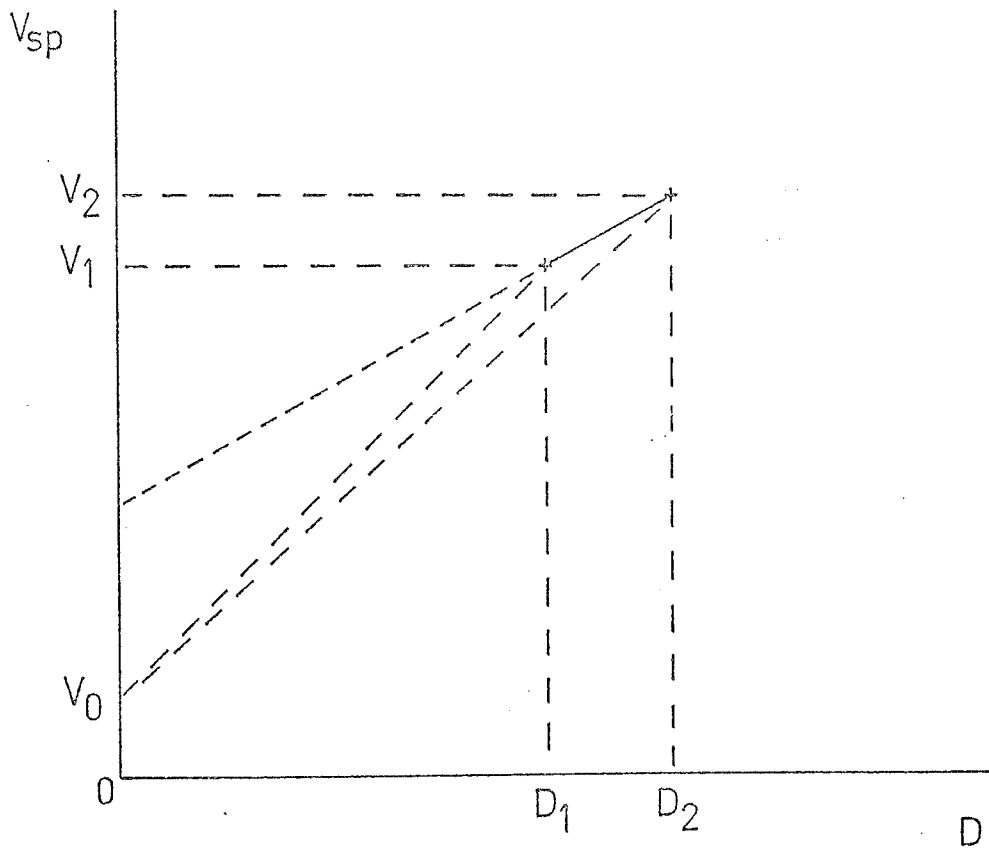


Fig. 10.1 Estimation of oxide field from sample-probe potential and oxide thickness data.

Integral fields: $E_1 = (V_1 - V_0)/D_1$, $E_2 = (V_2 - V_0)/D_2$.

Incremental field: $\Delta V/\Delta D = (V_2 - V_1)/(D_2 - D_1)$.

unknown potential difference V_{0I} for this particular current, providing the oxide field and V_{0I} did not vary much among the formation end points.

A less laborious approach is to initially obtain the current-voltage characteristic of the unanodized sample with respect to an invariant probe over the range of anodizing currents to be used. This characteristic yields correction factors for any formation current to be deducted from subsequent sample - probe potential measurements during anodization, assuming gas pressure and discharge current can be accurately reproduced. The problems here are that the unanodized sample possesses a thin 'thermal' oxide, and although this may be corrected for after analysis of the total ellipsometry data, its electrical properties may differ from those of the subsequent anodic oxide. Furthermore, the thin oxide may increase in thickness during the initial I-V measurement.

This method was modified slightly to use the sample floating potential between formations as a reference level rather than that of the probe, since the latter could not be positioned reproducibly with respect to the oxide surface. Thus, the oxide field strength at given oxide thickness D and anodizing current I was taken as

$$E_{ox} = \frac{(V_s - V_u)_I - (V_s - V_u)_{I=0}}{D - D_u} \quad (10.1)$$

where the subscript u denotes measurements on the unanodized sample, and V_s (or V_u) was the voltage difference between the sample (or unanodized sample) and the anode. The sample-probe potential difference was still monitored continuously on a chart recorder as in Fig. 8.3 to provide an indication of anodization progress.

Finally, as a possible improvement on the above, a gold-plated sample was used for the initial I-V measurements to avoid the complications

due to the oxide on the unanodized sample. In this case the field was taken as

$$E_{\text{ox}} = \frac{(V_s - V_{\text{Au}}) I - (V_s - V_{\text{Au}})_{I=0}}{D} \quad (10.2)$$

where V_{Au} denotes the voltage of the gold-plated sample with respect to the anode. This method is subject to the same assumptions mentioned in section 9.3.3 with respect to gold-plated sample measurements.

10.3 Variation of Voltage with Time at Constant Total Current

Figure 10.2 shows a plot of the potential V_{sp} of a niobium sample relative to a probe during anodization at constant current. The plot is fairly typical of both tantalum and niobium specimens in that the potential rises rapidly when the current is first applied and then settles to a slower, more or less constant rate of rise. The explanation of the fast initial rise is probably as follows. Since the current is mostly electronic the effect is clearly an increase of resistance to electronic current. Electron injection from the plasma appears to occur at comparatively low fields. With little or no space charge in the oxide, the field throughout the oxide is also low. However, electronic space charge develops due to capture of electrons by the heavy concentration of traps present in the amorphous oxide. This would cause the field at the plasma interface to be reduced so that a higher mean field would be required to maintain the given electronic current. Finally, a steady state would be reached in which the slow rise of voltage would be due more or less entirely to the slow rate of growth of the oxide. An alternative explanation is possible in terms of patching of leaky spots in the oxide, but this seems unlikely in view of the fact that the same behaviour was exhibited by films prepared by wet anodization and then tested in the

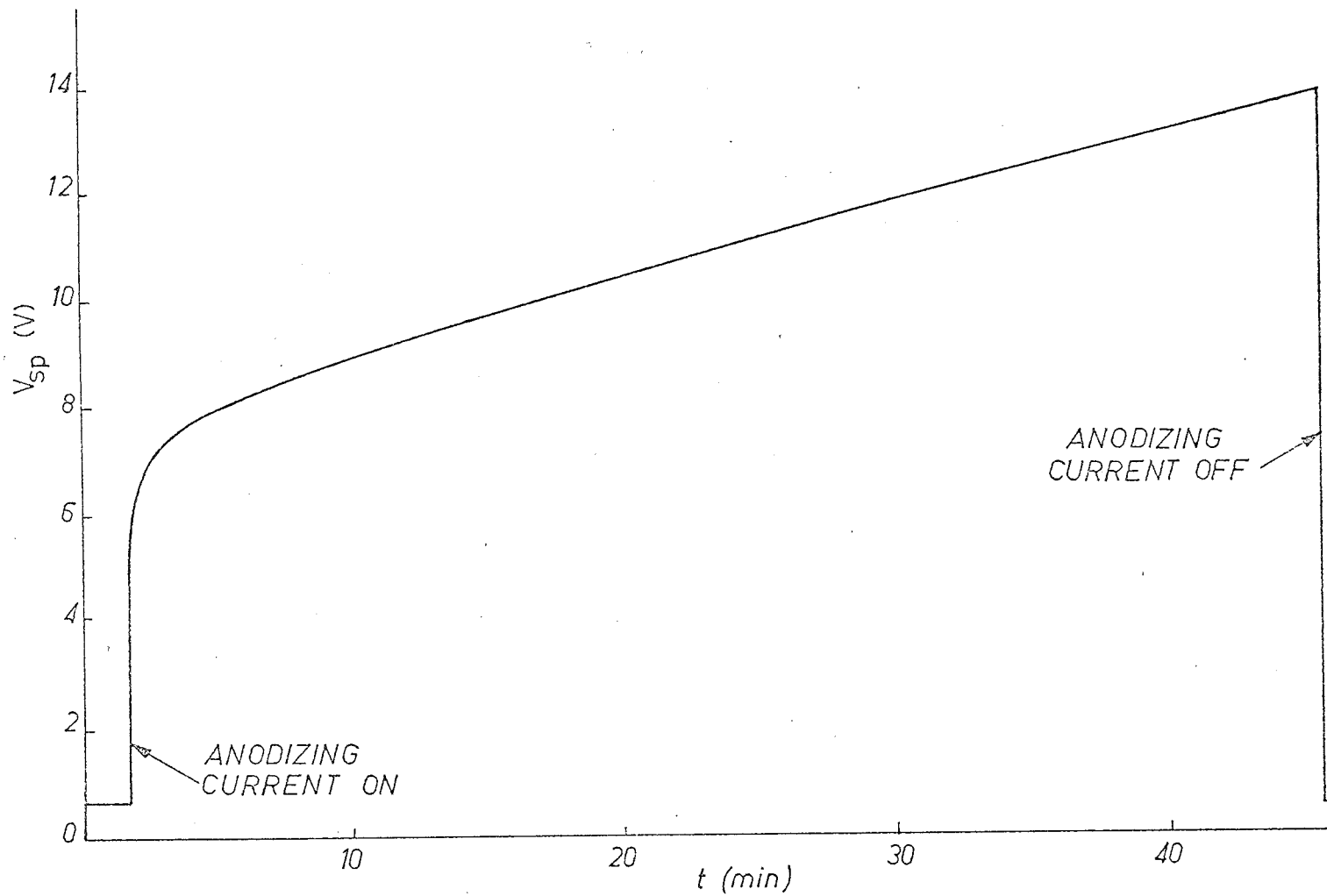


Fig. 10.2 Typical variation of sample potential with respect to a floating probe during a constant current formation (niobium sample in negative glow of system A).

plasma.

10.4 Voltage vs. Thickness for Steady-State Conditions

Figure 10.3 (which is for niobium) shows voltages with respect to a nearby probe recorded at the end of each of a series of formations at the same total current in the negative glow of system A, plotted against the corresponding thickness of oxide. The corresponding ionic current density, as deduced from the change of thickness during the anodization period, is recorded beside each point. Clearly the linear dependence of voltage on thickness indicates a constant mean field strength in the film in the latter part of each formation. This constant field gave a more or less constant ionic current. This is analogous with wet anodization, but does not mean necessarily that the field was constant through the thickness of the film.

10.5 Thickness and Oxide Potential Difference Versus Time During a Formation

In contrast to Fig. 10.3, which shows data obtained at the end of several formations at a current of 0.5 mA, Fig. 10.4 shows estimated oxide p.d. and thickness versus time during a particular formation on niobium under similar conditions but at a higher current level of 1 mA (see also Fig. 8.11). Such a large variation in growth rate was not typical, but is presented to illustrate a possible source of error in ionic currents calculated from mean growth rates. It is interesting to find that the data of Fig. 10.4 is consistent with an exponential dependence of growth rate on field, as will be shown below.

10.6 Variation of Ionic Current with Estimated Oxide Field

In Fig. 10.5, ionic current densities obtained from the anodiza-

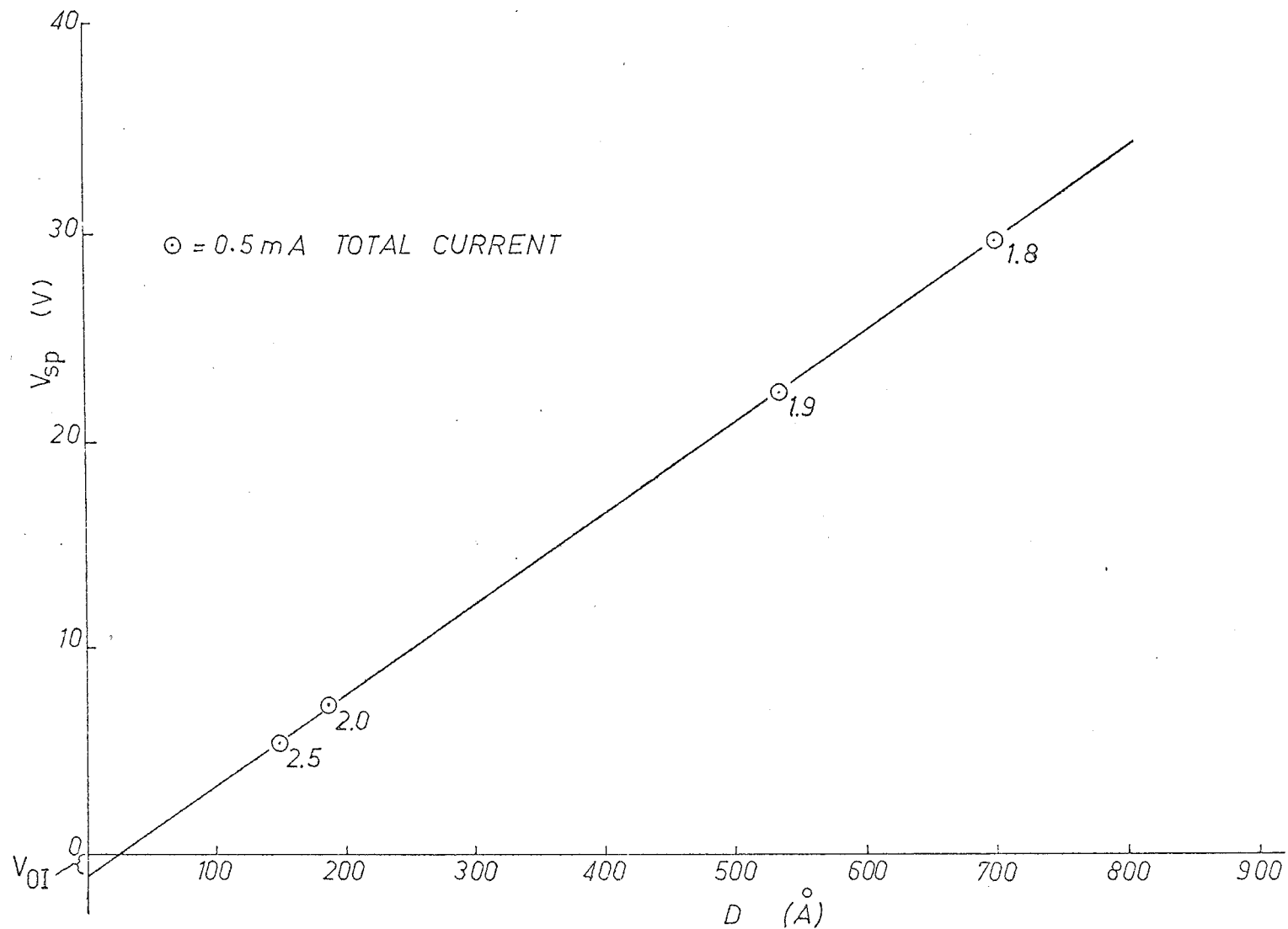


Fig. 10.3 Variation of sample-probe voltage with thickness for a niobium sample (Nb1) as recorded at the end of four formations at the same constant total current of 0.5mA.

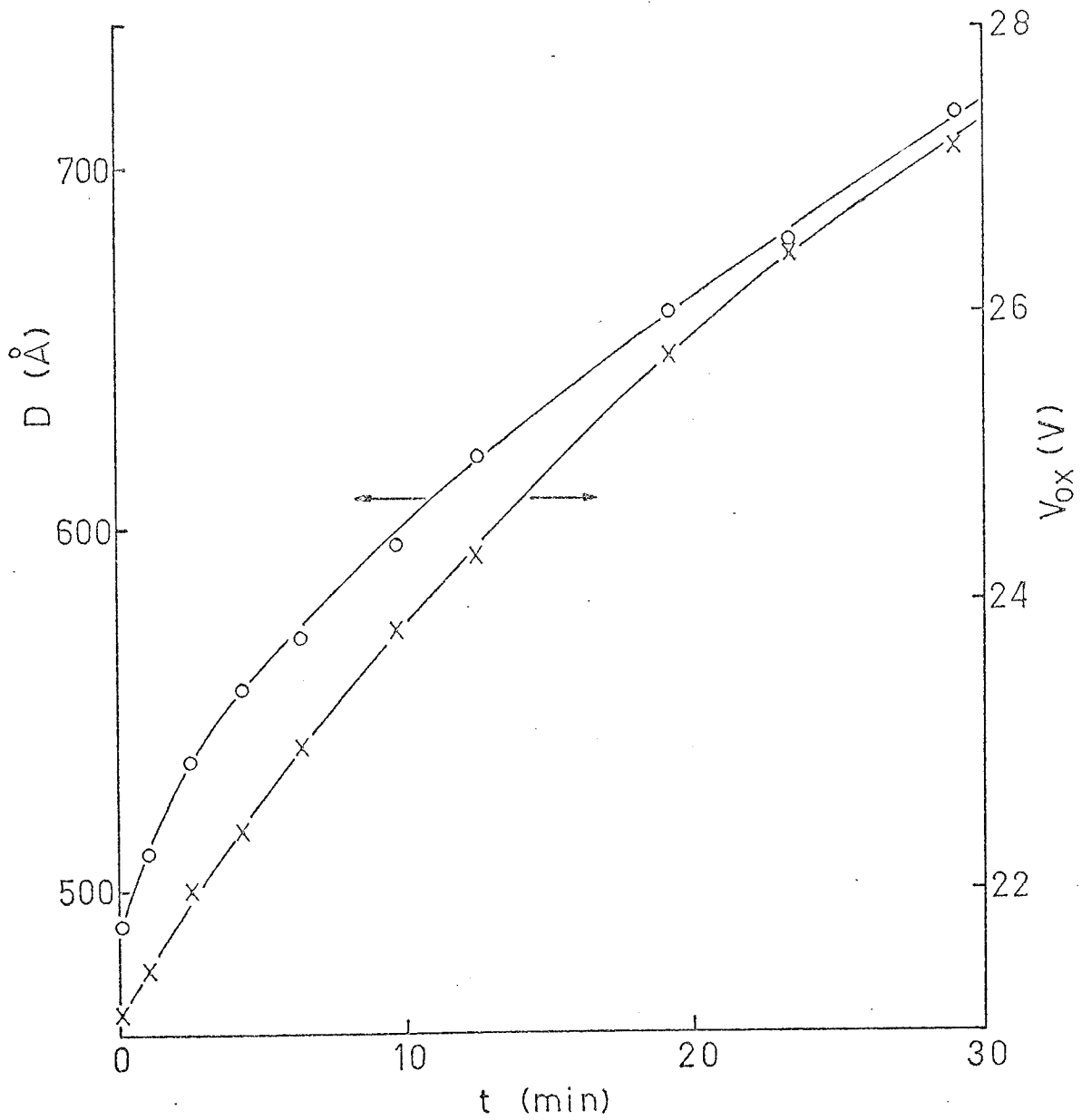


Fig. 10.4 Variation of oxide thickness and estimated voltage across oxide during anodization of a niobium sample (Nb5) at 1 mA/cm^2 in the negative glow of system A.

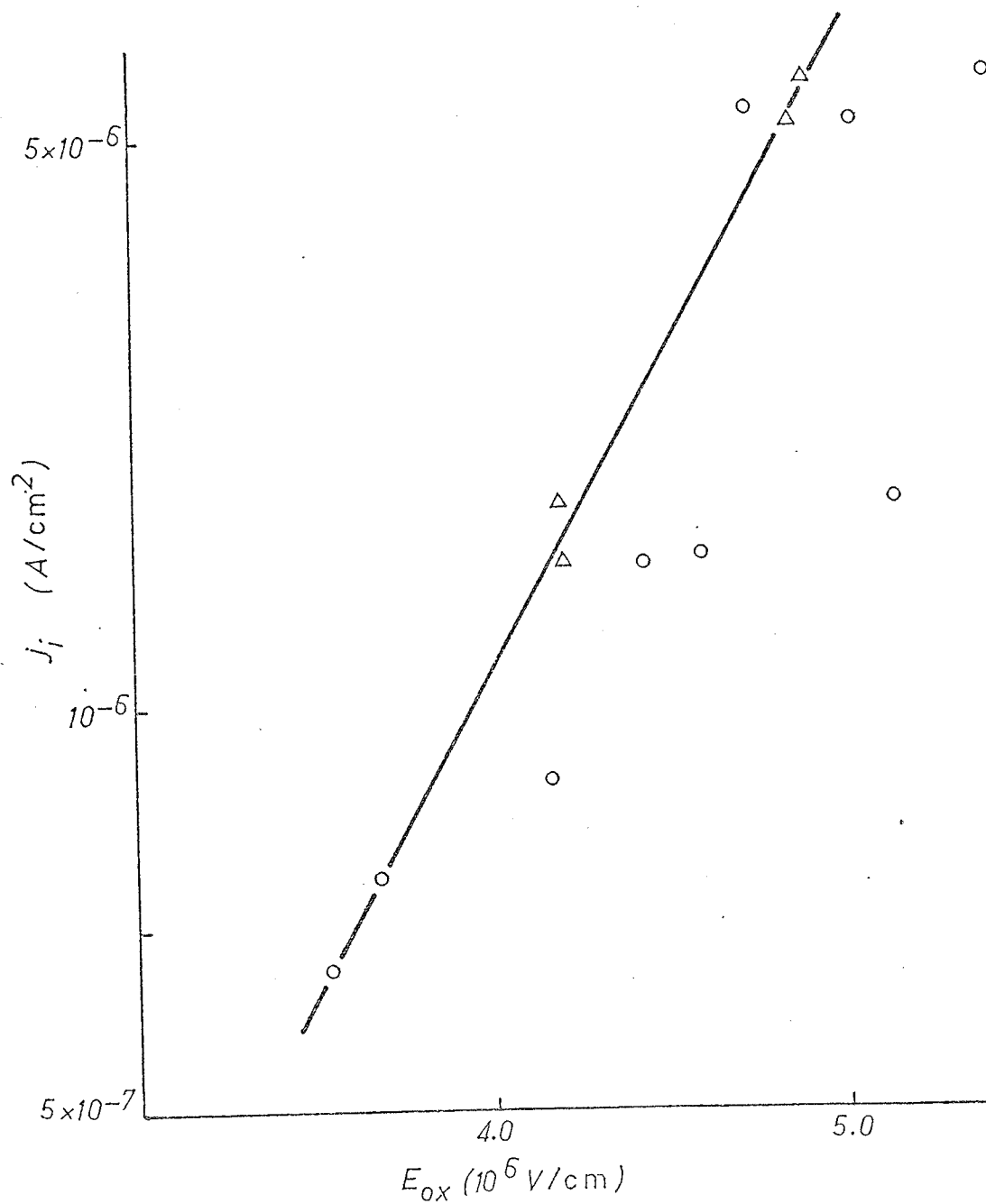


Fig. 10.5 Ionic current versus estimated oxide field (Tafel plot) for anodization of sample Nb2 at 30°C in the negative glow of system A, showing data uncorrected (o), and corrected (Δ) for V_{OI} factors.

tion of an electropolished polycrystalline niobium sample at 30°C in the negative glow of system A are plotted against oxide field evaluated at the end of each formation. The current densities j_i were calculated from mean growth rates using Eqn. 3.1 and assuming the oxide density to be 4.74 gm/cm³ as found for wet anodic Nb₂O₅ (Schrijner and Middlehoek 1964), and the fields for the points (O) were estimated according to

$$E_{\text{ox}} = \frac{(V_{\text{sp}})_I - (V_{\text{sp}})_{I=0}}{D}$$

Some of these fields were corrected using factors V_{0I} obtained from plots similar to Fig. 10.3, and are shown as the points (Δ). The corrected values reduce the scatter, and suggest that the ionic current is indeed determined by the field in the oxide, with an exponential dependence. This view is also supported by Fig. 10.6, which shows incremental growth rates (as ionic currents) and integral field estimates during a single formation, namely that associated with Fig. 10.4. This 1 mA/cm² formation followed one of about an hour at the relatively low current density of 0.2 mA/cm², and a space charge effect is indicated. Alternatively it is possible that the new oxide grown at 1 mA/cm² required a lower field to sustain the electronic current than the pre-existing oxide layer, which has received a low current 'forming' treatment (see section 3.1).

Ionic current - oxide field data for the anodization of a polycrystalline tantalum sample (Ta2) at 30°C using three different pressures in the constricted positive column of system B are shown in Fig. 10.7. The oxide field estimations were made with the aid of data from a gold-plated sample according to equation 10.2. An exponential relation is again evident, and it is essentially independent of pressure. Another remarkable aspect of this data is the range of magnitudes of the fields. In the

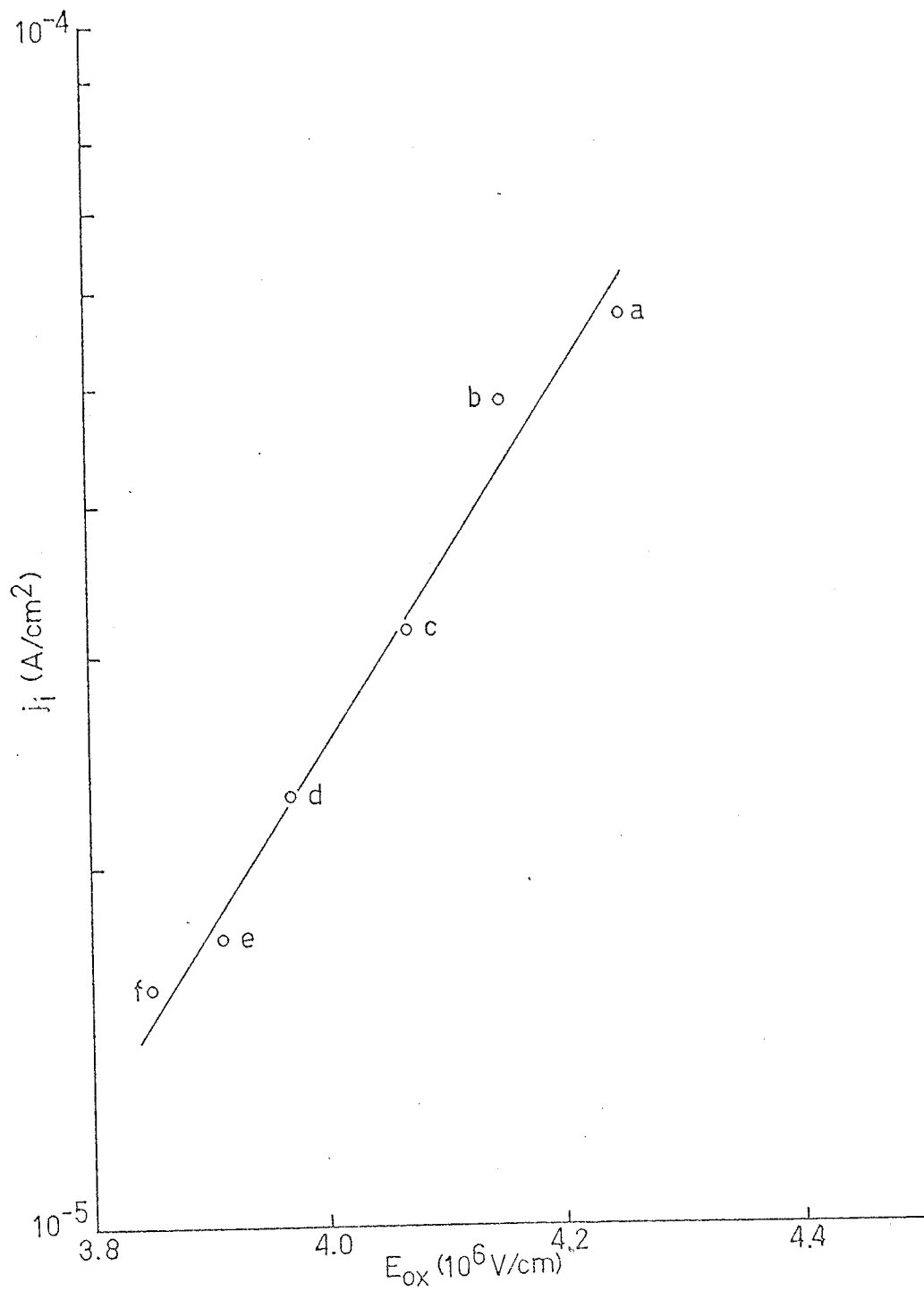


Fig. 10.6 Ionic current (from incremental growth rates) versus estimated oxide field during a particular constant current formation on sample Nb5 (determined from data of Fig. 10.4).

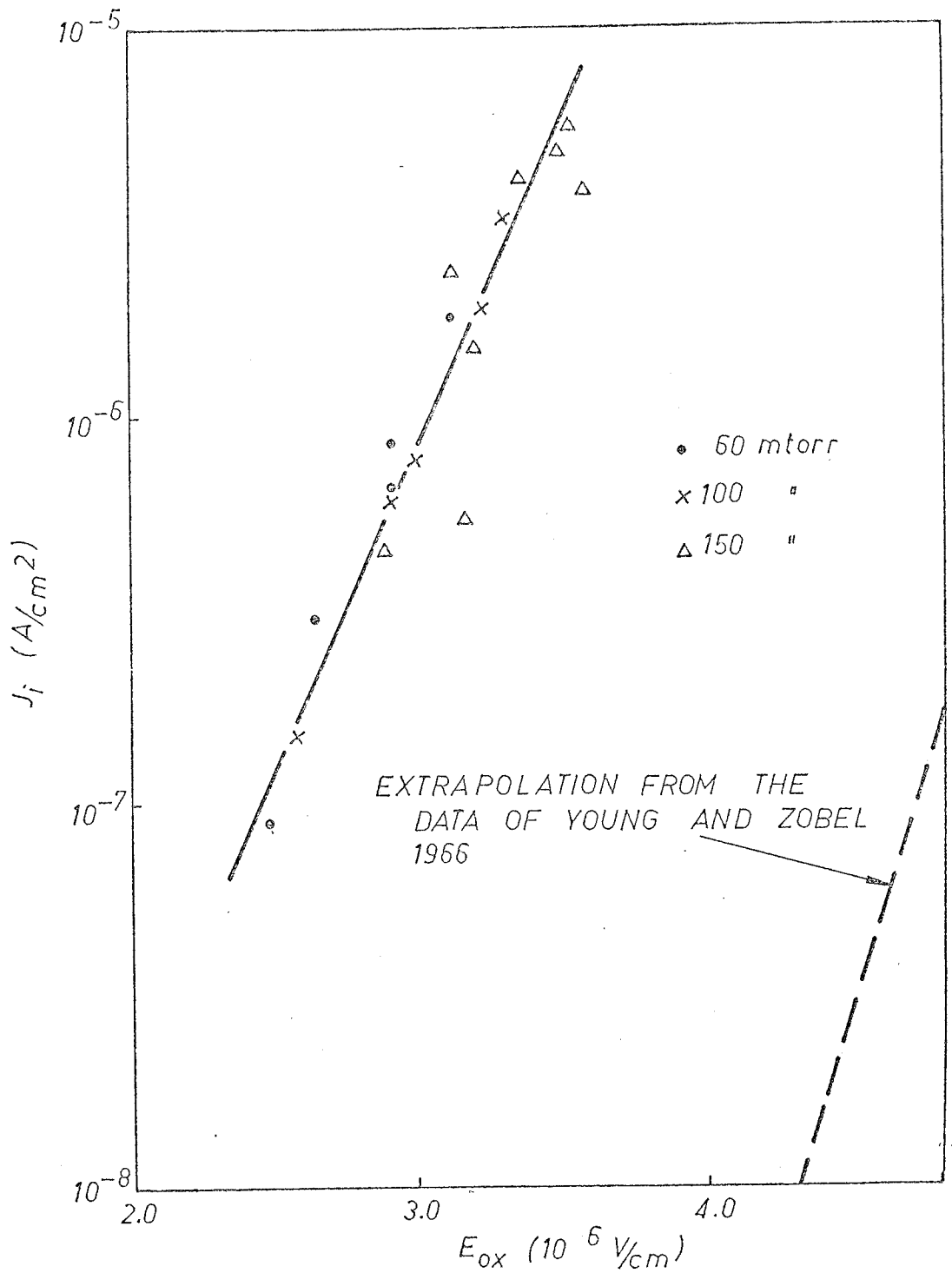


Fig. 10.7 Ionic current density versus oxide field for the anodization of sample Ta2 at 30°C in the positive column of system B at different pressures (extrapolation from wet anodization data also shown).

anodization of tantalum in dilute sulphuric acid, the same ionic current density range of between 10^{-7} and 10^{-6} A/cm² is observed to require field strengths almost a factor of two higher, i.e. 4.6×10^6 to 5.0×10^6 V/cm. The broken line in Fig. 10.7 is from an empirical relation for the solution anodization case (Young and Zobel 1966).

The large discrepancy in fields was not observed for niobium or tantalum anodized in the negative glow of system A (although there were deviations from the solution anodization relation - see Lee et al. 1970) and it may be a consequence of conditions in the positive column of system B, particularly the amount of ultra-violet radiation falling on the sample. The effect of uv radiation on solution anodization has been studied by various investigators. In a recent ellipsometric study, Dell'Oca 1969 found that uv irradiation of tantalum during anodization in dilute sulphuric acid resulted in appreciable oxide growth at fields down to $\sim 1 \times 10^6$ V/cm, i.e. at field strengths that alone would not support any noticeable growth. He found the photo-grown oxide to consist of two layers growing simultaneously, the outer layer being thicker than the inner, and of a higher refractive index according to his overall ellipsometry data. Similarly, the present ellipsometry results can be fitted by a two layer model for the plasma oxide, with the outer layer approximately four times as thick and of a higher refractive index (1.88) than the inner layer (1.63)*.

Furthermore, Dell'Oca found that the photo-grown oxide took

* Both of these values are considerably lower than the refractive index found at 6328Å in section 8.3.1 for the oxide grown normally in dilute sulphuric acid.

up water, and lost it on prolonged drying. Compared to this reversible process, a more drastic but perhaps related phenomenon was observed with the plasma-grown oxide. When the anodized sample was exposed to the atmosphere for the first time (after initially letting the vacuum system up to atmospheric pressure with nitrogen gas from a cylinder), the uniformly coloured oxide film developed many lighter-coloured circular spots which over a period of 30 minutes expanded in number and size to cover the whole surface. Under microscopic observation these light areas were found to be regions where the oxide film had separated from the tantalum substrate. This phenomenon, which was only observed with tantalum and niobium samples anodized to oxide thicknesses of 1000-2000Å in the positive column of system B, suggests a somewhat open oxide structure susceptible to the absorption of water in common with the oxide photo-grown in solution. It is discussed further in section 10.8.

10.7 Dependence of Ionic Current on Temperature

Measurements on the anodization of tantalum at 31°C and 77°C in the negative glow of system A (Lee et al. 1970) indicated that the so-called Tafel plot of $\log j_i$ versus E_{ox} shifted to lower field strengths as the temperature was raised, in agreement with a field-assisted thermal activation process for the ionic conduction mechanism. However, the slopes $d \log j_i / d E_{ox}$ for plasma anodization were considerably lower than the corresponding slopes for solution anodization at these temperatures, whereas in the work to be described below on aluminum, reasonable agreement with solution anodization data was obtained.

The sample consisted of a 2400Å layer of aluminum vacuum evaporated from 99.999% Al wire on a tungsten filament onto the polished surface of a silicon substrate at a pressure of $\sim 1 \times 10^{-5}$ torr. This

produced a highly reflecting Al film while giving better thermal contact to the sample holder than would a glass slide. The Si wafer was mounted on the sample holder with conducting silver paint, which was also brought over the front surface to contact the edge of the Al layer.

In view of the moisture effects on films produced in the positive column reported in the previous section, and also to obtain faster growth rates, an alternative annular geometry cathode was introduced into system B to permit anodization in the negative glow region. This cathode consisted of a planar 3 turn coil of 1.5 mm diameter 99.999% Al wire mounted on a pyrex tube having a tungsten wire feedthrough, and could be located between the anode and the plane of the sample in the position marked AC in Fig. 7.1. The cathode regions of the discharge extended from both faces of this coil, i.e. towards the sample as well as towards the anode, although no portion of the discharge current flowed to the original hollow cathode which was isolated. The positive column was absent with this arrangement, so that although the sample was surrounded by the negative glow region, its floating potential was only about 7 volts negative with respect to the grounded anode.

The aluminum sample was anodized at current densities of 0.1 to 1.5 mA/cm² and temperatures of 40°C and 70°C with a reduced discharge current of 20 mA (to decrease the possible sputtering from the cathode) and pressure of 100 mtorr. The results of ellipsometry measurements made at the end of each formation are shown in Fig. 10.8. These measurements were made in two zones with the calibrated Soleil Babinet compensator as quarter wave plate, and were corrected for window errors as indicated in section 7.2.3(d). The solid curve was fitted to the points using the program by Dell'Oca 1969 suitably modified to deal with sharply

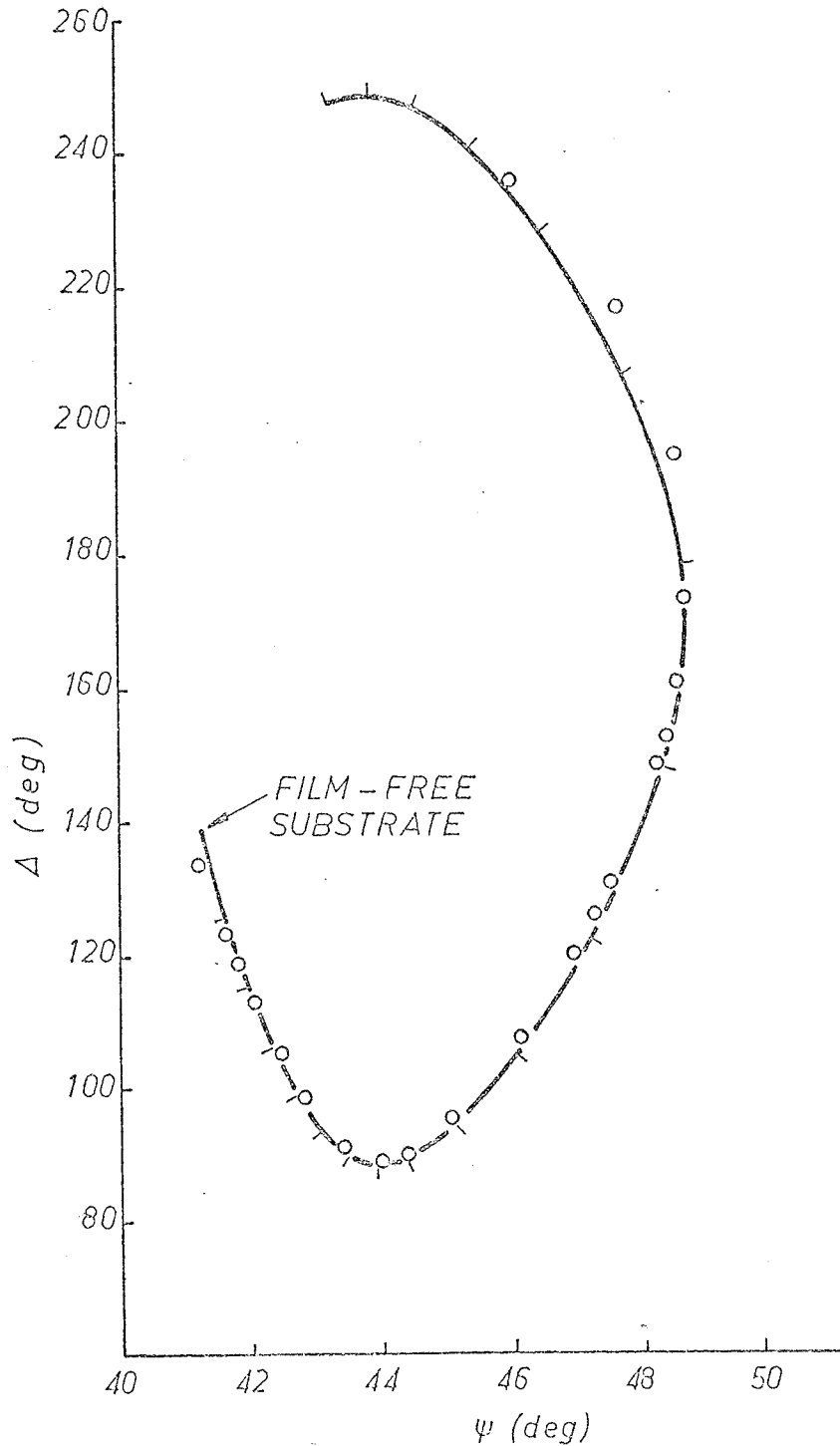


Fig. 10.8 Ellipsometry data for the anodization of evaporated aluminum (sample A11) in the negative glow of system B. Solid curve is for single oxide film, $N_1 = 1.45$, growing on substrate of index $N_2 = 1.22-6.17j$, $\theta_0 = 69.29^\circ$, $\lambda = 6328\text{\AA}$. Markers on curve are 100Å film thickness increments.

turning closed loops, and the model arrived at was a single non-absorbing oxide film of refractive index 1.45 on a substrate of index 1.22 - 6.17j. While other investigators (Waxman and Zaininger 1968, Locker and Skolnick 1968) have evaluated the refractive index of plasma-anodized alumina, their results (1.68, 1.75 respectively) pertained to a wavelength of 5461\AA . The values quoted here may be compared with 1.65 for anodic Al_2O_3 grown in ammonium pentaborate (Goldstein et al. 1970), 1.58 for sputtered Al_2O_3 (Ruiz-Urbeita et al. 1971) and 1.21 - 6.93j for evaporated annealed aluminum (Hass and Waylonis 1961), all at 6328\AA .

Mean growth rates obtained from the above fit were converted to ionic current densities by assuming an oxide density of 3.1 gm/cm^3 as for wet anodic Al_2O_3 (Young 1961) and are shown plotted against oxide field strength in Fig. 10.9. The fields were estimated according to Eqn. 10.1, which was considered to be a reasonable approximation since the (possibly erroneous) correction voltage across the $\sim 10\text{\AA}$ of thermal oxide would be small compared with $(V_s - V_u)_I$. The solid lines in Fig. 10.9 were calculated from the relation given by Harkness and Young 1966 for the aqueous solution anodization of bulk aluminum, and it can be seen that there is good agreement at both temperatures. The improved agreement over the data for tantalum or niobium may be a consequence of a number of possible factors, e.g. a greatly decreased uv effect in the negative glow region, or more accurate field measurements resulting from (a) a smaller space charge effect in Al_2O_3 , as evidenced by linear V_{sp} versus time plots, and/or (b) reduced potential drops in the plasma with the annular cathode arrangement.

In order to investigate the effect of the different sample temperatures usually obtained in different types of discharge, a silicon sample was anodized in system B (positive column) at several temperatures

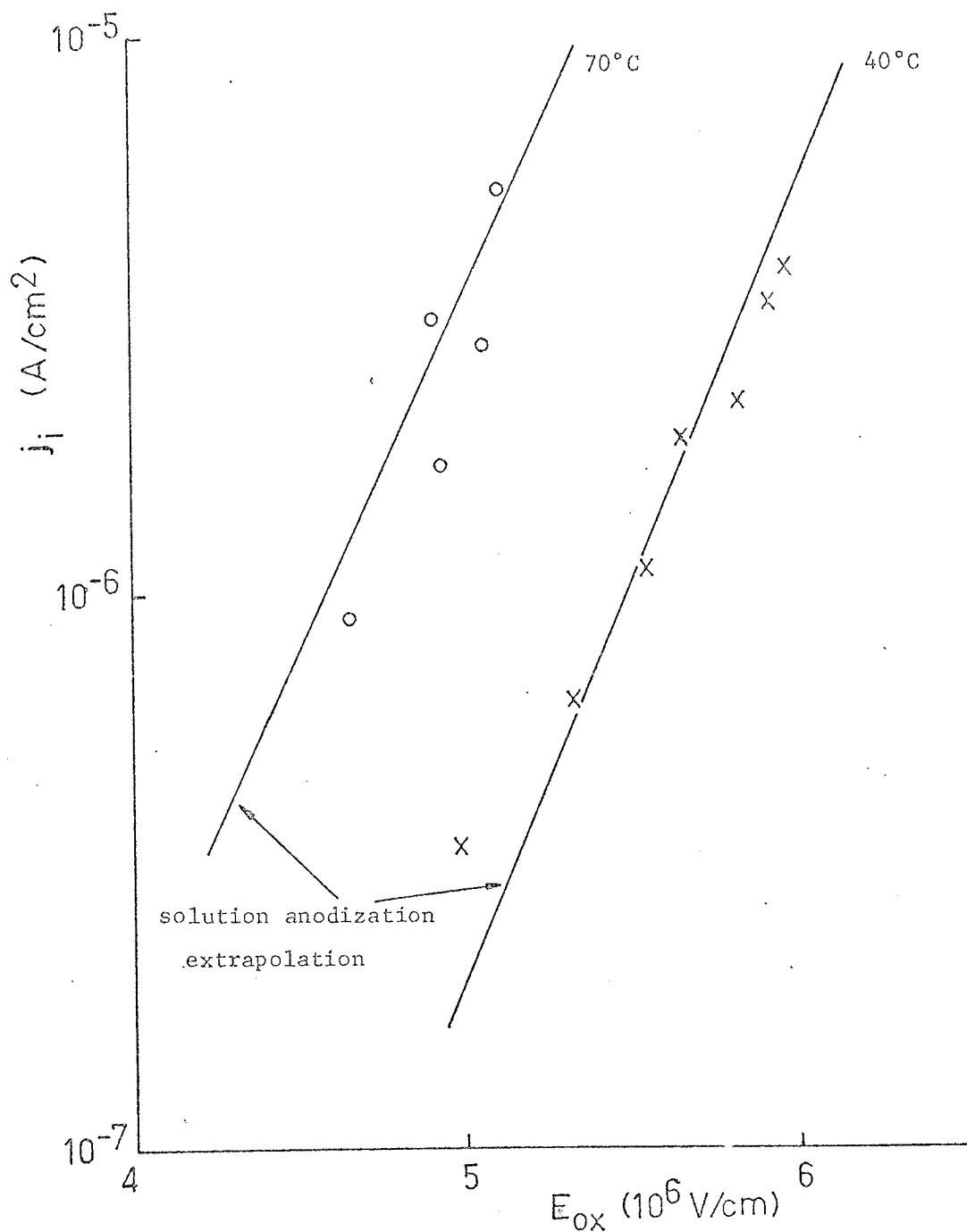


Fig. 10.9 Ionic current densities and estimated oxide fields for the anodization of sample All (negative glow, system B) at 40°C(x) and 70°C(o). The solid lines are calculated for these temperatures from a relation given for solution anodization of bulk aluminum (Harkness and Young 1966).

for comparison with growth rate data for the anodization of silicon in an rf excited plasma (Hathorn, Pulfrey and Young, unpublished). The 1.8 cm square sample was cut from one of several 1-1/4" diameter n-type (phosphorus dopant) wafers with resistivities in the range 3 to 6 Ωcm purchased from the Monsanto Company. These wafers had received a chemical-mechanical polish ('Syton') on one face. To make an ohmic contact to the wafer, the latter was first cleaned in a 20% by volume HF etch (1 volume 49% HF in 5 vols. distilled H_2O) for 1 minute, rinsed in distilled water and blown dry with nitrogen gas. Then a $\sim 3000\text{\AA}$ layer of Au + 0.1% Sb alloy was deposited on the back surface by vacuum evaporation from a molybdenum boat, and the gold layer was alloyed to the silicon by heating the wafer to 425°C for 5 minutes in a stream of dry nitrogen. The sample was mounted on the sample holder with the mica mask in place, and was anodized in the positive column at a pressure of 100 mtorr with sample temperatures of 30, 50, 70 and 80°C using values of sample current I_s from 0.2 to 0.8 mA, and a discharge current I_d of 40 mA. At constant I_d and I_s the oxide growth rates increased with temperature as shown in Fig. 10.10. For various values of I_s , straight lines have been drawn through the points and extrapolated to higher temperatures, where three growth rates for the anodization of silicon in the rf system are shown. Since I_s is predominantly electronic the straight line extrapolation, implying a temperature-independent oxide field term in the ionic current activation energy, is only justified if the electronic current-field relation in the oxide has a very small temperature dependence. Furthermore, the oxide field required for a given total current to be drawn through the oxide from the plasma might be expected to depend on the energy distribution of the electrons reaching the oxide surface as discussed in

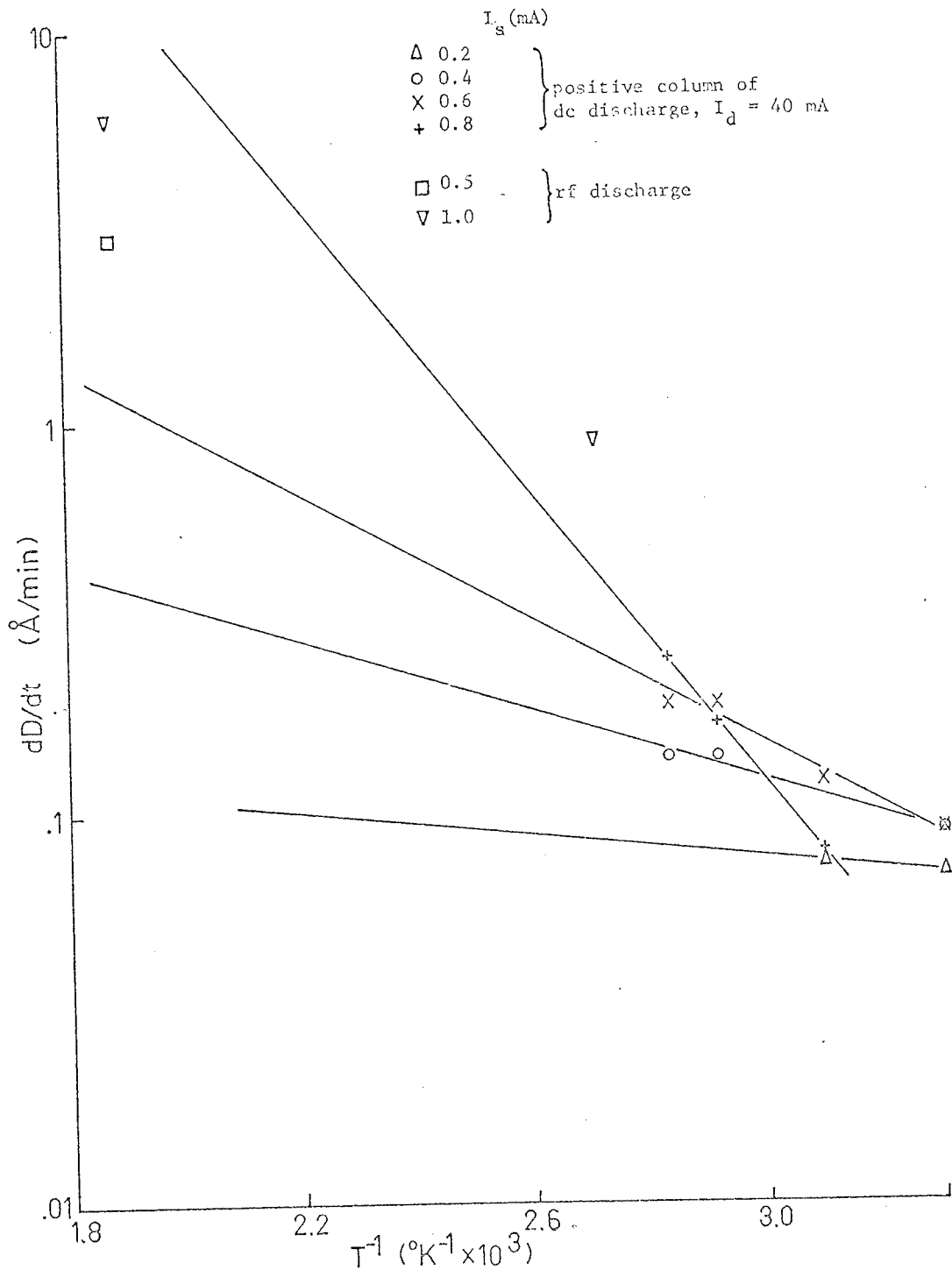


Fig. 10.10 Rates of anodization of silicon (sample Si1) at various temperatures in the dc and rf discharges.

section 8.4. Nevertheless, as can be seen from Fig. 10.10, oxide growth rates obtained in the rf-induced plasma with higher sample temperatures are in the general region of extrapolation from the lower temperature dc plasma data, which tends to support thermally activated high field ionic transport as a growth-rate-determining process with both plasmas, and partially explains the higher growth rates in rf plasmas (see also section 8.4). Mikhalkin and Odynets 1971 and Makara et al. 1971 have recently published Tafel plots for the anodization of tantalum and niobium respectively in an rf induced discharge which have good linearity at several temperatures as in Fig. 10.9 and are reported to be independent of discharge conditions, although the parameters varied were not given.

10.8 Discussion

The possibility that across-the-sheath transport of negative ions could give rise to the observed exponential dependence of growth rate on field through an electronic current-field relationship (as outlined in section 4.3) appears to have been eliminated by the results of section 9.3. Thus, the results presented above suggest that in the case of dc discharge anodization the growth mechanism is basically the same as in solution anodization, but with limitations on the oxide field strengths involved due to the energy spread of plasma electrons, and with more or less pronounced modifications due to the different nature of the oxide-electrolyte interface. These modifications may be produced by uv irradiation as already mentioned, or alternatively by random bombardment of high-energy particles. It appears that the thermally activated high field ionic conduction mechanism is operative in rf-discharge anodization also, with sample temperatures having the appropriate effect on the growth rates, but the data as presently exist do not permit a generalization of

this conclusion to all types of discharge used in plasma anodization.

The oxide lifting phenomenon observed on niobium and tantalum samples anodized in the positive column of system B is of considerable interest. It constitutes evidence for both a plane of weakness and a compressive stress in the oxide film. The former is most probably associated with the sample surface preparation treatment, as it is known that adhesion of anodic oxides is affected by the preexisting film produced by chemical polishing. The cause of the compressive stress which produces the lifting of the oxide away from the substrate is of more general significance. It is sometimes stated that if an oxide film occupies more volume than the metal used in its growth, then it will be under compressive stress. This statement strictly only holds for growth on a convex surface and where the new oxide is produced at the oxide-metal interface. Vermilyea 1963 found a tensile stress in anodic oxides formed on tantalum and niobium in aqueous solutions. A localized compressive stress could arise during anodization from the smoothing out of asperities in the metal surface (Young 1961). However the compressive stress involved in the present effect may not develop until the film is exposed to water vapour, as is the case with evaporated SiO films. For instance, Holland et al. 1960 found that SiO films deposited rapidly at low pressure ($<5 \times 10^{-5}$ torr) tend to be deficient in oxygen and are initially under tension which changes to compression as they absorb gas when exposed to the atmosphere. Priest et al. 1963 found this effect to be accentuated when the evaporation was at other than normal incidence and they observed buckling of the SiO film from its substrate within a few minutes of exposure to air. As in this study the effect was attributed to the absorption of water vapour, since no stress change

was measured for exposure to dry nitrogen at atmospheric pressure.

It is possible then that the plasma-anodized oxide may be unstressed after formation, but have a high porosity to water similar to photo-grown anodic oxides. On exposure to air this high porosity permits extensive hydration of the oxide with a resulting compressive stress. This mechanism is the converse of one proposed by Vermilyea 1963 to explain his observations on stress in anodic oxides. He suggested that oxides formed with aqueous electrolytes are initially hydrated, but that dehydration occurs by proton migration during continued anodization and produces the observed tensile stress.

It should be mentioned that marked mechanical instability has also been observed in plasma-anodized silicon oxide films produced under certain conditions in an rf plasma (Pulfrey and Reche, unpublished) and in plasma-anodized alumina (Morgan 1971), although water vapour was not implicated in these examples.

11. THE PRODUCTION OF DIELECTRIC FILMS FOR METAL-INSULATOR-SEMICONDUCTOR DEVICES

11.1 Introduction

One of the most important potential applications of plasma anodization is the production of thin dielectric films for the gate insulator in active solid state devices such as the metal-oxide-semiconductor field effect transistor (MOSFET or MOST).

Thermally grown silicon dioxide has been used almost exclusively in monolithic silicon technology, because of its well understood properties and its generally good compatibility and satisfactory interface with silicon, but it does not meet all of the requirements for this application. These requirements are outlined below with a consideration of possible alternative materials, followed by a review of current investigations in this area.

Plasma anodization appears to be particularly well suited to the fabrication of double insulator layer field effect devices for memory applications similar to the metal-nitride-oxide-silicon (MNOS) transistor (Wallmark and Scott 1969). These devices utilize the storage of charge at the interface between a thin SiO_2 layer (adjacent to the silicon) and a thicker outer layer of higher permittivity dielectric such as silicon nitride. The present devices require rather large write/erase voltages on account of the oxide-nitride permittivity ratio and the minimum pin-hole free nitride thickness which can be employed, so that the use of an outer layer insulator of higher permittivity than silicon nitride is desirable, as is closer control over the insulator film thickness. Such double insulator structures may be produced by

first vacuum-depositing an appropriate layer of the chosen metal (e.g. Al) on the silicon substrate and then plasma anodizing such that the metal is completely converted to oxide and the desired intermediate* layer of SiO_2 is produced. However, the success of this approach depends on the uniformity of and accuracy with which the intermediate layer thickness can be controlled, and an experimental investigation of this problem was undertaken. The production of double insulator structures in two separate stages (thermal oxidation and/or plasma anodization) has been investigated recently by Pappu 1972.

11.2 Dielectric Materials for Gate Insulation

The operation and characteristics of metal-insulator-semiconductor devices are very sensitive to the properties of the insulator film. This leads to a set of basic requirements for the film material (Zaininger and Wang 1969), some of the most important of which are:

- (a) Acceptable interface with the semiconductor - low surface state density
- (b) High dielectric strength
- (c) High permittivity
- (d) Low dielectric losses
- (e) Impermeability to impurities
- (f) Special requirements such as radiation resistance for satellite circuitry.

*

It is possible that the SiO_2 layer might be produced at the outer surface of the Al_2O_3 , by field-assisted migration of Si ions through the Al_2O_3 rather than oxygen ions through the Al_2O_3 to the substrate. Evidence of enhanced mobility of silicon has been provided recently by helium ion back-scattering measurements on heat-treated layers of gold on silicon (Hiraki et al. 1972).

Requirement (a) is of paramount importance, as surface states can seriously degrade the operation and characteristics of MOS transistors in the areas of leakage currents, noise, frequency response and current amplification. Needless to say it does not apply to an outer oxide film in double insulator layer FET's. The use of materials with similar dielectric strength but higher permittivity than SiO_2 would be advantageous in providing lower threshold voltages and increased transconductance for the same voltage ratings. This can be seen from the way that the gate insulator capacitance per unit area C_i enters the following expressions for an idealized n-channel enhancement transistor (Sze 1969):

$$\text{threshold voltage } V_T = 2\psi_B + \frac{[2\epsilon_s q N_A (2\psi_B)]^{1/2}}{C_i}$$

and saturation transconductance

$$g_m \triangleq \left. \frac{\partial I_D}{\partial V_G} \right|_{V_D = \text{const}} = \frac{w}{\ell} \mu C_i (V_G - V_T)$$

where w and ℓ are the width and length of the channel, μ is the channel carrier (electron) mobility, V_G is the gate voltage, ψ_B the potential difference between the Fermi and intrinsic Fermi levels of the semiconductor, ϵ_s its permittivity, and N_A the acceptor dopant concentration.

In choosing dielectric materials, an examination by Harrop and Campbell 1968 of the periodic table and the dielectric properties of various metal oxides indicates oxides of the groups Ti, Zr and Hf; V, Nb and Ta; Cr, Mo and W to be of interest for high permittivity. These authors suggest that oxides having a higher mean atomic number per molecule generally have higher permittivities but also higher losses and lower breakdown fields. However, there are some exceptions, for instance

wet anodized Ta_2O_5 has quite acceptable losses (<1%), and TiO_2 can have a high value of relative permittivity (up to 80 in thin film form - Feuer-sanger 1964). Titanium having the same valency as Si, TiO_2 might be expected to give an interface with the silicon lattice similar to that of SiO_2 . A factor in favour of Ta among the valve metals is that Ta- Ta_2O_5 thin film technology is well established, and the use of plasma-anodized Ta_2O_5 as a gate insulator should facilitate the fabrication of integrated circuits comprising thin film passive and active devices.

11.3 Brief Review of Recent Work on Metal Oxide Thin Films Useful for Gate Insulation

Apart from silicon nitride, alumina has perhaps received the most attention as an alternative to SiO_2 . Salama 1970 found alumina films deposited on silicon by rf sputtering to give a surface charge density less than 10^{11} charges/cm² after annealing but to have a charge trapping instability. Alumina produced by plasma anodization has enabled the fabrication of MOS transistors with improved performance in the area of radiation resistance (Micheletti et al. 1970). MOS transistors fabricated with reactively sputtered TiO_2 have been reported (Wakefield and Gamble 1970), and while the devices showed increased transconductance, the increase was not as great as expected, due perhaps to the influence of the TiO_2 -Si interface on the carrier mobility in the enhanced n-channel. TiO_2 films have been deposited on silicon by chemical vapour deposition (Wang et al. 1970), but they had excessively high conductance, oxide charge and interface state density. Zirconium has been plasma-anodized (Ramasubramanian 1970), but the oxide properties were not given. Some work has also been performed on plasma-anodized HfO_2 , and C(V)

measurements on MIS capacitor structures demonstrated the modulation of semiconductor surface potential (Norris and Zaininger 1970).

Nb_2O_5 and Ta_2O_5 films deposited on silicon by chemical vapour deposition (Wang et al. 1970) were found to have a low interface state density and oxide charge, and their radiation resistance was better than that of thermal SiO_2 , but they were not effective barriers against ionic impurities. As mentioned earlier, Lee et al. 1970 found the permittivities of plasma-anodized Nb_2O_5 and Ta_2O_5 films produced on the bulk metals to be 34 and 17 respectively, and the loss factors were about 1%. Similar values were reported by Jennings and McNeill 1969 for Ta_2O_5 obtained using an ion cathode. Vratny 1967 prepared both plasma-anodized and reactively sputtered films of Ta_2O_5 . The dielectric strengths were lower and losses higher than for wet anodic Ta_2O_5 , but it is possible that his plasma-anodized films also contained reactively sputtered Ta_2O_5 as pointed out by O'Hanlon 1970.

Of the group $\overline{\text{VIA}}$ metals, chromium was plasma-anodized in the early work of Miles and Smith 1963, but no properties of the oxide were given, and molybdenum has also been investigated (O'Hanlon 1970) but no details are available.

Recently bulk Ti, Zr, V, Nb, Ta and W have been anodized by the ion cathode method (Husted et al. 1971), and the resulting oxides had loss factors in the range 1% to 6%. Permittivities were given for Nb_2O_5 and Ta_2O_5 only (28 and 22 respectively), and breakdown fields were not evaluated.

11.4 Plasma Anodization of Metal Films on Silicon

11.4.1 Introduction

The anodization of a metal film coated on a silicon substrate

may be used to fabricate a gate insulation layer for FET's. However, as has been pointed out by Norris and Zaininger 1970, for the simple MOS transistor structure it is essential that the anodization be terminated as soon as the metal layer has been completely converted to oxide, since the growth of an anodic SiO_2 layer on the silicon would introduce intolerable hysteresis effects due to charge trapping. On the other hand, the production of a controlled thickness of SiO_2 is essential to the fabrication of the memory type device. Thus, the monitoring of the oxide film thickness is of considerable importance^{*}, and it was decided to study the anodization of metal films on silicon substrates with the automated ellipsometer, in combination with in situ measurement of the small signal ac differential capacitance of the anodized film - silicon system as a function of dc bias. This latter measurement is sensitive to the conditions at the silicon surface, as will be shown below. The metals chosen for initial examination were Al and Ta - the first because it can be deposited with ease in thin film form by vacuum evaporation, and the second because of its present application in microelectronics.

11.4.2 Ellipsometric considerations

Computations were undertaken to evaluate the expected form and thickness sensitivity of the $\Delta - \psi$ ellipsometry curve traced out as a metal layer of appropriate thickness is converted to its oxide, and then as the silicon surface anodizes to give an increasing thickness of SiO_2 beneath the now constant thickness of metal oxide. The sensitivity of the ellipsometric measurement to film thickness varies considerably with thickness, being highest in the region of the $\Delta - \psi$ curve where ψ

* The sample voltage versus time plot cannot be expected to reveal the metal consumption point since the growth of SiO_2 rather than the metal oxide, say Al_2O_3 , would cause only a gradual change of the slope dV/dt from that typical of Al_2O_3 towards that typical of SiO_2 .

is a maximum. Referring to Fig. 10.8, this is seen to correspond to about 1250Å of Al_2O_3 on aluminum. The ratio of alumina thickness $t_{\text{Al}_2\text{O}_3}$ produced to aluminum thickness t_{Al} consumed is given by

$$\frac{t_{\text{Al}_2\text{O}_3}}{t_{\text{Al}}} = \frac{W_{\text{Al}_2\text{O}_3}}{2W_{\text{Al}}} \cdot \frac{\rho_{\text{Al}}}{\rho_{\text{Al}_2\text{O}_3}}$$

where W and ρ are molecular weight and film density respectively and the oxide is assumed stoichiometric. Using the density of solution anodic Al_2O_3 (3.1 gm/cm³, Young 1961) and a value of 2.58 gm/cm³ for the density of thin film aluminum (Hartman 1965) gives $t_{\text{Al}_2\text{O}_3}/t_{\text{Al}} = 1.57$ so that ~800Å of aluminum should produce ~1250Å of Al_2O_3 . The theoretical ellipsometry curve for the conversion of 800Å of Al to 1250Å of Al_2O_3 on a silicon substrate and the subsequent growth of an SiO_2 layer is shown in Fig. 11.1. The refractive indices at 6328Å used for the various media were as follows: 3.87 - 0.017j for silicon (imaginary part from Phillip and Taft 1960, real part from data obtained in the silicon anodization reported in section 10.7), 1.47 for SiO_2 (section 10.7), 1.21 - 6.93j for Al (Hass and Waylonis 1961) and 1.45 for Al_2O_3 (from Fig. 10.8). On comparing this figure with Fig. 10.8, the normal infinite Al substrate curve is seen to be 'peeled open' as the optical properties of the silicon substrate become dominant via the increasing transmittance of the diminishing metal film. The point at which the last of the metal is finally consumed and anodization of the silicon commences is clearly identifiable as a very sharp local minimum in Δ and ψ . This turning point, together with the high sensitivity to film thickness on each side of the point, demonstrate that ellipsometry is potentially useful as a monitor of this critical stage of the process, despite statements to the contrary (Norris and Zaininger 1970). In the case

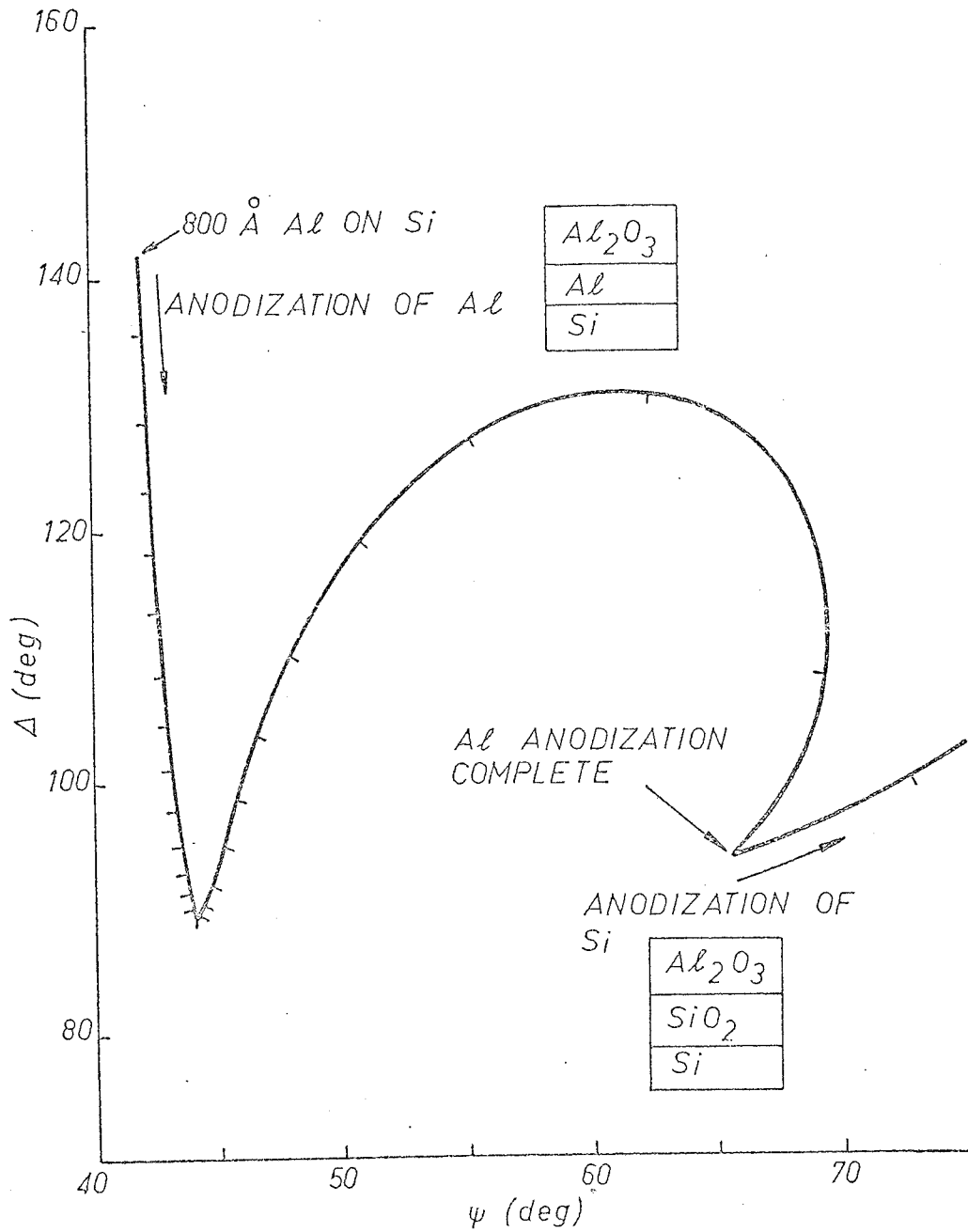


Fig. 11.1 Computed ellipsometry curve for the anodization of an 800Å evaporated aluminum film ($N_2 = 1.21 - 6.93j$) on silicon ($N_3 = 3.87 - 0.017j$) to 1280Å of Al_2O_3 ($N_1 = 1.45$) and the subsequent growth of an intermediate film of SiO_2 ($N_2 = 1.47$), $\theta_0 = 70^\circ$, $\lambda = 6328\text{Å}$. Markers on curve are 50Å increments of Al_2O_3 or SiO_2 .

of tantalum, however, the sensitivity to the point of total metal conversion is very much inferior. Using 15.6 and 8.0 gm/cm³ for the densities of Ta and anodic Ta₂O₅ respectively gives the ratio $t_{\text{Ta}_2\text{O}_5}/t_{\text{Ta}} = 2.38$, and Fig. 11.2 shows a calculated ellipsometry curve for the conversion of 450Å of sputtered Ta to 1071Å of Ta₂O₅ and the subsequent growth of an SiO₂ layer. The value of 450Å was the lowest Ta film thickness among some sputtered Ta on Si samples made available by Microsystems International Ltd., and the refractive index of 2.99-2.82j used for the tantalum was determined from a fit to experimental ellipsometry data obtained during the solution anodization of a similar sputtered tantalum layer (see section 8.3.1). The value of 1.85 for the refractive index of plasma-grown Ta₂O₅ was taken from section 10.6. The point at which all the tantalum is just consumed and silicon anodization commences is only a slight indentation on an otherwise smooth curve. The lack of sensitivity relative to the aluminum case is principally a consequence of the lower optical absorption of the tantalum (although the indentation is somewhat more marked for a lower initial tantalum thickness), and for this reason the experimental investigation was concentrated on the use of aluminum.

11.4.3 C(V) measurements

The measurement of the capacitance of MIS structures as a function of bias is presently the principal tool for the investigation of silicon surface phenomena (Gray 1969), and such measurements at frequencies of 100 kHz or 1 MHz can be made conveniently by using a Boonton capacitance meter. For in situ measurements on samples in the anodization cell, a probe assembly was fabricated which enabled an electrode to be brought into intimate contact with the outer surface of the anodic oxide. Three cases can be anticipated as anodization of the aluminum-on-silicon sample progresses:

- (a) For the case where the Al layer is continuous over the silicon, the capacitance measured will be that of the probe through the Al₂O₃ to this layer, since the series capacitance of the

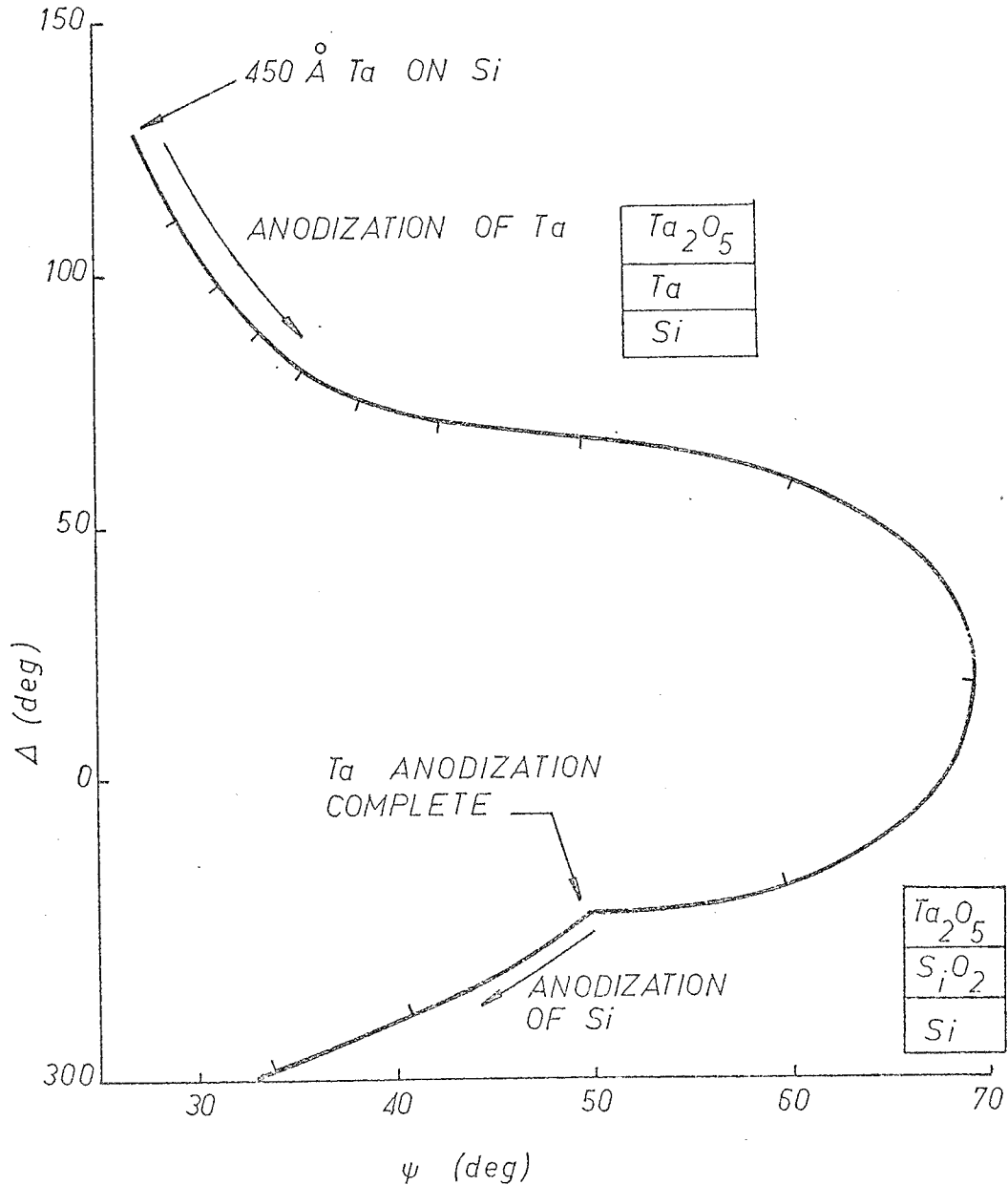


Fig. 11.2 Computed ellipsometry curve for the anodization of a 450Å sputtered tantalum film ($N_2 = 2.99 - 2.82j$) on silicon ($N_3 = 3.87 - 0.017j$) to 1071Å of Ta₂O₅ ($N_1 = 1.85$) and the subsequent growth of an intermediate film of SiO₂ ($N_2 = 1.47$), $\theta_0 = 70^\circ$, $\lambda = 6328\text{Å}$. Markers on curve are 100Å increments of Ta₂O₅ or SiO₂.

large area Al-Si junction will be much larger by comparison. This Al_2O_3 capacitor is not expected to be voltage variable.

- (b) For the case where the metal layer has just been consumed, the structure will comprise a single insulator layer MIS capacitor and the usual high frequency $C(V)$ curve typical of such structures should be observed (with deviations from the ideal curve due to work function differences, oxide charge and surface states). The theoretical basis for the analysis of such curves is fully discussed by Sze 1969. Briefly the ideal form of the high frequency $C(V)$ curve, shown in Fig. 11.3 for an n-type substrate, can be understood as follows:

If the metal contact is biased positively with respect to the n-type silicon substrate then electrons will be attracted to the surface to form an accumulation layer, and the measured capacitance is just that of the oxide C_0 which is independent of voltage. An applied negative bias will repel surface electrons resulting in a surface depletion layer having a fixed volume charge density equal to the silicon donor impurity concentration N_D . This layer devoid of free carriers constitutes a capacitance C_D in series with C_0 and reduces the total capacitance C . Biasing more negatively widens the space charge layer, reducing C_D and C until finally a thin layer of minority carrier holes forms at the surface, which is then said to be inverted. Further negative bias will increase the number of holes in the inversion layer but will not widen the space charge layer appreciably, and since the hole concentration is not able to follow the high frequency ac signal the total capacitance C remains constant.

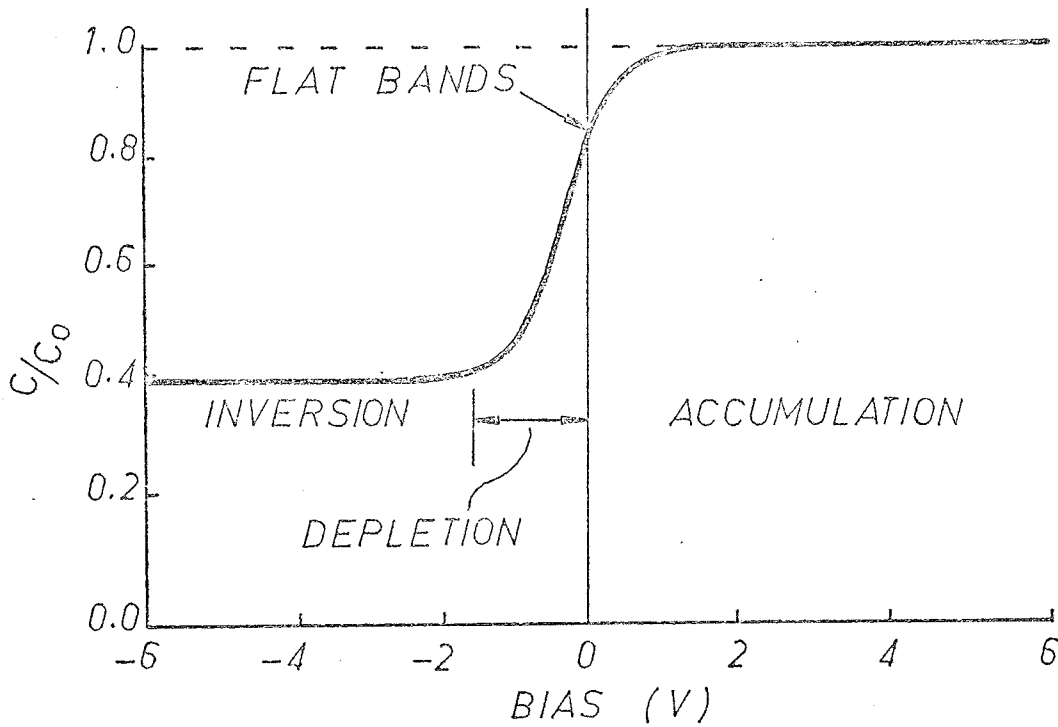


Fig. 11.3 Form of high frequency capacitance-voltage curve for an ideal MIS capacitor (n-type semiconductor).

- (c) After a thin silicon dioxide layer has grown between the Al_2O_3 and the silicon the C(V) curve is expected to show semipermanent storage effects (Wallmark and Scott 1969) or at least very strong hysteresis varying with the bias voltage as charge transfer occurs between the the silicon and states at the $\text{SiO}_2 - \text{Al}_2\text{O}_3$ interface.

11.4.4 Experimental

A sample was prepared by first producing an ohmic contact on the back of a Monsanto 5 Ωcm n-type silicon wafer and then vacuum evaporating 99.999% Al onto the polished front surface as in section 10.7. A shutter was used to control the deposition in conjunction with a quartz crystal oscillator thickness deposit monitor and a suitable film thickness was obtained (705Å as estimated from the final frequency of the monitor after the crystal had cooled down to room temperature). The sample was mounted with the mica mask on the sample holder using a small quantity of conductive silver paint, and ellipsometer readings taken as usual prior to system assembly and pump down for determination of the window correction factor.

The probe fabricated for the in situ capacitance voltage measurements is shown in Fig. 11.4, and consisted of a ~1.5 mm diameter gold ball, sealed when molten onto a .05 mm diameter tungsten wire and having a flattened face. A cushion of indium was pressed onto the face of the ball, which was supported in a countersunk recess in the end of a drilled teflon insert (T) sliding in an aluminum housing. The housing was pressed in an aluminum arm mounted on a pyrex tube (P), with a tungsten feedthrough, that passed through an 'O' ring seal in the anode end cap (A). A micrometer-type barrel (B) threaded

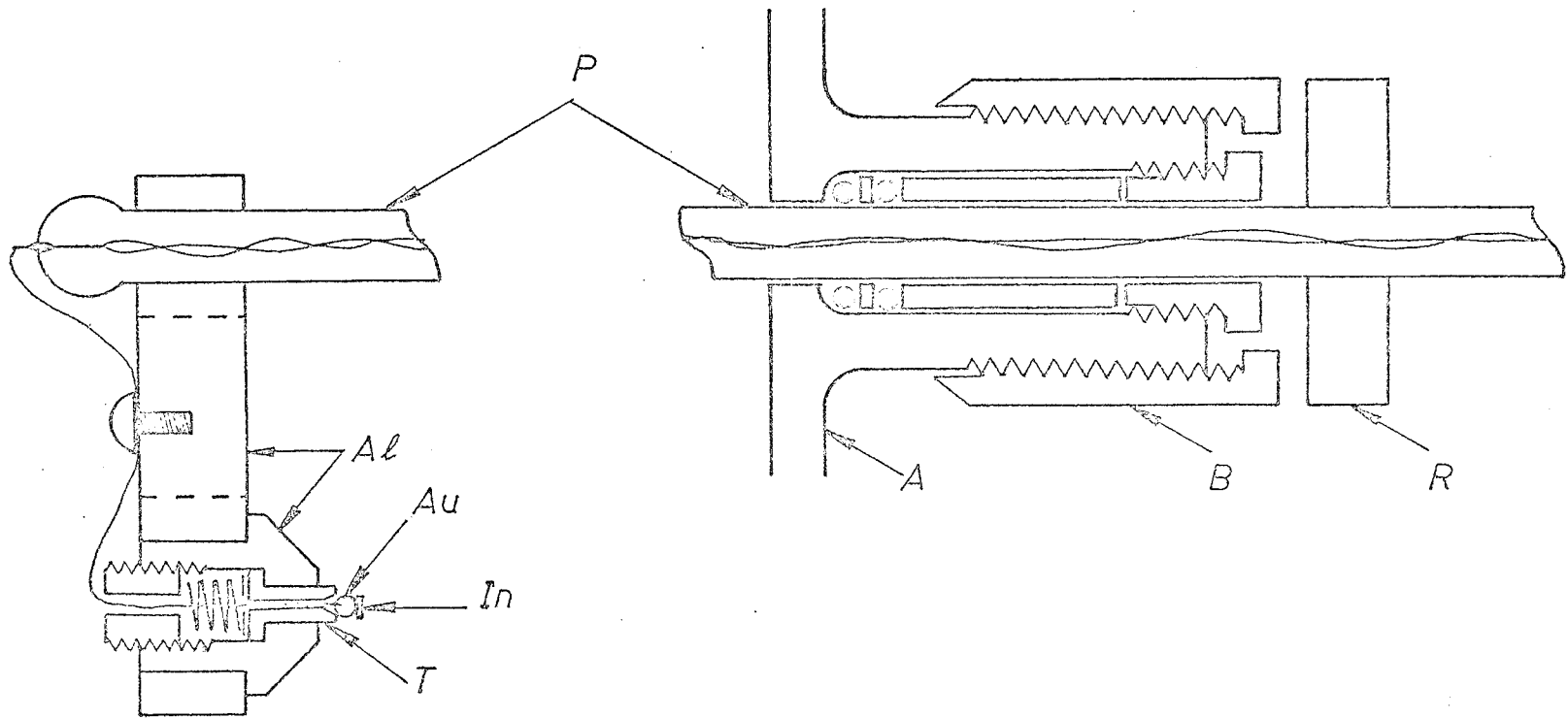


Fig. 11.4 Probe for in situ capacitance measurements.

on the seal housing could be brought to bear on a ring (R) clamped on the tube so that the probe could be brought into contact with the sample surface, and a spring between the teflon insert and a drilled screw served to apply a reproducible load to the indium contact.

Using the annular cathode with a discharge current of 20 mA and oxygen pressure of 100 mtorr, the sample was anodized in the negative glow at current levels from 0.1 to 1.5 mA, and the growth monitored closely by balancing the ellipsometer at one minute intervals. In situ capacitance measurements at 1 MHz were made with a Boonton model 71A capacitance meter after switching the discharge off at certain points. After connecting the probe to the meter high terminal and the sample to the low terminal, the probe was contacted to the oxide and a dc bias or slow ramp voltage was applied across these terminals via the meter circuitry. The meter analog output and the dc bias voltage were also fed to an x-y recorder, and in this way the variation of the probe- Al_2O_3 - Al/SiO_2 -silicon small-signal ac differential capacitance as a function of dc bias could be obtained.

11.4.5 Results

The two-zone-averaged $\Delta - \psi$ values obtained from readings between formations are shown in Fig. 11.5. The solid curve in Fig. 11.5 is the best fit to the experimental $\Delta - \psi$ data which could be obtained, and is for an initial 670\AA of aluminum (of refractive index 1.21-6.80j) giving 1100\AA of Al_2O_3 (of index 1.45 - 0.02j). The tighter loop in this curve compared to that in Fig. 11.1 is a consequence of the smaller starting thickness of aluminum. It is evident that the anodization of the last 70\AA or so of aluminum does not proceed according to the assumed model of a well-defined plane oxide-metal interface moving uniformly towards the silicon surface

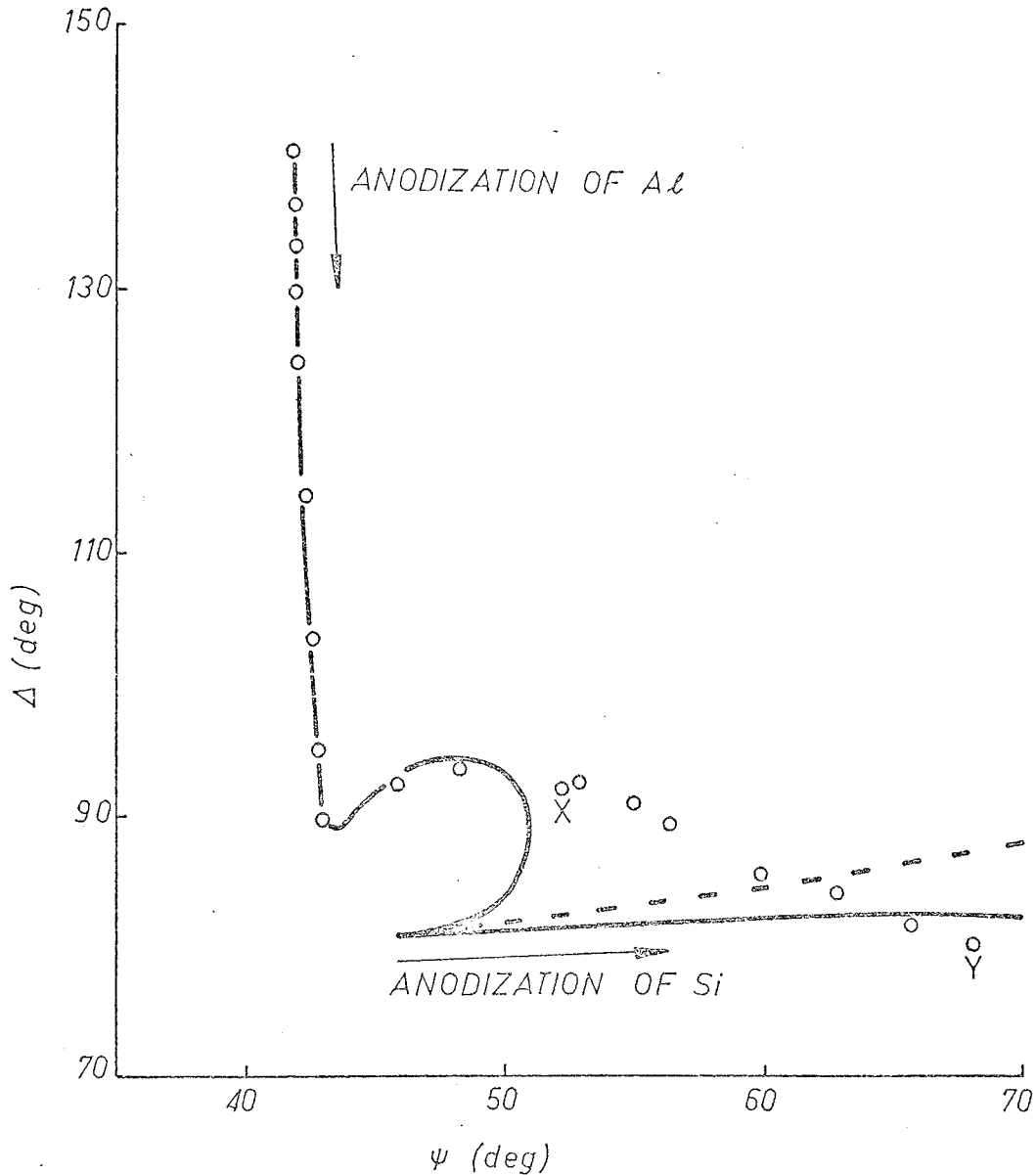


Fig. 11.5 Ellipsometry data for the anodization of an evaporated aluminum film on a silicon substrate (sample Al-Si₁) in the negative glow of system B. Solid curve is for initial 670Å of Al ($N_2 = 1.21 - 6.80j$) forming 1100Å of Al₂O₃ ($N_1 = 1.45 - 0.02j$), on Si ($N_3 = 3.87 - 0.017j$) followed by growth of intermediate film of SiO₂ ($N_2 = 1.47$), $\theta_0 = 69.29^\circ$, $\lambda = 6328\text{Å}$. Broken line is for SiO₂ growth on top of Al₂O₃ layer.

(and parallel to the latter) until the metal layer thickness decreases to zero. Instead there appears to be a gradual transition of the 70\AA layer between the Al_2O_3 and the silicon from a metallic nature to a dielectric nature. This effect could result from the Al_2O_3 -Al interface having a roughness on the scale of 100\AA , such that the Al film eventually becomes discontinuous with a topography similar to a slice of Swiss cheese. The oxide holes would then grow at the expense of the metal until the film becomes islands of aluminum which eventually disappear completely. The 1 mm diameter of the ellipsometer light beam would have an averaging effect on these processes, giving the measured gradual transition. The experimental data between points X and Y in Fig. 11.5 are more consistent with oxygen ion motion producing SiO_2 under the Al_2O_3 layer than with silicon ion motion producing SiO_2 on top of the Al_2O_3 - the broken line shown in the figure is the calculated curve for the latter possibility.

Another possible source of the effect is the thin native oxide present on the silicon surface, which has been ignored in calculating the theoretical curves in Figures 11.1 and 11.5. However, this oxide is expected to be largely 'absorbed' by the highly reactive aluminum when it first arrives from the evaporation source, and cause only a minor change in the optical properties of the aluminum next to the silicon. Even if the oxide persists as an intact layer, it would only move the turning point slightly.

In situ capacitance measurements made at point X in Fig. 11.5 varied only very slightly with dc bias, showing that the Al film was still essentially continuous at this stage, but measurements at point Y gave the characteristic high frequency C(V) curve of an MIS capacitor shown in Fig. 11.6 (curve A). The ~ 40 V spread of the sloping portion

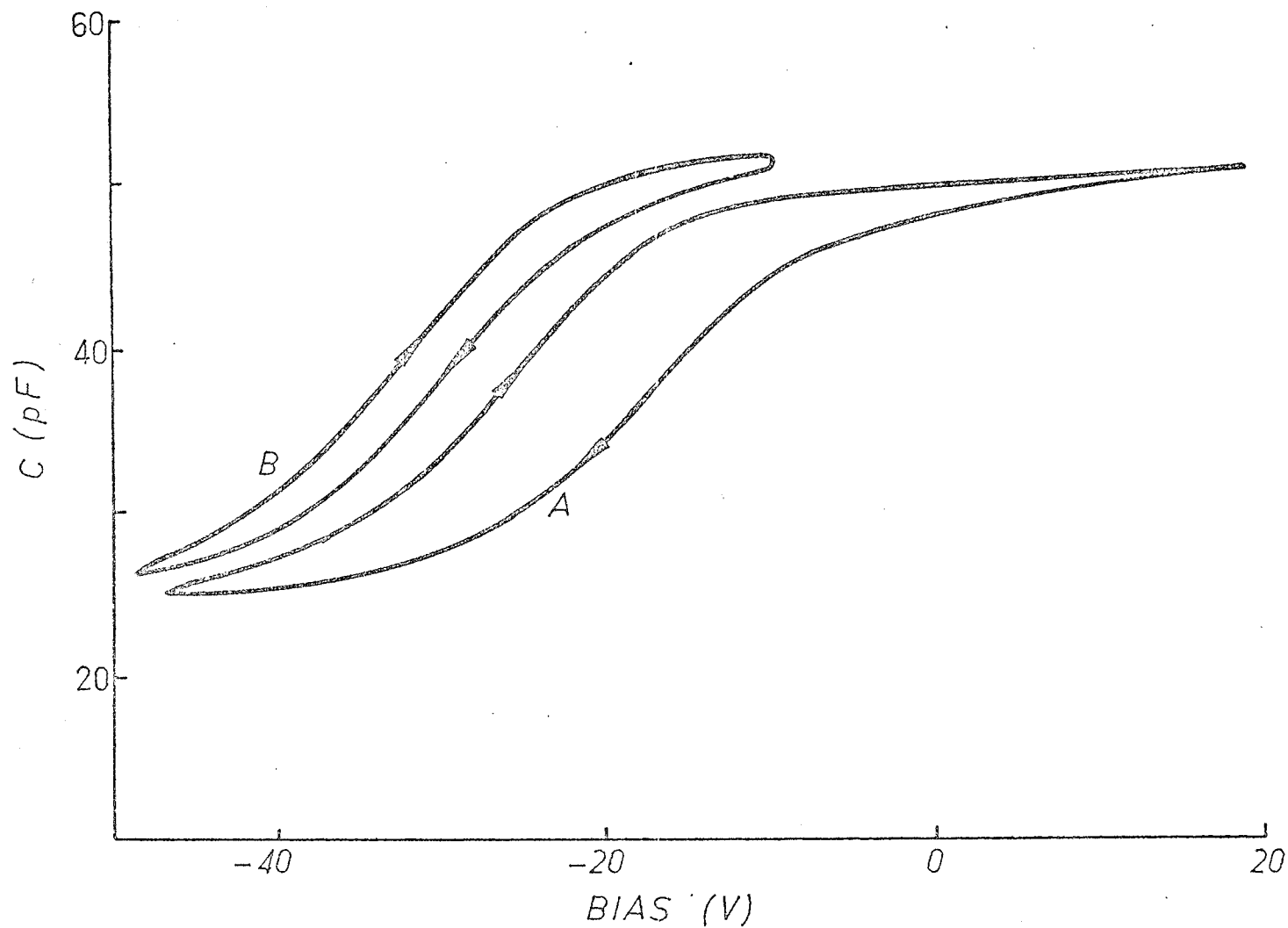


Fig. 11.6 High frequency capacitance-voltage curves obtained in situ at point Y in Fig. 11.5. Curve A: initial, curve B: after application of -50V for 10 secs. to probe electrode.

of the curve indicates the presence of a large number of surface states and the hysteresis is in the direction of trapping of holes from the silicon at sites within the oxide. A more quantitative analysis is not feasible because of the uncertainty in the oxide thickness and indium probe contact area. Evidence of charge storage in the oxide at sites more remote from the silicon surface was suggested by the voltage displacement to curve B which was obtained after applying a bias of -50 V to the probe for 10 seconds (the smaller hysteresis in B is due to the smaller bias sweep amplitude). Curve B relaxed at zero bias towards curve A over a period of several minutes, or it could be returned by application of a positive bias.

In an attempt to ascertain whether the effective nonuniformity in the residual metal layer thickness was a consequence of the anodization process itself, that is, a development of irregularities in the oxide-metal interface as anodization progresses, a sample consisting of only 200Å of Al on Si was prepared in the same manner and anodized under the same conditions as before using currents from 0.1 to 0.8 mA. The ellipsometry results are shown in Fig. 11.7, together with the closest theoretical curve found, which was for 200Å of Al (of refractive index 1.2-6.30j) giving 320Å of Al_2O_3 (of index 1.52-0.02j). The experimental points again show a smoothing out relative to the calculated curve, but over a smaller range and with less deviation from the curve than in Fig. 11.5 so that the degree of nonuniformity may have been less for the shorter anodization. In situ C(V) measurements taken at point X already showed modulation of surface charge in the silicon, but the curves were unstable and not reproducible. Measurements at point Y were more stable, but with some hysteresis. The sample was subsequently removed from the

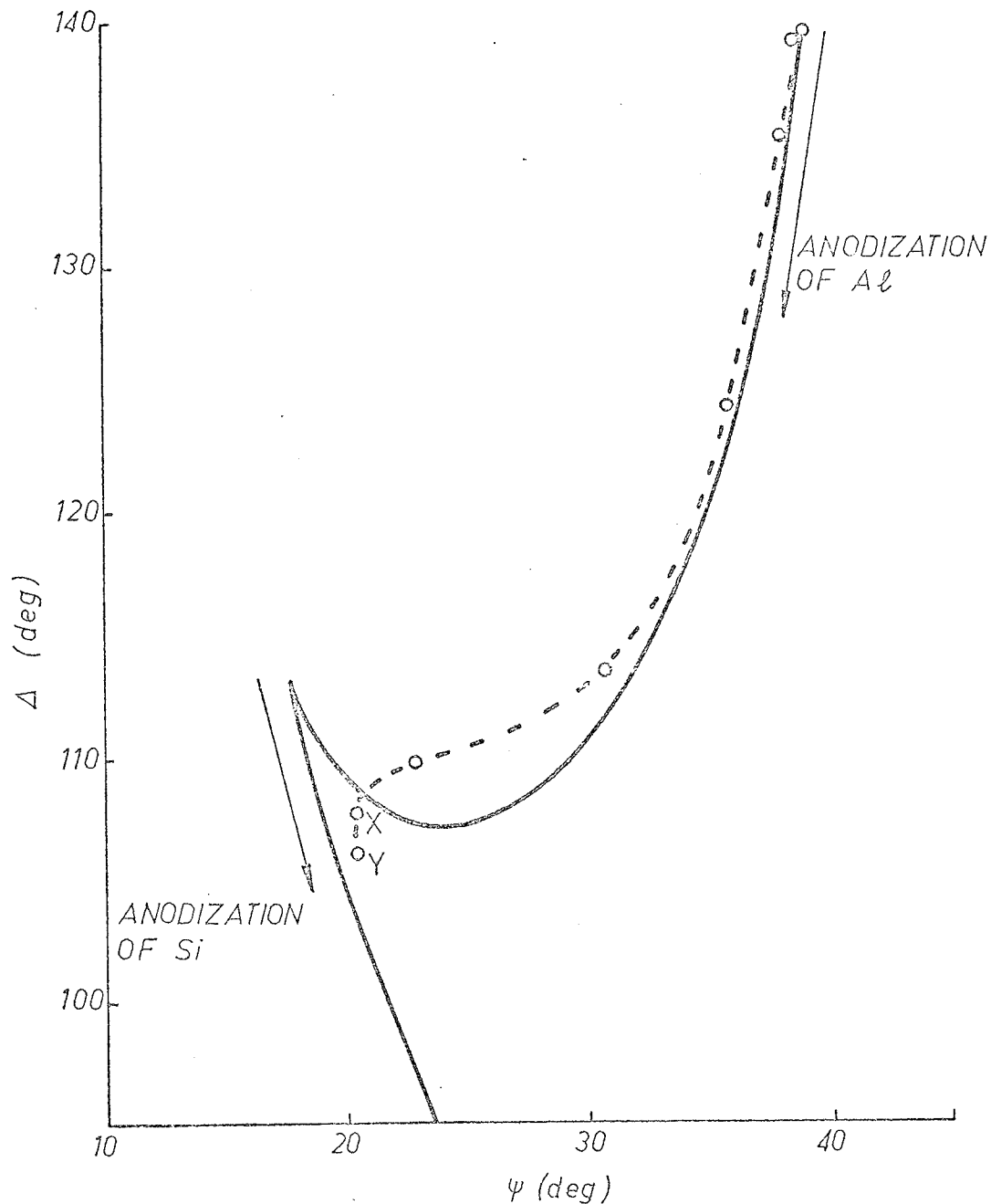


Fig. 11.7 Ellipsometry data for the anodization of a 200Å evaporated aluminum film on silicon (sample Al-Si2, system B, negative glw). Solid curve is for 200Å of Al ($N_2 = 1.21 - 6.30j$) forming 320Å of Al_2O_3 ($1.52 - 0.02j$) followed by growth of intermediate film of SiO_2 ($N_2 = 1.47$), $\theta_0 = 69.29^\circ$, $\lambda = 6328\text{Å}$.

vacuum system and 0.76 mm dia. gold counterelectrodes were deposited over the anodized area. $C(V)$ measurements were made using these electrodes, and also after each of two thermal annealing treatments, namely a 30 minute anneal in nitrogen at 300°C , and a one hour anneal in hydrogen at 350°C . Such treatments are commonly used to reduce interface state densities in MIS structures (Kooi 1966). Figures 11.8 and 11.9 show $C(V)$ curves obtained for two adjacent electrodes before annealing. These curves are steep and have a high ratio of maximum to minimum capacitance, as expected for a thin insulator layer of higher permittivity than SiO_2 . Taking the total anodic oxide to consist of 320\AA of Al_2O_3 and 65\AA of SiO_2 , i.e. the idealized model values close to point Y in Fig. 11.7, and assuming the SiO_2 layer to have a relative permittivity of 3.8 (as for thermal oxide, Sze 1969), the maximum capacitance value (C_0) gives 6.8 for the relative permittivity of the Al_2O_3 . This may be compared with a value of 8 found by Norris and Zaininger 1970. For the MIS diode of Fig. 11.8, the amount of hysteresis was small and relatively independent of the amplitude of the triangular bias sweep. However, by sweeping about a mean level of -3V (Au electrode relative to silicon) the curve could be shifted bodily 2V negative (curve A to curve B). The second diode showed larger hysteresis, which was also dependent on the amplitude of the bias sweep (Fig. 11.9).

The steepness of the curves suggests a low density of interface states (a quantitative estimate of the density could be made by comparison with the ideal curve, but calculation of the latter requires precise knowledge of the oxide thicknesses and permittivities). This is supported by the observation that neither of the annealing procedures produced steeper curves, although the anneal in nitrogen did cause a small (-0.5V)

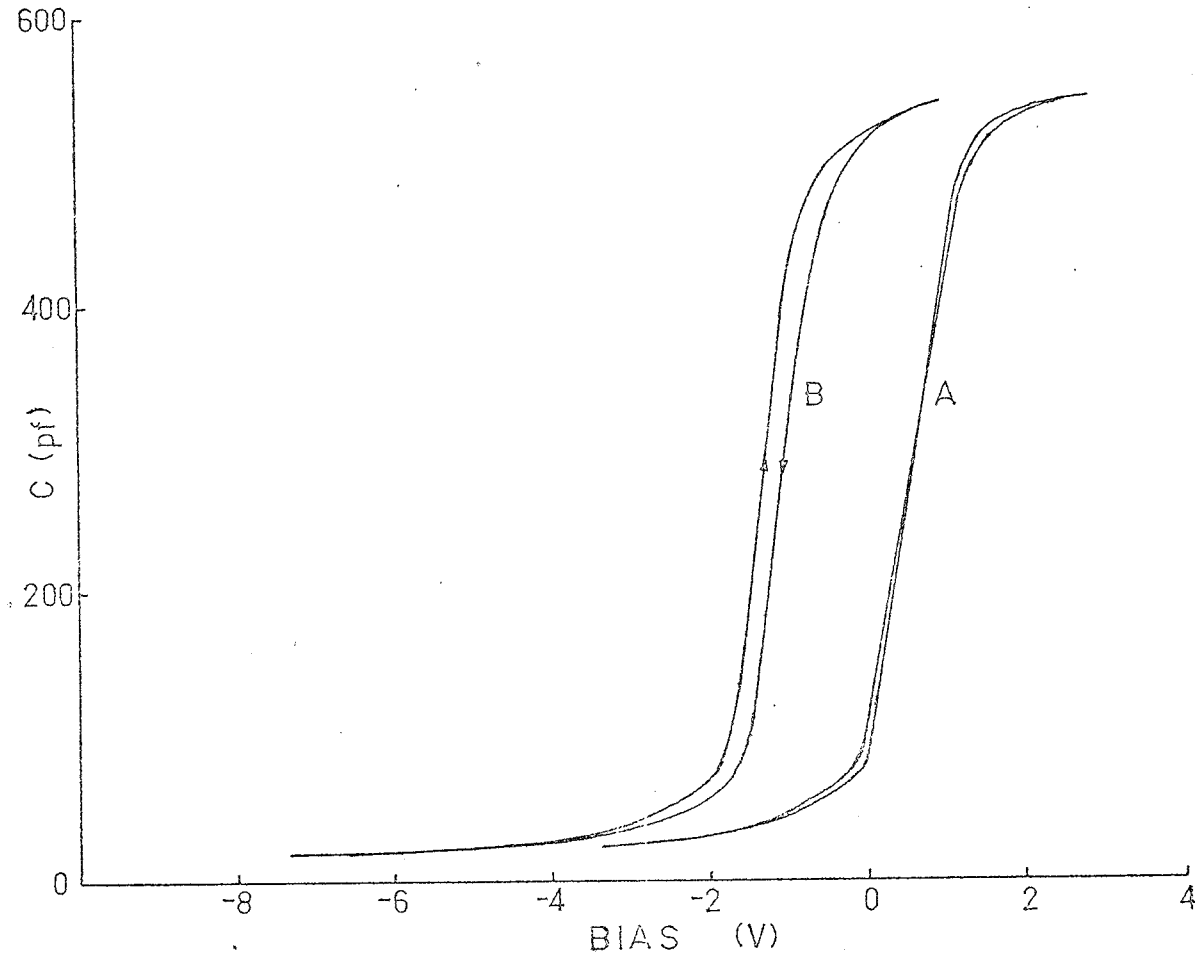


Fig. 11.8 High frequency capacitance-voltage curves for $\text{Al}_2\text{O}_3\text{-SiO}_2\text{-Si}$ sample (Al-Si2) anodized to point Y in Fig. 11.7 obtained with evaporated gold counterelectrode. Curve A: sweeping symmetrically about zero bias, curve B: sweeping about -3V.

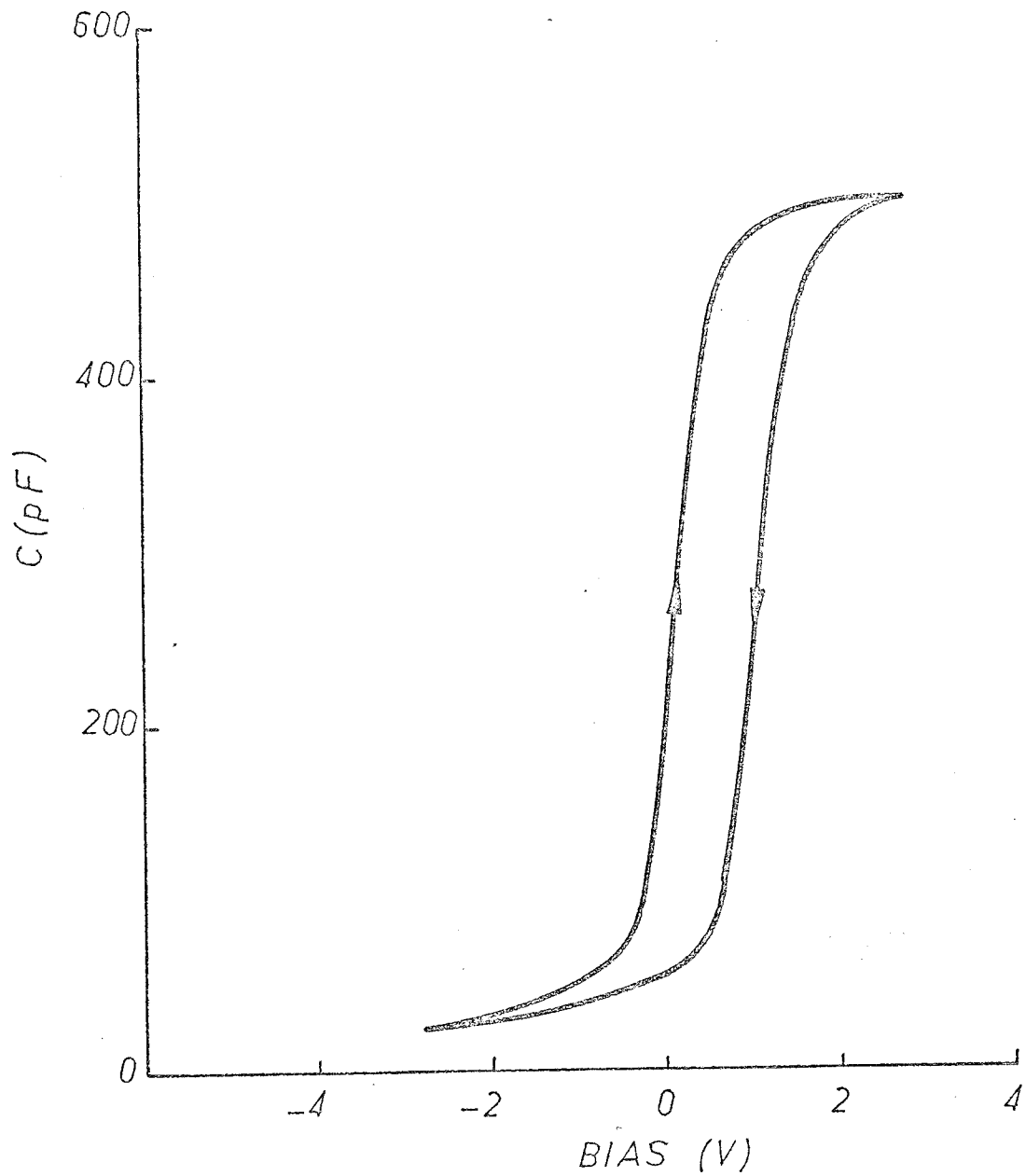


Fig. 11.9 High frequency capacitance-voltage curve for gold electrode on sample Al-Si₂ adjacent to MIS diode of Fig. 11.8, showing larger hysteresis.

shift of the curves in the positive direction. Fig. 11.10 presents $C(V)$ curves taken after the anneal in hydrogen, which show the above shift compared to Figures 11.8 and 11.9 and also the effect of dc bias amplitude on the amount of hysteresis.

While the above measurements did not yield a quantitative measure of the density of interface states at the Al_2O_3 -Si or SiO_2 -Si interface, for the latter case an estimate of surface charge was obtained from $C(V)$ measurements on the plasma-anodized silicon sample referred to in section 10.7. Fig. 11.11 shows a 1 MHz $C(V)$ curve for an evaporated gold counter-electrode on this sample, which had a 700Å thick oxide. Evaluation of the flat-band voltage for this curve and equating this to Q_{ss}/C_0 where Q_{ss} is the surface state charge (neglecting any fixed oxide charge and work-function differences) at flat-bands gives Q_{ss} as 1.4×10^{12} positive charges/cm². This value is similar to those obtained for other thin film dielectrics on silicon (Zaininger and Wang 1969), e.g. 2×10^{12} for Al_2O_3 , 5×10^{11} for Nb_2O_5 and 4×10^{12} for Ta_2O_5 .

11.5 Discussion

The ellipsometry and $C(V)$ results above indicate that for the evaporated aluminum films studied here, the Al- Al_2O_3 interface is non-planar during the final stages of plasma anodization of the metal. This interface roughness, which must be eliminated before satisfactory double insulator layer devices can be fabricated, may originate in several ways. A native SiO_2 layer is expected to have a small effect as mentioned above. The roughness appeared to be larger for the more prolonged anodization of the thicker film although the anodization process more usually has a smoothing effect on the metal-oxide interface. A more likely source

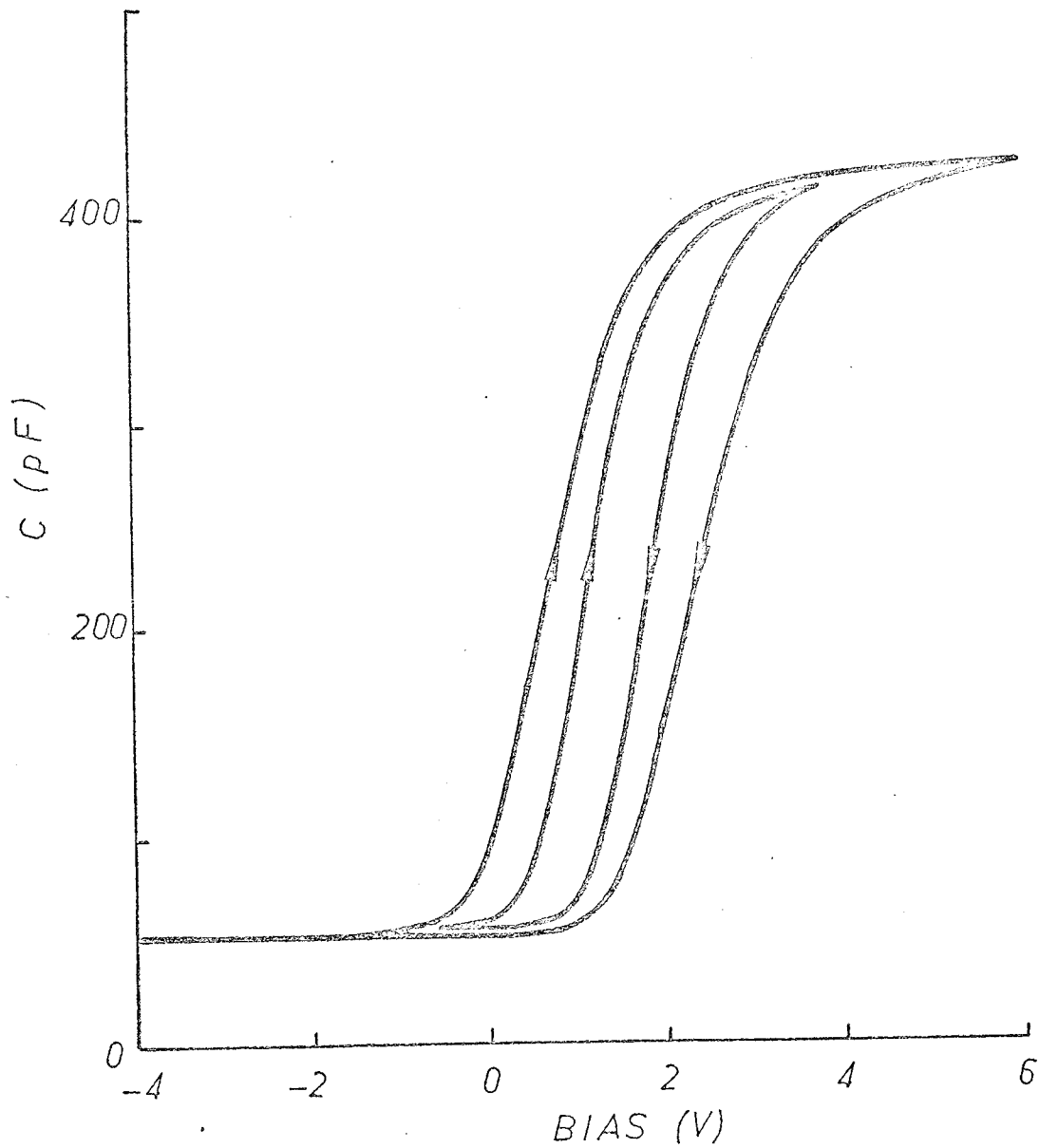


Fig. 11.10 High frequency capacitance voltage curves for sample Al-Si₂ after annealing for 30 minutes at 300°C in nitrogen and then for one hour at 350°C in hydrogen.

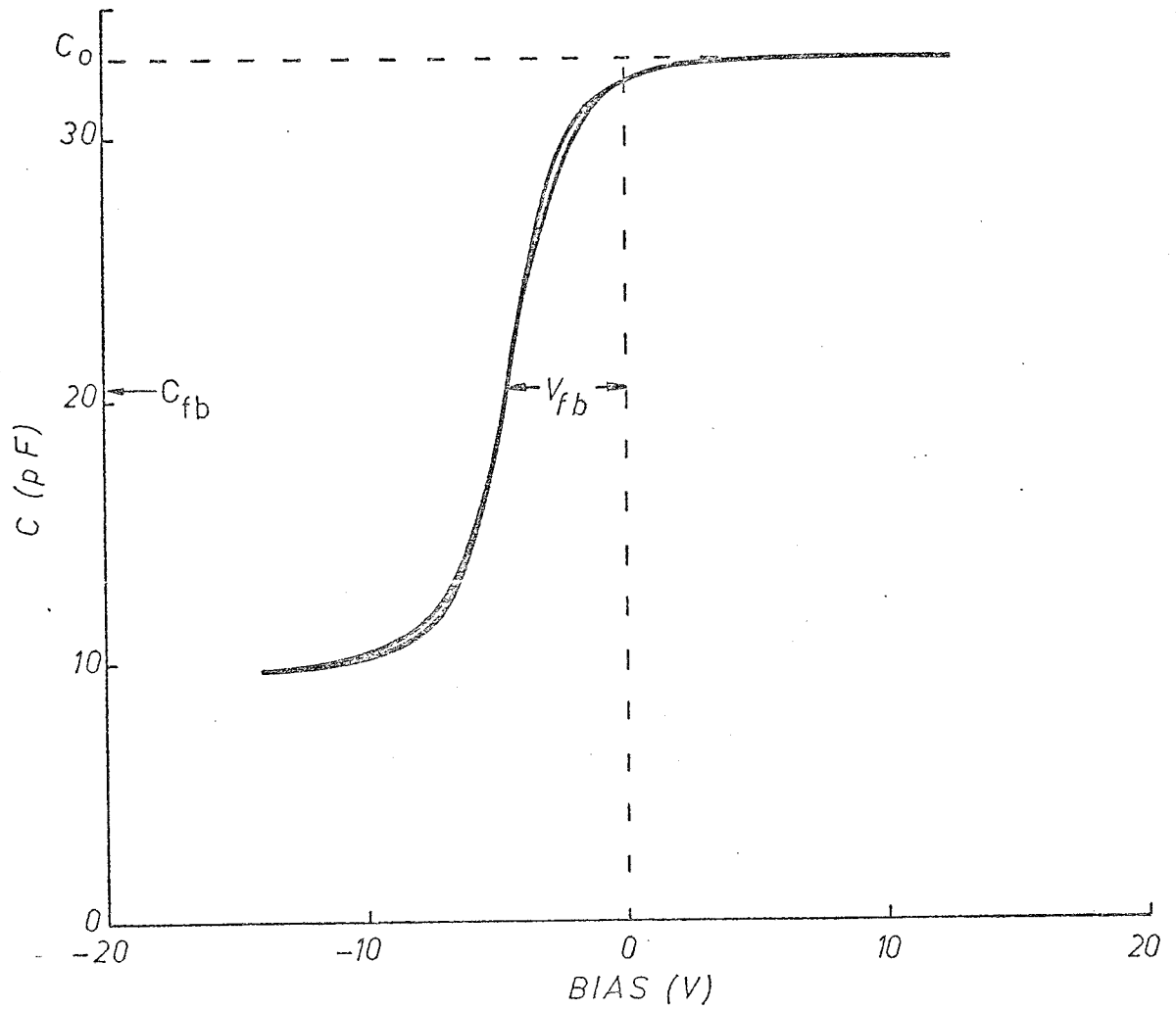


Fig. 11.11 High frequency capacitance-voltage curve for sample Si1 anodized in the positive column of system B (see section 10.7), with evaporated gold counterelectrode. Oxide thickness = 700Å, substrate donor concentration $N_D = 1 \times 10^{15} \text{ cm}^{-3}$.

of the interface roughness could be roughness in the original outer surface of the aluminum film. While the aluminum films vacuum evaporated on the polished silicon surface had a mirror-like appearance to the unaided eye, some samples were found to scatter the ellipsometer laser light over a wide angular range, even approaching the 70° angle of the incident beam direction. A certain surface roughness must be expected because of the randomness of the vacuum deposition process. For films deposited on room temperature substrates (as here) where little surface diffusion is possible after impingement, porous film structures can result, and considerable roughness which increases with film thickness may be observed (Neugebauer 1970). Thus the interface roughness problem might be largely alleviated by depositing the aluminum film onto heated substrates, and removal of the native SiO_2 film prior to metal deposition (e.g. by rf sputter etching) may yield additional improvement. A porous aluminum film structure may also be the cause of the rather low permittivity and refractive index of the Al_2O_3 films. Because of the above problems with film uniformity only a very rudimentary switching behaviour was observed, and it could not be determined beyond doubt that this behaviour was due to charge transfer to the oxide - oxide interface as opposed to the filling of hole traps associated with oxide defects near the semiconductor-oxide interface. However, the anodization approach offers promise, at least for certain applications not requiring long storage retention times such as memory switches for matrix-addressed electroluminescent displays (Fischer 1971).

XII. CONCLUSIONS

The phenomenon of anodization in the plasma of a low pressure oxygen glow discharge has been studied from both the viewpoint of the mechanisms involved and that of potential applications of the process. Using automated in situ ellipsometry and electrical probe techniques, the following aspects were investigated: (a) the dependence of the anodization rate on conditions in the discharge, (b) the significance of the supply of negative oxygen ions from the neutral plasma, (c) the relation between ionic current, electrostatic field strength and temperature in the oxide, and (d) an initial study of the anodization of metal films on silicon for MIS devices.

The following results were obtained in these studies:

- (1) The anodization process does not utilize gaseous negative oxygen ions present in the neutral plasma. This was demonstrated by the negligible variation in anodization rate when the transport of such ions to the sample surface was varied by means of combined dc and rf biasing.
- (2) The mechanism of species transport through the oxide during plasma anodization is the same high field ionic conduction process that is operative in solution anodization. Evidence for this was that the ionic current density during plasma anodization was exponentially dependent on the oxide field strength, and this relation and its temperature dependence agreed with the data for solution anodization of the respective metal, the agreement being excellent in the case of an aluminum sample anodized in the negative glow region. A deviation from

solution anodization field strength values observed under certain conditions was thought to be the result of ultraviolet radiation from the discharge.

- (3) With the above observations, the variation of the anodization rate with discharge conditions such as pressure, discharge current and discharge dimensions can be attributed principally to a dependence of the electric field strength in the oxide on the energy distribution and density of electrons in the plasma, with these implications:

(a) The anodization rate is governed by the high field ionic transport mechanism in the oxide, and is limited to about 1 to $10\overset{\circ}{\text{A}}$ per minute by the magnitude of the random electron current density of the plasma, which determines the maximum current density that can be drawn from the plasma without disturbing the electron energy distribution, and therefore the maximum oxide field strength. This is shown by the decrease in growth rate obtained when the total current density drawn from the plasma is increased too far above the random flux level.

(b) The low current efficiency of the plasma process appears to be a consequence of the plasma electrons having a wide distribution of energies, some of which may be quite high compared with those encountered in the solution case. These high electron energies result in hot electrons injected in the oxide, which give very large currents through the oxide at the field strengths necessary for ionic transport.

(c) The type of plasma best suited to anodization would be

one in which the electrons all have relatively low energies but are present in a sufficient density to maintain the conductivity of the plasma. This seems to be borne out by the increased anodization rates obtainable in dc arc and rf induced discharges.

- (4) In the fabrication of thin dielectric films for MIS devices by the plasma anodization of deposited metal films on silicon, the utility of ellipsometry for identifying the point when the metal is totally converted to oxide depends strongly on the optical properties of the metal. By anodizing thin layers of aluminum on silicon substrates, MIS structures were obtained with a surface state density low enough to allow strong modulation of surface charge in the silicon, and storage effects were observed, although these were only short-lived. The optical measurements indicated considerable spacial nonuniformity in the conversion of the residual metal layer to oxide, which was attributed to inhomogeneties in the starting layer of aluminum. Careful control of metal deposition conditions should permit devices with stable memory storage properties to be fabricated.

REFERENCES

1. Alexeff, I., and Jones, W.D., Appl. Phys. Lett. 9, 77 (1966).
2. Amsel, G., Cherki, C., Feillade, G., and Nadai, J.P., J. Phys. Chem. Solids 30, 2117 (1969).
3. Archer, R.J., J. Opt. Soc. Am. 52, 970 (1962).
4. Aspnes, D.E., *ibid.* 61, 1077 (1971).
5. Aspnes, E.D. and Studna, A.A., Applied Opt. 10, 1024 (1971).
6. Azzam, R.M.A. and Bashara, N.M., J. Opt. Soc. Am. 61, 1380 (1971).
7. Barrett, M.A., in "Ellipsometry in the Measurement of Surfaces and Thin Films", Symposium Proceedings, Washington, 1963.
8. Bean, C.P., Fisher, J.C., and Vermilyea, D.A., Phys. Rev. 101, 551 (1956).
9. Bellina, J.J., Jr., Lederich, R.J., and O'Neal, J.E., J. Appl. Phys. 43, 287 (1972).
10. Born, M. and Wolf, E., "Principles of Optics", Pergamon Press, 1959.
11. Boyd, R.L.F. and Thompson, J.B., Proc. Roy. Soc. A 252, 102 (1959).
12. Burge, D.K. and Bennett, H.E., J. Opt. Soc. Am. 54, 1428 (1964).
13. Cobine, J.D., "Gaseous Conductors", Dover, New York, 1958.
14. Cornish, W.D., M.A.Sc. Thesis, U.B.C., Dept. of Elec. Eng., 1972.
15. Davies, J.A., Domeij, B., Pringle, J.P.S., and Brown, F., J. Electrochem. Soc. 112, 675 (1965).
16. Dell'Oca, C.J., Ph.D. Thesis, U.B.C., Dept. of Elec. Eng., 1969.
17. Dell'Oca, C.J. and Young, L., Surface Sci. 16, 331 (1969).
18. Dell'Oca, C.J., Pulfrey, D.L. and Young, L., Physics of Thin Films 6, 1 (1971).
19. Dignam, M.J., Goad, D. and Sole M., Can. J. Chem. 43, 800 (1965).
20. Dote, T., Ichimiya, T., Takeuchi, M. and Yabuuchi, S., J. Phys. Soc. Japan 21, 2426 (1966).
21. Engel, A. von, "Ionized Gases", Oxford Univ. Press, London, 1965.
22. Feuersanger, A.E., Proc. IEEE 52, 1463 (1964).

23. Fischer, A.G., IEEE Trans. Electron Devices 15, 802 (1971).
24. Francis, G., "Ionization Phenomena in Gases", Butterworth, Wash. D.C., 1960.
25. Golovashkin, A.I., Sov. Phys. JETP, 29, 27 (1969).
26. Goldstein, R.M., Lederich, R.J. and Leonhard, F.W., J. Electrochem. Soc. 117, 503 (1970).
27. Goruk, W.S., Young, L. and Zobel, F.G.R., in "Modern Aspects of Electrochemistry", (J.O'M. Bockris, ed.), Vol. 4, p. 176, Plenum Press, New York, 1966.
28. Gray, P.V., Proc. IEEE 57, 1543 (1969).
29. Harkness, A.C. and Young, L., Can. J. Chem. 44, 2409 (1966).
30. Harrop, P.J. and Campbell, D.S., Thin Solid Films 2, 273, (1968).
31. Hartman, T.E., J. Vac. Sci. Technol. 2, 239 (1965).
32. Hass, G. and Waylonis, J.E., J. Opt. Soc. Am. 51, 719 (1961).
33. Hathorn, F.G.M., Pulfrey, D.L. and Young, L., unpublished data (1972).
34. Hiraki, A., Lugujo, E. and Mayer, J.W., J. Appl. Phys. 43, 3643 (1972).
35. Holland, L., Putner, T. and Ball, R., Brit. J. Appl. Phys. 11, 167 (1960).
36. Holmes, D.A., J. Opt. Soc. Am. 54, 1115 (1964).
37. Husted, D., Gruss, L. and Mackus, T., J. Electrochem. Soc. 118, 1989 (1971).
38. Ignatov, D.V., Dokl. Akad. Nauk. SSSR 54, 331 (1946).
39. Ignatov, D.V., J. Chim. Phys. 54, 96 (1957).
40. Jaeger, N.I., Klein, G.P. and Myrvaagnes, B., J. Electrochem. Soc. 119, 1531 (1972).
41. Jeans, J.H., "An Introduction to the Kinetic Theory of Gases", Cambridge Univ. Press, 1940.
42. Jennings, T.A. and McNeill, W., J. Electrochem. Soc. Extended Abstr. 6, 53 (1969).
43. Johnson, M.C., IEEE Trans. Component Parts 11, 1 (1964).

44. Kooi, E., "The Surface Properties of Oxidized Silicon", Springer-Verlag: New York, 1966 .
45. Kraitchman, J., J. Appl. Phys. 38, 4323 (1967).
46. Kumagai, S. and Young. L., J. Electrochem. Soc. 111, 1411 (1964).
47. Lee, W.L., Olive, G., Pulfrey, D.L. and Young, L., J. Electrochem. Soc. 117, 1172 (1970).
48. Ligenza, J.R., J. Appl. Phys. 36, 2703 (1965).
49. Ligenza, J.R., Washington Meet., Electrochem. Soc., 1971 Extended Abstr. No. 6 (1971).
50. Ligenza, J.R. and Kuhn, M., Solid State Technol. 13, 33 (1970).
51. Llewellyn-Jones, F., "The Glow Discharge", Methuen, London, 1966.
52. Locker, L.D. and Skolnick, L.P., Appl. Phys. Lett. 12, 396 (1968).
53. Loeb, L.B., "Basic Processes in Gaseous Electronics", Univ. of Calif. Press, 1955.
54. MacKenzie, K.R., Taylor, R.J., Cohn, D., Ault, E. and Ikezi, H., Appl. Phys. Lett. 18, 529 (1971).
55. Makara, E.V., Mikhalkin, V.S. and Odynets, L.L., Elektrokimiya 7, 1096 (1971).
56. Masing, L., Orme, J.E. and Young L., J. Electrochem. Soc., 108, 428 (1961).
57. McCrackin, F.L., Passaglia, E., Strombert, R.R. and Steinberg, H.A., J. Res. Nat. Bur. Stand. A, 67, 303 (1963).
58. McCrackin, F.L., "A Fortran Program for Analysis of Ellipsometer Measurements", NBS Tech. Note 479 (U.S. Gov't. Printing Office, Washington, D.C., 1969).
59. McCrackin, F.L., J. Opt. Soc. Am. 60, 57 (1970).
60. McDaniel, E.W., "Collision Phenomena in Ionized Gases", Wiley, New York, 1964.
61. Micheletti, F.B., Norris, P.E. and Zaininger, K.H., RCA Review, 31, 330 (1970).
62. Mikhalkin, V.S. and Odynets, L.L., Elektrokimiya 6, 359 (1970).
63. Mikhalkin, V.S. and Odynets, L.L., Elektrokimiya 7, 848 (1971).
64. Miles, J.L. and Smith, P.H., J. Electrochem. Soc. 110, 1240 (1963).

65. Morgan, R., *J. Mater. Sci.* 6, 1227 (1971).
66. Nazarova, R.I., *Russ. J. Phys. Chem.* 36, 522 (1962).
67. Neugebauer, CA., in "Handbook of Thin Film Technology", (Maisel L.I. and Glang R. Eds.), McGraw-Hill, New York, 1970.
68. Nicollian, E.H. and Berglund, C.N., *J. Appl. Phys.* 41, 3052 (1970).
69. Nilson, J.A. and McKay, D.H., RCA Report No. MNLD-71-TR-003, 1971.
70. Norris, P.E. and Zaininger, K.H., Final Report, U.S. Navy Contract No. N00039-69-C0540, Feb. 1970.
71. O'Hanlon, J.F., *Appl. Phys. Lett.* 14, 127 (1969).
72. O'Hanlon, J.F., *J. Vac. Sci. Technol.* 7, 330 (1970).
73. O'Hanlon, J.F., *J. Electrochem. Soc.* 118, 270 (1971).
74. O'Hanlon, J.F. and Pennebaker, W.B., *Appl. Phys. Lett.*, 18, 554 (1971).
75. Oldham, W.G., *J. Opt. Soc. Am.* 57, 617 (1967).
76. Olive, G., M.A.Sc. Thesis, U.B.C., Department of Electrical Engineering, 1969.
77. Olive, G., Pulfrey, D.L. and Young, L., *J. Electrochem. Soc.* 117, 945 (1970).
78. Olive, G., Pulfrey, D.L. and Young, L., *Thin Sol. Films* 12, 427 (1972).
79. Ord, J.L., *Surface Sci.* 16, 155 (1969).
80. Ord, J.L., Hopper, M.A. and Wang, W.P., *J. Electrochem. Soc.* 119, 439 (1972).
81. Pappu, R.V., Ph.D. Thesis, Carleton Univ., 1972.
82. Passaglia, E., Stromberg, R.R. and Kruger, J., "Ellipsometry in the Measurement of Surfaces and Thin Films", Symposium Proceedings, Washington 1963.
83. Pelleg, J., *J. Less-Common Metals* 12, 419 (1967).
84. Philipp, H.R. and Taft, E.A., *Phys. Rev.* 120, 37 (1960).
85. Pickar, K.A., *Solid State Electr.* 13, 303 (1970).
86. Priest, J., Caswell, H.L. and Budo, Y., *J. Appl. Phys.* 34, 347 (1963).
87. Pulfrey, D.L. and Roche, J., to be published in *Applied Optics*, July 1973.

88. Ramasubramanian, N., J. Electrochem. Soc. 117, 947 (1970).
89. Randall, J.J., Bernard, W.J. and Wilkinson, R.R., Electrochim. Acta 10, 183 (1965).
90. Ruiz-Urbieta, M., Sparrow, E.M. and Eckert, E.R.G., J. Opt. Soc. Am. 61, 351 (1971).
91. Salama, C.A.T., J. Electrochem. Soc. 117, 913 (1970).
92. Scholz, F., M.A.Sc. Thesis, U.B.C., Dept. of Elect. Eng., 1971.
93. Schrijner, A.J. and Middlehoek, A., J. Electrochem. Soc. 111, 1167 (1964).
94. Shousha, A.H.M., Pulfrey, D.L. and Young, L., J. Appl. Phys. 43, 16 (1972).
95. Simpson, A.W. and Lucas, J.M., Proc. Brit. Ceramic Soc. No. 18, 117 (1970).
96. Skelt, E.R. and Howells, G.M., Surface Sci. 7, 490 (1967).
97. Slawicki, G.D., Ph.D. Thesis, Univ. of Maryland, 1969.
98. Swift, J.D. and Schwar, M.J.R., "Electrical Probes for Plasma Diagnostics", Iliffe, London, 1970.
99. Sze, S.M., "Physics of Semiconductor Devices", Wiley, New York, 1969.
100. Thompson, J.B., (a) Proc. Roy. Soc. A262, 503 (1961).
101. Thompson, J.B., (b) Proc. Roy. Soc. A262, 519 (1961).
102. Tibol, G.J., Insulation (Libertyville, Ill.) 11, 25 (1965).
103. Tibol, G.J. and Hull, R.W., J. Electrochem. Soc. 111, 1368 (1964).
104. Tibol, G.J. and Kauffman, W.M., Proc. IEEE 52, 1465 (1964).
105. Twiddy, N.D., Proc. Roy. Soc. A262, 379 (1961).
106. Vermilyea, D.A., J. Electrochem. Soc. 110, 345 (1963).
107. Vratny, F., J. Amer. Ceram. Soc. 50, 283 (1967).
108. Wakefield, J. and Gamble, H.S., Electronics Letters 6, 507 (1970).
109. Wallmark, J.T. and Scott, J.H., Jr., RCA Review 30, 335 (1969).
110. Wang, C.C., Zaininger, K.H. and Duffy, M.T., RCA Review 31, 728 (1970).
111. Waxman, A. and Mark, G., Solid State Electr. 12, 751 (1969).

112. Waxman, A. and Zaininger, K.H., Appl. Phys. Lett. 12, 109 (1968).
113. Weinreich, O.A., J. Appl. Phys. 37, 2924 (1966).
114. Whitlock, W.S. and Bounden, J.E., Proc. Phys. Soc. 77, 845 (1961).
115. Whitmore, R.E. and Vossen J.L., IEEE Trans. Parts, Mater. Pakag. (1), S10 (1965).
116. Winterbottom, A.B., "Optical Studies of Metal Surfaces", The Royal Norwegian Scientific Society Report No. 1, F. Bruns, publisher, 1955.
117. Worledge, P.L. and White, D., Brit. J. Appl. Phys. 18, 1337 (1967).
118. Young, L., Proc. Roy. Soc., London, Ser. A 244, 41 (1958).
119. Young, L., (a) Proc. Roy. Soc., London, Ser. A 258, 496 (1960).
120. Young, L., (b) Can. J. Chem. 38, 1141 (1960).
121. Young, L., "Anodic Oxide Films", Academic Press, New York, 1961.
122. Young, L. and Zobel, F.G.R., J. Electrochem. Soc. 113, 277 (1966).
123. Zaininger, K.H. and Wang. C.C., Proc. IEEE 57, 1564 (1964).

APPENDICES

The origin of some formulae used in the text are given in appendices A and B below. They are mostly from standard results of the kinetic theory of gases, and are taken from Jeans 1940 and McDaniel 1964. Appendix C is a brief summary of a recently reported method of determining the plasma potential, with some experimental results relevant to this method.

Appendix A: Velocity and Energy Distributions.

The particles of a gas in thermodynamic equilibrium at temperature T have speeds distributed according to Maxwell's distribution, which may be expressed in the form

$$f(v)dv = 4\pi n \left(\frac{m}{2\pi kT}\right)^{3/2} v^2 \exp\left[-\frac{mv^2}{2kT}\right] dv \quad (\text{A.1})$$

where $f(v)dv$ is the number of particles with speeds between v and $v+dv$, m is the particle mass and n the number density of particles in the gas. For an isotropic distribution the random particle flux crossing a unit area in one direction is given by $n\bar{v}/4$, where \bar{v} is the mean random speed and the factor $(1/4)$ arises because only half the population density have a component of velocity towards the probe, and the average of the direction cosine over a hemisphere = $1/2$. The distribution function of (A.1) gives \bar{v} as

$$\bar{v} = \frac{1}{n} \int_0^{\infty} f(v)v dv = \left(\frac{8kT}{\pi m}\right)^{1/2} \quad (\text{A.2})$$

Making the substitutions $\epsilon = mv^2/2$ and $dv = d\epsilon/(2m\epsilon)^{1/2}$ in (A.1) gives the energy distribution:

$$f(\epsilon)d\epsilon = C n \epsilon^{1/2} \exp\left[\frac{-\epsilon}{kT}\right] d\epsilon \quad (\text{A.3})$$

where $f(\epsilon) d\epsilon$ is the number of particles with kinetic energy in the range ϵ to $\epsilon + d\epsilon$ and $C = 2(\pi)^{-1/2} (kT)^{-3/2}$.

For particles in an external force field, the Boltzmann factor $\exp(-V/kT)$, where V is the potential energy perparticle, must be included in (A.3) above to give the Maxwell-Boltzmann energy distribution:

$$f(\epsilon) d\epsilon = C n_0 \epsilon^{1/2} \exp\left[-\frac{+V}{kT}\right] d\epsilon \quad (\text{A.4})$$

where n_0 is the particle number density at a point at which $V = 0$.

In this case the variation of particle density with position is given by Boltzmann's law:

$$n = n_0 \exp\left[\frac{-V}{kT}\right] \quad (\text{A.5})$$

Appendix B: Mean Free Path Lengths and Sheath Thickness

(a) Mean free paths according to a solid elastic sphere model.

Consider a gas containing N_g molecules/cm³. If the molecules are assumed to be impenetrable elastic spheres of diameter d_g whose velocities are distributed according to the Maxwellian law with a mean velocity \bar{v} , it can be shown (Jeans 1940) that the number of collisions per cm³ per sec. is $(\pi/\sqrt{2})N_g^2 d_g^2 \bar{v}$. Each collision marks the end of two free paths (one for each of the collision partners), so that the total number of free paths executed per cm³-sec. is $\sqrt{2}\pi N_g^2 d_g^2 \bar{v}$. The total length of all these free paths is $N_g \bar{v}$, so that the mean free path length is

$$\lambda = \frac{1}{\sqrt{2}\pi N_g d_g^2} \quad (\text{B.1})$$

If the gas also contains N_c charged carriers of diameter d_c then the mean free path of the carriers is

$$\lambda_c = [\sqrt{2}\pi N_c d_c^2 + \pi N_g d_{gc}^2 (1 + m_c/m_g)^{1/2}]^{-1} \quad (\text{B.2})$$

where m_c and m_g are the carrier and gas molecule masses respectively, and $d_{gc} = (d_g + d_c)/2$.

For positive ions moving in their own gas, $m_c = m_g$ and (B.2) reduces to (B.1). In the case of electrons, $m_c \ll m_g$ and $d_c \ll d_g$ giving

$$\lambda_e = \frac{4}{\pi N_g d_g^2} \quad (\text{B.3})$$

This simplified treatment assumes the rigid sphere particles to interact only at the instant of impact, and may be seriously in error for electrons. However, it can be used to obtain an expression for the mobility μ of ions in a low electric field (Langevin's simple theory - see McDaniel 1964). On collision with a molecule, each ion was assumed to lose all of the energy that it had acquired from the field during the preceding free path, and the expression arrived at was

$$\mu = \frac{e\lambda}{m\bar{v}} \quad (\text{B.4})$$

(b) Estimation of the sheath thickness (McDaniel 1964)

The interface between a plasma and a solid surface consists of a sheath region with a net space charge which in effect protects the plasma from the physical boundary. In order to estimate the thickness of the sheath consider a thin slab-like region, of half-width L , perpendicular to the x axis and centred about the origin of the latter, in which the electron concentration n_e greatly exceeds the positive ion concentration n_+ . The resulting net charge gives rise to a potential

difference ΔV between the centre of the slab and the neutral plasma boundaries governed by Poisson's equation, which gives

$$\frac{d^2V}{dx^2} = \frac{n_e e}{\epsilon_0} \quad (\text{B.5})$$

where ϵ_0 is the free space permittivity. Integrating and putting

$\frac{dV}{dx} = 0$ and $V = 0$ at $x = 0$ gives

$$V = \frac{n_e e x^2}{2\epsilon_0} \quad (\text{B.6})$$

i.e.

$$\Delta V = \frac{n_e e L^2}{2\epsilon_0} \quad (\text{B.7})$$

The potential appears as a "hill" to electrons and a "trough" to ions.

The width of the region over which $n_e \gg n_+$ cannot be arbitrarily large, since a point would be reached at which the electrical potential energy would exceed the mean thermal energy and charge flow would then occur in such a way as to restore neutrality. Taking the mean kinetic energy in one direction as $kT_e/2$ leads to

$$\frac{kT_e}{2} = \frac{n_e e^2 L_{\max}^2}{2\epsilon_0} \quad (\text{B.8})$$

i.e.

$$L_{\max} = \left[\frac{\epsilon_0 kT_e}{n_e e^2} \right]^{1/2} \quad (\text{B.9})$$

This expression for the distance over which a plasma can have an appreciable departure from charge equilibrium is equivalent to the Debye shielding length for ions by electrons as derived by applying Poisson's equation to the charge distribution around a single ion in the neutral plasma. Thus the thickness of the space charge sheath region in front

of a probe at moderate potential, i.e. $\leq kT_e/e$ from plasma potential, is of the order of the Debye length.

Appendix C: The 'Sounding Probe' Method of Determining Plasma Potential

This method, proposed by Dote et al. 1966, is based on the dependence of the charged particle density within the sheath region of a probe on the probe potential. As the probe is biased negatively with respect to plasma potential, the electron density at a position in the sheath decreases (some electrons are repelled and a net positive space charge results). When the probe is biased above plasma potential, the electron density in the now negative space charge sheath again decreases, since the electron current density to the sheath edge is the constant random current from the plasma, whereas the electron velocity increases with positive probe bias. The same arguments can be applied to the positive ion density, so that the densities of both positively and negatively charged particles in the sheath become a maximum when the probe is at plasma potential. The current to a very small probe ('sounding probe') placed close to a larger reference probe and held at constant voltage (with respect to the anode) is used as a measure of charge carrier density. Assuming that variations in the sounding probe current when the reference probe voltage is varied are due only to carrier density variations in the sheath region of the larger probe, then plasma potential is taken as the reference probe voltage which maximizes the sounding probe current.

For the above assumption to be valid, the sounding probe should be biased well into either its positive ion or electron saturation current collection regions, rather than between (or near) plasma potential and floating potential where the net current depends on the competition between both carrier densities. This can be seen in Fig. C.1, where

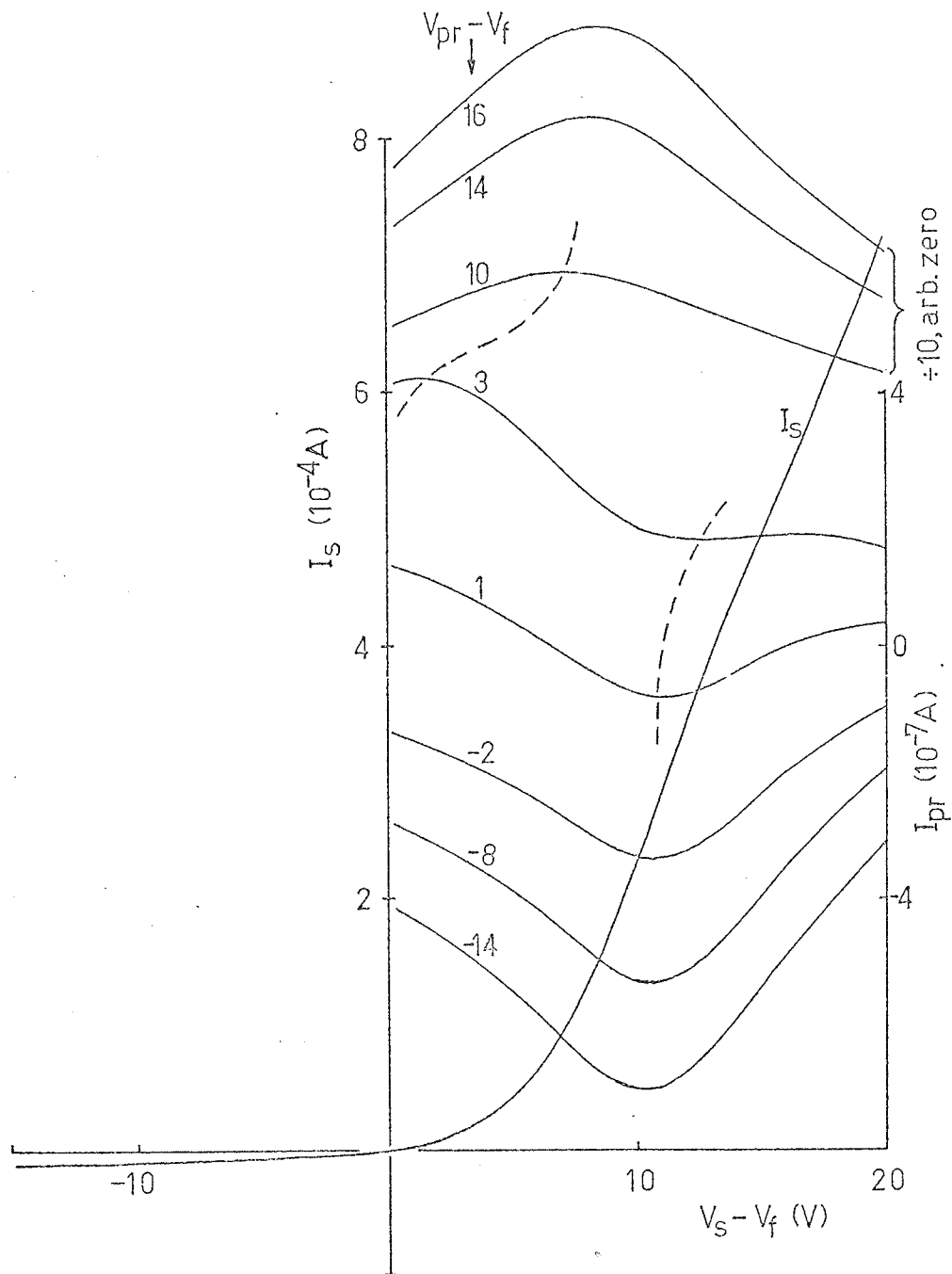


Fig. C.1 Sounding probe current versus reference probe voltage for various values of sounding probe bias. Reference probe: 8.5 mm dia. gold-plated tantalum sample; sounding probe: 1 mm dia. gold ball probe. Reference probe current-voltage characteristic also shown.

sounding probe current (I_{pr}) versus reference probe voltage ($V_s - V_f$) curves for all three regions are given. An oxide-masked, gold-plated 8.5 mm diameter area on a tantalum sample constituted the reference probe, and the 1 mm diameter gold ball sounding probe was situated 2 mm in front. An order of magnitude estimate of the sheath thickness, as furnished by the Debye shielding length $\lambda_d = (\epsilon_o kT_e / n_e e^2)^{1/2}$, gives ~1 mm for the measured values $kT_e = 2\text{eV}$ and $n_e = 1 \times 10^8 \text{ cm}^{-3}$, but from the results in Fig. C.1 the sounding probe is clearly within the influence of the reference probe field. However, it appears that the electron current maximum may be the more reliable indicator of plasma potential, since the reference probe voltage which maximized the positive ion current was found to vary with sounding probe-reference probe distance in the range 0.5 mm to 4 mm, whereas the electron peak was relatively stable.

Appendix D: Summary of in situ Ellipsometry Results for the
Plasma Anodization of Niobium and Tantalum

The following sets of Δ , ψ pairs were obtained from ellipsometry measurements at different stages of oxide growth, and the pairs in each set are arranged in order of measurement, i.e., increasing oxide thickness. The first three data sets, from system A, were determined using light of wavelength 5461Å and an angle of incidence of 65°.

Sample Nb1: electropolished polycrystalline niobium.

| Δ | ψ |
|----------|--------|
| 125.50 | 31.55 |
| 116.84 | 32.03 |

| Δ | ψ |
|----------|--------|
| 109.86 | 32.49 |
| 99.88 | 33.29 |
| 91.14 | 34.50 |
| 80.58 | 37.70 |
| 64.58 | 49.66 |
| 60.42 | 54.18 |
| 58.48 | 55.78 |
| 1.70 | 73.04 |
| 344.50 | 73.11 |
| 280.32 | 49.02 |
| 268.82 | 39.57 |
| 247.68 | 32.50 |
| 232.96 | 30.56 |

This data was fitted by a model consisting of two non-absorbing films growing simultaneously but at different rates. Assuming optical constants of 3.60-3.60j for the niobium substrate (Young and Zobel 1966), the outer film had a refractive index of 2.15 and comprised 40% of the total oxide thickness, and the inner film had an index of 2.37.

Sample Nb2: electropolished polycrystalline niobium.

| Δ | ψ |
|----------|--------|
| 131.20 | 31.30 |
| 118.52 | 32.18 |
| 97.62 | 33.88 |
| 73.25 | 43.37 |
| 54.58 | 60.25 |
| 47.98 | 64.79 |

| Δ | ψ |
|----------|--------|
| 41.44 | 67.98 |
| 10.36 | 73.85 |
| 307.50 | 68.45 |
| 298.70 | 65.13 |
| 286.08 | 57.46 |
| 274.70 | 46.07 |
| 258.38 | 34.19 |

This data was also fitted with a two non-absorbing films model and with the same substrate optical constants as above. The inner and outer film indices were 2.38 and 2.12 respectively, with the outer film comprising 47.5% of the total thickness.

Sample Nb5: electropolished polycrystalline niobium.

| Δ | ψ |
|----------|--------|
| 134.85 | 31.24 |
| 107.41 | 32.07 |
| 77.09 | 38.92 |
| 43.15 | 61.71 |
| 29.60 | 66.84 |
| 262.99 | 35.49 |
| 251.10 | 32.67 |
| 122.91 | 32.04 |
| 94.48 | 34.41 |

This data was analyzed using a two non-absorbing films model, the outer film of refractive index 2.17 comprising 20% of the total oxide thickness, the inner film having an index of 2.36 on a substrate with optical constants 3.60-3.60j.

The remaining results were all obtained at a wavelength of 6328Å with an angle of incidence of 69.29°, in system B.

Sample Nb4: electropolished single crystal niobium, orientation (110).

| Δ | ψ |
|----------|--------|
| 112.58 | 31.59 |
| 106.54 | 32.21 |
| 95.20 | 33.49 |
| 88.74 | 34.37 |
| 85.52 | 34.83 |
| 84.99 | 34.98 |
| 81.31 | 35.77 |
| 74.96 | 37.54 |
| 68.03 | 41.12 |
| 60.32 | 52.03 |
| 57.46 | 56.82 |
| 50.90 | 63.99 |
| 33.19 | 72.22 |
| 8.37 | 75.69 |
| 349.36 | 75.86 |
| 332.16 | 74.52 |
| 314.56 | 70.63 |
| 301.38 | 63.63 |
| 294.59 | 56.24 |
| 292.56 | 52.94 |
| 289.02 | 46.68 |
| 286.29 | 42.70 |
| 284.54 | 40.88 |

A simple model of a single non-absorbing oxide film with a refractive index of 2.36 growing on a substrate of index 3.90-4.49j was found to fit this data without a separate substrate index determination, and growth rates were estimated on this basis.

Sample Nb3: electropolished polycrystalline niobium.

| Δ | ψ |
|----------|--------|
| 122.73 | 29.51 |
| 107.57 | 30.88 |
| 92.04 | 34.19 |
| 87.34 | 35.08 |
| 81.03 | 36.51 |
| 66.51 | 43.51 |
| 60.43 | 51.84 |
| 39.84 | 69.83 |
| 340.86 | 75.55 |
| 307.27 | 66.66 |
| 295.27 | 55.57 |
| 293.44 | 53.34 |
| 289.48 | 47.03 |
| 281.17 | 38.28 |
| 258.41 | 32.20 |
| 257.89 | 31.99 |
| 212.30 | 28.93 |
| 166.71 | 28.43 |

The model used to fit this data consisted of two non-absorbing films growing simultaneously on a substrate of refractive index 3.55-3.75j, the outer film of index 1.80 comprising 28% of the total oxide thickness,

the inner film having an index of 2.24. The substrate optical constants used here were determined with data from the solution anodization of a similar polycrystalline sample.

Sample Ta2: electropolished polycrystalline tantalum.

| Δ | ψ |
|----------|--------|
| 100.27 | 27.62 |
| 81.62 | 31.71 |
| 68.95 | 38.12 |
| 63.09 | 51.67 |
| 62.28 | 56.94 |
| 61.64 | 59.90 |
| 59.49 | 65.11 |
| 50.03 | 74.20 |
| 33.03 | 79.16 |
| 10.06 | 81.50 |
| 347.37 | 81.81 |
| 340.73 | 81.60 |
| 321.03 | 80.55 |
| 302.61 | 77.20 |
| 289.90 | 70.12 |
| 285.36 | 64.44 |
| 282.19 | 58.64 |
| 280.34 | 53.33 |
| 277.81 | 45.94 |
| 275.81 | 40.70 |
| 271.93 | 35.70 |
| 260.02 | 30.66 |

| Δ | ψ |
|----------|--------|
| 241.87 | 27.01 |
| 219.53 | 24.88 |
| 197.41 | 23.87 |
| 176.14 | 23.74 |
| 151.64 | 24.58 |
| 132.45 | 25.75 |
| 131.52 | 25.92 |
| 122.51 | 26.67 |
| 116.17 | 27.20 |

Using 2.46-2.56j for the optical constants of the substrate as determined from solution anodization measurements, the best fit obtained for the above data was given by an oxide model of two non-absorbing films growing simultaneously, the outer film of index 1.88 comprising 80% of the total oxide thickness, the inner film having an index of 1.63.